

ABSTRACT

TIAN, CHUAN. Density Functional Investigation of the Electronic Structures of Some Transition Metal Magnetic Solids and Statistical Methods on Drug Discovery. (Under the direction of Dr. Mike Whangbo, Lexin Li, and Wenbin Lu).

We studied the electronic structures of several transition-metal magnetic solids on the basis of density functional theory (DFT) calculations to account for their physical properties. Our study is focused on two subjects. One is concerned with the ferroelectric polarization induced by a spiral-spin order in magnetic solids. A spiral-spin order arises from spin frustration and removes inversion symmetry, thereby leading to ferroelectric polarization. The spiral-spin along one crystallographic direction can be cycloidal as found in MnWO_4 or helical as found in MnSb_2S_4 . We examined the spin frustration leading to these spiral-spin structures and calculate the ferroelectric polarizations of these compounds. The second subject is concerned with how the electron localization in transition metal ions is affected by their chemical environments. At the current level of DFT, the electron correlation associated with transition metal d states is treated by DFT plus onsite repulsion U (DFT+ U) calculations in which U acts as an empirical parameter. In general, with increasing the spatial extension of the d orbital, the associated electron correlation should decrease, thereby decreasing their on-site repulsion U . An apparent exception to this expectation is found in the magnetic solids $\text{RbMn}[\text{Fe}(\text{CN})_6]$ and Sr_2MOsO_6 ($M = \text{Cu}, \text{Ni}$). We explored the cause for this seemingly puzzling observation.

Statistical modeling on drug discovery data, the first step of a new drug development process, is very important from both chemistry and statistics perspectives. From the chemistry perspective, it is very costly and almost impossible to select new drug candidates via huge amount of experiments, even with the help of new techniques in

high throughput screening and combinatorial chemistry. From the statistics perspective, drug discovery data modeling has been challenging because it is difficult to build regression model giving the three features of the data, i.e., high dimensional, imbalance, and mixture regression. In this dissertation, we focus on statistical modeling of drug discovery data. Corresponding to the challenges of modeling drug discovery data, we propose two methods, i.e., the sufficient dimension reduction (SDR) based clustering and the weighted boosting based classification, to model drug discovery data. SDR reduces the dimension of the descriptor set without loss of regression information. The reduced space is constructed by the information that differentiates the different clusters as well as the underlying regression structure of each cluster. Ranking along the dimension reduction direction is proposed to cluster drug discovery data and found to have the best performance in our simulation studies in terms of mean within group error rate. Classical clustering methods are applied in both the reduced space and the original space finding that the SDR based clustering has smaller error rate than clustering in the original space. Two weighted boosting algorithms are proposed, and one of them is implemented for unbalanced data classification. Both the classification rules are proved satisfying Bayes rule, however, only one has closed-form solutions. These classification results are compared to a benchmark existing method, Adaboost, in both simulated data and real data, and we find that the weighted boosting based classification has smaller mean-within-group error rate. This research work provides a theoretical improvement and sheds a light on future research directions in statistical modeling on drug discovery data.

Density Functional Investigation of the Electronic Structures of Some Transition
Metal Magnetic Solids and Statistical Methods on Drug Discovery

by
Chuan Tian

A dissertation submitted to the Graduate Faculty of
North Carolina State University
in partial fulfillment of the
requirements for the Degree of
Doctor of Philosophy

Chemistry and Statistics

Raleigh, North Carolina

2011

APPROVED BY:

Dr. Jerry Whitten

Dr. Paul Maggard

Dr. Lexin Li
Co-chair of Advisory Committee

Dr. Wenbin Lu
Co-chair of Advisory Committee

Dr. Mike H. Whangbo
Chair of Advisory Committee

DEDICATION

I would like dedicate this work to my parents and my boyfriend.

BIOGRAPHY

Chuan Tian was born to Boqiu Tian and Shuhui Zhao at Jilin, P. R. China in 1984. She graduated from Peking University in 2006 with a BS degree in Chemistry. In 2006 fall she started her graduate studies at North Carolina State University co-majoring in Chemistry and Statistics, and carried out research on the electronic structures of some magnetic solids with Professor Mike H. Whangbo in Chemistry and on drug discovery problems with Professors Lexin Li and Wenbin Lu in Statistics. She received her MS degree in Statistics in 2010, and completed her PhD requirements in both Department of Chemistry and Department of Statistics one year later. Now she is working at Quintiles, a pharmaceutical services company, as a biostatistician.

ACKNOWLEDGMENTS

Warmest thanks to Dr. Mike H. Whangbo, my advisor in Chemistry, for his guidance, inspiration, patience, and support in my decisions. It's Dr. Whangbo that makes me who I am today. To my advisor Dr. Lexin Li and Wenbin Lu, it's really a pleasant journey to learn and work with these two professors on statistics research. To my committee members for their constructive comments and the suggestion for letting me finish my work one by one. Thanks to Dr. Arroway and Dr. Hughes-Oliver for their help along my degree seeking and for bringing in the friendly environment.

Special thanks to my lab mates Dr. Erjun Kan, Dr. Changhoon Lee, Dr. Hongjing Xiang, as well as other group members, for the useful discussions and collaborations. To my good friends for sharing the up and down in all these years in graduate school.

My grateful thanks to my wonderful parents, Boqiu Tian and Shuhui Zhao, always believe in me and support me no matter what my decision is.

Thank you to my boyfriend, Jingyu Zhang, for his love and support. Without him, this would never have come true.

Finally, I appreciate the precious opportunity and friendly environment the Department of Chemistry and Statistics has provided. And, I am grateful to all the faculty, staff, fellow students, and friends who ever helped.

TABLE OF CONTENTS

LIST OF TABLES	viii
LIST OF FIGURES	xi
Part I Density Functional Investigation of Spin-Orbit Coupling Effects on the Magnetic Properties of Some Transition-Metal Magnetic Oxides.....	
	1
Chapter 1 Introduction.....	
	2
1.1 Spin exchange interactions	2
1.2 Spin-orbit coupling in magnetic materials	10
1.3 Magnetic insulating versus metallic state	14
1.4 Charge transfer in magnetic materials	16
1.5 Computational Method	16
1.6 Dissertation outline	20
Chapter 2 Magnetic Structure and Ferroelectric Polarization of MnWO₄ Investigated by Density Functional Calculations and Classical Spin Analysis.....	
	28
2.1 Introduction	30
2.2 Computational details	32
2.3 Spin exchange parameters	33
2.4 Classical spin analysis	37
2.5 Ferroelectric polarization	41
2.6 Concluding remarks	42
Chapter 3 Analysis of the Magnetic Structure and Ferroelectric Polarization of Monoclinic MnSb₂S₄ by Density Functional Calculations	
	59
3.1 Introduction	61
3.2 Computational details	63
3.3 Spin exchanges and magnetic structure	64
3.4 Ferroelectric polarization	67
3.5 Concluding remarks	68
Chapter 4 On the Magnetic Insulating States, Spin Frustration and Dominant Spin Exchange of the Ordered Double-Perovskites Sr₂CuOsO₆ and Sr₂NiOsO₆: Density Functional Analysis.....	
	76
4.1 Introduction	77

4.2	Magnetic insulating state and its implication	80
4.3	Spin exchange interactions	83
4.4	Discussion	85
4.5	Concluding remarks	88
Chapter 5 π-Backdonation Effect of the Cyanide Ligands on the Electron Correlation and Charge Transfer in Prussian Blue $\text{RbMn}[\text{Fe}(\text{CN})_6]$		104
Chapter 6 Conclusions		120
Part II Statistical Methods on Drug Discovery Data . . .		123
Chapter 7 Introduction		124
7.1	Drug Discovery	124
7.2	Statistics in Drug Discovery	127
7.3	Summary and Outline of this Part of the Dissertation	130
Chapter 8 Dimension Reduction Based Clustering on Drug Discovery Data		133
8.1	Introduction	133
8.2	Dimension Reduction Methods	134
8.2.1	Unsupervised Dimension Reduction	135
8.2.2	Supervised Dimension Reduction	136
8.2.3	Sliced Inverse Regression (SIR)	139
8.2.4	Sliced Average Variance Estimation (SAVE)	141
8.2.5	Directional Regression for Dimension Reduction (DIR)	142
8.2.6	Local Sliced Inverse Regression (L-SIR)	144
8.3	Clustering Methods	146
8.3.1	K -means Clustering	146
8.3.2	Model Based Clustering Method	147
8.3.3	Ranking Along Dimension Reduction Direction	150
8.4	Evaluation Criteria	151
8.4.1	Table of confusion	151
8.4.2	Receiver Operating Characteristic (ROC) Curve	152
8.5	Performance on High Dimensional Unbalanced Data	152
8.5.1	Simulation Setup	152
8.5.2	Tune Parameter k in L-SIR	154
8.5.3	Performance of Dimension Reduction (DR) Methods	156
8.5.4	Comparison to Classical Clustering Methods	165
8.6	XUE Data Investigation	167
8.6.1	DR Based Clustering on XUE Data	168

8.6.2	Cross Validation	172
8.7	Concluding Remarks	174
Chapter 9	Boosting Method for Unbalanced Data Classification	176
9.1	Introduction	176
9.2	AdaBoost and Exponential Loss	178
9.2.1	Additive Model	179
9.2.2	Adaboost versus Forward Stagewise Additive Modeling	180
9.3	Weighted Adaboost	184
9.3.1	Mean Within Group Error Rate	185
9.3.2	Weighted Adaboost-1	186
9.3.3	Weighted Adaboost-2	191
9.4	Gradient Boosting and Negative Binomial Log-likelihood	195
9.4.1	Gradient Boosting Algorithm	196
9.4.2	Gradient Boosting Using Negative Binomial Log-likelihood	197
9.4.3	Minimization of Negative Binomial Log-likelihood	198
9.5	Simulation Studies	202
9.6	Real Data Investigation	212
9.7	Concluding Remarks	214
Chapter 10	Conclusions	216
	Bibliography	220

LIST OF TABLES

Table 2.1 Mn...Mn distances (in \AA) associated with the spin exchange paths $J_1 - J_9$ of MnWO_4 and the values of $J_1 - J_9$ (in $k_B K$) determined by Ehrenberg et al. [4] from their neutron scattering study and by the present GGA+U calculations.....	47
Table 2.2 Relative energies (in meV per two formula units) of the ordered spin states of MnWO_4 determined by the present GGA+U calculations.	48
Table 2.3 Four arrangements of the $//c$ -chains with $\uparrow\uparrow\downarrow\downarrow$ spin order and their interchain spin exchange energies, E , per spin site.....	49
Table 2.4 (a) Fractional coordinates of the spin sites in MnWO_4 , (b) Pairs (μ, ν) of the spin sites $(\mu, \nu = 1, 2)$ leading to the spin exchanges $J_1 - J_9$ in MnWO_4 within a unit cell at $[0, 0, 0]$ as well as between unit cells $[0, 0, 0]$ and $[n, k, l]$.	50
Table 3.1 Mn...Mn distances (in \AA) associated with the spin exchange paths $J_1 - J_5$ of monoclinic MnSb_2S_4 and the values of $J_1/k_B - J_5/k_B$ (in K) determined from GGA+U calculations with $U_{eff} = 4$ and 6 eV.....	72
Table 4.1 Relative energies ΔE (in meV per two FUs) of the three ordered spin states of $\text{Sr}_2\text{CuOsO}_6$ determined from the DFT+U calculations as a function of the U_{Cu} and U_{Os} values (in eV). Whether each state is metallic (no band gap) or magnetic insulating (nonzero band gap) is also indicated, where “No” and “Yes” refer to the absence and presence of a band gap, respectively.	92
Table 4.2 Relative energies ΔE (in meV per two FUs) of the four ordered spin states of $\text{Sr}_2\text{NiOsO}_6$ determined from the DFT+U calculations as a function of the U_{Ni} and U_{Os} values (in eV). Whether each state is metallic (no band gap) or magnetic insulating (nonzero band gap) is also indicated, where “No” and “Yes” refer to the absence and presence of a band gap, respectively.	93

Table 4.3 Geometrical parameters associated with the spin exchange paths $J_{ij} = J_1 - J_7$ (in meV) of Sr_2MOsO_6 ($M = \text{Cu}, \text{Ni}$).	94
Table 4.4 Spin exchange parameters $J_{ij}^{eff} = S_i S_j J_{ij}$ of $\text{Sr}_2\text{CuOsO}_6$ and $\text{Sr}_2\text{NiOsO}_6$ (in meV), where $J_{ij} = J_1 - J_7$, determined from the DFT+U calculations with $U_{Cu} = 6$ eV and $U_{Os} = 4$ eV.	95
Table 5.1 Spin moments of the Mn and Fe sites obtained for the HT structure of $\text{RbMn}[\text{Fe}(\text{CN})_6]$ by GGA+U calculations.	113
Table 5.2 Bond length and spin moments Mn and Fe sites obtained for the HT structure of $\text{RbMn}[\text{Fe}(\text{CN})_6]$ by GGA+U for various values of U_{Mn} with U_{Fe} fixed at 1 eV.	114
Table 5.3 Spin moments of the Mn and Fe sites obtained for the LT structure of $\text{RbMn}[\text{Fe}(\text{CN})_6]$ by GGA+U calculations for various values of U_{Mn} with U_{Fe} fixed at 1 and 2 eV (results for $U_{Fe} = 2$ eV in parentheses).	114
Table 5.4 Bond length and spin moments Mn and Fe sites obtained for the LT structure of $\text{RbMn}[\text{Fe}(\text{CN})_6]$ by GGA+U for various values of U_{Mn} with U_{Fe} fixed at 1 eV.	115
Table 8.1 Table of confusion (<i>table</i>).	151
Table 8.2 Selection of k for L-SIR with AUCs.	155
Table 8.3 Mean difference settings and AUCs.	157
Table 8.4 Variance difference settings and AUCs.	161
Table 8.5 Mean and variance difference settings and AUCs.	161
Table 8.6 Proportion variation for mean difference settings and AUCs.	163

Table 8.7 Proportion variation for variance difference settings and AUCs	163
Table 8.8 Proportion variation for both mean and variance difference settings and AUCs	166
Table 8.9 Mean Within Group Error Rate	166
Table 8.10 Kmeans and Mclust <i>table</i> of SIR on X along the first direction	170
Table 8.11 Kmeans and Mclust <i>table</i> of DIR on X along the first two directions.	170
Table 8.12 Kmeans and Mclust <i>table</i> of SAVE on X along the first two directions	170
Table 8.13 Kmeans and Mclust <i>table</i> on Original Space	171
Table 8.14 Mean Within Group Error Rate	171
Table 8.15 Cross-validation <i>table</i> of SIR on X along the first direction	172
Table 8.16 Cross-validation <i>table</i> of DIR on X along the first direction	173
Table 8.17 Cross-validation <i>table</i> of SAVE on X along the first direction	173
Table 9.1 Mean Within Group Misclassification Error Rate on Testing Data	205
Table 9.2 Mean Within Group Misclassification Error Rate on Real Data	213

LIST OF FIGURES

- Figure 1.1 Orbital interaction between two spin sites described by the magnetic orbitals ϕ_1 and ϕ_2 leading to the dimer levels Ψ_1 and Ψ_2 separated by the energy gap Δe 24
- Figure 1.2 Triangular spin frustration and non-collinear spin arrangement in a triangle of spin sites described by the nearest-neighbor AFM spin exchange J (< 0): (a) Spin frustration that occurs when the spins are collinear. (b) Compromised non-collinear spin arrangement that minimizes the total spin exchange interactions. 24
- Figure 1.3 (a) Linear spin frustration in a 1D chain of spin sites described by the nearest-neighbor and next-nearest-neighbor spin exchange (J_{nn} and J_{nnn} , respectively). A typical case occurs when $J_{nn} > 0$) and $J_{nnn} < 0$. (b) Spiral spin arrangement that minimizes the total spin exchange interactions. 25
- Figure 1.4 Schematic illustration of three types of spin-spiral magnetic structures in a 1D chain of magnetic ions: (a) cycloidal, (b) sinusoidal, and (c) screw (or helical). 26
- Figure 1.5 Two electronic states that a system with a half-filled band can have: (a) Non-magnetic metallic state, in which both the up-spin and down-spin states are half-filled. (b) Magnetic insulating state, in which the up-spin band is completely filled, but the down-spin band, separated from the up-spin band by a band gap, is empty. 26
- Figure 1.6 Split patterns of the up-spin and down-spin levels ($\phi \uparrow$ and $\phi \downarrow$, respectively) for the two extreme cases of spin arrangements for a 1D chain with one orbital per site: (a) FM state in which all sites have up-spins. (b) AFM state in which up-spin and down-spin sites alternate. Only two adjacent spin sites of the chain are shown for simplicity. 27
- Figure 2.1 Perspective views of (a) a zigzag MnO_4 chain, (b) a zigzag WO_4 chain, and (c) the three-dimensional arrangement of the MnO_4 and WO_4 chains in MnWO_4 . The Mn, W and O atoms are represented by large, medium and small spheres, respectively. 52
- Figure 2.2 (a) Four spin exchange paths $J_1 - J_4$ in MnWO_4 within each //bc-layer of Mn^{2+} ions. (b) Five spin exchange paths $J_5 - J_9$ between adjacent

- //bc-layers of Mn^{2+} ions in MnWO_4 . The numbers 1 - 9 refer to the spin exchange paths $J_1 - J_9$, respectively. 53
- Figure 2.3 Ordered spin arrangements in each //bc-layer of Mn^{2+} ions in the FM, A1, A2 and A3 states of MnWO_4 . The up-spin and down-spin Mn^{2+} sites are represented by filled and unfilled circles, respectively. 53
- Figure 2.4 Ordered spin arrangements in two successive //bc-layers of Mn^{2+} ions in the A4 and A5 states of MnWO_4 . The up-spin and down-spin Mn^{2+} sites are represented by filled and unfilled circles, respectively. 54
- Figure 2.5 Ordered spin arrangements in four successive //bc-layers of Mn^{2+} ions in the A6, A7, A8 and A9 states of MnWO_4 . The up-spin and down-spin Mn^{2+} sites are represented by filled and unfilled circles, respectively. 55
- Figure 2.6 Spin arrangements of the (a) AF1, (b) AF4, (c) AF5 and (d) AF4 states of MnWO_4 , which are generated in terms of the //c-chains with the $\uparrow\downarrow$ spin order. 56
- Figure 2.7 Plane of spin spiral found in MnWO_4 56
- Figure 2.8 Two arrangements of the //c-chains of Mn^{2+} ions with spiral-spin order along the b-direction: (a) AFM and (b) FM. The zigzag chains are represented as straight chains to emphasize the spin spiral order. 57
- Figure 2.9 Perspective view of the commensurate spiral-spin arrangement of MnWO_4 within a (4a, b, 2c) supercell, which was employed for the GGA+U+SOC calculation of FE polarization. The plane of the spin spiral is defined as in Fig. 2.7, so that the spins spiral along the a- and c- directions. 57
- Figure 2.10 Cycloidal components of the spiral-spin state with the (4a, b, 2c) superstructure used to simulate the spiral-spin ordered state AF2. (a) The projection view of the spiral-spin propagation along the a-direction on the ab-plane. (b) that along the c-direction on the bc-plane, where the zigzag chain was represented as a straight chain to emphasize the spin spiral order. The polarization direction is represented by red arrows. 58
- Figure 3.1 Crystal and magnetic structures of MnSb_2S_4 : (a) MnSb_2S_4 chain of monoclinic MnSb_2S_4 , which results from a MnS_4 chain of edge-sharing MnS_6 octahedra capped with SbS_3 pyramids. The pink, purple and yellow spheres (the large, medium and small circles), respectively. (b) Projection view of MnSb_2S_4 chains in monoclinic MnSb_2S_4 along the b-direction. (c) Projec-

tion view of MnSb_2S_4 layers in orthorhombic MnSb_2S_4 along the b-direction, where SbS_3 pyramids cap each MnS_4 chain and interconnect between adjacent MnS_4 chains. (d) Spin arrangement of the MnSb_2S_4 chains in monoclinic MnSb_2S_4 . The chain are represented by showing only the Mn atoms. The unshaded and shaded circles, representing the Mn atoms, differ in their b-axis height by $b/2$ 73

Figure 3.2 Five spin exchange paths $J_1 - J_5$ of monoclinic MnSb_2S_4 . For simplicity, only the Mn atoms are shown as circles. The circles joined by cylinders represent the MnS_4 chains along the b-direction. The numbers 1 - 5 refer to the spin exchange paths $J_1 - J_5$, respectively. 74

Figure 3.3 Six ordered spin states of monoclinic MnSb_2S_4 defined in terms of the (a, 5b, c) supercell, where the unshaded and shaded circles represent the up-spin and down-spin Mn^{2+} sites, respectively. The numbers in each parenthesis (from left to right) refer to the relative energies (in meV per 4 FUs) determined from GGA+U calculations with $U_{\text{eff}} = 4$ and 6 eV, respectively. 74

Figure 4.1 Schematic representation of the double-perovskite $\text{Sr}_2\text{CuOsO}_6$: (a) A projection view, along the c-direction, of an isolated //ab-layer of corner-sharing CuO_6 and OsO_6 octahedra. (b) A perspective view of two //ab-layers of corner-sharing CuO_6 and OsO_6 octahedra. The blue, red and white circles represent the Cu, Os and O atoms, respectively. The numbers 1 - 7 refer to the spin exchange paths $J_1 - J_7$, respectively. 96

Figure 4.2 Schematic representations of the G-type and A-type antiferromagnetic spin arrangements of the double-perovskite $\text{Sr}_2\text{CuOsO}_6$ using the ordered spin arrangements of an isolated //ab-layer of Cu^{2+} and Os^{6+} ions: (a) In the G-type arrangement AF1, the given layer repeats antiferromagnetically along the c-direction. (b) In the A-type arrangement AF2, the given layer repeats antiferromagnetically along the c-direction. (c) In the A-type arrangement AF3, the given layer repeats ferromagnetically along the c-direction. The filled and unfilled large circles represent the up-spin and down-spin magnetic ion sites, respectively. 97

Figure 4.3 Spin arrangements in the AF1 - AF7 states of Sr_2MOsO_6 ($M = \text{Cu}, \text{Ni}$) used to evaluate the $J_1 - J_7$ values. In each state, the two //ab-layers with the given ordered spin arrangements alternate along the c-direction. In the AF3 state, the two //ab-layers have the same spin arrangement. In the FM state (not shown), the //ab-layer with the FM spin arrangement repeats ferromagnetically along the c-direction. In each state of Sr_2MOsO_6 ($M = \text{Cu},$

- Ni), the number in the parenthesis refers to the relative energies with respect to the FM state (in meV per two FUs), which was obtained from the DFT+U calculations with $U_M = 6$ eV and $U_{Os} = 4$ eV..... 98
- Figure 4.4 Schematic views of (a, b) the eg-type magnetic orbitals of the M^{2+} ion and (c, d) the t2g-type magnetic orbitals of the Os^{6+} ion in Sr_2MOsO_6 ($M = Cu, Ni$)..... 99
- Figure 4.5 Orbitals involved in (a, b) the x2-y2/xz and x2-y2/yz spin exchange interactions of the M-Oeq-Os path and (c, d) those of the M-Oax-Os path in Sr_2MOsO_6 ($M = Cu, Ni$). For simplicity, the orbital contributions unrelated to the exchange paths are not shown. 100
- Figure 4.6 Orbitals involved in (a, b) the z2/xz and z2/yz spin exchange interactions of the Ni-Oeq-Os path and (c, d) those of the Ni-Oax-Os path in Sr_2NiOsO_6 . For simplicity, the orbital contributions unrelated to the exchange paths are not shown. 101
- Figure 4.7 PDOS plots calculated for the (a) Os 5d, (b) Sr 4d and (c, d) Cu 3d orbitals in the AF2 state of Sr_2CuOsO_6 , where the horizontal axis is in units of eV, and the vertical axis in states/eV/atom. The spin-up and spin-down states are represented by black and red curves, respectively, and their PDOS values are represented by positive and negative numbers, respectively. Fig. 7d is a zoomed-in view of the circled region of Fig. 7c. 102
- Figure 5.1 (a) Perspective view of the crystal structure of the HT cubic phase of $RbMn[Fe(CN)_6]$. The red and blue circles represent the Fe and Mn atoms, respectively, and the yellow and turquoise circles the C and N atoms, respectively. (b) Arrangement of the Rb atoms in the Mn_4Fe_4 cubes. 116
- Figure 5.2 PDOS plots of the Mn and Fe 3d states of $RbMn[Fe(CN)_6]$ obtained from GGA+U calculations for (a) the HT cubic structure with $U_{Mn} = U_{Fe} = 4$ eV, (b) the HT structure with $U_{Mn} = 8$ eV and $U_{Fe} = 1$ eV, and (c) the LT structure with $U_{Mn} = 8$ eV and $U_{Fe} = 1$ eV. The up- and down-spin densities are indicated by positive and negative values, respectively. (d) is the PDOS for optimized structure at $U_{Mn} = 4$ eV and $U_{Fe} = 1$ eV..... 117
- Figure 5.3 Interaction of the Fe t_{2g} and Mn t_{2g} orbitals with the (a) π_{CN} and (b) π_{*CN} orbitals of the CN ligand in each Fe-CN-Mn linkage of $RbMn[Fe(CN)_6]$. 118
- Figure 5.4 Plots of (a) the spin density and (b) a part of the charge density distribution obtained for the LT phase of $RbMn[Fe(CN)_6]$ from GGA+U

calculations with $U_{Mn} = 8$ eV and $U_{Fe} = 1$ eV. The large red and turquoise spheres represent the Fe and Mn atoms, respectively.....	118
Figure 7.1 Connection between chapters	131
Figure 8.1 ROC curve of L-SIR for k equals to 5, 20,...,600 and SIR, the legend is illustrated in the figures for Setting 1 the variance difference	155
Figure 8.2 ROC curve of L-SIR for k equals to 5, 20,...,600 and SIR, the legend is illustrated in the figures for Setting 2 the mean difference.....	156
Figure 8.3 ROC curve of SIR, DIR and L-SIR on X with mean difference	158
Figure 8.4 Summary plots of SIR, DIR and L-SIR on X^2 with variance difference. Blue dots represent inactive compounds, while red dots represent the active ones	159
Figure 8.5 ROC curve of SIR, DIR and L-SIR on X^2 with variance difference ..	160
Figure 8.6 ROC curve of SIR, DIR and L-SIR on X and X^2 with mean and variance difference	162
Figure 8.7 ROC curve of SIR, DIR and L-SIR on different proportion of mean difference	164
Figure 8.8 ROC curve of SIR, DIR and L-SIR on different proportion of variance difference	165
Figure 8.9 ROC curve of SIR, DIR and L-SIR on different proportion of mean and variance difference.....	167
Figure 8.10 SIR, SAVE and DIR on X of XUE data. Red dots represent inactive compounds, blue and green dots represent active compounds of two different mechanisms.....	169
Figure 9.1 Mean Within Group Misclassification Error Rate of $M1$	206
Figure 9.2 Mean Within Group Misclassification Error Rate of $M2$	206
Figure 9.3 Mean Within Group Misclassification Error Rate of $M3$	207
Figure 9.4 Mean Within Group Misclassification Error Rate of $M4$	207

Figure 9.5 Mean Within Group Misclassification Error Rate of $M5$	208
Figure 9.6 Mean Within Group Misclassification Error Rate of $M6$	208
Figure 9.7 Mean Within Group Misclassification Error Rate of $M7$	209
Figure 9.8 Mean Within Group Misclassification Error Rate of $M8$	209
Figure 9.9 Mean Within Group Misclassification Error Rate of $L1$	210
Figure 9.10 Mean Within Group Misclassification Error Rate of $L2$	210
Figure 9.11 Mean Within Group Misclassification Error Rate of $L3$	211
Figure 9.12 Mean Within Group Misclassification Error Rate of $L4$	211
Figure 9.13 Mean Within Group Misclassification Error Rate of Real Data	213

Part I

Density Functional Investigation of Spin-Orbit Coupling Effects on the Magnetic Properties of Some Transition-Metal Magnetic Oxides

Chapter 1

Introduction

In this Chapter we briefly review some of the fundamental concepts that are needed in understanding the electronic structures of magnetic insulators. In our study the electronic structures of the magnetic solids studied in our work are generated by density functional theory (DFT). Thus, we also briefly describe the essential aspects of DFT as well as the computational methods employed in our work.

1.1. Spin exchange interactions

The energies of a magnetic solid are generally described by using a spin Hamiltonian \hat{H}_{spin} ,

$$\hat{H}_{\text{spin}} = -\sum_{i<j} J_{ij} \hat{S}_i \cdot \hat{S}_j, \quad (1)$$

which is defined as a sum of spin exchange interactions between adjacent spin sites i and j , $-J_{ij} \hat{S}_i \cdot \hat{S}_j$, where \hat{S}_i and \hat{S}_j are the spin operators at the sites i and j , respectively, and J_{ij} is the associated spin exchange parameter. With the sign convention of Eq. 1, J_{ij} is antiferromagnetic (AFM) when $J_{ij} < 0$, but is ferromagnetic (FM) when $J_{ij} > 0$. This Hamiltonian expresses excitation energies of a magnetic solid in terms of a set of spin exchange parameters J_{ij} . The geometrical pattern of these parameters (i.e., the spin lattice) determines the topology of the excitation energy spectrum. Provided that the spin sites i and j

are represented by the magnetic orbitals ϕ_i and ϕ_j , respectively, the sign and magnitude of the spin exchange parameter J_{ij} are determined by the interaction between ϕ_i and ϕ_j .

In analyzing experimental results (e.g., magnetic susceptibility, specific heat and spin wave dispersion) in terms of \hat{H}_{spin} (Eq. 1), the spin exchange parameters J_{ij} are numerical fitting parameters needed to reproduce these results. Consequently, the signs and magnitudes of these “experimental” J_{ij} parameters depend on the spin lattice chosen for the spin Hamiltonian, and two different sets of J_{ij} values may provide an equally acceptable fitting [1]. Interesting but irrelevant interpretations for a given magnetic solid often result when the spin lattice is chosen by merely inspecting the geometrical pattern of the magnetic ion arrangement or by seeking the novelty of the physics the chosen model generates, as found for $(\text{VO})_2\text{P}_2\text{O}_7$, [2] $\text{Na}_3\text{Cu}_2\text{SbO}_6$ and $\text{Na}_2\text{Cu}_2\text{TeO}_6$, [3] and $\text{Bi}_4\text{Cu}_3\text{V}_2\text{O}_{14}$, [4] Azurite $\text{Cu}_3(\text{CO}_3)_2(\text{OH})_2$, [5] and $\text{Cu}_3(\text{P}_2\text{O}_6\text{OH})_2$. [6] Since the magnetic orbitals of a given magnetic solid are highly anisotropic in shape, the relative strengths of their spin exchange interactions do not necessarily produce a pattern that resembles the geometrical pattern of the magnetic ion arrangement. It is essential to examine the electronic structure of a magnetic solid to obtain a relevant spin lattice. [1]

1.1. 1. Qualitative aspect

For a spin dimer made up of two equivalent spin sites with one electron per site, suppose that the two spin sites 1 and 2 are described by the magnetic orbitals ϕ_1 and ϕ_2 , respectively. The interaction between ϕ_1 and ϕ_2 leads to the molecular levels ψ_1 and ψ_2 of the

dimer separated by Δe in energy (**Fig. 1.1**). The allowed spin states of this spin dimer are the singlet and triplet states with the energy difference between them as $\Delta E = E_S - E_T$. This energy spectrum is reproduced by the spin Hamiltonian,

$$\hat{H}_{\text{spin}} = -J\hat{S}_1 \cdot \hat{S}_2, \quad (2)$$

if with $J = \Delta E$. When the spin sites 1 and 2 are described by the magnetic orbitals ϕ_1 and ϕ_2 , respectively, then the J parameter is written as [1,7]

$$J = J_F + J_{AF} = 2K_{12} - \frac{(\Delta e)^2}{U^{\text{eff}}}. \quad (3)$$

The FM component J_F is proportional to the exchange integral K_{12} , which increases with increasing the overlap density $\phi_1\phi_2$. The AFM component J_{AF} is proportional to $(\Delta e)^2$ and is inversely proportional to the effective on-site repulsion U^{eff} . Since Δe is proportional to the overlap integral $\langle \phi_1 | \phi_2 \rangle$, the magnitude of J_{AF} increases with increasing $\langle \phi_1 | \phi_2 \rangle$. Therefore, a spin exchange becomes AFM when the overlap integral $\langle \phi_1 | \phi_2 \rangle$ is large and the overlap density $\phi_1\phi_2$ is small, but becomes FM when the overlap integral $\langle \phi_1 | \phi_2 \rangle$ is small and the overlap density $\phi_1\phi_2$ is large.

In magnetic solids made up of MO_m polyhedra, the interaction between spin sites, say, $M1$ and $M2$, takes place through the superexchange $M1\text{-O-}M2$ path or through the super-superexchange $M1\text{-O}\dots\text{O-}M2$ path. The magnetic orbitals of MO_m have the M nd orbitals combined out-of-phase with the O $2p$ orbitals. Therefore, the overlap density $\phi_1\phi_2$ and the overlap integral $\langle \phi_1 | \phi_2 \rangle$ between the magnetic orbitals ϕ_1 and ϕ_2 are governed primarily by

their O 2p orbitals located on the bridging O atom in the case of the M1-O-M2 superexchange and by those lying on the two O atoms in the case of the M1-O...O-M2 super-superexchange. Namely, the sign and magnitude of a spin exchange interaction between two spin sites is determined primarily by the tail parts (i.e., the O 2p orbitals) of their magnetic orbitals lying only in the region between them. [1] This is the reason why a spin Hamiltonians defined in terms of only pair-wise spin exchange interactions can provide a good description for the excitation energy spectrum of a given magnetic solid.

It is important to recall that, for magnetic solids consisting of both M-O-M superexchange and M-O...O-M super-superexchange paths, spin exchange interactions that occur through super-superexchange paths with short O...O contact distances (i.e., around the van der Waals distance and shorter) can be much stronger than those through M-O-M paths, and hence should not be neglected. [1] In particular, for a M1-O...O-M2 super-superexchange path in which the O...O contact is linked through a d^0 cation M'^{n+} (e.g., V^{5+} , Mo^{6+} and W^{6+}) to form an O...M'...O linkage, the empty d-orbitals of M' can overlap effectively with the magnetic orbitals of both M1 and M2 and hence dramatically enhance or reduce the spin exchange interaction between M1 and M2, [8,9] depending on the symmetry of the linkage. Even when the O...O contact is linked through an alkaline earth cation A^{2+} (e.g., Sr^{2+}) to form an O...A...O linkage, whether the M1-O...A...O-M2 spin exchange is FM or AFM can be influenced by the virtual d-orbitals of A^{2+} . [10]

1.1. 2. Quantitative evaluation by energy-mapping

Spin exchange parameters are quantitatively evaluated by performing the energy mapping analysis based on DFT+U calculations. Suppose one identifies a set of N spin exchange paths to consider for a given magnetic solid. To evaluate the values of the associated spin exchange parameters J_1, J_2, \dots, J_N , the energy-mapping method determines the electronic energies E_{elec} of the $N+1$ ordered spin states (i.e., broken-symmetry states) ($i = 1, 2, \dots, N+1$) by DFT+U calculations so as to obtain N relative energies ΔE_{elec} . For these calculations, it is important to make sure that all ordered-spin states are magnetic insulating states. The total spin exchange energies E_{spin} of the $N+1$ ordered spin states can be determined by using the spin Hamiltonian \hat{H}_{spin} (Eq. 1) defined in terms of J_1, J_2, \dots, J_N (namely, $J_{ij} = J_1 - J_N$) so as to determine N relative energies ΔE_{spin} expressed in terms of N parameters $J_1 - J_N$. In writing the expression of the total spin exchange energy for an ordered spin state in terms of $J_1 - J_N$, we employ the energy expressions for the FM and AFM arrangements of a general spin dimer whose spin sites i and j possess N_i and N_j unpaired spins (hence, spins $S_i = N_i/2$ and $S_j = N_j/2$), respectively. [11] Given J_{ij} as the spin exchange parameter for this spin dimer, the FM and AFM arrangements of this spin dimer lead to the spin exchange energies

$$\begin{aligned}
 \text{FM arrangement:} & \quad -N_i N_j J_{ij} / 4 = -S_i S_j J_{ij} \\
 \text{AFM arrangement:} & \quad +N_i N_j J_{ij} / 4 = +S_i S_j J_{ij}
 \end{aligned} \tag{4}$$

Thus, the total spin exchange energy of an ordered spin arrangement is obtained by summing up all pair-wise interactions. Then, by mapping the N relative energies ΔE_{elec} onto the N

relative energies ΔE_{spin} , we obtain the values of $J_1 - J_N$. In determining N spin exchanges J_1, J_2, \dots, J_N , one may employ more than $N+1$ ordered spin states, hence obtaining more than N relative energies ΔE_{elec} and ΔE_{spin} for the mapping.[1] In this case, the N parameters $J_1 - J_N$ can be determined by performing least-squares fitting analysis. In comparing the relative strengths of spin exchange parameters J_{ij} involving spin sites with different numbers of unpaired spins, it is necessary to use the effective spin exchange parameters J_{ij}^{eff} that incorporate the values of the associated spins S_i and S_j , namely,

$$J_{ij}^{\text{eff}} = S_i S_j J_{ij} \quad (5)$$

The energy-mapping method described above is objective in that, once a set of spin exchange paths is chosen for a magnetic solid, it does not presume whether the associated spin exchange parameters should be FM or AFM. This method simply maps the electronic energy spectrum of DFT+U calculations onto the energy spectrum of the spin Hamiltonian defined by a set of spin exchange parameters. However, the values of the resulting spin exchange parameters depend on what set of exchange paths one selects. In identifying the spin lattice appropriate for a magnetic solid under consideration, therefore, energy-mapping analysis should be carried out for a set of spin exchange paths large enough to include all important ones. In particular, for magnetic solids consisting of both M-O-M and M-O...O-M spin exchange paths, those M-O...O-M paths with short O...O contact distances should not be omitted in the energy-mapping analysis.

When a set of spin exchange parameters are evaluated by performing DFT+U calculations as a function of U , it is generally found that the values of AFM spin exchanges

become smaller in magnitude with increasing U . [3c,4a,12] For magnetic systems with well localized electrons, for which increasing U does not increase the moment on each spin site, this is expected because the AFM component J_{AF} of a spin exchange decreases in strength with increasing the effective on-site repulsion U^{eff} , i.e., $J_{AF} = -(\Delta e)^2/U^{\text{eff}}$. Given several sets of spin exchange parameters calculated for a magnetic solid from DFT+ U calculations with various U values, the relative strengths of the spin exchange parameters are not strongly affected by U , hence predicting an identical spin lattice for the magnetic system. To check the proper range of U values, one may calculate the Curie-Weiss temperature θ in the mean-field approximation, which is given by [13]

$$\theta = \frac{S(S+1)}{3k_B} \sum_i z_i J_i, \quad (6)$$

where the summation runs over all nearest neighbors of a given spin site, z_i is the number of nearest neighbors connected by the spin exchange parameter J_i , and S is the spin quantum number of each spin site.

1.1. 3. Spin frustration

The spin Hamiltonian, Eq. 1, expresses the total energy of a magnetic system as a sum of pair-wise spin exchange interactions. Each individual term $-J_{ij}\hat{S}_i \cdot \hat{S}_j$ forces the spins \vec{S}_i and \vec{S}_j to be collinear; the energy-lowering is maximum when the two spins are antiparallel and parallel if J_{ij} is AFM ($J_{ij} < 0$) and FM ($J_{ij} > 0$), respectively. A collinear spin arrangement is energetically unfavorable for a certain spin lattice composed of several

different spin exchange paths, if the spin lattice generates either triangular or linear spin frustration. An archetypal example of triangular spin frustration is found for a triangular lattice made up of nearest-neighbor AFM spin exchange paths (**Fig. 1.2a**), [14,15] and the minimum-energy spin configuration for such a triangle is given by a non-collinear configuration (**Fig. 1.2b**). An archetypal example of linear spin frustration is found for a 1D chain in which, for example, the nearest-neighbor exchange J_{nn} is FM while the next-nearest-neighbor exchange J_{nnn} is AFM (**Fig. 1.3a**). [9b,16,17] When $|J_{nn}| < 4|J_{nnn}|$, [9a, 18] the 1D lattice adopts a non-collinear configuration in which the spins spiral along the chain (**Fig. 1.3b**). When the classical spin approximation is used to describe the 1D chain defined by J_{nn} and J_{nnn} , the periodicity q of the spiral-spin order is given by

$$q = \frac{1}{2\pi} \arccos\left(-\frac{J_{nn}}{4J_{nnn}}\right). \quad (7)$$

It should be noted that the non-collinearity dictated by spin frustration deals only with the relative spin arrangement, and has nothing to say about the preferred spin orientation in space. For example, the spin-spiral plane in the spin-frustrated chain can be perpendicular to the chain (helical) or parallel to the chain (cycloidal) as depicted in **Fig. 1.3b**. What determines the preferred spin orientation in space is spin-orbit coupling (SOC) [19] and/or magnetic dipole-dipole (MDD) [20] interaction, which will be discussed in the next section. The electronic structures of non-collinear magnetic states are described by non-collinear spin-polarized DFT+U calculations.

For an AFM system with spin frustration, its Curie-Weiss temperature θ is large in magnitude compared with its Néel temperature T_N (i.e., the 3D AFM ordering temperature).

Some extent of spin frustration exists in most AFM systems, so that T_N is typically lower than $|\theta|$. Experimentally, an AFM system with the ratio $f = |\theta|/T_N$ greater than 6 is often regarded as spin frustrated.³³ For a magnetic system with high degree of spin frustration, its magnetic ground state is highly degenerate because a large number of different spin arrangements have the same energy. On lowering the temperature, such a system tends to lower its energy by undergoing a slight structural distortion and hence reducing the extent of spin frustration.

1.2. Spin-orbit coupling in magnetic materials

The energy states of a magnetic system are commonly described in terms of crystal field splitting, spin exchange interaction, and spin-orbit coupling. In general, crystal field splitting and spin exchange interactions are stronger than SOC interactions. Nevertheless, SOC plays a crucial role in determining the magnetic properties of compounds with unpaired spins, which include several important physical properties, such as uniaxial magnetism, spin orientation in space, and multiferroicity.

The SOC of a magnetic ion is discussed in terms of the Hamiltonian

$$\hat{H}_{\text{SOC}} = \lambda \hat{L} \cdot \hat{S} , \quad (8)$$

where λ is the SOC constant of the ion, and \hat{L} and \hat{S} are the orbital and spin angular momentum operators of the magnetic ion, respectively. For a transition-metal ion with lower than d^5 electron count, $\lambda > 0$, so the orbital and spin moments couple antiparallel to each other to produce the lowest-energy angular momentum state $J = -L + S$. For a transition-

metal ion with higher than d^5 electron count, $\lambda < 0$, so the orbital and spin moments couple parallel to each other to produce the lowest-energy angular momentum state $J = L + S$. For a high-spin d^5 metal ion, $L = 0$, to a first approximation (i.e., in the sense of free transition-metal ion), so the effect of SOC is expected to be weak.

1.2.1. Multiferroicity

Multiferroic materials exhibit more than one ferroic properties, (e.g. ferromagnetism, ferroelectricity, ferroelasticity, antiferromagnetism, and ferrimagnetism), simultaneously [21]. Multiferroicity can be induced by several different mechanisms. The multiferroicity driven by charge ordering usually occurs in a compound containing ions of mixed valence and with geometrical or magnetic frustration [22]. As found for LuFe_2O_4 [23], the arrangement of these ions may form a ferroelectric (FE) structure (i.e., a structure with no inversion symmetry), hence leading to FE polarization. These ions form a polar arrangement, causing improper ferroelectricity (i.e. no ionic displacement). With magnetic ions, a magnetic order can also occur and may be coupled to the ferroelectricity. The multiferroicity driven by magnetic ordering often occurs when a magnetic system made up of identical magnetic ions possess geometric spin frustration. Such materials may relieve their spin frustration by adopting a non-collinear spin arrangement (e.g. spiral spin arrangement), as we discussed in previous section, which has no inversion symmetry and hence lead to FE polarization. The magnetic order driven multiferroicity can also occur with collinear spins as found in $\text{Ca}_3\text{CoMnO}_6$, when an up-up-down-down ($\uparrow\uparrow\downarrow\downarrow$) spin order occurs in one-dimensional (1D) chain systems that are made up of two different magnetic ions alternating along the chain

because the $\uparrow\uparrow\downarrow\downarrow$ spin order in such systems removes inversion symmetry. The lone pair driven multiferrocity is found in certain perovskites ABO_3 , in which corner sharing BO_6 octahedral form a three-dimensional (3D) lattice with every B_8 cube containing one A cation carrying a lone pair (e.g. Pb^{2+} , Bi^{3+}). The lone pair formation at the A-site cations leads to FE distortion in the 3D lattice while the partially filled states of transition metal at the B-site contribute to a magnetic ordering.

For a 1D chain of identical magnetic ions with spin-spiral order, Katsura, Nagaosa and Balatsky (KNB) showed that its FE polarization arises from the effect of SOC [24]. In essence, the SOC induces mixing between the occupied and unoccupied magnetic states (obtained in the absence of SOC effects), and the electronic structure resulting from this mixing loses the lattice inversion symmetry even if the ions of the lattice do not move from their centro-symmetric positions [24].

Given \vec{S}_i and \vec{S}_j as the spin moments at the adjacent spin sites i and j of a 1D chain of magnetic ions, respectively, and \vec{e}_{ij} as the vector connecting the two spin sites, the FE polarization \vec{P} is related to \vec{e}_{ij} , \vec{S}_i and \vec{S}_j as [24,25,26]

$$\vec{P} \propto \vec{e}_{ij} \times (\vec{S}_i \times \vec{S}_j), \quad (8)$$

which is known as the KNB model. As illustrated in **Fig. 1.4** [25,26], the spins of a 1D chain might undergo one of the three kinds of spiral spin order, i.e., cycloidal, sinusoidal and helical. According to the KNB model, only the cycloidal spin order leads to a nonzero FE polarization.

1.2.2. Spin orientation in space

In a magnetic solid the magnetic moment of each spin site results from the spin moment interacting with the unquenched orbital moment under the SOC Hamiltonian, $\hat{H}_{SO} = \lambda \hat{L} \cdot \hat{S}$. An important consequence of this interaction is that each spin site gets a preferred orientation in space with respect to the crystal lattice. Typically, the term $\hat{L} \cdot \hat{S}$ is written as

$$\hat{L} \cdot \hat{S} = \hat{L}_z \hat{S}_z + \hat{L}_x \hat{S}_x + \hat{L}_y \hat{S}_y = \hat{L}_z \hat{S}_z + \frac{1}{2} \hat{L}_+ \hat{S}_- + \frac{1}{2} \hat{L}_- \hat{S}_+. \quad (9)$$

This expression does not provide any information concerning how to think about the spin orientation in space. This is so because it employed an identical coordinate system (x, y, z) for both the orbital and spin angular momentum operators.

A more informative expression of $\hat{L} \cdot \hat{S}$ is obtained if we use one coordinate system (x, y, z) for the orbital angular momentum operator and another coordinate system (x', y', z') for the spin angular momentum operator. Suppose that the z' -axis of the spin angular momentum is aligned along the $\hat{n}(\theta, \phi)$ direction with respect to the z -axis of the orbital angular momentum, $\hat{S}'_n = \hat{S}'_{z'}$, $\hat{S}'_+ = \hat{S}'_{x'} + i\hat{S}'_{y'}$, and $\hat{S}'_- = \hat{S}'_{x'} - i\hat{S}'_{y'}$. Then, the $\hat{L} \cdot \hat{S}$ term is written as [27]

$$\begin{aligned} \hat{L} \cdot \hat{S} = & \hat{S}'_n \left(\hat{L}_z \cos \theta + \frac{1}{2} \hat{L}_+ e^{-i\phi} \sin \theta + \frac{1}{2} \hat{L}_- e^{i\phi} \sin \theta \right) \\ & + \frac{1}{2} \hat{S}'_+ \left(-\hat{L}_z \sin \theta - \hat{L}_+ e^{-i\phi} \sin^2 \frac{\theta}{2} + \hat{L}_- e^{i\phi} \cos^2 \frac{\theta}{2} \right) \\ & + \frac{1}{2} \hat{S}'_- \left(-\hat{L}_z \sin \theta + \hat{L}_+ e^{-i\phi} \cos^2 \frac{\theta}{2} - \hat{L}_- e^{i\phi} \sin^2 \frac{\theta}{2} \right) \end{aligned} \quad (10)$$

This equation shows how SOC affects the spin direction, and hence provides information about what spin direction is energetically favored by SOC for a given spin in a magnetic solid. To determine the easy-axis direction of a magnetic solid on the basis of DFT calculations, its total energy including SOC interactions should be calculated as a function of the spin direction [28]. Then, the easy-axis direction is the spin direction with the lowest total energy. Experimentally, neutron diffraction refinements at a very low temperature provide information about the magnitudes and orientations of the moments at the spin sites of a magnetic solid.

1.3. Magnetic insulating versus metallic state

The electronic properties of crystalline magnetic solids are commonly discussed on the basis of density functional theory (DFT) electronic band structure calculations. There are several different ways of doing DFT calculations for crystalline solids, namely, the non-spin-polarized DFT, the spin-polarized DFT, and the spin-polarized DFT+U, where U refers to the on-site repulsion on magnetic ions. In the non-spin-polarized DFT method, each energy level of a given band accommodates two electrons (i.e., up-spin and down-spin electrons) so that a given band consists of up-spin and down-spin subbands degenerate in energy (**Fig. 1.5a**). Consequently, any solid with partially filled bands has no energy gap between the highest-occupied and the lowest-unoccupied band levels, and is therefore predicted to be a non-magnetic metal. However, a solid with partially-filled bands can be a magnetic insulator, [29,30] in which up-spin and down-spin subbands differ in energy such that an energy gap (i.e., a band gap) occurs between the highest-occupied and the lowest-unoccupied subbands

(**Fig. 1.5b**). It should be recalled that the presence of partially-filled bands is only a necessary condition for a system to become either a metal or a magnetic insulator. The failure of the non-spin-polarized DFT method in describing magnetic insulators is partly remedied by employing the spin-polarized DFT method, which allows up-spin and down-spin subbands to have different spatial orbitals and hence differ in energy. For most magnetic insulators, however, this splitting of up-spin and down-spin subbands given by the spin-polarized DFT method is not large enough to produce a band gap. Currently, this deficiency of the spin-polarized DFT method is empirically corrected by using the spin-polarized DFT+U method, [31] which adds on-site repulsion U on the magnetic transition-metal atoms to enhance the spin polarization of their nd orbitals (see below, **Fig. 1.6**).

At the current level of DFT, it is unfortunately impossible to predict whether a solid with partially-filled bands will be a metal or a magnetic insulator. Nevertheless, once such a solid is experimentally known to be a magnetic insulator, it is always possible to generate its magnetic insulating states in terms of spin-polarized DFT+U calculations by gradually increasing the value of U . For most cases, this empirical approach is successful. However, it is an unsettled question when to stop increasing the U value. In short, the spin-polarized DFT+U method, currently employed to describe magnetic insulating states, is empirical because U is an empirical parameter. In describing a magnetic insulator by this method, therefore, it is important to first establish a range of U values producing a band gap and then explore their chemistry and physics on the basis of consistent trends resulting from such U parameters.

1.4. Charge transfer in magnetic materials

Charge transfer (CT) between different atomic sites in a given system can be induced by photo-excitation, temperature change or pressure change. Pressure-induced CT occurs when spin and charge states are strongly correlated with the lattice, as found in (*n*-C₅H₁₁)₄N[Fe^{II}Fe^{III}(dto)₃] [32]. Photo-induced CT, which constitutes the scientific basis of photography, electro-photography and many biological processes, has been widely investigated [33]. Temperature-induced CT may induce spin-crossover or intermolecular electron transfer [34,35,36].

1.5 Computational Method

Physical properties of discrete molecules and extended solids can be explained in terms of their electronic structures determined from density functional theory (DFT) calculations. In this section, we briefly review the essence of DFT and the computational methods used in our calculations.

1.5.1 Introduction to Density Functional Theory

In quantum mechanics, the electronic structure of a system is obtained by solving the Schrödinger equation,

$$\hat{H}\Psi(\vec{r},\vec{R}) = E\Psi(\vec{r},\vec{R}), \quad (11)$$

where $\Psi(\vec{r},\vec{R})$ is the wave function of the system and \hat{H} is the Hamiltonian

$$\widehat{H}(r, R) = -\sum_i \frac{\hbar^2}{2m_e} \nabla_{r_i}^2 + \frac{1}{2} \sum_i \frac{e^2}{|r_i - r_i|} - \sum_i \frac{\hbar^2}{2M_j} \nabla_{R_j}^2 + \frac{1}{2} \sum_i \frac{Z^2 e^2}{|R_j - R_j|} - \sum_{i,j} \frac{Ze^2}{|r_i - R_j|}. \quad (12)$$

In the above expression, r and R are the electron and nuclear coordinates, respectively, and M and m_e refer to the nuclear and electron masses, respectively. In Eq. 12, the first term is the kinetic energy of the electrons, the second term the electron-electron repulsion, the third term the kinetic energy of the nuclei, the fourth term the repulsion between nuclei, and the last term the attraction between the electrons and the nuclei.

According to the Born-Oppenheimer approximation, the Hamiltonian is simplified as

$$H(r, R) = -\sum_i \frac{\hbar^2}{2m_e} \nabla_{r_i}^2 + \frac{1}{2} \sum_i \frac{e^2}{|r_i - r_i|} - \sum_{i,j} \frac{Ze^2}{|r_i - R_j|}, \quad (13)$$

which contains electronic kinetic energy, electron-electron repulsion and electron-nucleus attraction. In the DFT [37], the Hamiltonian of a system at external potential V_{ext} can be written as

$$H = -\sum_i \frac{\hbar^2}{2m} \nabla_i^2 + V_{\text{ext}} + \frac{1}{2} \sum_{i \neq j} \frac{e^2}{|r_i - r_j|} \quad (21)$$

and the associated energy E_0 at the ground-state electron density ρ_0 is

$$\begin{aligned} E_0 &= E_v[\rho_0] = \overline{T}[\rho_0] + \overline{V}_{Ne}[\rho_0] + \overline{V}_{ee}[\rho_0] \\ &= \int \rho_0(r) v(r) dr + \overline{T}[\rho_0] + \overline{V}_{ee}[\rho_0] = \int \rho_0(r) v(r) dr + F[\rho_0], \end{aligned} \quad (22)$$

where E_v emphasizes the dependence of E_0 on the external potential $v(r)$, \overline{T} , \overline{V}_{Ne} and \overline{V}_{ee} are the electronic-kinetic energy, electron-nuclear attractions, and electron-electron repulsions, respectively. $F[\rho_0]$ is an unknown functional independent of the external

potential. Thus, if we know the ground-state electron density ρ_0 , it is possible in principle to calculate all the ground-state molecular properties without having to find the wave function. However, no practical solution is provided to calculate E_0 from ρ_0 , nor does it provide a way to find ρ_0 without first finding the wave function.

The Kohn-Sham theory [38] proposes to use the energy expression of the kinetic energy and the electron-electron repulsion of the noninteracting system, and put the energy difference between the interacting and the noninteracting system together, as the exchange-correlation energy functional, $E_{xc}[\rho_0] = \Delta T[\rho_0] + \Delta V_{ee}[\rho_0]$, to solve. Thus the many-body exchange correlation interactions are all included in the exchange correlation term, and the accuracy of the DFT result depends on the exchange correlation energy.

The two commonly used approximations for the exchange correlation integral are the local spin density approximation (LSDA) [39] and the generalized gradient approximation (GGA) [39]. LSDA is widely used when the exchange correlation interaction is a local effect, such as in solid state where the exchange interaction is a short-range interaction. The LSDA can also be used when the electron density varies extremely slowly in space. The LSDA uses the local exchange correlation interaction in homogenous electron gas to replace the interaction in non homogenous electron gas. However, when the electron density varies gradually, such as electron density between two atoms reduces to 0 with the distance increasing, the LSDA is not a good approximation. The GGA is used in situations where the electron density varies with position globally. The exchange correlation integral in the GGA is a function of the electron density $\rho(r)$ and the density gradient $|\nabla\rho(r)|$. The GGA

improves the estimation of the exchange correlation in atoms and molecules. The exchange correlation integral of the LSDA and GGA are given as follows.

$$E_{xc}^{LSDA}[\rho^\alpha, \rho^\beta] = \int \varepsilon_{xc}(\rho^\alpha(\vec{r}), \rho^\beta(\vec{r})) \rho(\vec{r}) d\vec{r} \quad (30)$$

$$E_{xc}^{GGA}[\rho^\alpha, \rho^\beta] = \int f(\rho^\alpha(\vec{r}), \rho^\beta(\vec{r}), \nabla\rho^\alpha(\vec{r}), \nabla\rho^\beta(\vec{r})) d\vec{r} \quad (31)$$

1.5.2. Computational Method

In this dissertation, we employ the DFT encoded in the Vienna Ab-initio Simulation Package (VASP) [40] in electronic band structure calculations for magnetic solids. For the exchange-correlation functional, we employ either the LSDA or the GGA. [39] For magnetic solids containing typically 3d transition metals, DFT calculations with LSDA or GGA invariably predict metallic electronic structures (i.e., electronic structure with partially filled bands) even if spin-polarized DFT calculations are performed as we discussed in 1.3. To remove this deficiency of DFT calculations, one typically employs the DFT plus on-site repulsion U (i.e., DFT+U) method [41], in which U of certain value is added to the transition metal atoms to ensure a large split between their up-spin and down-spin states so that the resulting electronic structure has a band gap. It is noted that DFT+U calculations are empirical because U is an empirical parameter. In our report, DFT + U calculations with LSDA and GGA are referred to as LSDA+U and GGA+U calculations, respectively. In addition, when these calculations include SOC effects [42], they are referred to as LSDA+U+SOC and GGA+U+SOC calculations, respectively. The values of ferroelectric

polarizations in this article were calculated by using the Berry phase method [43,44] encoded in the VASP.

1.6. Dissertation outline

In the following we present results of our research concerning the structure-property relationships in the magnetic systems MnWO_4 , MnSb_2S_4 , Sr_2MOsO_6 ($M = \text{Cu}, \text{Ni}$) and $\text{RbMn}[\text{Fe}(\text{CN})_6]$, which we explore on the basis of first principles DFT calculations. These studies were all published in the literature. Our studies on the multiferroic compounds MnWO_4 and MnSb_2S_4 are presented in Chapters 2 and 3, respectively. Our investigations on the magnetic systems Sr_2MOsO_6 ($M = \text{Cu}, \text{Ni}$) and $\text{RbMn}[\text{Fe}(\text{CN})_6]$ are described in Chapters 4 and 5, respectively.

References

- (1) M.-H. Whangbo; H.-J. Koo; D. Dai, *J. Solid State Chem.* **2003**, 176, 417.
- (2) (a) A. W. Garret; S. E. Nagler; D. A. Tennant; B. C. Sales; T. Barnes, *Phys. Rev. Lett.* **1997**, 79, 745. (b) H. -J. Koo; M. -H. Whangbo; P. D. VerNooy; C. C. Torardi; W. J. Marshall, *Inorg. Chem.* **2002**, 41, 4664.
- (3) (a) Y. Miura; R. Hirai; Y. Kobayashi; M. Sato, *J. Phys. Soc. Jpn.* **2006**, 75, 84707. (b) S. Derakhshan; H. L. Cuthbert; J. E. Greedan; B. Rahman; T. Saha-Dasgupta, *Phys. Rev. B* **2007**, 76, 104403. (c) H. -J. Koo; and M. -H. Whangbo, *Inorg. Chem.* **2008**, 47, 128. (d) H. Sakurai; K. Yoshimura; K. Kosuge; N. Tsujii; H. Abe; H. Kitazawa; G. Kido; H. Michor; G. Hilscher, *J. Phys. Soc. Jpn.* **2002**, 71, 1161.

- (4) (a) H. Sakurai; K. Yoshimura; K. Kosuge; N. Tsujii; H. Abe; H. Kitazawa; G. Kido; H. Michor; G. Hilscher, *J. Phys. Soc. Jpn.* **2002**, *71*, 1161. (b) K. Okamoto; T. Tonegawa; M. Kaburagi, *J. Phys. Condens. Matter* **2003**, *15*, 5979. (c) H. -J. Koo; M. -H. Whangbo, *Inorg. Chem.* **2008**, *47*, 4779.
- (5) (a) H. Kikuchi; Y. Fujii; M. Chiba; S. Mitsudo; T. Idehara; T. Tonegawa; K. Okamoto; T. Sakai; T. Kuwai; H. Ohta, *Phys. Rev. Lett.* **2005**, *94*, 227201. (b) G. Bo; G. Su, *Phys. Rev. Lett.* **2006**, *97*, 089701. (c) K. C. Rule; A. U. B. Wolter; S. Süllo; D. A. Tennant; A. Brühl; S. Köhler; B. Wolf; M. Schreuer Lang, J., *Phys. Rev. Lett.* **2008**, *100*, 117202. (d) J. Kang; C. Lee; R. K. Kremer; M.-H. Whangbo, *J. Phys.:Condens. Matter*, **2009**, *21*, 392201.
- (6) (a) M. Hase; M. Kohno; H. Kitazawa; N. Tsujii; O. Suzuki; K. Ozawa; G. Kido; M. Imai; X. Hu, *Phys. Rev. B* **2006**, *73*, 104419. (b) M. Hase; M. Matsuda; K. Kakurai; K. Ozawa; H. Kitazawa; N. Tsujii; A. Dönni; M. Kohno; X. Hu, *Phys. Rev. B* **2007**, *76*, 064431. (c) H. -J. Koo; M. -H. Whangbo, *Inorg. Chem.* **2010**, *49*, 9253.
- (7) P. J. Hay; J. C. Thibeault; R. Hoffmann, *J. Am. Chem. Soc.* **1975**, *97*, 4884.
- (8) H. -J. Koo; M. -H. Whangbo, *Inorg. Chem.* **2006**, *45*, 4440.
- (9) (a) D. Dai; H. -J. Koo; M. -H. Whangbo, *Inorg. Chem.* **2004**, *43*, 4026. (b) H. -J. Koo; C. Lee; M.-H. Whangbo; G. J. McIntyre; R. K. Kremer, *Inorg. Chem.*, in press.
- (10) C. Tian; A. C. Wibowo; H. -C. zur Loye; M. -H. Whangbo, *Inorg. Chem.*, in press.
- (11) (a) D. Dai; M.-H. Whangbo, *J. Chem. Phys.* **2001**, *114*, 2887. (b) D. Dai; M.-H. Whangbo, *J. Chem. Phys.* **2003**, *118*, 29.
- (12) H. J. Xiang; C. Lee; M.-H. Whangbo, *Phys. Rev. B* **2007**, *76*, 220411(R).

- (13) J. S. Smart; *Effective Field Theory of Magnetism*: Saunders, Philadelphia, 1966.
- (14) J. E. Greedan, *J. Mater. Chem.* **2001**, *11*, 37, and the references cited therein.
- (15) D. Dai; M.-H. Whangbo, *J. Chem. Phys.* **2004**, *121*, 672.
- (16) H. J. Xiang; M. -H. Whangbo, *Phys. Rev. Lett.*, **2007**, *99*, 257203.
- (17) M. G. Banks; R. K. Kremer; C. Hoch; A. Simon; B. Ouladdiaf; J.-M. Broto; H. Rakoto;
C. Lee; M. -H. Whangbo, *Phys. Rev. B* **2009**, *80*, 024404.
- (18) C. K. Majumdar; D. Ghosh, *J. Math. Phys.* **1969**, *10*, 1388.
- (19) D. Dai; H. J. Xiang; M. -H. Whangbo, *J. Comput. Chem.* **2008**, *29*, 2187.
- (20) H.-J. Koo; H. J. Xiang; C. Lee; M-H. Whangbo, *Inorg. Chem.* **2009**, *48*, 9051.
- (21) Hans Schmid, *Ferroelectrics* **1994**, *162*, 317
- (22) J. van den Brink and D. Khomskii, *Cond-Mat.* **2008**, 0803, 2964
- (23) N. Ikeda et al., *Nature.* **2005**, 436, 1136
- N. A. Spaldin, *J. Phys. Chem. B.* **2000**, *104* (29), 6694
- (24) H. Katsura, N. Nagaosa and V. Balatsky, *Phys. Rev. Lett.* **2005**, *95*, 057205.
- (25) A. H. Arkenbout, T. T. M. Palstra, T. Siegrist, and T. Kimura *Phys. Rev. B* **2006**, *74*, 184431
- (26) T. Kimura *Annu. Rev. Matter. Res.* **2007**, *37*, 387
- (27) D. Dai, H. Xiang, M. -H. Whangbo, *Journal of Computational Chemistry.* **2008**, *29*, 2187
- (28) Kuneš, J.; Novák, P.; Diviš, M.; Oppeneer, *P. M. Phys Rev B* **2001**, *63*, 205111
- (29) N. F. Mott, *Metal-Insulator Transitions*, 2nd ed.; Taylor & Francis: London, 1990.
- (30) M. -H. Whangbo, *J. Chem. Phys.* **1979**, *70*, 4963.

- (31) S. L. Dudarev; G. A. Botton; S. Y. Savrasov; C. J. Humphreys; A. P. Sutton, *Phys. Rev. B* **1998**, *57*, 1505.
- (32) Kobayashi, Y. *J. Magnetism and Magnetic Materials* **2004**, *272*, 1091
- (33) Relaxation of Excited States and Photoinduced Structural Transitions, edited by K. Nasu
Springer-Verlag, Berlin, 1977
- (34) Kahn, O. *Molecular Magnetism*; VCH: New York, 1993.
- (35) Lis, T. *Acta Crystallogr., Sect. B* **1980**, *B36*, 2042.
- (36) Güttlich, P.; Hauser, A.; Spiering, H. *Angew. Chem., Int. Ed. Engl.* **1994**, *33*, 2024.
- (37) P. Hohenberg and W. Kohn, *Phys. Rev.* **1964**, *136*, B864.
- (38) W. Kohn and L. J. Sham, *Phys. Rev.* **1965**, *140*, A1133.
- (39) T.-H. Arima, *J. Phys. Soc. Jpn.* **2007**, *76*, 073702.
- (40) V. G. Zubkov, G. V. Bazuev, I. A. P. Tyutyunnik, and I. F. Berger, *J. Solid State Chem.* **2001**, *160*, 293.
- (41) T. A. Kaplan and S. D. Mahanti, *arXiv*: 0808.0336v3.
- (42) D. Dai and M.-H. Whangbo, *Inorg. Chem.* **2005**, *44*, 4407.
- (43) King-Smith R. D.; Vanderbilt, D. *Phys. Rev. B* **1993**, *47*, 1651.
- (44) Resta, R. *Rev. Mod. Phys.* **1994**, *66*, 899.

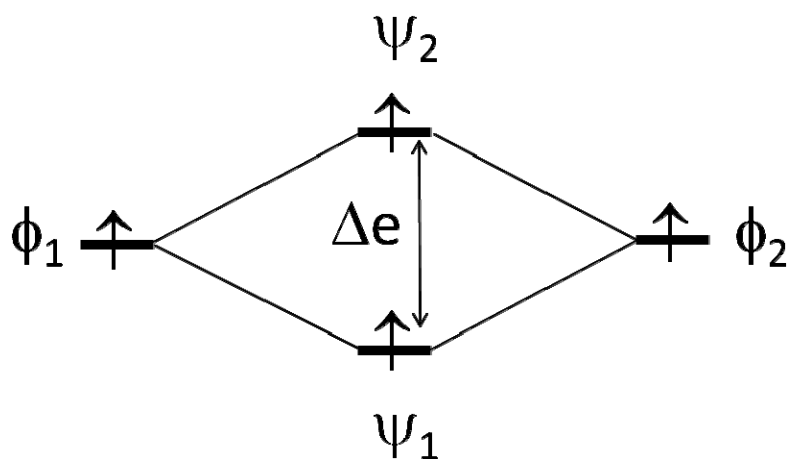


Figure 1.1. Orbital interaction between two spin sites described by the magnetic orbitals ϕ_1 and ϕ_2 leading to the dimer levels ψ_1 and ψ_2 separated by the energy gap Δe .

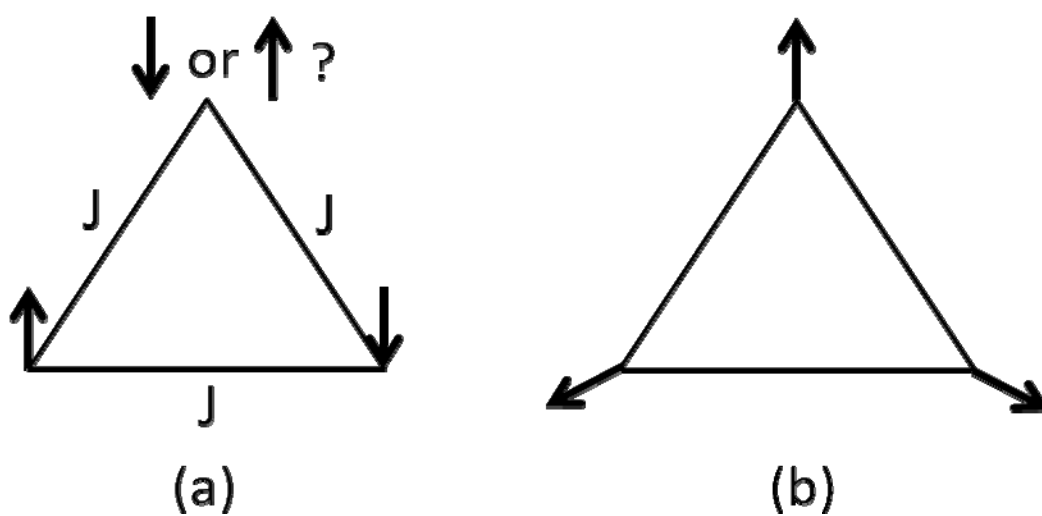


Figure 1.2. Triangular spin frustration and non-collinear spin arrangement in a triangle of spin sites described by the nearest-neighbor AFM spin exchange $J (< 0)$: (a) Spin frustration

that occurs when the spins are collinear. (b) Compromised non-collinear spin arrangement that minimizes the total spin exchange interactions.

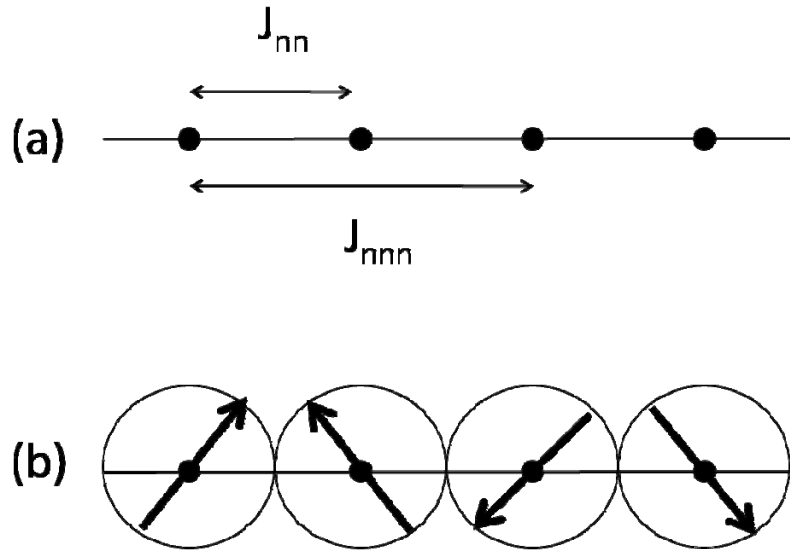


Figure 1.3. (a) Linear spin frustration in a 1D chain of spin sites described by the nearest-neighbor and next-nearest-neighbor spin exchange (J_{nn} and J_{nnn} , respectively). A typical case occurs when $J_{nn} > 0$ and $J_{nnn} < 0$. (b) Spiral spin arrangement that minimizes the total spin exchange interactions.

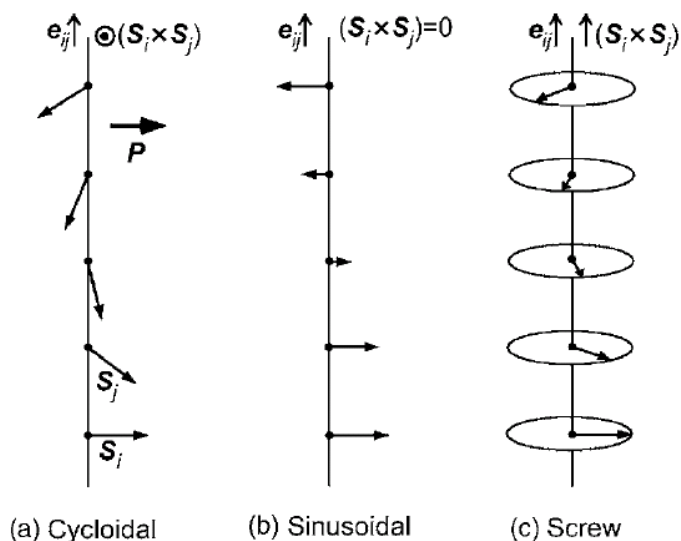


Figure 1.4 Schematic illustration of three types of spin-spiral magnetic structures in a 1D chain of magnetic ions: (a) cycloidal, (b) sinusoidal, and (c) screw (or helical).

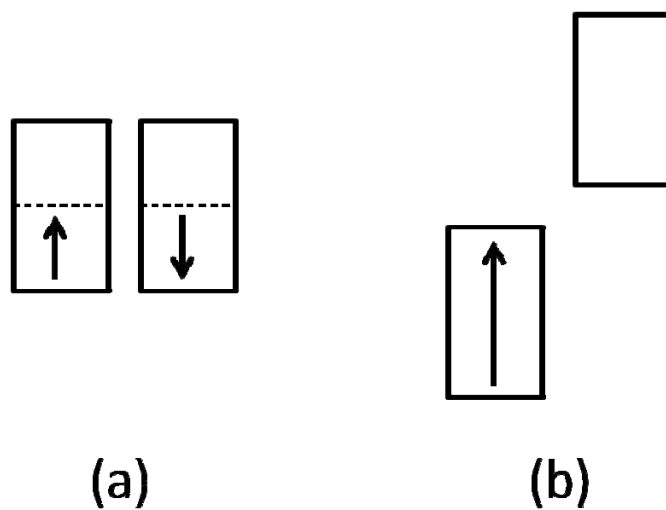


Figure 1.5. Two electronic states that a system with a half-filled band can have: (a) Non-magnetic metallic state, in which both the up-spin and down-spin states are half-filled. (b)

Magnetic insulating state, in which the up-spin band is completely filled, but the down-spin band, separated from the up-spin band by a band gap, is empty.

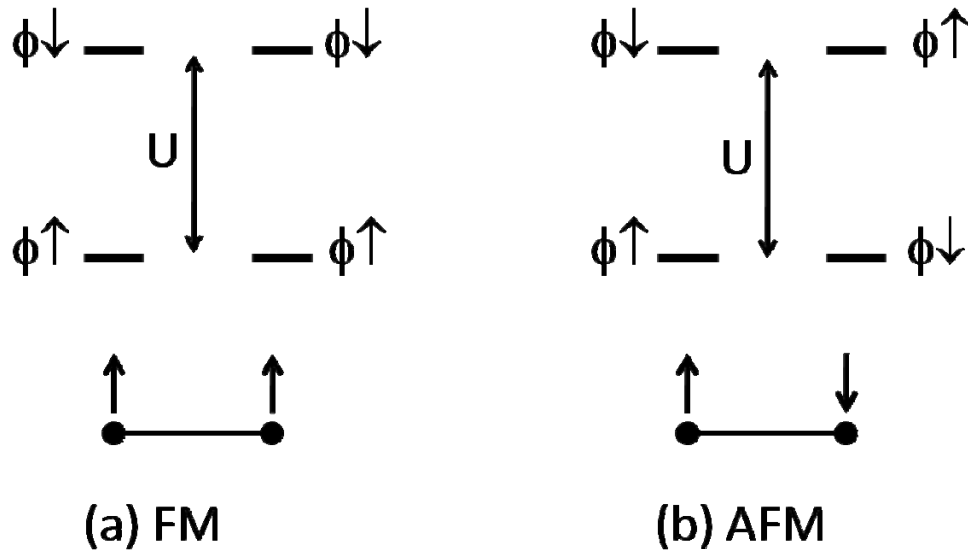


Figure 1.6. Split patterns of the up-spin and down-spin levels ($\phi\uparrow$ and $\phi\downarrow$, respectively) for the two extreme cases of spin arrangements for a 1D chain with one orbital per site: (a) FM state in which all sites have up-spins. (b) AFM state in which up-spin and down-spin sites alternate. Only two adjacent spin sites of the chain are shown for simplicity.

Chapter 2

Magnetic Structure and Ferroelectric Polarization of MnWO_4 Investigated by Density Functional Calculations and Classical Spin Analysis

A paper published in Physical Review B.

Phys. Rev. B, Vol. 80, 104426, 2009

Chuan Tian¹, Changhoon Lee¹, Hongjun Xiang², Yuemei Zhang¹, Christophe Payen³, Stéphane Jobic³, and Myung-Hwan Whangbo^{1*}

¹ Department of Chemistry, North Carolina State University, Raleigh, NC 27695-8204

² National Renewable Energy Laboratory, Golden, Colorado 80401

³ Institut des Matériaux Jean Rouxel, Université de Nantes, CNRS, 2 rue de la Houssinière, BP 32229, 44322 Nantes, France

Abstract

The ordered magnetic states of MnWO_4 at low temperatures were examined by evaluating the spin exchange interactions between the Mn^{2+} ions of MnWO_4 on the basis of first principles density functional calculations and by performing classical spin analysis with the resulting spin exchange parameters. Our work shows that the spin exchange interactions are frustrated within each zigzag chain of Mn^{2+} ions along the c-direction and between such chains of Mn^{2+} ions along the a-direction. This explains the occurrence of a spiral-spin order along the c- and a-directions in the incommensurate magnetic state AF2, and that of a $\uparrow\uparrow\downarrow\downarrow$ spin order along the c- and a-directions in the commensurate magnetic state AF1. The ferroelectric polarization of MnWO_4 in the spiral-spin state AF2 was examined by performing Berry phase calculations for a model superstructure to find that the ferroelectric polarization occurs along the b-direction, in agreement with experiment.

I. Introduction

Manganese tungstate MnWO_4 is made up of MnO_6 octahedra with high-spin Mn^{2+} (d^5) ions and WO_6 octahedra with diamagnetic W^{6+} (d^0) ions [1-3]. The MnO_6 octahedra share their *cis* edges to form zigzag MnO_4 chains along the *c*-direction (**Fig. 2.1a**). Similarly, the WO_6 octahedra share their *cis* edges to form zigzag WO_4 chains along the *c*-direction (**Fig. 2.1b**). These MnO_4 and WO_4 chains share their octahedral corners to form the three-dimensional structure of MnWO_4 (**Fig. 2.1c**). As a result, layers of Mn^{2+} ions parallel to the *bc*-plane (hereafter, the //*bc*-layers of Mn^{2+} ions) alternate with layers of W^{6+} ions parallel to the *bc*-plane along the *a*-direction. The neutron diffraction study by Lautenschläger *et al.* [3] established that MnWO_4 undergoes three magnetic phase transitions below 14 K, namely, the paramagnetic to the AF3 state at T_N (13.5 K), the AF3 to the AF2 state at T_2 (12.3 K), and the AF2 to the AF1 state at T_1 (8.0 K). The magnetic structures of the AF3 and AF2 states are incommensurate with the propagation vector $(-0.214, 0.5, 0.457)$, while that of the AF1 state is commensurate with the propagation vector $(-0.25, 0.5, 0.5)$. Ehrenberg *et al.* [4] analyzed the spin wave dispersion curves of the magnetic state AF1 of MnWO_4 , determined from inelastic neutron scattering measurements [4], in terms of nine spin exchange parameters (**Fig. 2.2, Table 2.1**); the exchanges J_1 and J_2 in the zigzag chains of Mn^{2+} ions along the *c*-direction (hereafter, the //*c*-chains of Mn^{2+} ions), the exchanges J_3 and J_4 between adjacent //*c*-chains of Mn^{2+} ions in each //*bc*-layer of Mn^{2+} ions, and the exchanges $J_5 - J_9$ between adjacent //*bc*-layers of Mn^{2+} ions along the *a*-direction. So far, it has not been tested whether the values of $J_1 - J_9$ extracted by Ehrenberg *et al.* [4] are consistent with other magnetic properties and the electronic structure of MnWO_4 .

Recently, MnWO_4 has received much attention due to the finding that it exhibits ferroelectric (FE) polarization in the AF2 state [5-7], because this state has a spiral-spin order [6,7] and hence has no inversion symmetry [8-10]. It was found that the spin spiral of the AF2 state propagates along the $//c$ -chain direction as well as along the interlayer direction (i.e., the a -direction) [7]. This implies that MnWO_4 has spin frustration in the exchange interactions within each $//c$ -chain and between the $//c$ -chains along the a -direction, because noncollinear spin arrangements occur generally to reduce the extent of geometric spin frustration [11-15]. Indeed, MnWO_4 has been known to be a moderately spin frustrated system with the frustration parameter is $f = -\theta/T_N \approx 5$, where the Curie-Weiss temperature θ is approximately -75 K and the Néel temperature T_N is 13.5 K [5,16]. In the spin exchange values of Ehrenberg *et al.* (**Table 2.1**) [4], the nearest-neighbor intrachain exchange J_1 is antiferromagnetic (AFM) while the next-nearest-neighbor intrachain exchange J_2 is ferromagnetic (FM). The latter means that the spin exchanges within each $//c$ -chain are not spin-frustrated, which is inconsistent with the occurrence of spiral-spin within each $//c$ -chain [7]. The incommensurate (AF2 and AF3) and the commensurate (AF1) states have a common feature in their propagation vectors, i.e., the magnetic order along the b -direction is AFM. The reason for this commensurate component is unclear, although one might speculate if it is a consequence of spin exchange interactions other than J_3 and J_4 because the latter two are quite weak according to Ehrenberg *et al.* [4]. One drawback of spin exchange parameters deduced from experiment is that the physical data of a given magnetic system (e.g., magnetic susceptibility, inelastic neutron scattering and heat capacity data) are often fitted equally well by more than one set of exchange parameters, as found, for example, for $(\text{VO})_2\text{P}_2\text{O}_7$ [17,18],

$\text{Na}_3\text{Cu}_2\text{SbO}_6$ and $\text{Na}_2\text{Cu}_2\text{TeO}_6$ [19-23], and $\text{Bi}_4\text{Cu}_3\text{V}_2\text{O}_{14}$ [24-27]. Ultimately, the correct set of exchange parameters should be consistent with the electronic structure of a magnetic system under consideration because it is the electronic structure that determines the magnetic energy spectrum [28-31]. In view of the fact that the magnetoelectric properties of MnWO_4 have attracted much attention in recent years, it is important to investigate the spin exchange interactions and the FE polarization of MnWO_4 in terms of electronic structure calculations.

In the present work, we examine the magnetic and FE properties of MnWO_4 on the basis of first principles density functional theory (DFT) electronic structure calculations. We first evaluate the nine spin exchange parameters of MnWO_4 by carrying out mapping analysis based on DFT calculations [29]. Then, we perform classical spin analysis [30] with the resulting spin exchange parameters to probe the incommensurate magnetic structure of MnWO_4 . Finally, we evaluate the FE polarization of MnWO_4 by using the Berry phase method [32,33].

II. Computational details

Our calculations employed the Vienna ab-initio simulation package [34-36], the generalized gradient approximations (GGA) for the exchange and correlation corrections [37], the plane-wave cutoff energy of 400 eV, 196 k-points for the irreducible Brillouin zone, and the threshold of 10^{-6} eV for the self-consistent-field convergence of the total electronic energy. To properly describe the electron correlation of the Mn 3d states, the GGA plus on-site repulsion U (GGA+U) method [38] was employed with an effective $U = 4$ and 6 eV on the Mn atom. The nine spin exchange parameters were evaluated by performing GGA+U

calculations for a number of ordered spin states of MnWO_4 (see below). On the basis of the resulting spin exchange parameters, we examined the magnetic structure of MnWO_4 by performing classical spin analysis as described elsewhere [30]. For the ferroelectricity driven by a magnetic order, it is essential to take into consideration spin-orbit coupling (SOC) effects in electronic structure calculations [13-15]. Thus, to estimate the FE polarization of MnWO_4 in the AF2 state, we performed GGA+U+SOC calculations for a model spiral-spin state of MnWO_4 (see below), which is designed to simulate the AF2 state of MnWO_4 . Then, the FE polarization was calculated by using the Berry phase method [32,33].

III. Spin exchange parameters

In the magnetic state AF1 the $\uparrow\uparrow\downarrow\downarrow$ spin order occurs along the c- and the a-directions, and the $\uparrow\downarrow\uparrow\downarrow$ spin arrangement along the b-direction. In addition, the phase of the $\uparrow\uparrow\downarrow\downarrow$ arrangement along the a-direction is shifted such that four different $\uparrow\uparrow\downarrow\downarrow$ arrangements occur (i.e., $\uparrow\downarrow\downarrow\uparrow$, $\downarrow\downarrow\uparrow\uparrow$, $\downarrow\uparrow\uparrow\downarrow$, $\uparrow\uparrow\downarrow\downarrow$). Consequently, the propagation vector of the AF1 state becomes $(-0.25, 0.5, 0.5)$. In general, the $\uparrow\uparrow\downarrow\downarrow$ arrangement along a certain direction occurs when there is geometric spin frustration, as found for the CuO_2 ribbon chains of LiCuVO_4 and LiCu_2O_2 [13]. The propagation vector of the incommensurate states AF2 and AF3, $(-0.214, 0.5, 0.457)$, is slightly different from that of the AF1 state. To gain insight into the occurrence of the ordered magnetic states AF1 and AF2 of MnWO_4 , we evaluate its spin exchange parameters $J_1 - J_9$ and discuss their trends.

A. Mapping analysis

To evaluate $J_1 - J_9$, we examine the 10 ordered spin states defined in **Figs. 3-5**. The relative energies of these states determined from our GGA+U calculations are summarized in **Table 2.2**. To extract the values of the spin exchange parameters $J_1 - J_9$, we express the total spin exchange interaction energies of the 10 ordered spin states in terms of the spin Hamiltonian,

$$\hat{H} = -\sum_{i<j} J_{ij} \hat{S}_i \cdot \hat{S}_j, \quad (1)$$

where J_{ij} ($= J_1 - J_9$) is the spin exchange parameter for the spin exchange interaction between the spin sites i and j , while \hat{S}_i and \hat{S}_j are the spin angular momentum operators at the spin sites i and j , respectively. Then, by applying the energy expressions obtained for spin dimers with N unpaired spins per spin site (in the present case, $N = 5$) [39,40], the total spin exchange energies of the 10 ordered spin states (per two formula units) are written as

$$E_{\text{FM}} = (-2J_1 - 2J_2 - 2J_3 - 2J_4 - 2J_5 - 2J_6 - 2J_7 - 2J_8 - 2J_9)(N^2 / 4)$$

$$E_{\text{AF1}} = (+2J_1 - 2J_2 + 2J_3 - 2J_4 - 2J_5 + 2J_6 + 2J_7 + 2J_8 + 2J_9)(N^2 / 4)$$

$$E_{\text{AF2}} = (+2J_2 - 2J_4 - 2J_5)(N^2 / 4)$$

$$E_{\text{AF3}} = (-2J_1 - 2J_2 + 2J_3 + 2J_4 - 2J_5 + 2J_6 + 2J_7 - 2J_8 - 2J_9)(N^2 / 4)$$

$$E_{\text{AF4}} = (-2J_1 - 2J_2 - 2J_3 - 2J_4 + 2J_5 + 2J_6 + 2J_7 + 2J_8 + 2J_9)(N^2 / 4)$$

$$E_{\text{AF5}} = (-3J_1 - 3J_2 - J_3 - J_4 - J_5 - J_6 - J_7 - J_8 - J_9)(N^2 / 8)$$

$$E_{\text{AF6}} = (-3J_1 - 3J_2 - 3J_3 - 3J_4 - 3J_5 - 3.5J_6 - 3J_7 - 3J_8 - 3J_9)(N^2 / 8)$$

$$E_{\text{AF7}} = (-3J_1 - 3J_2 - 3J_3 - 3J_4 - 3J_5 - 3J_6 - 3J_7 - 3.5J_8 - 3J_9)(N^2 / 8)$$

$$\begin{aligned}
E_{AF8} &= (-3J_1 - 3J_2 - 3J_3 - 3J_4 - 3J_5 - 3.5J_6 - 3.5J_7 - 3J_8 - 3J_9)(N^2/8) \\
E_{AF9} &= (-3J_1 - 3J_2 - 3J_3 - 3J_4 - 3J_5 - 3J_6 - 3J_7 - 3J_8 - 3.5J_9)(N^2/8)
\end{aligned} \tag{2}$$

Thus, by mapping the relative energies of the 10 ordered spin states determined by the GGA+U calculations onto the corresponding relative energies determined from the above spin exchange energies, we obtain the values of $J_1 - J_9$ summarized in **Table 2.1**.

B. Trends in the spin exchange interactions

Let us first comment on the values of $J_1 - J_9$ calculated in the previous section. In the mean field theory [41], which is valid in the high-temperature paramagnetic limit, the Curie-Weiss temperature θ is related to the spin exchange parameters of MnWO_4 as follows:

$$\theta = \frac{S(S+1)}{3k_B} \sum_i z_i J_i, \tag{3}$$

where the summation runs over all nearest neighbors of a given spin site, z_i is the number of nearest neighbors connected by the spin exchange parameter J_i , and S is the spin quantum number of each spin site Mn^{2+} (i.e., $S = 5/2$ in the present case). Thus, according to the spin exchange paths defined in **Fig. 2.2**, θ is expressed as

$$\theta = \frac{20(J_1 + J_2 + J_3 + J_4 + J_5 + J_6 + J_7 + J_8 + J_9)}{k_B} \tag{4}$$

From the J_i values from the GGA+U calculations (**Table 2.1**), the Curie-Weiss temperature is found to be $\theta_{\text{cal}} = -357$ and -232 K for $U = 4$ and 6 eV, respectively. The experimental Curie-Weiss temperature is $\theta_{\text{exp}} \approx -75$ K, so that θ_{cal} is greater than θ_{exp} by a factor of

approximately 3 – 5. The latter means that the calculated J_i values are overestimated by a factor of approximately 3 – 5, which is consistent with the finding that DFT electronic structure calculations generally overestimate the magnitude of spin exchange interactions by a factor of approximately 4 [39,42-44]. In terms of the J_i values of Ehrenberg *et al.* [4] (**Table 2.1**) the Curie-Weiss temperature is calculated to be -32 K, so that their J_i values are underestimated by a factor of approximately 2.5 as far as the Curie-Weiss temperature is concerned.

Our calculations (**Table 2.1**) show that both J_1 and J_2 are AFM, and $J_2/J_1 \gg 0.25$, so that geometric spin frustration exists within each //c-chain. This finding accounts for the occurrence, in each //c-chain, of the spiral-spin order in the AF2 state and the $\uparrow\uparrow\downarrow\downarrow$ spin order in the AF1 state. To see if there exists spin frustration along the a-direction, we consider four commensurate spin arrangements of MnWO_4 generated by using the //c-chains with $\uparrow\uparrow\downarrow\downarrow$ spin order as the building units (**Fig. 6**). In the AF1 state (**Fig. 2.6a**), the //c-chains have a $\uparrow\downarrow\uparrow\downarrow$ order (i.e., an AFM coupling) along the b-direction and a $\uparrow\uparrow\downarrow\downarrow$ spin order along the a-direction. The AF4 state (**Fig. 6b**) differs from the AF1 state, only in that the //c-chains have a $\uparrow\downarrow\uparrow\downarrow$ order along the a-direction. The AF5 (**Fig. 6c**) and AF6 (**Fig. 2.6d**) states differ from the AF1 and AF4 states only in that the //c-chains have a $\uparrow\uparrow\uparrow\uparrow$ order (i.e., an FM coupling) along the b-direction, respectively. Per spin site, these four commensurate spin arrangements give rise to the interchain spin exchange energies listed in **Table 2.3**. The exchange parameters $J_1 - J_9$ of Ehrenberg *et al.* as well as those obtained from our GGA+U calculations predict that the AF1 state is the most stable state of the four. The J_1

– J_9 values from the GGA+U calculations show that the //c-chains with $\uparrow\uparrow\downarrow\downarrow$ spin order prefer to have a $\uparrow\downarrow\uparrow\downarrow$ order rather than a $\uparrow\uparrow\uparrow\uparrow$ order along the b-direction, in agreement with experiment. Furthermore, the $J_1 - J_9$ values from the GGA+U calculations predict that the AF4 state (i.e., a $\uparrow\downarrow\uparrow\downarrow$ order along the a-direction) is close in energy to the AF1 state (i.e., a $\uparrow\uparrow\downarrow\downarrow$ order along the a-direction). In other words, along the a-direction, the interaction between the //c-chains with the $\uparrow\uparrow\downarrow\downarrow$ spin order is effectively frustrated because the spin order can be either $\uparrow\uparrow\downarrow\downarrow$ or $\uparrow\downarrow\uparrow\downarrow$, the extent of which may be reduced by an incommensurate spiral-spin order along the a-direction. This topic will be discussed further in the next section.

IV. Classical spin analysis

To examine the occurrence of the incommensurate magnetic structure (i.e., the AF2 and AF3 states) in MnWO_4 , we calculate the total spin exchange energy of MnWO_4 by using the Freiser method [30,45]. This approach assumes that spins adopt all possible directions in space (i.e., the classical spin approximation), and the spin exchange interactions are isotropic (i.e., a Heisenberg description). These assumptions are appropriate for MnWO_4 , because the local magnetic anisotropy of the high spin Mn^{2+} ($S = 5/2$, $L = 0$) ions is very small. Indeed, MnWO_4 is well described as a Heisenberg antiferromagnet, as shown by the very small anisotropy of the paramagnetic susceptibility [5]. This also means that the complex low-temperature magnetic properties of MnWO_4 do not arise from a competition between the

local anisotropy and the spin exchange interactions, but from the frustration of the spin exchange interactions.

In a long-range ordered magnetic state of a magnetic system, the spin sites μ ($= 1, 2, \dots, m$) of its unit cell located at the coordinate origin (i.e., the lattice vector $\mathbf{R} = 0$) have the spin moments σ_{μ}^0 . For a magnetic solid with repeat vectors \mathbf{a} , \mathbf{b} and \mathbf{c} , the ordered spin arrangement is described by the spin functions $\sigma_{\mu}(\mathbf{k})$,

$$\sigma_{\mu}(\mathbf{k}) = \frac{1}{\sqrt{M}} \sum_{\mathbf{R}} \sigma_{\mu}^0 \exp(i\mathbf{k} \cdot \mathbf{R}), \quad (5)$$

where M is the number of unit cells in the magnetic solid, \mathbf{k} is the wave vector, and \mathbf{R} is the direct lattice vector [46]. The ordered magnetic state $\psi_i(\mathbf{k})$ ($i = 1 - m$) is then expressed as a linear combination of the spin functions $\sigma_{\mu}(\mathbf{k})$,

$$\psi_i(\mathbf{k}) = C_{1i}(\mathbf{k}) \sigma_1(\mathbf{k}) + C_{2i}(\mathbf{k}) \sigma_2(\mathbf{k}) + \dots + C_{mi}(\mathbf{k}) \sigma_m(\mathbf{k}). \quad (6)$$

To determine the energy $E_i(\mathbf{k})$ of the state $\psi_i(\mathbf{k})$ and the coefficients $C_{\mu i}(\mathbf{k})$ ($\mu = 1 - m$), one needs to evaluate the spin exchange interaction energies $\xi_{\mu\nu}(\mathbf{k})$ between every two spin functions $\sigma_{\mu}(\mathbf{k})$ and $\sigma_{\nu}(\mathbf{k})$,

$$\xi_{\mu\nu}(\mathbf{k}) = - \sum_{\mathbf{R}} J_{\mu\nu}(\mathbf{R}) \exp(i\mathbf{k} \cdot \mathbf{R}), \quad (7)$$

where $J_{\mu\nu}(\mathbf{R}) = J_1, J_2, J_3, J_4, J_5, J_6, J_7, J_8$, or J_9 . The resulting interaction matrix $\Xi(\mathbf{k})$ is given by

$$\Xi(\mathbf{k}) = \begin{pmatrix} \xi_{11}(\mathbf{k}) & \xi_{12}(\mathbf{k}) & \dots & \xi_{1m}(\mathbf{k}) \\ \xi_{21}(\mathbf{k}) & \xi_{22}(\mathbf{k}) & \dots & \xi_{2m}(\mathbf{k}) \\ \dots & \dots & \dots & \dots \\ \xi_{m1}(\mathbf{k}) & \xi_{m2}(\mathbf{k}) & \dots & \xi_{mm}(\mathbf{k}) \end{pmatrix}. \quad (8)$$

We obtain $E_i(\mathbf{k})$ of the state $\psi_i(\mathbf{k})$ by diagonalizing this matrix. This method predicts the superstructure of a magnetic system by finding the wave vector at which its global energy minimum occurs [30,45].

There are two Mn^{2+} ion sites in a crystallographic unit cell of MnWO_4 (**Table 2.3a**), so that $m = 2$ in Eq. 8. The spin exchanges $J_1 - J_9$ occur for various pairs of spin sites (μ, ν) within a unit cell located at $[0, 0, 0]$ as well as between adjacent unit cells $[0, 0, 0]$ and $[n, k, l]$ ($n, k, l = -1, 0, +1$), as summarized in **Table 2.3b**. Consequently, we obtain the following matrix elements $\xi_{\mu\nu}(\mathbf{k})$ ($\mu, \nu = 1, 2$),

$$\begin{aligned} \xi_{11}(\mathbf{k}) = \xi_{22}(\mathbf{k}) &= -J_2[\exp(-i2\pi x_c) + \exp(+i2\pi x_c)] \\ &\quad - J_4[\exp(-i2\pi x_b) + \exp(+i2\pi x_b)] \\ &\quad - J_5[\exp(-i2\pi x_a) + \exp(+i2\pi x_a)] \\ \xi_{12}(\mathbf{k}) = \xi_{21}(\mathbf{k})^* &= -J_1\{1 + \exp[i2\pi(-x_c)]\} \\ &\quad - J_3\{\exp[i2\pi(+x_b)] + \exp[i2\pi(+x_b - x_c)]\} \\ &\quad - J_6\{\exp[i2\pi(+x_a + x_b - x_c)] + \exp[i2\pi(-x_a + x_b)]\} \\ &\quad - J_7\{\exp[i2\pi(-x_a + x_b - x_c)] + \exp[i2\pi(+x_a + x_b)]\} \\ &\quad - J_8\{\exp[i2\pi(+x_a - x_c)] + \exp[i2\pi(-x_a)]\} \\ &\quad - J_9\{\exp[i2\pi(+x_a)] + \exp[i2\pi(-x_a - x_c)]\} \end{aligned} \quad (9)$$

where x_a, x_b and x_c are dimensionless numbers [46].

Thus, at any given wave vector \mathbf{k} , one can determine the numerical values of $\xi_{\mu\nu}(\mathbf{k})$ ($\mu, \nu = 1, 2$) by using the $J_1 - J_9$ values listed in **Table 2.1** and hence diagonalize the $\Xi(\mathbf{k})$

matrix to obtain $E_i(\mathbf{k})$ ($i = 1, 2$). Then, the propagation vector \mathbf{q} of the incommensurate magnetic state is determined as the \mathbf{k} value at which the lower energy $E_1(\mathbf{k})$ has the minimum. Our calculations show that $\mathbf{q} = (-0.29, 0.5, 0.44)$ from the $J_1 - J_9$ values of Ehrenberg *et al.*, and $(-0.35, 0.5, 0.49)$ and $(-0.36, 0.5, 0.48)$ from the calculated $J_1 - J_9$ values with $U = 4$ and 6 eV, respectively. These results are in qualitative agreement with the appearance of the incommensurate AF2 state with $\mathbf{q} = (-0.214, 0.5, 0.457)$. From this finding and our discussion in the previous section (**Fig. 2.6**), it is clear that the AFM coupling along the b -direction both in the incommensurate state AF2 and in the commensurate state AF1 arises to lower the energy associated with the spin exchange interactions other than the weak interchain exchanges J_3 and J_4 .

The observation of the collinear commensurate state AF1 as the magnetic ground state below 8 K is due most likely to a weak local magnetic anisotropy of Mn^{2+} , which is not included in the Heisenberg model. Since the entropy is greater in the spiral-spin incommensurate state AF2 than in the collinear commensurate AF1 state, the AF2 state would be energetically favored over the AF1 state at temperature higher than 8 K. It is interesting to note that doping the Mn^{2+} sites of MnWO_4 with a small amount of Fe^{2+} (d^6 , $S = 2$) ions stabilizes the AF1 state [47], which is due to the large local magnetic anisotropy of the high-spin Fe^{2+} ions.

V. Ferroelectric polarization

In this section, we examine the FE polarization of the spiral-spin state AF2 of MnWO_4 . The spin-spiral plane is perpendicular to the ac-plane and is tilted away from the a-axis by 35° (**Fig. 2.7**). The incommensurate propagation vector of the AF2 state is $(-0.214, 0.5, 0.457)$, the closest commensurate approximation of which is $(-0.25, 0.5, 0.5)$. The latter requires the use of the supercell (4a, 2b, 2c) for our GGA+U+SOC calculations of FE polarization. **Fig. 2.8** shows the AFM and FM arrangements, along the b-direction, of the //c-chains with spiral-spin order. In both the AFM and the FM arrangements, each //c-chain has the same chirality of spin spiral, and hence leads to a same sign of FE polarization. In addition, the interchain exchange interactions J_3 and J_4 are very weak, as already mentioned. Thus, for the purpose of FE polarization, we assume the FM ordering of the //c-chains along the b-direction and hence employ the supercell (4a, b, 2c) for our calculations. In making the spiral-spin arrangement with the (4a, b, 2c) supercell, we employed the plane of the spin spiral defined in **Fig. 2.7** so that the spins spiral along the a- and c-directions. In our GGA+U+SOC calculations (with $U = 6$ eV) for the electronic structure of this model spiral-spin state, the atom positions of the (4a, b, 2c) supercell were not relaxed. Our subsequent Berry phase calculations show that the FE polarization is along the positive b-direction with $P_b = 17.2 \mu\text{C}/\text{m}^2$. Experimentally, P_b is found to be smaller than $\sim 50 \mu\text{C}/\text{m}^2$ [5].

It is of interest to examine the calculated FE polarization from the viewpoint of the Katsura-Nagaosa-Balatsky (KNB) model [48], which predicts that the FE polarization \vec{P} of a

spiral-spin chain with spins \vec{S}_i and \vec{S}_j at the adjacent spin sites connected by the vector \vec{e}_{ij} is given by

$$\vec{P} \propto \vec{e}_{ij} \times (\vec{S}_i \times \vec{S}_j), \quad (10)$$

according to which FE polarization arises only from spin-spiral chains of cycloidal type (i.e., those chains whose spin-spiral planes contain the chains). In the (4a, b, 2c) superstructure with the (-0.25, 0, 0.5) spiral-spin order, the spiral-spin propagation along the a-direction has a cycloidal component when the spins are projected on the ab-plane (**Fig. 2.10a**), while that along the c-direction has a cycloidal component when the spins are projected on the bc-plane (**Fig. 2.10b**). It is reasonable to assume that the sign of the coefficient in Eq. 10 for the ab-plane is the same as that for the bc-plane. Then, the cycloidal component in the ab-plane gives a positive FE polarization along the b-direction (**Fig. 2.10a**), whereas that in the bc-plane gives a negative FE polarization along the b-direction (**Fig. 2.10b**). Since the angle between the ab- and the spin-spiral planes is 35° , the FE polarization arising from the ab-plane cycloidal component is greater than that from the bc-plane cycloidal component. As a consequence, the net FE polarization is along the positive b-direction, as found from our GGA+U calculations.

VI. Concluding remarks

The spin exchange interactions of MnWO_4 extracted from the present GGA+U calculations reveal that the spin exchange interactions are frustrated within each //c-chain of Mn^{2+} ions and between such //c-chains along the a-direction. This finding is in agreement

with the experimental observation that a spiral-spin propagates along the c- and the a-directions in the incommensurate state AF2, and a $\uparrow\uparrow\downarrow\downarrow$ spin arrangement occurs along the c- and a-directions in the collinear magnetic state AF1. The classical spin analysis with the extracted spin exchange parameters leads to an incommensurate state with propagation vector in qualitative agreement with that found for the AF2 state. The AFM coupling between the //c-chains along the b-direction does not result from the weak interchain exchanges J_3 and J_4 but from the combined effect of other strong spin exchange interactions. The Berry phase calculations for a model (4a, b, 2c) superstructure with spiral-spin order show FE polarization along the b-direction, in agreement with experiment.

Acknowledgments

The research was supported by the Office of Basic Energy Sciences, Division of Materials Sciences, U.S. Department of Energy, under Grant No. DE-FG02-86ER45259, and by the NERSC Center (under Contract No. DE-AC02-05CH11231) and the HPC Center of the NCSU campus.

References

- [1] H. Weitzel, Z. Kristallogr. Kristallgeom. Kristallphys. Kristallchem. 144, 238 (1976).
- [2] J. Macavei and H. Schulz, Z. Kristallogr. 207, 193 (1993).
- [3] G. Lautenschläger, H. Weitzel, T. Vogt, R. Hock, A. Böhm, M. Bonnet and H. Fuess, Phys. Rev. B 48, 6087 (1993).

- [4] H. Ehrenberg, H. Weitzel, H. Fuess and B. Hennion, *J. Phys.: Condens. Matter* 11, 2649 (1999).
- [5] A. H. Arkenbout, T. T. M. Palstra, T. Siegrist and T. Kimura, *Phys. Rev. B* 74, 184431 (2006).
- [6] O. Heyer, N. Hollmann, I. Klassen, S. Jodlauk, L. Bohatý, P. Becker, J. A. Mydosh, T. Lorenz and D. Khomskii, *J. Phys.: Condens. Matter* 18, L471 (2006).
- [7] K. Taniguchi, N. Abe, T. Takenobu, Y. Iwasa and T. Arima, *Phys. Rev. Lett.* 97, 097203 (2006).
- [8] M. Fiebig, *J. Phys. D* 38, R123 (2005).
- [9] Y. Tokura, *Science* 312, 1481 (2006).
- [10] S.-W. Cheong and M. Mostvov, *Nat. Mater.* 6, 13 (2007).
- [11] J. E. Greedan, *J. Mater. Chem.* 11, 37 (2001).
- [12] D. Dai and M.-H. Whangbo, *J. Chem. Phys.* 121, 672 (2004).
- [13] H. J. Xiang and M.-H. Whangbo, *Phys. Rev. Lett.* 99, 257203 (2007).
- [14] H. J. Xiang and M.-H. Whangbo, *Phys. Rev. B.* 76, 220411(R) (2007).
- [15] H. J. Xiang, S.-H. Wei, M.-H. Whangbo and J. L. F. Da Silva, *Phys. Rev. Lett.* 101, 037209 (2008).
- [16] H. Dachs, *Solid State Commun.* 7, 1015 (1969).
- [17] A. W. Garret, S. E. Nagler, D. A. Tennant, B. C. Sales and T. Barnes, *Phys. Rev. Lett.* 79, 745 (1997).
- [18] H.-J. Koo, M.-H. Whangbo, P. D. VerNooy, C. C. Torardi and W. J. Marshall, *Inorg. Chem.* 41, 4664 (2002).

- [19] J. Xu, A. Assoud, N. Soheilnia, S. Derakhshan, H. L. Cuthbert, J. E. Greedan, M.-H. Whangbo and H. Kleinke, *Inorg. Chem.* 44, 5042 (2005).
- [20] Y. Miura, R. Hirai, Y. Kobayashi and M. Sato, *J. Phys. Soc. Jpn.* 75, 84707 (2006).
- [21] S. Derakhshan, H. L. Cuthbert, J. E. Greedan, B. Rahman and T. Saha-Dasgupta, *Phys. Rev. B* 76, 104403 (2007).
- [22] H.-J. Koo and M.-H. Whangbo, *Inorg. Chem.* 47, 128 (2008).
- [23] Y. Miura, Y. Yasui, T. Moyoshi, M. Sato and K. Kakurai, *J. Phys. Soc. Jpn.* 77, 104789 (2008).
- [24] H. Sakurai, K. Yoshimura, K. Kosuge, N. Tsujii, H. Abe, H. Kitazawa, G. Kido, H. Michor and G. Hilscher, *J. Phys. Soc. Jpn.* 71, 1161 (2002).
- [25] S. Okubo, T. Hirano, Y. Inagaki, H. Ohta, H. Sakurai, H. Yoshimura and K. Kosuge, *Physica B* 346, 65 (2004).
- [26] K. Okamoto, T. Tonegawa and M. Kaburagi, *J. Phys. Condens. Matter* 15, 5979 (2003).
- [27] H.-J. Koo and M.-H. Whangbo, *Inorg. Chem.* 47, 4779 (2008).
- [28] F. Illas, I. de P. R. Moreira, C. de Graaf and D. Varone, *Theoret. Chem. Acc.* 104, 265 (2000).
- [29] M.-H. Whangbo, H.-J. Koo and D. Dai, *J. Solid State Chem.* 176, 417 (2003).
- [30] M.-H. Whangbo, D. Dai and H.-J. Koo, *Solid State Sci.* 7, 827 (2005).
- [31] D. Dai, H. J. Xiang and M.-H. Whangbo, *J. Comput. Chem.* 29, 2187 (2008).
- [32] R. D. King-Smith and D. Vanderbilt, *Phys. Rev. B* 47, 1651 (1993).
- [33] R. Resta, *Rev. Mod. Phys.* 66, 899 (1994).
- [34] G. Kresse and J. Hafner, *Phys. Rev. B* 62, 558 (1993).

- [35] G. Kresse and J. Furthmüller, *Comput. Mater. Sci.* 6, 15 (1996).
- [36] G. Kresse and J. Furthmüller, *Phys. Rev. B* 54, 11169 (1996).
- [37] J. P. Perdew, S. Burke and M. Ernzerhof, *Phys. Rev. Lett.* 77, 3865 (1996).
- [38] S. L. Dudarev, G. A. Botton, S. Y. Savrasov, C. J. Humphreys and A. P. Sutton, *Phys. Rev. B* 57, 1505 (1998).
- [39] D. Dai and M.-H. Whangbo, *J. Chem. Phys.* 114, 2887 (2001).
- [40] D. Dai and M.-H. Whangbo, *J. Chem. Phys.* 118, 29 (2003).
- [41] J. S. Smart, *Effective Field Theory of Magnetism*; Saunders: Philadelphia, 1966.
- [42] D. Dai, H.-J. Koo and M.-H. Whangbo, *J. Solid State Chem.* 175, 341 (2003).
- [43] D. Dai, M.-H. Whangbo, M.-H. Koo, X. Rocquefelte, S. Jobic and A. Villesuzanne, *Inorg. Chem.* 44, 2407 (2005).
- [44] R. Grau-Crespo, N. H. de Leeuw and C. R. Catlow, *J. Mater. Chem.* 13, 2848 (2003).
- [45] M. J. Freiser, *Phys. Rev.* 123, 2003 (1951).
- [46] Given the lattice vector written as $\mathbf{R} = n_a \mathbf{a} + n_b \mathbf{b} + n_c \mathbf{c}$, where n_a , n_b and n_c are integers, and the wave vector \mathbf{k} written as $\mathbf{k} = x_a \mathbf{a}^* + x_b \mathbf{b}^* + x_c \mathbf{c}^*$, where \mathbf{a}^* , \mathbf{b}^* and \mathbf{c}^* are the reciprocal vectors, and x_a , x_b and x_c are dimensionless numbers, the $\exp(i\mathbf{k}\cdot\mathbf{R})$ term becomes $\exp[i2\pi(x_a n_a + x_b n_b + x_c n_c)]$.
- [47] F. Ye, Y. Ren, J. A. Fernandez-Baca, H. A. Mook, J. W. Lynn, R. P. Chaudhury, Y. Q. Wang, B. Lorenz and C. W. Chu, *Phys. Rev. B* 78, 193101 (2008).
- [48] H. Katsura, N. Nagaosa and A. V. Balatsky, *Phys. Rev. Lett.* 95, 057205 (2005).

Table 2.1 Mn...Mn distances (in Å) associated with the spin exchange paths $J_1 - J_9$ of MnWO_4 and the values of $J_1 - J_9$ (in k_BK) determined by Ehrenberg et al. [4] from their neutron scattering study and by the present GGA+U calculations.

	Mn...Mn	Ehrenberg <i>et al.</i>	GGA+U (U = 4 eV)	GGA+U (U = 6 eV)
J_1	3.283	-0.195	-2.343	-1.856
J_2	4.992	+0.414	-4.222	-2.691
J_3	4.398	-0.135	-0.174	-0.186
J_4	5.753	+0.021	-0.418	-0.209
J_5	4.823	-0.423	-2.714	-1.775
J_6	6.561	-1.273	-2.378	-1.334
J_7	6.492	+0.491	-0.638	-0.360
J_8	5.873	-0.509	-3.364	-2.146
J_9	5.795	+0.023	-1.601	-1.032

Table 2.2 Relative energies (in meV per two formula units) of the ordered spin states of MnWO_4 determined by the present GGA+U calculations.

	U = 4 eV	U = 6 eV
FM	0.00	0.00
A1	-22.62	-14.88
A2	-20.42	-13.24
A3	-7.75	-4.49
A4	-23.04	-14.32
A5	-10.88	-6.91
A6	-4.72	-3.07
A7	-4.49	-2.94
A8	-4.35	-2.83
A9	-4.59	-2.98

Table 2.3 Four arrangements of the //c-chains with $\uparrow\uparrow\downarrow\downarrow$ spin order and their interchain spin exchange energies, E, per spin site.

	// b	// a	E (per Mn)	E (k _B K per Mn) ^a		
				Case A	Case B	Case C
AF1	$\uparrow\downarrow\uparrow\downarrow$	$\uparrow\uparrow\downarrow\downarrow$	$+J_6 - J_7 + J_8 - J_9 + J_4$	-2.75	-3.92	-2.30
AF4	$\uparrow\downarrow\uparrow\downarrow$	$\uparrow\downarrow\uparrow\downarrow$	$+J_5 + J_4$	-0.40	-3.13	-1.98
AF5	$\uparrow\uparrow\uparrow\uparrow$	$\uparrow\uparrow\downarrow\downarrow$	$-J_6 + J_7 + J_8 - J_9 - J_4$	+1.21	+0.40	+0.07
AF6	$\uparrow\uparrow\uparrow\uparrow$	$\uparrow\downarrow\uparrow\downarrow$	$+J_5 - J_4$	-0.44	-2.30	-1.57

^a Case A: Calculated from the $J_1 - J_9$ by Ehrenberg *et al.*

Case B: Calculated from the $J_1 - J_9$ of the present GGA+U calculations with $U = 4$ eV.

Case C: Calculated from the $J_1 - J_9$ of the present GGA+U calculations with $U = 6$ eV.

Table 2.4 (a) Fractional coordinates of the spin sites in MnWO_4 , (b) Pairs (μ, ν) of the spin sites $(\mu, \nu = 1, 2)$ leading to the spin exchanges $J_1 - J_9$ in MnWO_4 within a unit cell at $[0, 0, 0]$ as well as between unit cells $[0, 0, 0]$ and $[n, k, l]$.

Spin site	Mn	x	y	z
1	Mn(1)	0.5	0.6853	0.25
2	Mn(2)	0.5	0.3147	0.75

Path	Within	Between	[n, k, l]
J ₁	(1,2)	(1,2)	[0, 0, -1]
	(2,1)	(2,1)	[0, 0, 1]
J ₂		(1,1)	[0, 0, -1] & [0, 0, 1]
		(2,2)	[0, 0, -1] & [0, 0, 1]
J ₃		(1,2)	[0, 1, 0] & [0, 1, -1]
		(2,1)	[0, -1, 0] & [0, -1, 1]
J ₄		(1,1)	[0, 1, 0] & [0, -1, 0]
		(2,2)	[0, 1, 0] & [0, -1, 0]
J ₅		(1,1)	[1, 0, 0] & [-1, 0, 0]
		(2,2)	[1, 0, 0] & [-1, 0, 0]
J ₆		(1,2)	[1, 1, -1] & [-1, 1, 0]
		(2,1)	[-1, -1, 1] & [1, -1, 0]
J ₇		(1,2)	[-1, 1, -1] & [1, 1, 0]
		(2,1)	[1, -1, 1] & [-1, -1, 0]
J ₈		(1,2)	[1, 0, -1] & [-1, 0, 0]
		(2,1)	[-1, 0, 1] & [1, 0, 0]
J ₉		(1,2)	[1, 0, 0] & [-1, 0, -1]
		(2,1)	[-1, 0, 0] & [1, 0, 1]

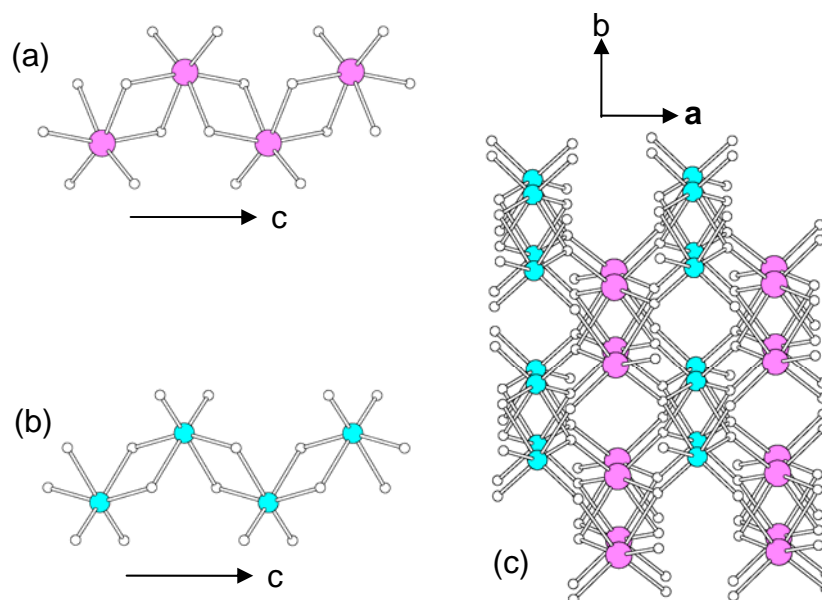


Figure 2.1 Perspective views of (a) a zigzag MnO₄ chain, (b) a zigzag WO₄ chain, and (c) the three-dimensional arrangement of the MnO₄ and WO₄ chains in MnWO₄. The Mn, W and O atoms are represented by large, medium and small spheres, respectively.

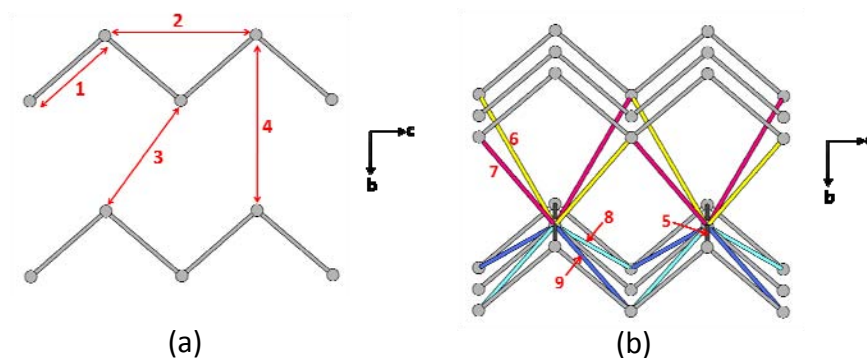


Figure 2.2 (a) Four spin exchange paths $J_1 - J_4$ in MnWO_4 within each //bc-layer of Mn^{2+} ions. (b) Five spin exchange paths $J_5 - J_9$ between adjacent //bc-layers of Mn^{2+} ions in MnWO_4 . The numbers 1 – 9 refer to the spin exchange paths $J_1 - J_9$, respectively.

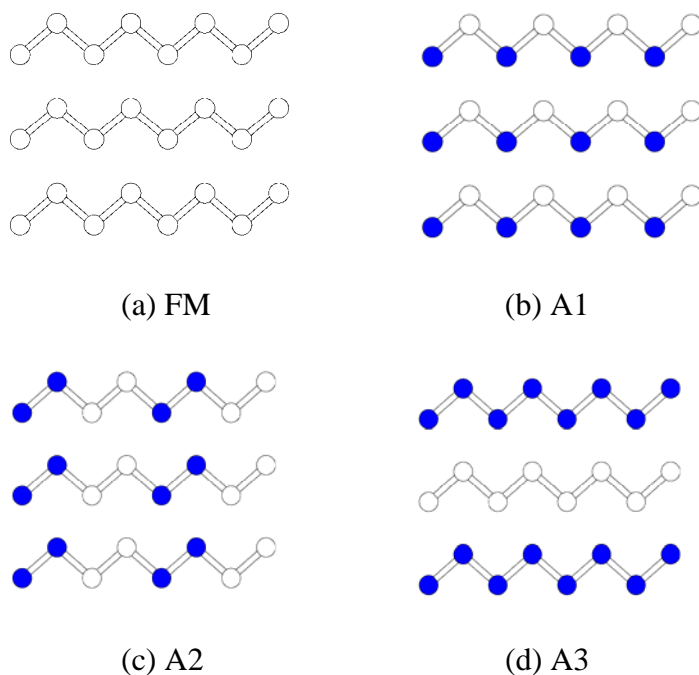
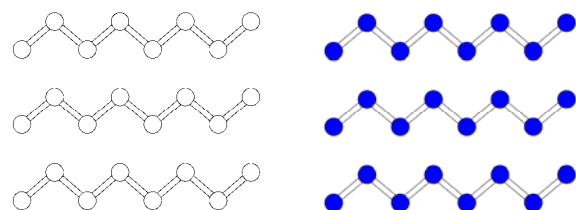
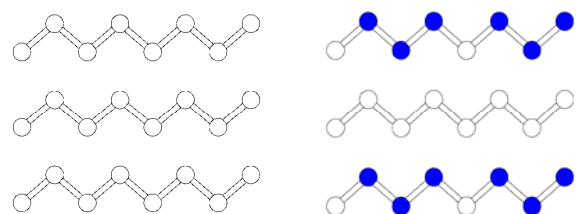


Figure 2.3 Ordered spin arrangements in each //bc-layer of Mn^{2+} ions in the FM, A1, A2 and A3 states of MnWO_4 . The up-spin and down-spin Mn^{2+} sites are represented by filled and unfilled circles, respectively.

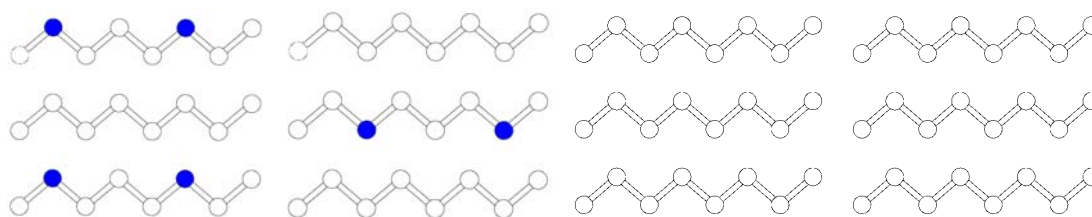


(a) A4

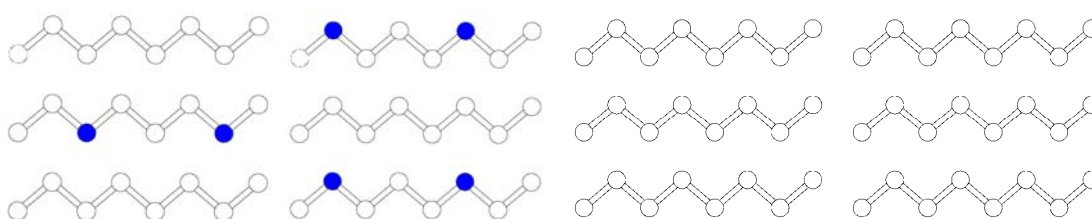


(b) A5

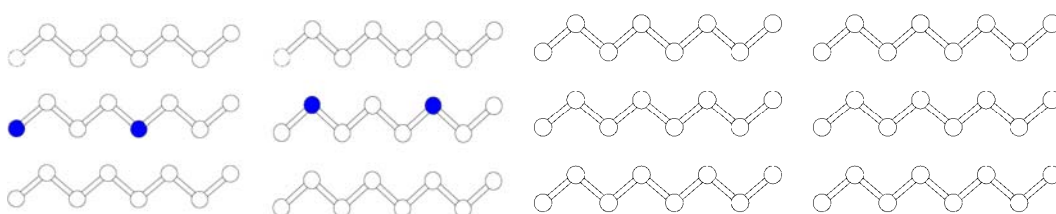
Figure 2.4 Ordered spin arrangements in two successive //bc-layers of Mn^{2+} ions in the A4 and A5 states of MnWO_4 . The up-spin and down-spin Mn^{2+} sites are represented by filled and unfilled circles, respectively.



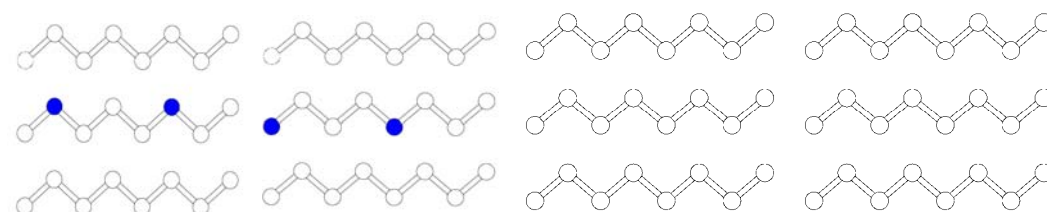
(a) A6



(b) A7



(c) A8



(d) A9

Figure 2.5 Ordered spin arrangements in four successive //bc-layers of Mn^{2+} ions in the A6, A7, A8 and A9 states of MnWO_4 . The up-spin and down-spin Mn^{2+} sites are represented by filled and unfilled circles, respectively.

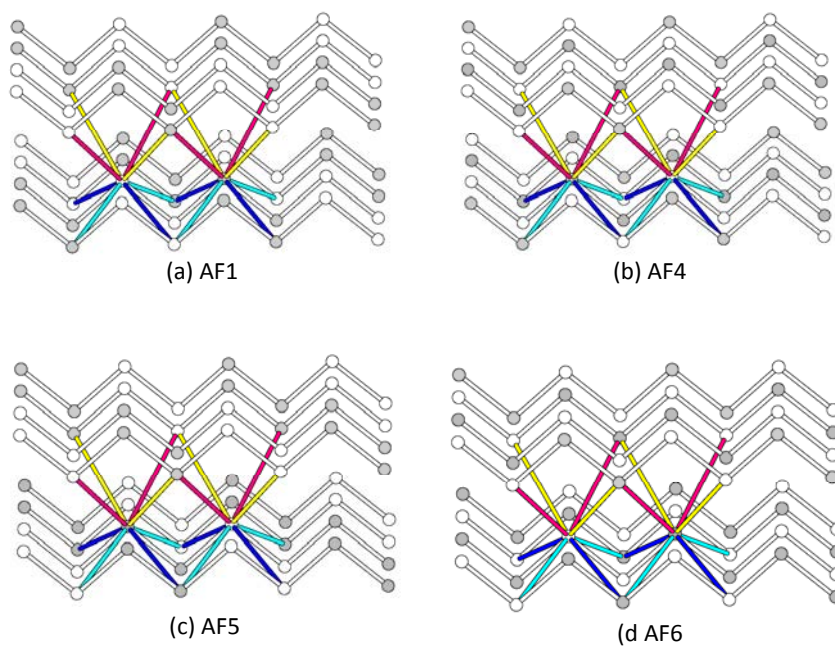


Figure 2.6 Spin arrangements of the (a) AF1, (b) AF4, (c) AF5 and (d) AF4 states of MnWO_4 , which are generated in terms of the //c-chains with the $\uparrow\uparrow\downarrow\downarrow$ spin order.

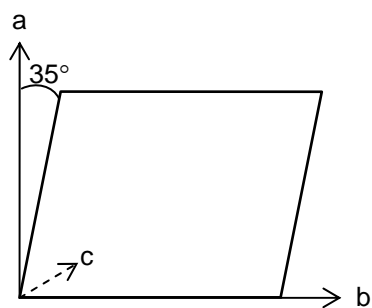


Figure 2.7 Plane of spin spiral found in MnWO_4 .

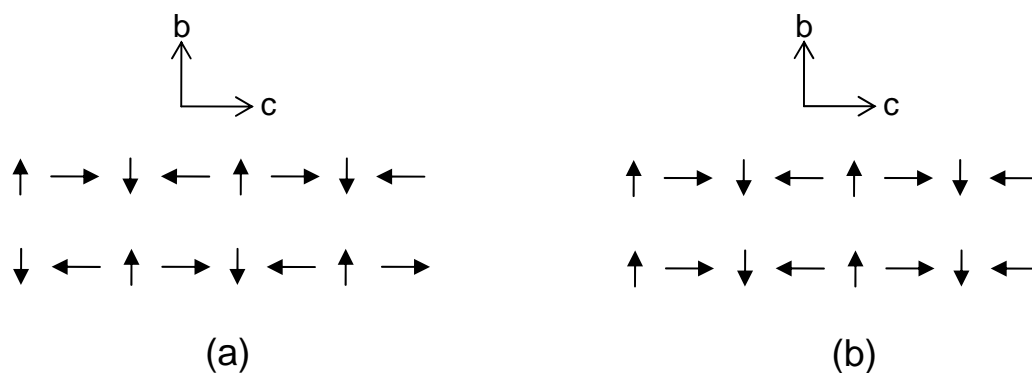


Figure 2.8 Two arrangements of the //c-chains of Mn^{2+} ions with spiral-spin order along the b -direction: (a) AFM and (b) FM. The zigzag chains are represented as straight chains to emphasize the spin spiral order.

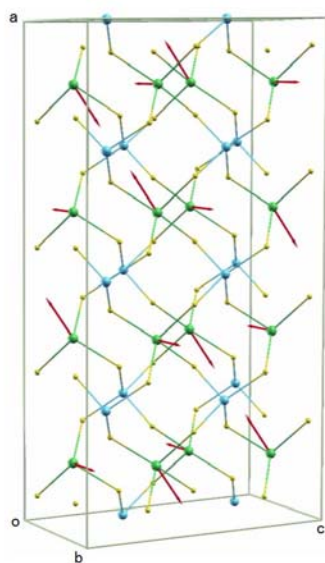


Figure 2.9 Perspective view of the commensurate spiral-spin arrangement of $MnWO_4$ within a $(4a, b, 2c)$ supercell, which was employed for the GGA+U+SOC calculation of FE polarization. The plane of the spin spiral is defined as in Fig. 2.7, so that the spins spiral along the a - and c - directions.

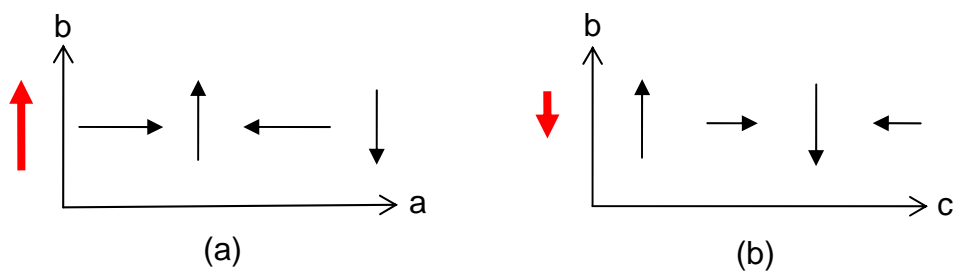


Figure 2.10 Cycloidal components of the spiral-spin state with the $(4a, b, 2c)$ superstructure used to simulate the spiral-spin ordered state AF2. (a) The projection view of the spiral-spin propagation along the a-direction on the ab-plane. (b) that along the c-direction on the bc-plane, where the zigzag chain was represented as a straight chain to emphasize the spin spiral order. The polarization direction is represented by red arrows.

Chapter 3

Analysis of the Magnetic Structure and Ferroelectric Polarization of Monoclinic MnSb_2S_4 by Density Functional Calculations

A paper published in Inorganic Chemistry

Inorg. Chem. Vol. 49 (23), 10956, 2010

Chuan Tian,¹ Changhoon Lee,¹ Erjun Kan,¹ Fang Wu^{1,2} and Myung-Hwan Whangbo^{1,*}

¹ Department of Chemistry, North Carolina State University, Raleigh, NC 27695-8204

² School of Science, Nanjing Forestry University, Nanjing, Jiangsu 210037, People's

Republic of China

Abstract

Monoclinic MnSb_2S_4 consists of MnS_4 chains made up of edge-sharing MnS_6 octahedra and adopts a $(0, 0.369, 0)$ magnetic superstructure below 25 K. This ordered magnetic structure, in which the spins of each MnS_4 chain possess a helical spin arrangement, has C_2' symmetry. On the basis of density functional calculations, we explored the origin of the observed noncollinear spin arrangement of MnSb_2S_4 by evaluating its spin exchanges to find that spin exchanges are frustrated not only within each MnS_4 chain but also between adjacent MnS_4 chains. Our analysis predicts that MnSb_2S_4 is a multiferroic with ferroelectric polarization of $\sim 14 \mu\text{C}/\text{m}^2$ along the chain direction, and a field-induced reversal of the ferroelectric polarization of MnSb_2S_4 can occur by reversing the direction of the helical spin rotation in each MnS_4 chain.

1. Introduction

For a crystalline solid to have ferroelectric (FE) polarization, it should not possess inversion symmetry.^{1,2} A magnetic solid that exhibits FE polarization is commonly referred to as a multiferroic. In principle, a noncentrosymmetric magnetic solid can have FE polarization independent of its magnetic structure. A centrosymmetric magnetic solid can lose inversion symmetry either by cooperative second-order Jahn-Teller distortion or by chiral magnetic order.¹⁻³ For a one-dimensional magnetic chain, Katsura *et al.* showed that a cycloidal spiral-spin order (in which the propagation vector of the chain lies in the plane of the spin rotation) leads to FE polarization, but neither a helical spiral-spin order (in which the propagation vector of the chain is perpendicular to the plane of the spin rotation) nor a sinusoidal spiral-spin order does.⁴ However, if chains with helical spiral spin order interact strongly to form a three-dimensional (3D) magnetic structure whose overall symmetry is C_2 (two-fold rotational symmetry) or C_2' (i.e., C_2 plus time reversal), then FE polarization occurs along the rotational axis.⁵ A further symmetry analysis⁶ showed that FE polarization also occurs even when the magnetic structure has no symmetry other than identity if it is composed of building blocks with symmetry m (mirror-plane symmetry) or m' (i.e., m plus time reversible), with the FE polarization lying in the mirror plane. So far, the phenomenon of magnetic-order-induced FE polarization has been found predominantly among transition metal magnetic oxides. To our knowledge, the layered disulfide AgCrS_2 ⁷ is the only reported example of a multiferroic not based on transition metal oxides. It is of interest to find more examples of non-oxide-based multiferroics induced by chiral magnetic order.

Manganese diantimony sulfide MnSb_2S_4 occurs in two different polymorphs, i.e., orthorhombic⁸ and monoclinic⁹ phases. Both polymorphs consist of MnS_4 chains that are made up of edge-sharing MnS_6 octahedra. In each MnS_4 chain of the monoclinic phase, every shared S atom plus its two adjacent unshared S atoms make a SbS_3 trigonal pyramid leading to a MnSb_2S_4 chain (**Fig. 3.1a**), and such MnSb_2S_4 chains are packed together to form the 3D lattice of monoclinic MnSb_2S_4 (**Fig. 3.1b**). In the orthorhombic phase, the SbS_3 trigonal pyramids are made within each MnS_4 chain as well as between MnS_4 chains to make strongly corrugated MnSb_2S_4 layers, which are packed to form the 3D lattice of orthorhombic MnSb_2S_4 (**Fig. 3.1c**). Matar *et al.*¹⁰ examined the electronic structures of both MnSb_2S_4 phases on the basis of density functional calculations within the local spin density approximation. Their study showed that both phases are antiferromagnetic (AFM) semiconductors, in agreement with the available experimental results.^{9, 11} However, the magnetic structure of monoclinic MnSb_2S_4 below its 3D AFM ordering temperature $T_N = 25$ K is not collinear but exhibits a helical arrangement along each MnS_4 chain (see below).¹¹

The magnetic properties of monoclinic MnSb_2S_4 arise from the high-spin Mn^{2+} ($S = 5/2$) ions. With the Curie-Weiss temperature $\theta = -63$ K and the Néel temperature $T_N = 25$ K,⁹ the spin frustration in MnSb_2S_4 is moderate because the ratio $f = |\theta|/T_N$ is considerably smaller than 6.¹² Nevertheless, the ordered magnetic structure of monoclinic MnSb_2S_4 below T_N , determined by powder neutron diffraction,¹¹ shows a noncollinear spin arrangement that is typically observed from magnetic systems with strong spin frustration; the spins of each MnS_4 chain have a helical rotation along the chain (i.e., along the b-direction) with propagation vector $q = (0, 0.369, 0)$ while the spins between adjacent chains have a

ferromagnetic (FM) arrangement along the *c*-direction but have a $\sim 70^\circ$ -rotated arrangement along the *a*-direction (**Fig. 3.1d**).¹¹ The noncollinear spin arrangements along the *b*- and *a*-directions indicates the existence of spin frustration not only along each MnS_4 chain but also between adjacent MnS_4 chains. Furthermore, the overall symmetry of this magnetic structure is C_2' with each MnS_4 chain as the rotational axis. This suggests that monoclinic MnSb_2S_4 is a non-oxide-based multiferroic with its FE polarization along the chain direction. In the present work, we verify this suggestion and analyze the noncollinear magnetic order of monoclinic MnSb_2S_4 causing FE polarization on the basis of density functional electronic structure calculations.

2. Computational details

To analyze the magnetic structure of monoclinic MnSb_2S_4 , it is necessary to determine its spin exchanges. We evaluate the five exchanges $J_1 - J_5$ of MnSb_2S_4 defined in **Fig. 3.2** by performing density functional calculations for the six ordered spin states constructed with a (*a*, *5b*, *c*) supercell (**Fig. 3.3**). In our calculations the experimental crystal structure⁹ of monoclinic MnSb_2S_4 was employed with no further structure optimization. Our density functional calculations employed the frozen-core projector augmented wave method encoded in the Vienna ab initio simulation packages,¹³ and the generalized-gradient approximation (GGA)¹⁴ with the plane-wave-cut-off energy of 400 eV and a set of 6 *k*-points for the irreducible Brillouin zone. To properly describe the effect of electron correlation in the Mn 3d states, the GGA plus on-site repulsion method (GGA+U)¹⁵ was used with the effective $U_{\text{eff}} = U - J$ values of 4 and 6 eV, typical values used for Mn.¹⁶

To simulate the electronic structure of the ordered magnetic state of MnSb_2S_4 below T_N , we approximate its $q = (0, 0.369, 0)$ incommensurate structure with the $q = (0, 1/3, 0)$ commensurate one, and carry out GGA+U calculations with spin-orbit coupling (SOC) interactions included. The resulting electronic structure is used to calculate the FE polarization of MnSb_2S_4 by employing the Berry phase method.¹⁷ The observed magnetic structure is chiral, i.e., the helical spin rotation in each MnS_4 chain is right-handed along the positive b-direction. Thus, we approximate the observed magnetic structure by the $q = (0, 1/3, 0)$ commensurate structure with the helical rotation angle $\phi = +120^\circ$. We also consider the $q = (0, 1/3, 0)$ commensurate structures with $\phi = 0^\circ$ and -120° to see if the FE polarization of MnSb_2S_4 can be reversed in sign by changing the direction of the helical rotation angle ϕ .

3. Spin exchanges and magnetic structure

Among the five spin exchanges defined in **Fig. 3.2**, J_1 and J_2 are the spin exchanges along each MnS_4 chain, and $J_3 - J_5$ are the interchain interactions between adjacent MnS_4 chains. The Mn...Mn distances associated with these exchange paths are summarized in **Table 3.1**. The relative energies of the six ordered spin states determined by GGA+U calculations are summarized in **Fig. 3.3**. In terms of the spin Hamiltonian,

$$\hat{H} = -\sum_{i<j} J_{ij} \hat{S}_i \cdot \hat{S}_j, \quad (1)$$

where $J_{ij} = J_1 - J_5$, the total spin exchange energies per formula unit (FU) of these states are obtained as

$$\begin{aligned}
\text{FM} &: (-4J_1 - 4J_2 - 8J_3 - 4J_4 - 8J_5)(N^2/4) \\
\text{AF1} &: (-4J_1 + 12J_2 - 26J_3 - 4J_4 - 26J_5)(N^2/20) \\
\text{AF2} &: (+12J_1 - 4J_2 - 6J_3 - 4J_4 - 6J_5)(N^2/20) \\
\text{AF3} &: (-4J_1 - 4J_2 + 8J_3 - J_4 + 8J_5)(N^2/4) \\
\text{AF4} &: (-4J_1 - 4J_2)(N^2/4) \\
\text{AF5} &: (-4J_1 - 4J_2 + 8J_3 + 4J_4 - 8J_5)(N^2/4)
\end{aligned} \tag{2}$$

by applying the energy expressions obtained for spin dimers with N unpaired spins per spin site (in the present case, $N = 5$).¹⁸ Thus, when the relative energies of the six ordered spin states determined by the GGA+U calculations are mapped onto the corresponding relative energies determined from the above spin exchange energies, we obtain the values of the $J_1 - J_5$ summarized in **Table 3.1**. The spin exchanges calculated with the larger U_{eff} are smaller in magnitude than those with the smaller U_{eff} , as is generally found for other magnetic solids.^{6,16,19} In terms of these exchanges, one can calculate the Curie-Weiss temperature θ of MnSb_2S_4 in the mean field approximation,²⁰

$$\theta \approx \frac{20(J_1 + J_2 + J_3 + J_4 + J_5)}{k_B}, \tag{3}$$

to obtain $\theta = -142$ and -57.8 K by using the spin exchanges determined from GGA+U calculations with $U_{\text{eff}} = 4$ and 6 eV, respectively. These values are in reasonable agreement with the experimental value of -63 K. Thus, our GGA+U calculations with $U_{\text{eff}} = 4$ overestimated the spin exchanges by a factor of approximately 2. In general, GGA+U calculations are known to overestimate the spin exchanges of magnetic oxides.^{18a,21}

Table 3.1 shows that the nearest-neighbor and next-nearest-neighbor intrachain exchanges (J_1 and J_2 , respectively) are both AFM, so the spin exchanges along each MnS_4

chain are frustrated as found for the CuO_2 ribbon chains of LiCuVO_4 and LiCuO_2 ²² and for CuCl_2 ribbon chains of CuCl_2 .²³ The spins of these CuO_2 and CuCl_2 ribbon chains (of edge-sharing CuO_4 and CuCl_4 square planes, respectively) have a cycloidal spiral-spin arrangement in their ordered magnetic states, while those of the MnS_4 chains have a helical spiral-spin arrangement in their ordered magnetic states. The spiral-spin order of cycloidal or helical type occurs to reduce the spin frustration generated by J_1 and J_2 , which occurs when $J_1 > 0$ and $J_2 < 0$ or when $J_1 < 0$ and $J_2 < 0$. In terms of the classical spin approximation for an isolated one-dimensional chain defined by J_1 and J_2 , the propagation vector q of the spiral-spin structure is related to the J_1/J_2 ratio as²⁴

$$q = \frac{1}{2\pi} \arccos\left(-\frac{J_1}{4J_2}\right), \quad (4)$$

from which we find $q = 0.281$ and 0.262 by using the J_1/J_2 values obtained from the GGA+U calculations with $U_{\text{eff}} = 4$ and 6 eV, respectively. These values are somewhat smaller than the experimental value of 0.369 . The discrepancy should not be surprising, because the interchain spin exchanges $J_3 - J_5$ are not taken into consideration in this analysis.

Of the three interchain spin exchange $J_3 - J_5$, J_3 is nearly as strongly AFM as the intrachain exchange J_2 whereas J_4 and J_5 are weakly FM (**Table 3.1**). As depicted in **Fig. 3.1c**, the adjacent chains along the c -direction have an FM arrangement but have a $\sim 70^\circ$ -rotated arrangement along the a -direction. The noncollinear spin arrangement along the a -direction indicates that the interchain spin exchanges along the a -direction are frustrated. Indeed, the spin exchanges in the (J_1, J_3, J_3) , (J_1, J_5, J_5) and (J_3, J_4, J_5) triangles, which occur between adjacent MnS_4 chains, are frustrated (**Fig. 3.2**). The spins have an FM arrangement along the

c-direction in the observed magnetic structure, which can be related to the minimization of the spin frustration in the (J_3 , J_4 , J_5) triangles. Every J_4 magnetic bond makes two different (J_3 , J_4 , J_5) triangles, and the J_5 is weaker than J_4 by a factor of approximately 2 (**Table 3.1**) so that the FM spin arrangement along the c-direction minimizes the interchain interaction energy, $2J_3 + J_4 + 2J_5$, per two (J_3 , J_4 , J_5) triangles.

4. Ferroelectric polarization

In general, the polarization P of an FE compound below a certain temperature T_N is a relative value, namely, the polarization below T_N minus that above T_N . In addition, the polarization of an FE compound should reverse its sign when the applied electric field E is reversed in direction below T_N . This is explained in terms of a double-well potential energy curve as a function of E for the transformation from one FE structure with $P > 0$ through a paraelectric (PE) structure with $P = 0$ to an alternative FE structure with $P < 0$. In the absence of the helical magnetic order along each MnS_4 chain (i.e., $\phi = 0^\circ$), the magnetic structure of monoclinic $MnSb_2S_4$ is centrosymmetric. Therefore, when the sign of the electric field E is switched, the polarization of monoclinic $MnSb_2S_4$ might reverse its sign by reversing the sense of the helical spin rotation along each MnS_4 chain, as has been considered for the multiferroic $Ba_3NbFe_3Si_2O_{14}$ with helical spiral spin order.²⁵

To confirm the above points, we perform GGA+U+SOC calculations for the (0, 1/3, 0) superstructures of $MnSb_2S_4$ with the helical spin rotation angle $\phi = +120^\circ$, 0° and -120° . The relative energies of the three structures are 13, 26 and 0 meV per Mn for $\phi = -120^\circ$, 0° and $+120^\circ$, respectively. Namely, the right-handed helical spin rotation ($\phi = +120^\circ$) is

energetically more stable than the left-handed helical spin rotation ($\phi = -120^\circ$). This is consistent with the experimental observation,¹¹ and reflects the effect of the interchain spin exchange interactions. The $(0, 1/3, 0)$ superstructure with $\phi = 0^\circ$ is less stable than those with $\phi = -120^\circ$ and $+120^\circ$, because of the intrachain spin frustration. Our subsequent Berry phase calculations for the $(0, 1/3, 0)$ superstructures show that $P = -14.2, 0,$ and $12.3 \mu\text{C}/\text{m}^2$ for $\phi = +120^\circ, 0^\circ,$ and -120° , respectively. (Here the positive and negative polarizations are directed along the positive and negative b-directions, respectively). Thus, the $(0, 1/3, 0)$ superstructure with $\phi = 0^\circ$ represents the PE structure of MnSb_2S_4 , and the FE polarization of MnSb_2S_4 is approximately $-14 \mu\text{C}/\text{m}^2$ and can change its sign by reversing the direction of the helical spin rotation.

5. Concluding remarks

Our GGA+U calculations reveal that the spin exchanges of monoclinic MnSb_2S_4 are frustrated not only within each MnS_4 chain but also between adjacent MnS_4 chains. This explains the occurrence of the helical spin arrangement in each MnS_4 chain and the noncollinear spin arrangement between adjacent MnS_4 chains along the a-direction. MnSb_2S_4 is predicted to be a multiferroic with FE polarization $P \approx -14 \mu\text{C}/\text{m}^2$ along the MnS_4 chain direction. A field-induced reversal of the FE polarization of MnSb_2S_4 is expected to occur by reversing the direction of the helical spin rotation in each MnS_4 chain. It should be noted that the spin exchanges between adjacent MnS_4 chains are substantial in MnSb_2S_4 , which explains why MnSb_2S_4 can be a multiferroic in spite of a helical spiral spin order in each MnS_4 chain.

Acknowledgments

This work was supported by the Office of Basic Energy Sciences, Division of Materials Sciences, U. S. Department of Energy, under Grant DE-FG02-86ER45259, and also by the computing resources of the NERSC center and the HPC center of NCSU. M.-H.W. thanks Christophe Payen and Stéphane Jobic for invaluable discussion during the development of this work.

References

- (1) (a) Ramesh, R.; Spaldin, N. A. *Nature Mater.* **2007**, *6*, 21. (b) Khomskii, D. *Physics*, **2009**, *2*, 20.
- (2) (a) Eerenstein, W.; Mathur, N. D.; Scott, J. F. *Nature (London)*, **2006**, *442*, 759. (b) Cheong, S. W.; Mostovoy, M. *Nature Mater.* **2007**, *6*, 13. (c) Tokura, Y. *J. Mag. Mag. Mater.* **2007**, *310*, 1145.
- (3) Kan, E. J.; Xiang, H. J.; Lee, C.; Wu, F.; Yang, J. L.; Whangbo, M.-H., *Angew. Chem. Int. Ed.* **2010**, *49*, 1603.
- (4) Katsura, H.; Nagaosa, N.; Balatsky, A. *Phys. Rev. Lett.* **2005**, *95*, 057205.
- (5) Arima, T.-H., *J. Phys.Soc. Japan.* **2007**, *76*, 073702.
- (6) Kan, E. J.; Xiang, H. J.; Zhang, Y.; Lee, C.; Whangbo, M.-H., *Phys. Rev. B.* **2009**, *80*, 104417.
- (7) K. Singh, A. Maignan, C. Martin, and Ch. Simon, *Chem. Mater.* **2009**, *21*, 5007.
- (8) Bente, K.; Edenharter, A., *Z. Kristallogr.* **1989**, *186*, 31.
- (9) Pfitzer, A.; Kurowski, D., *Z. Kristallogr.* **2000**, *215*, 373.

- (10) Matar, S. F.; Wehrich, R.; Kurowski, D.; Pfitzner, A.; Eyert, V., *Phys. Rev. B* **2005**, *71*, 235207.
- (11) Leone, P.; Doussier, C.; Andre, G.; Moelo, Y., *Phys. Chem. Minerals* **2008**, *35*, 201.
- (12) (a) Greedan, J. E. *J. Mater. Chem.* **2001**, *11*, 37. (b) Dai, D.; Whangbo, M.-H. *J. Chem. Phys.* **2004**, *121*, 672.
- (13) (a) Kresse, G.; Hafner, J.; *Phys. Rev. B* **1993**, *47*, 558. (b) Kresse, G.; Furthmüller, J. *Comput. Mater. Sci* **1996**, *6*, 15. (c) Kresse, G.; Furthmüller, J. *Phys. Rev. B* **1996**, *54*, 11169.
- (14) Perdew, J. P.; Burke, K.; Ernzerhof, M. *Phys. Rev. Lett.* **1996**, *77*, 3865.
- (15) Dudarev, S. L.; Botton, G. A.; Savrasov, S. Y.; Humphreys, C. J.; Sutton, A. P. *Phys. Rev. B* **1998**, *57*, 1505.
- (16) Tian, C.; Lee, C.; Xiang, H. J.; Zhang, Y.; Payen, C.; Jovic, S.; Whangbo, M.-H. *Phys. Rev. B* **2009**, *80*, 104426.
- (17) (a) King-Smith, R. D.; Vanderbilt, D. *Phys. Rev. B* **1993**, *47*, 1651. (b) Resta, R. *Rev. Mod. Phys.* **1994**, *66*, 899.
- (18) (a) Dai, D.; Whangbo, M.-H., *J. Chem. Phys.* **2001**, *114*, 2887. (b) Dai, D.; Whangbo, M.-H., *J. Chem. Phys.* **2003**, *118*, 29.
- (19) (a) Xiang, H. J.; Lee, C.; Whangbo, M.-H. *Phys. Rev. B: Rapid Commun.* **2007**, *76*, 220411(R). (b) Koo, H.-J.; Whangbo, M.-H. *Inorg. Chem.* **2008**, *47*, 128. (c) Koo, H.-J.; Whangbo, M.-H. *Inorg. Chem.* **2008**, *47*, 4779.
- (20) Smart, J. S., *Effective Field Theory of Magnetism*; Saunders: Philadelphia, 1966.

- (21) (a) Dai, D.; Koo, H.-J.; Whangbo, M.-H. *J. Solid State Chem.* **2003**, *175*, 341. (b) Dai, D.; Whangbo, M.-H.; Koo, H.-J.; Rocquefelte, X.; Jobic, S.; Villesuzanne, A. *Inorg. Chem.* **2005**, *44*, 2407. (c) Grau-Crespo, R.; de Leeuw, N. H.; Catlow, C. R. *J. Mater. Chem.* **2003**, *13*, 2848.
- (22) Xiang, H. J.; Whangbo, M.-H. *Phys. Rev. Lett.* **2007**, *99*, 257203.
- (23) Banks, M. G., Kremer, R. K.; Hoch, C.; Simon, A.; Ouladdiaf, B.; Broto, J.-M.; Rakoto, H.; Lee, C.; Whangbo, M.-H. *Phys. Rev. B* **2009**, *80*, 024404.
- (24) Dai, D.; Koo, H.-J.; Whangbo, M.-H. *Inorg. Chem.* **2004**, *43*, 4026.
- (25) Lee, C.; Kan, E. J.; Xiang, H. J.; Whangbo, M.-H., *Chem. Mater.*, **2010**, *22*, 5290.

Table 3.1 Mn...Mn distances (in Å) associated with the spin exchange paths $J_1 - J_5$ of monoclinic MnSb_2S_4 and the values of $J_1/k_B - J_5/k_B$ (in K) determined from GGA+U calculations with $U_{\text{eff}} = 4$ and 6 eV.

	Mn...Mn (Å)	$U_{\text{eff}} = 4$ eV	$U_{\text{eff}} = 6$ eV
J_1/k_B	3.799	-2.18	-0.44
J_2/k_B	7.598	-2.80	-1.43
J_3/k_B	6.651	-2.54	-1.31
J_4/k_B	7.553	0.28	0.19
J_5/k_B	7.890	0.15	0.10

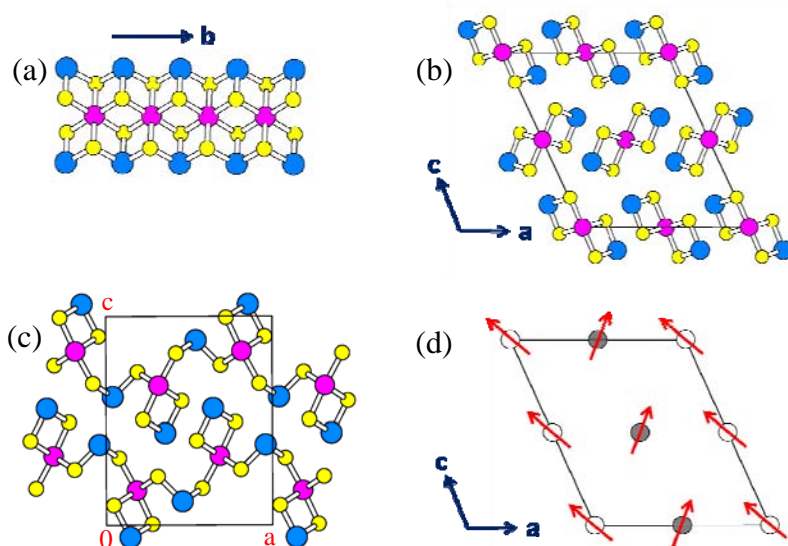


Figure 3.1 Crystal and magnetic structures of MnSb_2S_4 : (a) MnSb_2S_4 chain of monoclinic MnSb_2S_4 , which results from a MnS_4 chain of edge-sharing MnS_6 octahedra capped with SbS_3 pyramids. The pink, purple and yellow spheres (the large, medium and small circles), respectively. (b) Projection view of MnSb_2S_4 chains in monoclinic MnSb_2S_4 along the b -direction. (c) Projection view of MnSb_2S_4 layers in orthorhombic MnSb_2S_4 along the b -direction, where SbS_3 pyramids cap each MnS_4 chain and interconnect between adjacent MnS_4 chains. (d) Spin arrangement of the MnSb_2S_4 chains in monoclinic MnSb_2S_4 . The chain are represented by showing only the Mn atoms. The unshaded and shaded circles, representing the Mn atoms, differ in their b -axis height by $b/2$.

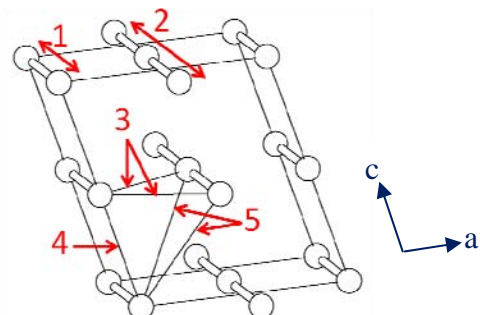


Figure 3.2 Five spin exchange paths $J_1 - J_5$ of monoclinic MnSb_2S_4 . For simplicity, only the Mn atoms are shown as circles. The circles joined by cylinders represent the MnS_4 chains along the b-direction. The numbers 1 – 5 refer to the spin exchange paths $J_1 - J_5$, respectively.

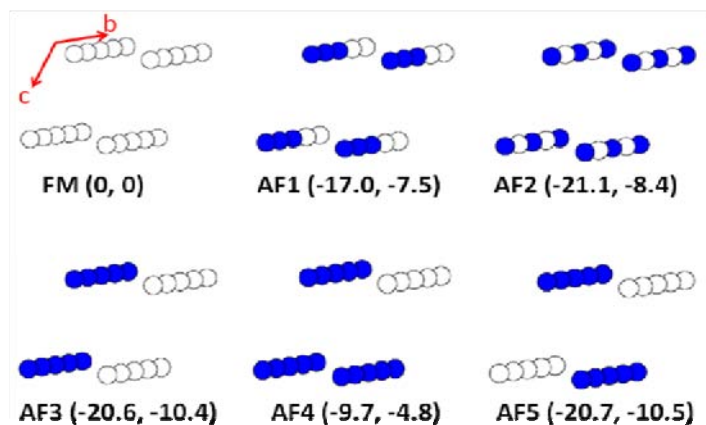
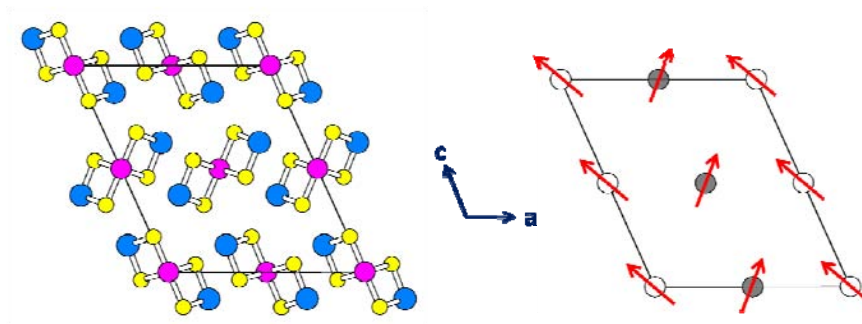


Figure 3.3 Six ordered spin states of monoclinic MnSb_2S_4 defined in terms of the (a, 5b, c) supercell, where the unshaded and shaded circles represent the up-spin and down-spin Mn^{2+} sites, respectively. The numbers in each parenthesis (from left to right) refer to the relative energies (in meV per 4 FUs) determined from GGA+U calculations with $U_{\text{eff}} = 4$ and 6 eV, respectively.

Synopsis

Monoclinic MnSb_2S_4 consists of MnS_4 chains made up of edge-sharing MnS_6 octahedra and adopts a $(0, 0.369, 0)$ magnetic superstructure below 25 K in which the spins of each MnS_4 chain possess a helical spin arrangement. On the basis of density functional calculations, we predict that MnSb_2S_4 is a multiferroic with ferroelectric polarization of $\sim 14 \mu\text{C}/\text{m}^2$ along the chain direction, and a field-induced reversal of the ferroelectric polarization should occur by reversing the direction of the helical spin rotation in each MnS_4 chain.



Chapter 4

On the Magnetic Insulating States, Spin Frustration and Dominant Spin Exchange of the Ordered Double-Perovskites $\text{Sr}_2\text{CuOsO}_6$ and $\text{Sr}_2\text{NiOsO}_6$: Density Functional Analysis

A paper published in Inorganic Chemistry

Inorg. Chem. Vol. 50 (9), 4142, 2011

Chuan Tian¹, Arief C. Wibowo², Hans-Conrad zur Loye², and Myung-Hwan Whangbo^{1,*}

¹ Department of Chemistry, North Carolina State University, Raleigh, North Carolina 27695-8204

² Department of Chemistry and Biochemistry, University of South Carolina, Columbia, South Carolina 29208

Abstract

The ordered double-perovskites Sr_2MOsO_6 ($M = \text{Cu}, \text{Ni}$) consisting of 3d and 5d transition-metal magnetic ions (M^{2+} and Os^{6+} , respectively) are magnetic insulators; the magnetic susceptibilities of $\text{Sr}_2\text{CuOsO}_6$ and $\text{Sr}_2\text{NiOsO}_6$ obey the Curie-Weiss law with

dominant antiferromagnetic and ferromagnetic interactions, respectively, and the zero-field-cooled and field-cooled susceptibility curves of both compounds diverge below ~ 20 K. In contrast, the available density functional studies predicted both $\text{Sr}_2\text{CuOsO}_6$ and $\text{Sr}_2\text{NiOsO}_6$ to be metals. We resolved this discrepancy on the basis of systematic density functional calculations. The magnetic insulating states of Sr_2MOsO_6 are found only when a substantially large on-site repulsion is employed for the Os atom although it is a 5d element. The cause for the divergence between the zero-field-cooled and field-cooled susceptibility curves in both compounds and the reason for the difference in their dominant magnetic interactions were investigated by examining their spin exchange interactions.

1. Introduction

The ordered double-perovskites $\text{Sr}_2\text{CuOsO}_6$,¹ crystallizing in a tetragonal space group $I4/m$, consists of corner-sharing CuO_6 and OsO_6 octahedra such that the CuO_6 and OsO_6 octahedra alternate in all three crystallographic directions with each Cu_4Os_4 cube containing a Sr^{2+} cation. The Cu-O-Os bridges in the layers parallel to the ab-plane (hereafter the //ab-layers) are bent (**Fig. 4.1a**) but those along the c-direction are linear (**Fig. 4.1b**). In $\text{Sr}_2\text{CuOsO}_6$, the Cu and Os atoms are present as Cu^{2+} (d^9 , $S = 1/2$) and Os^{6+} (d^2 , $S = 1$) ions, respectively. Each CuO_6 octahedron exhibits a strong Jahn-Teller distortion associated with the $(t_{2g})^6(e_g)^3$ electron configuration of the Cu^{2+} ion, with two long Cu- O_{ax} bonds along the c-direction and four short Cu- O_{eq} bonds in the ab-plane [i.e., $\text{Cu-O}_{\text{ax}} = 2.315$ ($\times 2$) \AA , $\text{Cu-O}_{\text{eq}} = 1.994$ ($\times 4$) \AA]. Each OsO_6 octahedron displays a weak Jahn-Teller distortion associated with the $(t_{2g})^2$ electron configuration of the Os^{6+} ion, with two long Os- O_{ax} bonds along the c-direction and four short Os- O_{eq} bonds in the ab-plane [i.e., $\text{Os-O}_{\text{ax}} = 1.928$ ($\times 2$) \AA , $\text{Os-O}_{\text{eq}} =$

1.888 ($\times 4$) Å]. As a consequence, the Cu-O_{eq} and Os-O_{eq} bonds of the Cu-O_{eq}-Os superexchange (SE) paths are considerably shorter in the //ab-layers than the Cu-O_{ax} and Os-O_{ax} bonds of the Cu-O_{ax}-Os SE path along the c-direction. In the 10 K structure of Sr₂NiOsO₆² each OsO₆ octahedron is axially elongated [i.e., Os-O_{ax} = 1.957 ($\times 2$) Å, Os-O_{eq} = 1.907 ($\times 4$) Å] whereas each NiO₆ octahedron shows a very weak axial elongation [i.e., Ni-O_{ax} = 2.040 ($\times 2$) Å, Ni-O_{eq} = 2.023 ($\times 4$) Å] although the Ni²⁺ (S = 1) ion is not Jahn-Teller active.

The magnetic susceptibility of Sr₂CuOsO₆¹ above 100 K is well described by a Curie-Weiss law with the Curie-Weiss temperature $\theta = -40$ K, which shows the presence of dominant antiferromagnetic (AFM) interactions. The field-cooled (FC) and zero-field-cooled (ZFC) magnetic susceptibility curves of Sr₂CuOsO₆ diverge below ~ 20 K suggesting the presence of spin frustration. Sr₂NiOsO₆ exhibits somewhat different magnetic properties;² the magnetic susceptibility of Sr₂NiOsO₆ above 150 K is well described by a Curie-Weiss law with the Curie-Weiss temperature $\theta = 27$ K, suggesting the presence of dominant ferromagnetic (FM) interactions. Nevertheless, the magnetic susceptibility shows a slight AFM downturn around 50 K and a deviation between the FC and ZFC susceptibility curves below ~ 20 K. All these magnetic properties reveal that both Sr₂CuOsO₆ and Sr₂NiOsO₆ are magnetic insulators. Contrary to these experimental observations, the density functional theory (DFT) calculations by Song *et al.*^{3,4} found both Sr₂CuOsO₆ and Sr₂NiOsO₆ to be metals.

A system with a partially-filled band can be a metal or a magnetic insulator depending on whether or not the width of the partially filled band is greater than the on-site repulsion U .^{5,6} Unfortunately, it is not possible at present to predict if such a system will be a metal or a magnetic insulator on the basis of first principles DFT electronic structure calculations. The latter predict a magnetic insulator to be metallic when spin-polarization is neglected, and is often predicted to be a metal even if spin polarization is taken into consideration. To correct this failure, DFT calculations are carried out by adding the on-site repulsion U on the magnetic ions to enhance their spin polarization.⁷ In such DFT plus U (DFT+ U) calculations, the effective U value ($U_{\text{eff}} = U - J$, where J is the Stoner intra-atomic parameter) is an empirical parameter; systematic DFT+ U calculations are necessary to establish the range of U_{eff} leading to a magnetic insulating state. For certain solids that have magnetic ions with spin-orbit coupling (SOC) located at high symmetry sites, DFT+ U plus SOC calculations are necessary to find a magnetic insulating state.⁸⁻¹⁰

$\text{Sr}_2\text{CuOsO}_6$ has two different magnetic ions (Cu^{2+} and Os^{6+}), and so does $\text{Sr}_2\text{NiOsO}_6$ (Ni^{2+} and Os^{6+}). Therefore, as found for the high-temperature magnetic structure of $\text{RbMn}[\text{Fe}(\text{CN})_6]$ with Mn^{2+} ($S = 5/2$) and Fe^{3+} ($S = 1/2$) ions,¹¹ predicting a magnetic insulating state for Sr_2MOsO_6 ($M = \text{Cu}, \text{Ni}$) by DFT+ U calculations is a nontrivial task. In the present work, we perform systematic DFT+ U calculations to find the U_{eff} values of both M ($= \text{Cu}, \text{Ni}$) and Os [hereafter U_M and U_{Os} , respectively] necessary for reproducing the magnetic insulating states of Sr_2MOsO_6 . Subsequently, we evaluate the spin exchange interactions of $\text{Sr}_2\text{CuOsO}_6$ and $\text{Sr}_2\text{NiOsO}_6$ to probe if the divergence between their FC and

ZFC susceptibility curves below ~20 K arises from the presence of spin frustration and why the dominant spin exchange interactions of the two compounds are opposite.

2. Magnetic insulating state and its implication

Our DFT calculations for Sr_2MOsO_6 ($M = \text{Cu}, \text{Ni}$) employed the frozen-core projector augmented wave (PAW) method encoded in the Vienna ab initio simulation packages (VASP),¹² and the generalized-gradient approximation (GGA)¹³ with the plane-wave-cut-off energy of 400 eV and a set of 16 k points for the irreducible Brillouin zone. To examine the effect of electron correlation in the M 3d and Os 5d states, the DFT+U method⁷ was employed with $U_M = 3, 4, 5$ and 6 eV and $U_{\text{Os}} = 2, 3$ and 4 eV.

A. $\text{Sr}_2\text{CuOsO}_6$

The magnetic orbital of a Cu^{2+} ion is an e_g orbital (i.e., x^2-y^2 due to the axial elongation of the CuO_6 octahedron) while those of an Os^{6+} (d^2) site are the t_{2g} orbitals (i.e., xz and yz due to the axial elongation of the OsO_6 octahedron). In $\text{Sr}_2\text{CuOsO}_6$, therefore, the overlap between the magnetic orbitals of the Cu^{2+} and Os^{6+} sites is zero for the linear $\text{Cu-O}_{\text{ax}}\text{-Os}$ SE paths or practically zero for the bent $\text{Cu-O}_{\text{eq}}\text{-Os}$ paths. Thus, to a first approximation, one might expect the $\text{Cu-O}_{\text{ax}}\text{-Os}$ and $\text{Cu-O}_{\text{eq}}\text{-Os}$ spin exchanges to be FM rather than AFM.¹⁴⁻¹⁶ Thus, the G-type AFM structure (referred to as the AF1 state, **Fig. 2a**) used for $\text{Sr}_2\text{CuOsO}_6$ by Song *et al.* in their DFT calculations,³ in which every Cu-O-Os exchange has an AFM coupling, may not be appropriate.

An AFM spin exchange can arise from the Cu-O...O-Cu and Os-O...O-Os super-superexchange paths within each //ab-plane layer and from the Os-O...O-Os super-superexchange paths between adjacent //ab-plane layers (see **Fig. 4.1**), because the magnetic orbitals in these exchange paths can overlap across their O...O contacts.¹⁶ (The Cu-O...O-Cu interactions between adjacent //ab-plane layers are not considered, their overlap through the O...O contact would be negligible.) These interactions can lead to the A-type AFM structure (referred to as the AF2 state, **Fig. 4.2b**) in which the Cu²⁺ and Os⁶⁺ spins are ferromagnetically coupled within each //ab-plane layer and such layers are antiferromagnetically coupled. Alternatively, the Cu²⁺ and Os⁶⁺ spins are ferromagnetically coupled within each layer parallel to the (110)-plane and such layers are antiferromagnetically coupled, leading to another A-type AFM structure (referred to as the AF3 state, **Fig. 4.2c**). It is important to see if the A-type AFM state is more stable than the G-type AFM state and whether the A-type AFM state is magnetic insulating.

We examine the aforementioned questions in terms of DFT+U calculations for Sr₂CuOsO₆. For various magnetic oxides of Cu²⁺ ions, the U_{Cu} values of 4 – 6 eV have been used to describe their magnetic properties. In general, the orbitals of a 5d element are much more diffuse than those of a 3d element, so that one might expect the U_{Os} value to be smaller than that of Cu. Thus, in our DFT+U calculations for the AF1, AF2 and AF3 states of Sr₂CuOsO₆, we varied U_{Os} from 2 – 4 eV with U_{Cu} fixed at 3, 4, 5 and 6 eV. Results of our calculations, summarized in **Table 4.1**, show that these states are all metallic when U_{Os} is smaller than 4 eV. With U_{Os} = 4 eV, the AF1 state remains metallic but both AF2 and AF3 states become magnetic insulating. In addition, the AF2 state becomes more stable than the

AF1 and AF3 states. The need to use a substantially large U_{Os} in producing a magnetic insulating state for Sr_2CuOsO_6 indicates that the d electrons of the Os^{6+} ions of Sr_2CuOsO_6 are strongly localized, which in turn means that the Os 5d orbitals are contracted due to the high oxidation state of the Os^{6+} ions. This reasoning is consistent with the fact that the Os-O bonds are considerably shorter than the Cu-O bonds in Sr_2CuOsO_6 [i.e., Os-O = 1.888 ($\times 4$), 1.928 ($\times 2$) Å vs. Cu-O = 1.994 ($\times 4$) and 2.315 ($\times 2$) Å].

B. Sr_2NiOsO_6

The positive Curie-Weiss temperature of Sr_2NiOsO_6 shows the presence of dominant FM interactions, but the magnetic susceptibility downturn below ~ 50 K indicates the presence AFM interactions. To identify the preferred spin arrangement for Sr_2NiOsO_6 , we examined the FM structure as well as three AFM structures, namely, the G-type, the A-type (the AF2 state), and the C-type (in which the FM chains made up of the Ni-O-Os exchange paths along the c-direction are antiferromagnetically coupled). Results of our DFT+U calculations with $U_{Ni} = 3 - 6$ eV and $U_{Os} = 4$ eV are summarized in **Table 4.2**, which shows that the FM spin arrangement is most stable among the four states examined. This finding is consistent with the positive Curie-Weiss temperature of Sr_2NiOsO_6 , but does not explain the magnetic susceptibility downturn below ~ 50 K. To examine a possible cause for the latter as well as the difference between Sr_2NiOsO_6 and Sr_2CuOsO_6 in their dominant spin exchange interactions, it is necessary to evaluate the spin exchange interactions of Sr_2NiOsO_6 and Sr_2CuOsO_6 .

3. Spin exchange interactions

To better understand the magnetic properties of Sr_2MOsO_6 ($M = \text{Cu}, \text{Ni}$), we examine the seven spin exchange interactions $J_1 - J_7$ defined in **Fig. 4.1**. The geometrical parameters associated with these exchange paths are listed in **Table 4.3**. To evaluate these interactions, we consider the relative energies of the eight ordered spin states, i.e., the AF1 – AF7 states (see **Fig. 4.3**) in addition to the FM state. The relative energies of these states calculated by performing DFT+U calculations with $U_M = 6$ eV and $U_{\text{Os}} = 4$ eV are summarized in **Fig. 4.3**.

To extract the values of $J_1 - J_7$, we express the total spin exchange interaction energies of the eight ordered spin states in terms of the spin Hamiltonian, $\hat{H} = -\sum_{i<j} J_{ij} \hat{S}_i \cdot \hat{S}_j$, where $J_{ij} = J_1 - J_7$ is the spin exchange constant for the interaction between the spins \hat{S}_i and \hat{S}_j at the sites i and j , respectively. By applying the energy expression obtained for spin dimers consisting of two spin sites with N_1 and N_2 unpaired spins (i.e., $N_1 = 1$ for Cu^{2+} and $N_2 = 2$ for Os^{6+} , and $N_1 = N_2 = 2$ for Ni^{2+} and Os^{6+}),¹⁷ the total spin exchange energies, per two formula units (FUs), of the eight ordered spin states are written as

$$\begin{aligned}
 E_{\text{FM}} &= (-4J_1 - 4J_5)(N_1^2/4) + (-4J_2 - 4J_6 - 8J_7)(N_2^2/4) + (-8J_3 - 4J_4)(N_1 N_2/4) \\
 E_{\text{AF1}} &= (-4J_1 - 4J_5)(N_1^2/4) + (-4J_2 - 4J_6 - 8J_7)(N_2^2/4) + (+8J_3 + 4J_4)(N_1 N_2/4) \\
 E_{\text{AF2}} &= (-4J_1 - 4J_5)(N_1^2/4) + (-4J_2 - 4J_6 + 8J_7)(N_2^2/4) + (-8J_3 + 4J_4)(N_1 N_2/4) \\
 E_{\text{AF3}} &= (4J_1 - 4J_5)(N_1^2/4) + (4J_2 - 4J_6)(N_2^2/4) + (-4J_4)(N_1 N_2/4) \\
 E_{\text{AF4}} &= (-2J_1 - 2J_5)(N_1^2/4) + (-4J_2 - 4J_6 - 8J_7)(N_2^2/4) + (-6J_3 - 3J_4)(N_1 N_2/4) \\
 E_{\text{AF5}} &= (-4J_1 - 4J_5)(N_1^2/4) + (-4J_6)(N_2^2/4) + (-4J_3 - 2J_4)(N_1 N_2/4) \\
 E_{\text{AF6}} &= (-2J_1)(N_1^2/4) + (-2J_2)(N_2^2/4) + (-4J_3)(N_1 N_2/4) \\
 E_{\text{AF7}} &= (-2J_1 - 2J_5)(N_1^2/4) + (-2J_2 - 2J_6 + 4J_7)(N_2^2/4) + (+2J_3 - 2J_4)(N_1 N_2/4)
 \end{aligned}$$

Thus, by mapping the relative energies of the eight ordered spin states determined from DFT+U calculations onto the corresponding relative energies determined from the above expressions, we obtain the values of $J_1 - J_7$. It should be noted from the energy expression for the FM state that there occur two J_3 and J_7 exchanges for every one of the remaining spin exchanges. This has an important consequence, as will be discussed below.

The two magnetic ions Cu^{2+} ($S = 1/2$) and Os^{6+} ($S = 1$) of $\text{Sr}_2\text{CuOsO}_6$ have different spin moments. Thus, in comparing the relative strengths of the spin exchanges between different spin sites, it is more meaningful to use the effective spin exchanges $J_{ij}^{\text{eff}} = S_i S_j J_{ij} = N_i N_j J_{ij}/4$, where $J_{ij} = J_1 - J_7$. For $\text{Sr}_2\text{NiOsO}_6$, $J_{ij}^{\text{eff}} = J_{ij}$ because $S_i = S_j = 1$ for Ni^{2+} and Os^{6+} . The $J_1^{\text{eff}} - J_7^{\text{eff}}$ values of $\text{Sr}_2\text{CuOsO}_6$ and $\text{Sr}_2\text{NiOsO}_6$ are listed in **Table 4.4**.

The $J_1^{\text{eff}} - J_7^{\text{eff}}$ values of $\text{Sr}_2\text{CuOsO}_6$ show that the spin exchanges within each //ab-layer are dominated by the Cu-O_{eq}-Os exchange J_3^{eff} , which is FM. Although J_5^{eff} is slightly greater than J_3^{eff} in magnitude, the effect of J_3^{eff} is stronger than that of J_5^{eff} because there are two J_3^{eff} interactions for every one J_5^{eff} interaction. This leads to an FM spin order in each //ab-layer. The spin exchanges between adjacent //ab-layers are dominated by J_7^{eff} , which is AFM. The latter gives rise to an AFM coupling between adjacent //ab-layers. Consequently, $\text{Sr}_2\text{CuOsO}_6$ is expected to adopt the A-type AFM structure, AF2, as the most stable ordered spin arrangement. Nevertheless, from **Fig. 4.1** and **Table 4.4**, we note the presence of significant spin frustration in the (J_1, J_3, J_3) and (J_2, J_3, J_3) triangles, in the (J_3, J_3, J_5) segments within each //ab-layer, and in the (J_6, J_7, J_7) triangles between adjacent //ab-layers. This

suggests that the divergence of the ZFC and FC magnetic susceptibility curves of $\text{Sr}_2\text{CuOsO}_6$ below ~ 20 K is caused by spin frustration.

In $\text{Sr}_2\text{NiOsO}_6$ the Ni-O_{ax}-Os spin exchange J_4^{eff} is by far the strongest, hence forming FM chains along the c-directions. Between adjacent FM chains, there occur the Ni-O_{eq}-Os exchange J_3^{eff} , which is very strongly FM, and the Os-O...O-Os exchange J_7^{eff} , which is AFM. The next-nearest-neighbor FM chains interact by the Ni-O...O-Ni exchange J_5^{eff} , which is strongly AFM. The effect of J_5^{eff} cannot overcome that of J_3^{eff} , because J_3^{eff} is stronger than J_5^{eff} in magnitude and there occur two J_3^{eff} interactions for every one J_5^{eff} interaction. The susceptibility downturn of $\text{Sr}_2\text{NiOsO}_6$ below 50 K might be related to the presence of the strong AFM interactions J_5^{eff} and J_7^{eff} between the FM chains made up of J_4^{eff} .

Fig. 4.1 and **Table 4.4** show the presence of significant spin frustration in the (J_3 , J_3 , J_5) segments within each //ab-layer and in the (J_3 , J_4 , J_7) triangles between adjacent //ab-layers. This suggests that the cause for the divergence of the ZFC and FC magnetic susceptibility curves of $\text{Sr}_2\text{NiOsO}_6$ below ~ 20 K is spin frustration.

4. Discussion

The striking differences between the spin exchanges of $\text{Sr}_2\text{CuOsO}_6$ and $\text{Sr}_2\text{NiOsO}_6$ are found for the M-O_{eq}-Os and M-O_{ax}-Os spin exchanges. Namely, $J_3^{\text{eff}} = 2.84$ meV and $J_4^{\text{eff}} = -1.56$ meV in $\text{Sr}_2\text{CuOsO}_6$, whereas $J_3^{\text{eff}} = 5.55$ meV and $J_4^{\text{eff}} = 8.70$ meV in $\text{Sr}_2\text{NiOsO}_6$. As already pointed out, J_3^{eff} and J_4^{eff} involve the e_g -orbitals of M^{2+} and the t_{2g} -orbitals of Os^{6+} , so

that they are expected to be FM, to a first approximation.¹⁴⁻¹⁶ However, the Cu-O_{ax}-Os exchange J_4^{eff} of Sr₂CuOsO₆ is slightly AFM, whereas the Ni-O_{ax}-Os exchange J_4^{eff} of Sr₂NiOsO₆ is strongly FM. In contrast, the M-O_{eq}-Os exchange J_3^{eff} is FM for both Sr₂CuOsO₆ and Sr₂NiOsO₆, but is stronger for Sr₂NiOsO₆. To account for these differences, we note that a spin exchange J between two spin sites i and j , described by the magnetic orbitals ϕ_i and ϕ_j , respectively, is written as $J = J_F + J_{AF}$. The FM component J_F becomes stronger with increasing the overlap density distribution $\phi_i\phi_j$, while the AFM component J_{AF} becomes stronger with increasing the overlap integral $\langle \phi_i | \phi_j \rangle$. The magnetic orbitals of the Cu²⁺, Ni²⁺ and Os⁶⁺ ions of Sr₂MOsO₆ (M = Cu, Ni) are depicted in **Fig. 4.4**. Each Cu²⁺ ion has the magnetic orbital x^2-y^2 (**Fig. 4.4a**), each Ni²⁺ ion has the magnetic orbitals x^2-y^2 and z^2 (**Fig. 4.4a,b**), and each Os⁶⁺ ion has the magnetic orbitals xz and yz (**Fig. 4.4c,d**). In the e_g magnetic orbital(s) of each M²⁺, the metal 3d orbitals make σ^* -antibonding interactions with the 2p orbitals of its first-coordinate O atoms. In the t_{2g} magnetic orbitals of Os⁶⁺, the metal 5d orbitals make π^* -antibonding interactions with the 2p orbitals of its first-coordinate O atoms. For the M-O_{eq}-Os and M-O_{ax}-Os exchange paths, therefore, the overlap integrals of the e_g magnetic orbital(s) of M²⁺ with the t_{2g} magnetic orbitals of Os⁶⁺ are zero, so that the J_{AF} components of their exchanges (J_3^{eff} and J_4^{eff} , respectively) are zero to a first approximation. Thus we need to examine only their J_F components.

Let us first consider Sr₂CuOsO₆. For the sake of simplicity, it will be assumed that the Cu-O_{eq}-Os exchange path is linear along the x-direction. Then, the J_F component of the Cu-O_{eq}-Os exchange is given by the x^2-y^2/xz and x^2-y^2/yz overlap densities. For the x^2-y^2/xz

interaction, both the x^2-y^2 and xz magnetic orbitals have an O 2p orbital contribution at the bridging atom O_{eq} (**Fig. 4.5a**), so that the x^2-y^2/xz overlap density is nonzero hence making J_F nonzero. For the x^2-y^2/yz interaction, the x^2-y^2 magnetic orbital has an O 2p orbital contribution at O_{eq} but the yz orbital does not (**Fig. 4.5b**), so that the x^2-y^2/yz overlap density is zero hence making its J_F zero. For the Cu- O_{ax} -Os exchange, both the x^2-y^2/xz and x^2-y^2/yz interactions have no overlap density because the x^2-y^2 magnetic orbital has no O 2p contribution at the O_{ax} atom (**Fig. 4.5c, d**). Thus, the J_F term is nonzero for the Cu- O_{eq} -Os exchange, but is zero for the Cu- O_{ax} -Os exchange. This explains why the Cu- O_{eq} -Os exchange J_3^{eff} is FM but the Cu- O_{ax} -Os exchange J_4^{eff} is not in Sr_2CuOsO_6 .

For each Ni^{2+} ion of Sr_2NiOsO_6 , the z^2 orbital is also a magnetic orbital. Thus, in examining the J_F components of the Ni- O_{eq} -Os and Ni- O_{ax} -Os exchanges in Sr_2NiOsO_6 , it is necessary to consider the z^2/xz and z^2/yz overlap densities in addition to the x^2-y^2/xz and x^2-y^2/yz overlap densities discussed above. For the Ni- O_{eq} -Os exchange, the z^2/xz interaction has a nonzero overlap density but the z^2/yz interaction does not (**Fig. 4.6a,b**). For the Ni- O_{ax} -Os exchange, both the z^2/xz and z^2/yz interactions have a large overlap density because the z^2 magnetic orbital has a large O 2p contribution at O_{ax} (**Fig. 4.6c,d**). By considering the overlap densities arising from both the x^2-y^2 and z^2 magnetic orbitals, it is understandable why the Ni- O_{ax} -Os exchange J_4^{eff} is more strongly FM than the Ni- O_{eq} -Os exchange J_3^{eff} in Sr_2NiOsO_6 (8.7 vs. 5.55 meV) and also why the Ni- O_{eq} -Os exchange J_3^{eff} of Sr_2NiOsO_6 is more strongly FM than the Cu- O_{eq} -Os exchange J_3^{eff} of Sr_2CuOsO_6 (5.55 vs. 2.84 meV).

Finally, we comment on why the Cu-O_{ax}-Os exchange J_4^{eff} of Sr₂CuOsO₆ is not FM but slightly AFM. As discussed above, both the J_F and J_{AF} terms of this J_4^{eff} exchange are practically zero so that one might expect J_4^{eff} to be nearly zero. However, it is calculated to be slightly AFM. The latter is possible if the Cu²⁺ ion of the Cu-O_{ax}-Os path interacts with the Os⁶⁺ ion indirectly through those Cu-O_{eq}...Sr²⁺...O_{eq}-Os paths in which the magnetic orbitals of both the Cu²⁺ and Os⁶⁺ ions have nonzero O 2p contributions on the O_{eq} atoms of the O_{eq}...Sr²⁺...O_{eq} linkage. In such paths, which involve the four Sr²⁺ cations surrounding each linear Cu-O_{ax}-Os path, the empty 4d orbitals of Sr²⁺ can overlap with the magnetic orbital of Cu²⁺ and also with that of Os⁶⁺. This is akin to the finding in Cs₂CuCl₄,¹⁸ in which the Cs 6p orbitals of the Cs⁺ ions strongly influence the spin exchange between two (CuCl₄)²⁻ ions when the two (CuCl₄)²⁻ anions and the Cs⁺ cations lying between them have an inversion or a mirror plane of symmetry. We confirm the above possibility by calculating the plots of the projected density of states (PDOS) for the Os 5d, Cu 3d and Sr 4d orbitals in the AF2 state of Sr₂CuOsO₆, which are shown in **Fig. 4.7**. In the PDOS plot of the Os 5d states (**Fig. 4.7a**), the states representing the magnetic orbitals of the Os⁶⁺ ion occur as two merged peaks immediately below the Fermi level. In this energy region of the Os⁶⁺ 5d states, the Sr 4d states appear as two merged peaks (**Fig. 4.7b**), and so do the Cu 3d states (**Fig. 4.7c,d**). Furthermore, the Sr 4d and Cu 3d contributions in this energy region are comparable in magnitude. These observations are in support of the reasoning that the Cu²⁺ ion magnetic orbital of the Cu-O_{ax}-Os path interacts with the Os⁶⁺ ion magnetic orbitals by overlapping with the Sr²⁺ ion 4d orbitals of the Cu-O_{eq}...Sr²⁺...O_{eq}-Os paths.

5. Concluding remarks

To describe the magnetic insulating states of $\text{Sr}_2\text{CuOsO}_6$ and $\text{Sr}_2\text{NiOsO}_6$ by DFT+U calculations, it is necessary to employ a substantially large U_{Os} value. This indicates that the 5d orbitals of the Os^{6+} ion are strongly contracted due to the high oxidation state. The magnetic structure of $\text{Sr}_2\text{CuOsO}_6$ is best approximated by the A-type AFM arrangement (AF2), and that of $\text{Sr}_2\text{NiOsO}_6$ by the FM arrangement. However, significant spin frustration exists within each //ab-layer and between adjacent //ab-layers in both compounds. The latter is most likely responsible for the divergence of their ZFC and FC magnetic susceptibility curves below ~ 20 K. The crucial difference between the magnetic properties of $\text{Sr}_2\text{CuOsO}_6$ and $\text{Sr}_2\text{NiOsO}_6$ lies in their $\text{M-O}_{\text{eq}}\text{-Os}$ and $\text{M-O}_{\text{ax}}\text{-Os}$ spin exchanges, which arises ultimately from the fact that the Cu^{2+} ion has only magnetic orbital (i.e., x^2-y^2) while the Ni^{2+} ion has two (i.e., x^2-y^2 and z^2). The $\text{Ni-O}_{\text{ax}}\text{-Os}$ exchange of $\text{Sr}_2\text{NiOsO}_6$ is strongly FM due to the z^2/xz and z^2/yz overlap densities. In contrast, the $\text{Cu-O}_{\text{ax}}\text{-Os}$ exchange of $\text{Sr}_2\text{CuOsO}_6$ is slightly AFM, which suggests indirect exchange interactions between the Cu^{2+} and Os^{6+} ions through the $\text{Cu-O}_{\text{eq}}\dots\text{Sr}^{2+}\dots\text{O}_{\text{eq}}\text{-Os}$ paths.

Acknowledgements

Work at NCSU by the Office of Basic Energy Sciences, Division of Materials Sciences, U. S. Department of Energy, under Grant DE-FG02-86ER45259, and also by the computing resources of the NERSC center and the HPC center of NCSU. HzL acknowledges support from the National Science Foundation via award DMR:0804209.

References

- (1) Lufaso, M.; Gemmill, W. R.; Mugavero, S. J.; Kim, S. J.; Lee, Y.; Vogt, T.; Loye, H.C., *J. Solid State Chem.* **2008**, *181*, 623.
- (2) Macquart, R.; Kim, S.-S.; Gemmill, W. R.; Stalick, J. K.; Lee, Y.; Vogt, T.; zur Loye, H.-
C. Inorg. Chem. **2005**, *44*, 9676.
- (3) Song, W.; Wang, J.; Wu, Z., *Chem. Phys. Lett.* **2009**, *482*, 246.
- (4) Song, W.; Zhao, E.; Meng, J.; Wu, Z. *J. Chem. Phys.* **2009**, *130*, 114707.
- (5) Mott, N. F., *Metal-Insulator Transitions*: Barnes and Noble, New York, 1974.
- (6) Whangbo, M.-H., *J. Chem. Phys.* **1979**, *70*, 4963.
- (7) Dudarev, S. L.; Botton, G. A.; Savrasov, S. Y.; Humphreys, C. J.; Sutton, A. P. *Phys. Rev. B* **1998**, *57*, 1505.
- (8) Xiang, H. J.; Whangbo, M.-H. *Phys. Rev. B* **2007**, *75*, 052407.
- (9) Sarkar, S.; De Raychaudhury, M.; Dasgupta, I.; Saha-Dasgupta, T. *Phys. Rev. B* **2009**, *80*, 201101.
- (10) Jeon, B. C.; Kim, C. H.; Moon, S. J.; Choi, W. S.; Jeong, H.; Lee, Y. S.; Yu, J.; Won, C. J.; Jung, J. H.; Hur, N.; Noh, T. W. *J. Phys.: Condens. Matter* **2010**, *25*, 345602.
- (11) Tian, C.; Kan, E. J.; Lee, C.; Whangbo, M.-H. *Inorg Chem.* 2010, *49*, 3086.
- (12) (a) Kresse, G.; Hafner, J.; *Phys. Rev. B* **1993**, *47*, 558. (b) Kresse, G.; Furthmüller, J. *Comput. Mater. Sci* **1996**, *6*, 15. (c) Kresse, G.; Furthmüller, J. *Phys. Rev. B* **1996**, *54*, 11169.
- (13) Perdew, J. P.; Burke, K.; Ernzerhof, M. *Phys. Rev. Lett.* **1996**, *77*, 3865.

- (14) Hay, P. J.; Thibeault, J. C.; Hoffmann, R., *J. Am. Chem. Soc.* **1975**, *97*, 4884.
- (15) Kahn, O., *Molecular Magnetism*:VCH, New York, 1993.
- (16) Whangbo, M.-H.; Koo, H.-J.; Dai, D., *J. Solid State Chem.* **2003**, *176*, 417.
- (17) (a) Dai, D.; Whangbo, M.-H., *J. Chem. Phys.* **2001**, *114*, 2887. (b) Dai, D.; Whangbo, M.-H., *J. Chem. Phys.* **2003**, *118*, 29.
- (18) Lee, C.; Kang, J.; Lee, K. H.; Whangbo, M.-H. *Inorg. Chem.* **2009**, *48*, 4185.

Table 4.1 Relative energies ΔE (in meV per two FUs) of the three ordered spin states of $\text{Sr}_2\text{CuOsO}_6$ determined from the DFT+U calculations as a function of the U_{Cu} and U_{Os} values (in eV). Whether each state is metallic (no band gap) or magnetic insulating (nonzero band gap) is also indicated, where “No” and “Yes” refer to the absence and presence of a band gap, respectively.

$(U_{\text{Cu}}, U_{\text{Os}})$	G-type (AF1)		A-type (AF2)		A-type (AF3)	
	ΔE	Gap	ΔE	Gap	ΔE	Gap
(4,2)	0	No	120	No	133	No
(5,2)	0	No	55	No	140	No
(4,3)	60	No	0	No	26	No
(5,3)	0	No	57	No	87	No
(3,4)	23	No	0	Yes	45	No
(4,4)	37	No	0	Yes	52	No
(5,4)	50	No	0	Yes	45	Yes
(6,4)	60	No	0	Yes	48	Yes

Table 4.2 Relative energies ΔE (in meV per two FUs) of the four ordered spin states of $\text{Sr}_2\text{NiOsO}_6$ determined from the DFT+U calculations as a function of the U_{Ni} and U_{Os} values (in eV). Whether each state is metallic (no band gap) or magnetic insulating (nonzero band gap) is also indicated, where “No” and “Yes” refer to the absence and presence of a band gap, respectively.

$(U_{\text{Ni}}, U_{\text{Os}})$	G-type AFM		A-type AFM		C-type AFM		FM	
	ΔE	Gap	ΔE	Gap	ΔE	Gap	ΔE	Gap
(3, 4)	220	Yes	87	Yes	132	Yes	0	Yes
(4, 4)	198	Yes	52	Yes	115	Yes	0	Yes
(5, 4)	178	Yes	59	Yes	99	Yes	0	Yes
(6, 4)	159	Yes	45	Yes	85	Yes	0	Yes

Table 4.3 Geometrical parameters associated with the spin exchange paths $J_{ij} = J_1 - J_7$ (in meV) of Sr_2MOsO_6 (M = Cu, Ni).

		$\text{Sr}_2\text{CuOsO}_6$	$\text{Sr}_2\text{NiOsO}_6$
J_1	M-O...O-M	O...O = 2.670($\times 2$) Å	O...O = 2.697($\times 2$) Å
J_2	Os-O...O-Os	O...O = 2.820($\times 2$) Å	O...O = 2.860($\times 2$) Å
J_3	M-O-Os	$\angle\text{Cu-O-Os} = 158.1^\circ$ Cu-O = 1.994 Å, Os-O = 1.888 Å	$\angle\text{Ni-O-Os} = 162.7^\circ$ Ni-O = 2.023 Å, Os-O = 1.907 Å
J_5	M-O...O-M	O...O = 3.775 Å	O...O = 3.815 Å
J_6	Os-O...O-Os	O...O = 3.988 Å	O...O = 4.045 Å
J_4	M-O-Os	$\angle\text{Cu-O-Os} = 180.0^\circ$ Cu-O = 2.315 Å, Os-O = 1.928 Å	$\angle\text{Ni-O-Os} = 180.0^\circ$ Ni-O = 2.040 Å, Os-O = 1.957 Å
J_7	Os-O...O-Os	O...O = 3.055($\times 2$) Å	O...O = 2.860($\times 2$) Å

Table 4.4 Spin exchange parameters $J_{ij}^{\text{eff}} = S_i S_j J_{ij}$ of $\text{Sr}_2\text{CuOsO}_6$ and $\text{Sr}_2\text{NiOsO}_6$ (in meV),

where $J_{ij} = J_1 - J_7$, determined from the DFT+U calculations with $U_{\text{Cu}} = 6$ eV and $U_{\text{Os}} = 4$ eV.

Exchange path		$\text{Sr}_2\text{CuOsO}_6$	$\text{Sr}_2\text{NiOsO}_6$
Within //ab-layer	J_1^{eff}	-0.97	-0.23
	J_2^{eff}	-1.42	-0.70
	J_3^{eff}	2.84	5.55
	J_5^{eff}	-2.87	-3.35
	J_6^{eff}	-0.60	0.00
Between //ab-layers	J_4^{eff}	-1.56	8.70
	J_7^{eff}	-1.07	-2.72

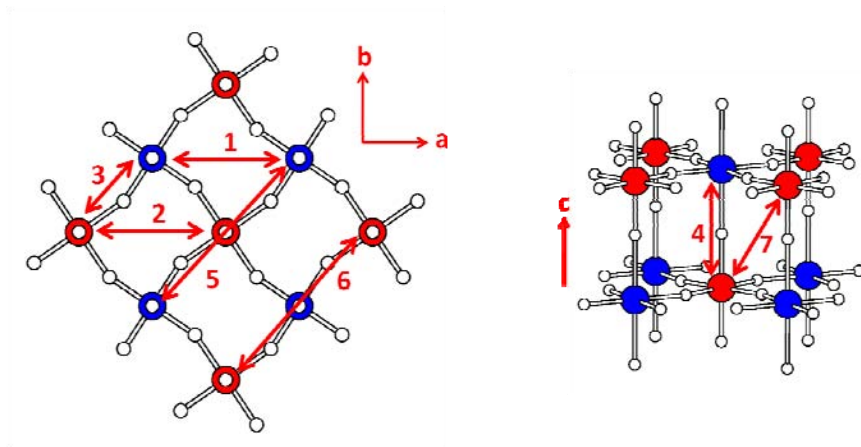


Figure 4.1 Schematic representation of the double-perovskite $\text{Sr}_2\text{CuOsO}_6$: (a) A projection view, along the c -direction, of an isolated $//ab$ -layer of corner-sharing CuO_6 and OsO_6 octahedra. (b) A perspective view of two $//ab$ -layers of corner-sharing CuO_6 and OsO_6 octahedra. The blue, red and white circles represent the Cu, Os and O atoms, respectively. The numbers 1 – 7 refer to the spin exchange paths J_1 – J_7 , respectively.

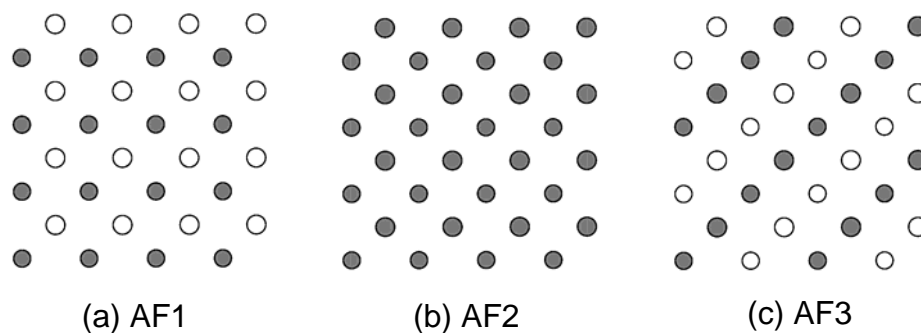


Figure 4.2 Schematic representations of the G-type and A-type antiferromagnetic spin arrangements of the double-perovskite $\text{Sr}_2\text{CuOsO}_6$ using the ordered spin arrangements of an isolated //ab-layer of Cu^{2+} and Os^{6+} ions: (a) In the G-type arrangement AF1, the given layer repeats antiferromagnetically along the c-direction. (b) In the A-type arrangement AF2, the given layer repeats antiferromagnetically along the c-direction. (c) In the A-type arrangement AF3, the given layer repeats ferromagnetically along the c-direction. The filled and unfilled large circles represent the up-spin and down-spin magnetic ion sites, respectively.

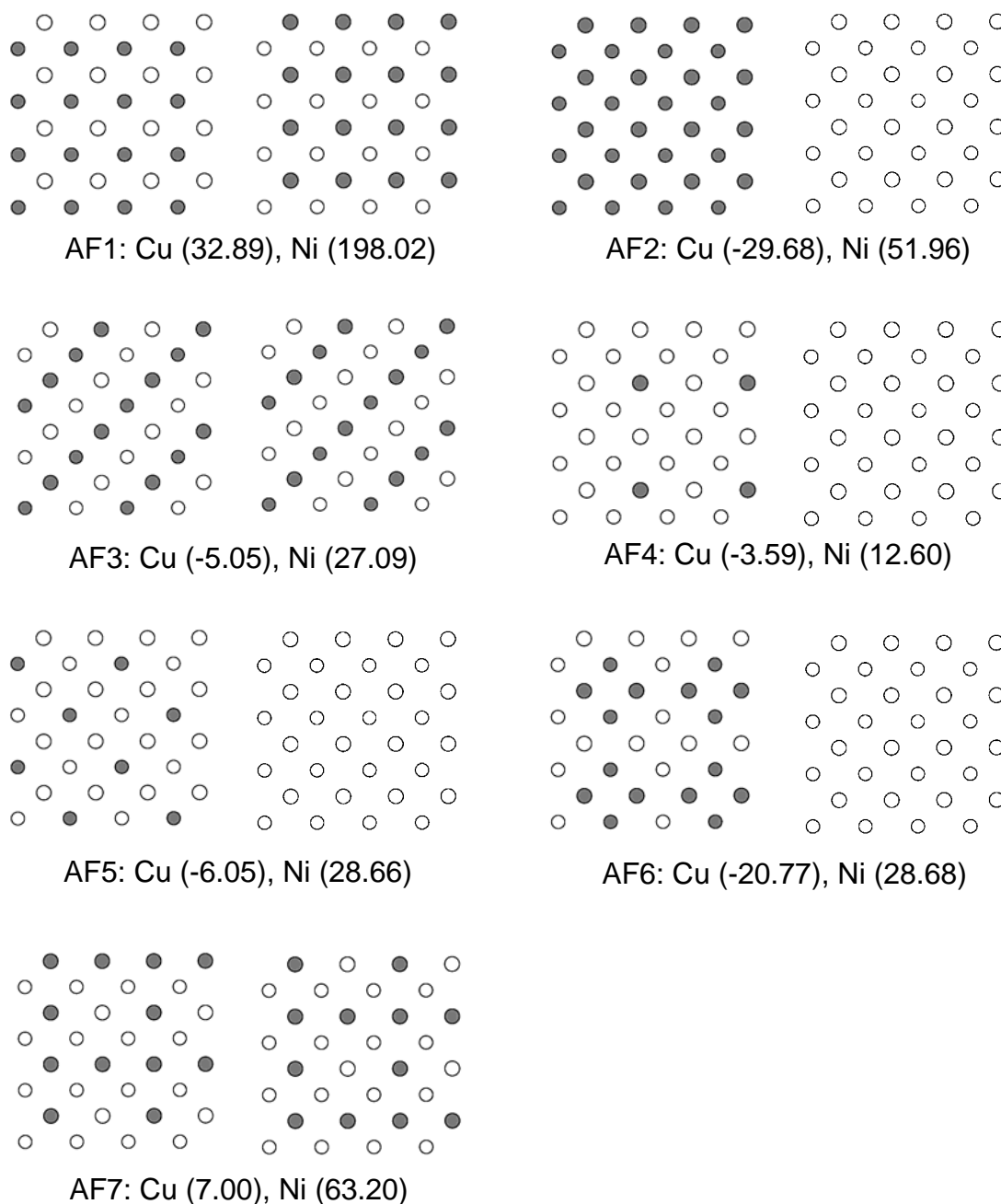


Figure 4.3 Spin arrangements in the AF1 – AF7 states of Sr_2MOsO_6 ($M = \text{Cu}, \text{Ni}$) used to evaluate the $J_1 - J_7$ values. In each state, the two //ab-layers with the given ordered spin arrangements alternate along the c-direction. In the AF3 state, the two //ab-layers have the

same spin arrangement. In the FM state (not shown), the //ab-layer with the FM spin arrangement repeats ferromagnetically along the c-direction. In each state of Sr_2MOsO_6 ($M = \text{Cu, Ni}$), the number in the parenthesis refers to the relative energies with respect to the FM state (in meV per two FUs), which was obtained from the DFT+U calculations with $U_M = 6$ eV and $U_{\text{Os}} = 4$ eV.

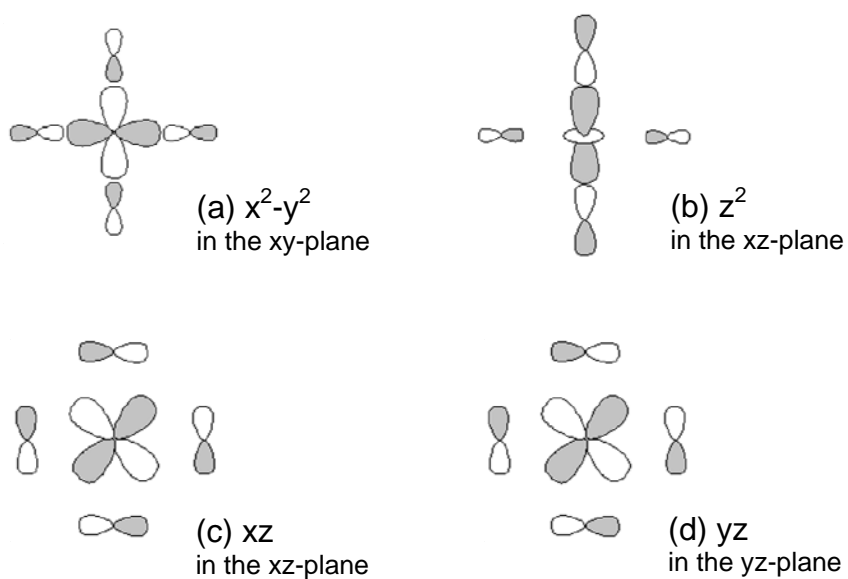


Figure 4.4 Schematic views of (a, b) the e_g -type magnetic orbitals of the M^{2+} ion and (c, d) the t_{2g} -type magnetic orbitals of the Os^{6+} ion in Sr_2MOsO_6 ($M = \text{Cu, Ni}$).

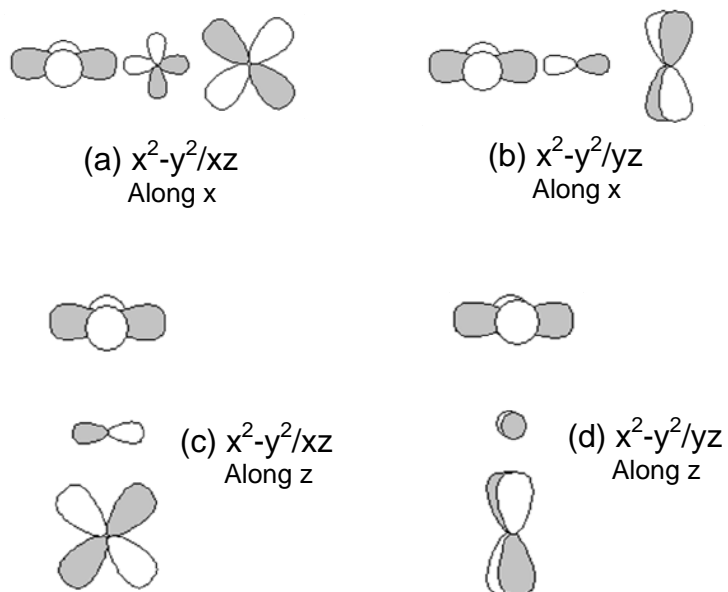


Figure 4.5 Orbitals involved in (a, b) the x^2-y^2/xz and x^2-y^2/yz spin exchange interactions of the M-O_{eq}-O_s path and (c, d) those of the M-O_{ax}-O_s path in Sr₂MOsO₆ (M = Cu, Ni). For simplicity, the orbital contributions unrelated to the exchange paths are not shown.

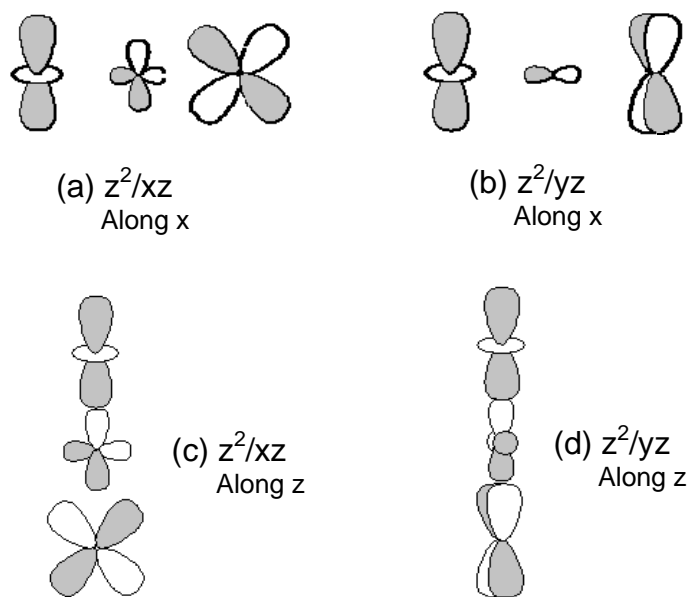


Figure 4.6 Orbitals involved in (a, b) the z^2/xz and z^2/yz spin exchange interactions of the Ni-O_{eq}-O_s path and (c, d) those of the Ni-O_{ax}-O_s path in Sr₂NiOsO₆. For simplicity, the orbital contributions unrelated to the exchange paths are not shown.

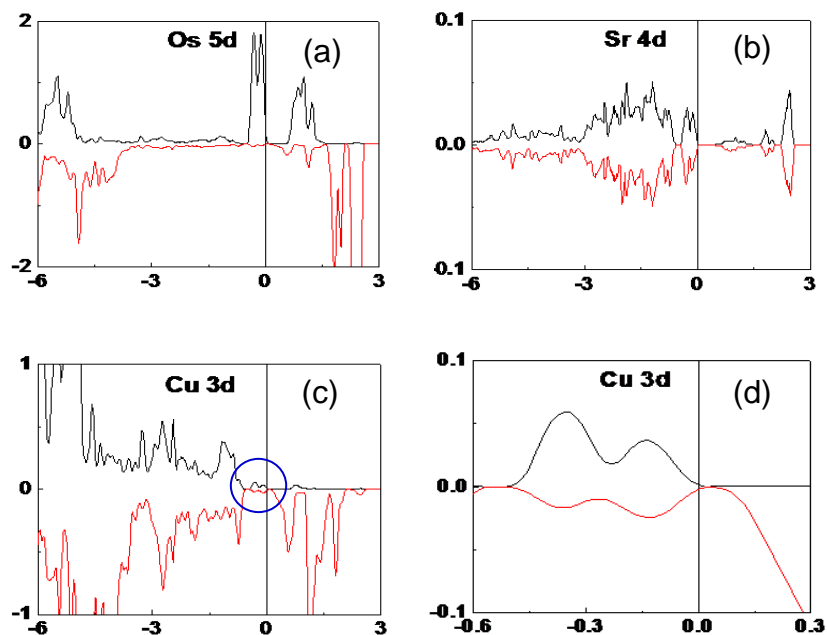
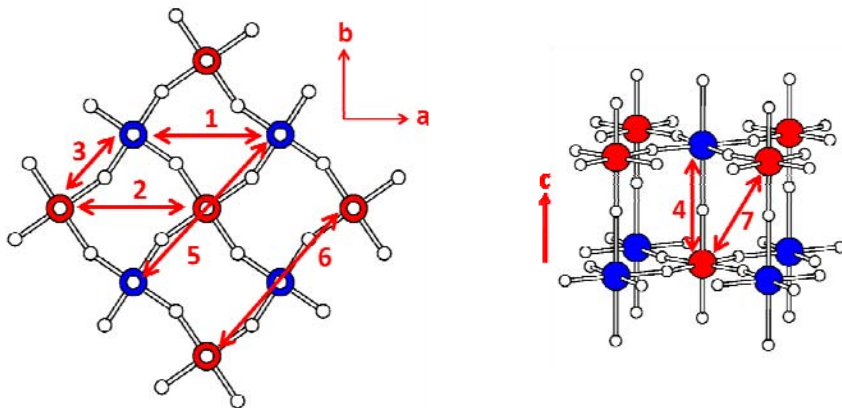


Figure 4.7 PDOS plots calculated for the (a) Os 5d, (b) Sr 4d and (c, d) Cu 3d orbitals in the AF2 state of $\text{Sr}_2\text{CuOsO}_6$, where the horizontal axis is in units of eV, and the vertical axis in states/eV/atom. The spin-up and spin-down states are represented by black and red curves, respectively, and their PDOS values are represented by positive and negative numbers, respectively. Fig. 7d is a zoomed-in view of the circled region of Fig. 7c.

Synopsis

The double-perovskites Sr_2MOsO_6 ($M = \text{Cu}, \text{Ni}$) consisting of 3d and 5d transition-metal magnetic ions (M^{2+} and Os^{6+} , respectively) are magnetic insulators. Density functional calculations reproduce this observation only when a substantially large on-site repulsion is employed for the Os atom. We examined the spin exchange interactions of Sr_2MOsO_6 ($M = \text{Cu}, \text{Ni}$) to explain why their zero-field-cooled and field-cooled susceptibility curves diverge below ~ 20 K and why their dominant magnetic interactions are opposite (i.e., antiferromagnetic and ferromagnetic for $M = \text{Cu}$ and Ni , respectively).



Chapter 5

π -Backdonation Effect of the Cyanide Ligands on the Electron Correlation and Charge Transfer in Prussian Blue $\text{RbMn}[\text{Fe}(\text{CN})_6]$

A paper published in Inorganic Chemistry

Inorg. Chem., Vol. 49 (7), 3086, 2010

Chuan Tian, Erjun Kan, Changhoon Lee and Myung-Hwan Whangbo*

Department of Chemistry, North Carolina State University, Raleigh, North Carolina 27695-8204

Abstract

The temperature-induced charge transfer between the Mn and Fe sites in $\text{RbMn}[\text{Fe}(\text{CN})_6]$ was analyzed by density functional calculations. Our analysis suggests that the extent of electron correlation (equivalently, the pairing energy or the on-site repulsion) is much greater for the Mn^{n+} ion than for the Fe^{n+} ($n = 2, 3$) ion. We believe this surprising and counterintuitive finding is a consequence of the π -backdonation effect of the CN ligands.

Intense research efforts have been devoted to structural and physical properties that can be controlled by changing the valency of their transition-metal ions.¹ In Prussian blues consisting of two different transition metal ions,^{2,3} charge transfer between them, and hence a change in their valency, can be induced by temperature,⁴ photoexcitation,⁵ pressure⁶ and electric field.⁷ Such materials with controllable charge-transfer are potentially important in multifunctional device applications. Among Prussian blues, $\text{RbMn}[\text{Fe}(\text{CN})_6]$ is unique because it is stoichiometric and hence suitable for precise structure analyses. This compound consists of $\text{Fe}(\text{CN})_6$ and $\text{Mn}(\text{NC})_6$ octahedra, which share their CN ligands to form the double-perovskite framework with the Fe-CN-Mn linkages (Fig. 5.1). The Rb^+ ions occupy every second Mn_4Fe_4 cubes such that the Rb^+ ions form a three-dimensional network of edge-sharing Rb_4 tetrahedra (Fig. 5.1b).

$\text{RbMn}[\text{Fe}(\text{CN})_6]$ undergoes a structural transition from the high-temperature (HT) cubic phase to the low temperature (LT) tetragonal phase at 231 K on lowering temperature, while the LT phase is converted to the HT phase at 304 K on raising temperature.^{4,8} In the HT cubic phase, both the $\text{Fe}(\text{CN})_6$ and the $\text{Mn}(\text{NC})_6$ octahedra are regular in shape [$\text{Mn-N} = 2.012$ ($\times 6$) Å, and $\text{Fe-C} = 2.170$ ($\times 6$) Å].⁴ In the LT tetragonal phase, each $\text{Mn}(\text{NC})_6$ octahedron shows a strong axial-elongation [$\text{Mn-N} = 1.991$ ($\times 4$), 2.268 ($\times 2$) Å], and each $\text{Fe}(\text{CN})_6$ octahedron a slight axial flattening [$\text{Fe-C} = 1.886$ ($\times 4$), 1.831 ($\times 2$) Å].⁴ Experimental studies reveal that the LT phase has high-spin (HS) Mn^{3+} (d^4 , $S = 2$) and low-spin (LS) Fe^{2+} (d^6 , $S = 0$) ions, while the HT phase has HS Mn^{2+} (d^5 , $S = 5/2$) and LS Fe^{3+} (d^5 , $S = 1/2$) ions.^{4,8} Namely, the temperature-induced phase transition involves a charge transfer between the Mn and Fe sites.

The HS $\text{Mn}^{3+}/\text{LS Fe}^{2+}$ configuration of the LT phase has been confirmed by electronic structure calculations,^{8,9} but there has been no such report concerning the HS $\text{Mn}^{2+}/\text{LS Fe}^{3+}$ configuration of the HT phase. In discussing the charge-transfer phenomenon of $\text{RbMn}[\text{Fe}(\text{CN})_6]$, it is essential that the electronic structures of both the HT and LT phases be equally well described under a given theoretical analysis. This need prompted us to carry out a systematic density functional study of the HT and LT phases. In the present Communication, we report surprising results of our investigation, which reveal that the extent of electron correlation is much greater for the Mn^{n+} ion than for the Fe^{n+} ($n = 2, 3$) ion in $\text{RbMn}[\text{Fe}(\text{CN})_6]$, and this counterintuitive finding is a consequence of the π -backdonation effect of the CN ligands.

Our spin-polarized density functional calculations employed the projector augmented wave method implemented in Vienna ab initio simulation package¹⁰ with the generalized gradient approximation (GGA)¹¹, the plane-wave cutoff energy of 400 eV, a set of $3 \times 3 \times 3$ k-point set¹², and the threshold 10^{-5} eV for energy convergence. Density functional calculations often predict magnetic insulators of 3d transition metal elements to be metallic because the strong electron correlation associated with their 3d states is not well described. In our work this deficiency was corrected by using the GGA plus on-site repulsion U (GGA+U) method.¹³ Since $\text{RbMn}[\text{Fe}(\text{CN})_6]$ has two different transition elements Mn and Fe, it is not a trivial task to find their U values (U_{Mn} and U_{Fe}) appropriate for GGA+U calculations especially when both atoms possess unpaired spins as found for the HT phase. In their elemental state Mn has less contracted 3d orbitals than does Fe so that U_{Fe} and U_{Mn} would be comparable in magnitude with $U_{\text{Mn}} < U_{\text{Fe}}$. Thus we begin our GGA+U calculations for the

HT phase with $U_{\text{Fe}} = U_{\text{Mn}} = 4$ eV, typical values used for oxides of Mn and Fe. Fig. 5.2a shows the projected density of states (PDOS) plots calculated for the up- and down-spin 3d states of the Mn and Fe atoms. Each Fe has the $t_{2g}\uparrow$ and $t_{2g}\downarrow$ states fully occupied, while each Mn has the $t_{2g}\uparrow$ states fully occupied and the $e_g\uparrow$ states half occupied. The spin moments of the Mn and Fe sites are calculated to be $\mu_{\text{Mn}} = 3.88 \mu_{\text{B}}$ and $\mu_{\text{Fe}} = 0.04 \mu_{\text{B}}$ (Table 5.1a). Namely, our calculations for the HT cubic phase with $U_{\text{Fe}} = U_{\text{Mn}} = 4$ eV does not converge to the HS $\text{Mn}^{2+}/\text{LS Fe}^{3+}$ configuration, but to the HS $\text{Mn}^{3+}/\text{LS Fe}^{2+}$ configuration that the LT tetragonal phase adopts, in disagreement with the experimental observations.^{4,8}

To find a range of U_{Mn} and U_{Fe} that reproduces the HS $\text{Mn}^{2+}/\text{LS Fe}^{3+}$ configuration of the HT phase, GGA+U calculations are carried out for various U_{Fe} with U_{Mn} fixed at 4 eV to find that the condition $U_{\text{Fe}} > U_{\text{Mn}}$ does not improve the situation, but the condition $U_{\text{Fe}} \ll U_{\text{Mn}}$ does (Table 5.1a). We verify this implication by performing GGA+U calculations for various U_{Mn} with U_{Fe} fixed at 1 and 2 eV. As summarized in Table 5.1b, μ_{Mn} and μ_{Fe} increase gradually with increasing the difference $U_{\text{Mn}} - U_{\text{Fe}}$, reaching the values of 4.59 and 1.09 μ_{B} , respectively, when $U_{\text{Mn}} = 8$ eV and $U_{\text{Fe}} = 1$ eV. These calculated moments are close to the values expected for the HS $\text{Mn}^{2+}/\text{LS Fe}^{3+}$ configuration (5 and 1 μ_{B} , respectively).^{4,8} The calculated total magnetic moments are proportionable to the difference of U_{Mn} and U_{Fe} , which are 22.4 μ_{B} for $U_{\text{Mn}} = 8$ eV and $U_{\text{Fe}} = 1$ eV, and 17.8 for $U_{\text{Mn}} = 4$ eV and $U_{\text{Fe}} = 1$ eV. The corresponding PDOS plots (Fig.5.2b) show the expected feature, i.e., each Mn has the $t_{2g}\uparrow$ and $e_g\uparrow$ states fully occupied, while each Fe has the $t_{2g}\uparrow$ states fully occupied and the $t_{2g}\downarrow$ states partially unoccupied. Thus, the observed HS $\text{Mn}^{2+}/\text{LS Fe}^{3+}$ configuration of the

HT cubic phase is reproduced only when $U_{\text{Mn}} \gg U_{\text{Fe}}$. To check the effectivity of U values adopted in our calculations, we have optimized the structures with such U sets. Our calculation result on the relaxed HT structure is listed in Table 5.2. The bond length of Mn-N is elongated with increasing U value, which is consistent with the more contracted 3d electrons. $U_{\text{Mn}} \gg U_{\text{Fe}}$ is essential to get the HS state. However, with the elongation of the Mn-N bond, a smaller U , i.e., 4 eV, is enough to obtain the HS state.

We note that the U_{Mn} and U_{Fe} values appropriate for the HT cubic phase are also valid for the LT tetragonal phase. As summarized in Table 5.3, $\mu_{\text{Mn}} = 3.93 \mu_{\text{B}}$ and $\mu_{\text{Fe}} = 0.07 \mu_{\text{B}}$ when $U_{\text{Mn}} = 8$ eV and $U_{\text{Fe}} = 1$ eV, which are very close to those expected for the HS $\text{Mn}^{3+}/\text{LS Fe}^{2+}$ configuration of the LT tetragonal phase (i.e., 4 and $1\mu_{\text{B}}$, respectively).^{4,8} The PDOS plots calculated for the LT tetragonal phase with $U_{\text{Mn}} = 8$ eV and $U_{\text{Fe}} = 1$ eV show the HS $\text{Mn}^{3+}/\text{LS Fe}^{2+}$ configuration (Fig. 5.2c). The relaxed structures excellently reproduce the experimental distortions for the LT structure, and the magnetic moments are also in good agreement with the experimental expectation (Table 5.4).

The HT cubic phase is calculated to be less stable than the LT tetragonal phase (by 2.4 meV per formula unit).

Our finding of $U_{\text{Mn}} \gg U_{\text{Fe}}$ is quite surprising, and such an observation has not been reported in density functional studies on magnetic oxides of transition metal elements. In such oxides, the ligands surrounding the transition metal ions are σ -donors. In $\text{RbMn}[\text{Fe}(\text{CN})_6]$, the CN ligands act as σ -donors to both Fe^{n+} and Mn^{n+} ($n = 2, 3$) ions. In addition, the π_{CN} and π^*_{CN} orbitals of the CN ligands interact with the Fe t_{2g} and Mn t_{2g}

orbitals. π_{CN} has a greater weight on the N atom, but π^*_{CN} on the C atom (Fig. 5.3). Consequently, the $(\text{Fe } t_{2g} - \pi^*_{\text{CN}})$ interaction is stronger than the $(\text{Fe } t_{2g} - \pi_{\text{CN}})$ interaction, whereas the $(\text{Mn } t_{2g} - \pi^*_{\text{CN}})$ interaction is weaker than the $(\text{Mn } t_{2g} - \pi_{\text{CN}})$ interaction. Thus, the CN ligands act as π -acceptors to the $\text{Fe}^{\text{n+}}$ ions, but as π -donors to the $\text{Mn}^{\text{n+}}$ ions. The π -backdonation effect of the CN ligands on the $\text{Fe}^{\text{n+}}$ ion, via the $(\text{Fe } t_{2g} - \pi^*_{\text{CN}})$ interaction, would delocalize the electron density of the $\text{Fe}^{\text{n+}}$ ion into the CN ligands, hence making the electron distribution around the $\text{Fe}^{\text{n+}}$ ion less contracted and reducing U_{Fe} . In contrast, the electron distribution around the $\text{Mn}^{\text{n+}}$ ion would become more contracted due to the π -donation effect of the CN ligands, hence increasing U_{Mn} .

In their study of the experimentally-deduced charge density distribution of $\text{RbMn}[\text{Fe}(\text{CN})_6]$ using the maximum entropy method,¹⁴ Kato *et al.* found that, in the charge-transfer transition from the HS $\text{Mn}^{2+}/\text{LS } \text{Fe}^{3+}$ to the HS $\text{Mn}^{3+}/\text{LS } \text{Fe}^{2+}$ configuration, the transferred electron is spread over the complex $[\text{Fe}(\text{CN})_6]^{4-}$ due to the $(\text{Fe } t_{2g} - \pi^*_{\text{CN}})$ interaction, which is consistent with our finding described above.

Finally, we discuss the spin density distribution calculated for the LT phase, presented in Fig. 5.4a. The formally diamagnetic Fe^{2+} ions participate in spin distribution; the Mn^{3+} spins are delocalized into each FeC_6 octahedron plus the N atoms of the two axial CN bonds, while the four equatorial CN bonds exhibit spin polarization. Due to the strong bonding between the N and Fe ions, the AFM distribution can be found in the spin density plot. The ferromagnetic coupling between the Mn sites, though separated with a long distance, arises from the spin delocalization through the intervening $\text{Fe}(\text{CN})_6$ octahedra,

which is caused by the ($\text{Fe } t_{2g} - \pi^*_{\text{CN}}$) interactions. In terms of charge distribution, the occurrence of electron delocalization between the Fe^{2+} ion and the CN ligands can be seen for a certain range of electron density values. An example is given in Fig. 5.4b, which shows electron delocalization between the Fe^{2+} ion and the axial CN ligands.

In summary, our analysis of the electronic structure of $\text{RbMn}[\text{Fe}(\text{CN})_6]$ suggests that the extent of electron correlation is much greater for the Mn^{n+} ion than for the Fe^{n+} ($n = 2, 3$) ion. We believe this finding originates from the π -backdonation effect of the CN ligands, which delocalizes the electron density of the Fe^{n+} ion into the surrounding CN ligands. This makes the electron distribution around the Fe^{n+} ion less contracted, but makes that around the Mn^{n+} ion more contracted. Consequently, $U_{\text{Mn}} \gg U_{\text{Fe}}$.

ACKNOWLEDGMENT The work was supported by U. S. DOE under Grant No. DE-FG02-86ER45259 and by the resources of the NERSC Center and the HPC Center of NCSU.

Reference

- (1) (a) Long, Y.; Hayashi, N.; Saito, T.; Azuma, M.; Muranaka, S.; Shimakawa, Y. *Nature* **2008**, *458*, 60. (b) Imada, M.; Fujimori, A.; Tokura, Y. *Rev. Mod. Phys.* **1998**, *70*, 1039.
- (2) (a) Sato, O.; Iyoda, T.; Fujishima, A.; Hashimoto, K. *Science* **1996**, *272*, 704. (b) Sato, O.; Iyoda, T.; Fujishima, A.; Hashimoto, K. *Science* **1996**, *271*, 49. (c) Coronado, E.; Galan-Mascaros, J. R.; Gomez-Garcia, C. J.; Laukhin, V. *Nature* **2000**, *408*, 447.

- (3) (a) Manriquez, J. M.; Yee, G. T.; Mclean, R. S.; Epstein, A. J.; Miller, J. S. *Science* **1991**, 252, 1415. (b) Ferlay, S.; Mallah, T.; Ouahes, R.; Veillet, P.; Verdagure, M. *Nature* **1995**, 378, 701.
- (4) (a) Ohkoshi, S.; Tokoro, H.; Utsunomiya, M.; Mizuno, M.; Abe, M.; Hashimoto, K. *J. Phys. Chem. B.* **2002**, 106, 2423. (b) Moritomo, Y.; Kato, K.; Kuriki, A.; Takata, M.; Sakata, M.; Tokoro, H.; Ohkoshi, S.; Hashimoto, K. *J. Phys. Soc. Jpn.* **2002**, 71, 2078.
- (5) (a) Liu, X.; Moritomo, Y.; Ichida, M.; Nakamura, A.; Kojima, N. *Phys. Rev. B.* **2000**, 61, 20. (b) Margadonna, S.; Prassides, K.; Fitch, A. *Angew. Chem. Int. Ed.* **2004**, 43, 6316.
- (6) Moritomo, Y.; Hanawa, M.; Ohishi, Y.; Kato, K.; Takata, M.; Nishibori, E.; Sakata, M.; Ohkoshi, S.; Tokoro, H.; Hashimoto, K. *Phys. Rev. B.* **2003**, 68, 144106.
- (7) Mahfoud, H.; Molnar, G.; Bonhommeau, S.; Cobo, S.; Salmon, L.; Demont, P.; Tokoro, H.; Ohkoshi, S.; Boukheddaden, K.; Bousseksou, A.; *J. Am. Chem. Soc.* **2009**, 131, 15049
- (8) Kato, K.; Moritomo, Y.; Takata, M.; Sakata, M.; Umekawa, M.; Hamada, N.; Ohkoshi, S.; Tokoro, H.; Hashimoto, K. *Phys. Rev. Lett.* **2003**, 91, 255502.
- (9) Umekawa, M.; Hamada, N.; Kodama, A.; Moritomo, Y. *J. Phys. Soc. Jpn.* **2004**, 73, 430.
- (10) (a) Blöchl, P. E. *Phys. Rev. B* **1994**, 50, 17953. (b) Kresse, G.; Hafner, J., *Phys. Rev. B* **1994**, 49, 14251.
- (11) Perdew, J. P.; Burke, K.; Ernzerhof, M. *Phys. Rev. Lett.* **1996**, 77, 3865.
- (12) Monkhorst, H. J.; Pack, J. D. *Phys. Rev. B* **1976**, 13, 5188.
- (13) Dudarev, S. L.; Botton, G. A.; Savrasov, S. Y.; Humphreys, C. J.; Sutton, A. P., *Phys. Rev. B* **1998**, 57, 1505.

- (14) Kato, K.; Moritomo, Y.; Tanaka, H.; Tokoro, H.; Ohkoshi, S.; Takata, M. *J. Phys. Soc. Jpn.* **2007**, *76*, 123602.

Table 5.1 Spin moments of the Mn and Fe sites obtained for the HT structure of RbMn[Fe(CN)₆] by GGA+U calculations.

(a) As a function of U_{Fe} with U_{Mn} fixed at 4 eV

U_{Fe} (eV)	1	2	4	6
μ_{Mn} (μ_{B})	4.01	3.91	3.88	3.89
μ_{Fe} (μ_{B})	0.36	0.16	0.04	0.01

(b) As a function of U_{Mn} with U_{Fe} fixed at 1 and 2 eV (results for $U_{\text{Fe}} = 2$ eV in parentheses)

U_{Mn} (eV)	4	6	8
μ_{Mn} (μ_{B})	4.01 (3.91)	4.30 (4.22)	4.58 (4.53)
μ_{Fe} (μ_{B})	0.36 (0.16)	0.64 (0.47)	1.01 (0.89)

Table 5.2 Bond length and spin moments Mn and Fe sites obtained for the HT structure of

$U_{\text{Mn}}(\text{eV})$	1	2	4	6	8
Mn-N (\AA)	2.085	2.188	2.211	2.216	2.219
Fe-C (\AA)	2.008	1.915	1.896	1.892	1.890
C-N (\AA)	1.189	1.179	1.175	1.174	1.173
$\mu_{\text{Mn}} (\mu_{\text{B}})$	1.744	4.267	4.581	4.695	4.768
$\mu_{\text{Fe}} (\mu_{\text{B}})$	0.321	0.673	0.931	0.963	0.956
$\mu_{\text{tot}} (\mu_{\text{B}})$	8.000	20.91	23.55	24.00	24.00

RbMn[Fe(CN)₆] by GGA+U for various values of U_{Mn} with U_{Fe} fixed at 1 eV.

Table 5.3 Spin moments of the Mn and Fe sites obtained for the LT structure of RbMn[Fe(CN)₆] by GGA+U calculations for various values of U_{Mn} with U_{Fe} fixed at 1 and 2 eV (results for $U_{\text{Fe}} = 2$ eV in parentheses).

$U_{\text{Mn}} (\text{eV})$	4	6	8
$\mu_{\text{Mn}} (\mu_{\text{B}})$	3.70 (3.71)	3.82 (3.83)	3.93 (3.93)
$\mu_{\text{Fe}} (\mu_{\text{B}})$	0.12 (0.12)	0.09 (0.09)	0.07 (0.06)

Table 5.4 Bond length and spin moments Mn and Fe sites obtained for the LT structure of RbMn[Fe(CN)₆] by GGA+U for various values of U_{Mn} with U_{Fe} fixed at 1 eV.

U_{Mn} (eV)	Exp	2	4	6	8
Mn-N (Å)	2.263/1.984	2.101/1.949	2.110/1.960	2.208/1.978	2.207/1.984
Fe-C (Å)	1.895/2.204	1.976/1.883	1.967/1.875	1.879/1.856	1.880/1.852
C-N (Å)	1.105/1.102	1.187/1.178	1.186/1.176	1.176/1.176	1.176/1.175
μ_{Mn} (μ_{B})	4	3.616	3.719	3.874	3.986
μ_{Fe} (μ_{B})	0	0.142	0.114	0.074	0.055
μ_{tot} (μ_{B})	16	16.00	16.00	16.00	16.00

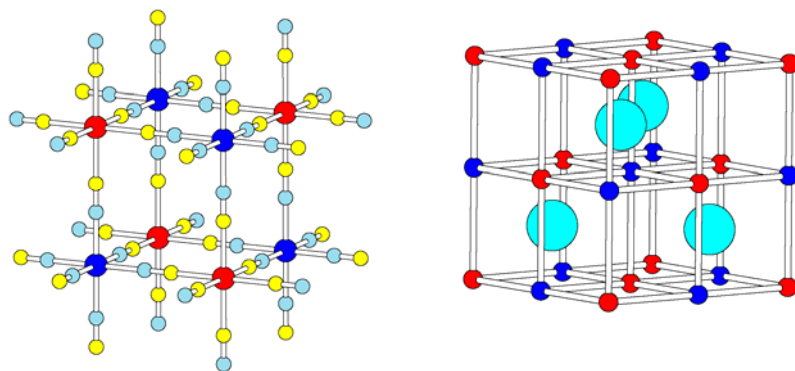


Figure 5.1 (a) Perspective view of the crystal structure of the HT cubic phase of $\text{RbMn}[\text{Fe}(\text{CN})_6]$. The red and blue circles represent the Fe and Mn atoms, respectively, and the yellow and turquoise circles the C and N atoms, respectively. (b) Arrangement of the Rb atoms in the Mn_4Fe_4 cubes.

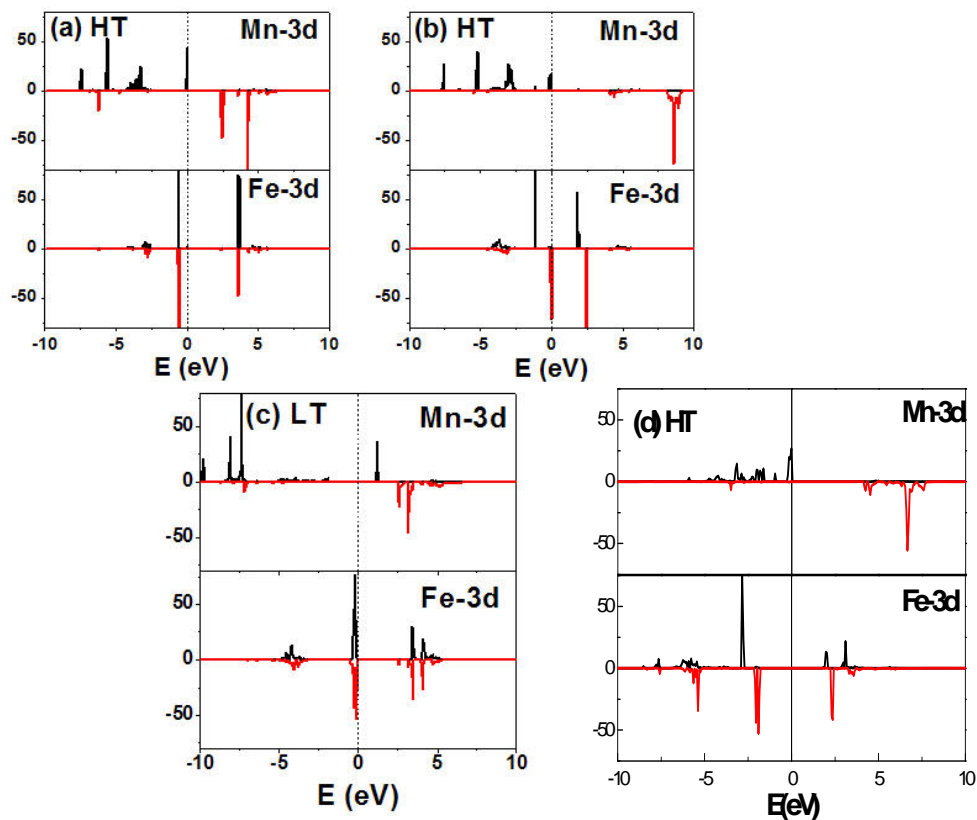


Figure 5.2 PDOS plots of the Mn and Fe 3d states of $\text{RbMn}[\text{Fe}(\text{CN})_6]$ obtained from GGA+U calculations for (a) the HT cubic structure with $U_{\text{Mn}} = U_{\text{Fe}} = 4$ eV, (b) the HT structure with $U_{\text{Mn}} = 8$ eV and $U_{\text{Fe}} = 1$ eV, and (c) the LT structure with $U_{\text{Mn}} = 8$ eV and $U_{\text{Fe}} = 1$ eV. The up- and down-spin densities are indicated by positive and negative values, respectively. (d) is the PDOS for optimized structure at $U_{\text{Mn}} = 4$ eV and $U_{\text{Fe}} = 1$ eV.

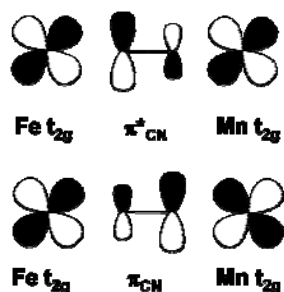


Figure 5.3 Interaction of the Fe t_{2g} and Mn t_{2g} orbitals with the (a) π_{CN} and (b) π^*_{CN} orbitals of the CN ligand in each Fe–CN–Mn linkage of $\text{RbMn}[\text{Fe}(\text{CN})_6]$.

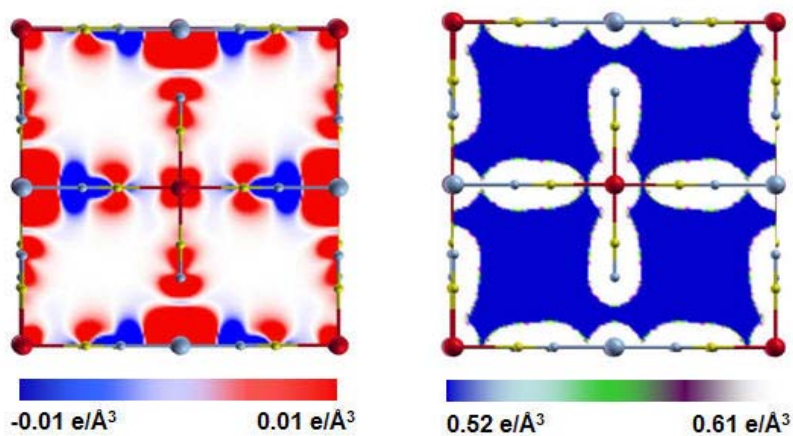
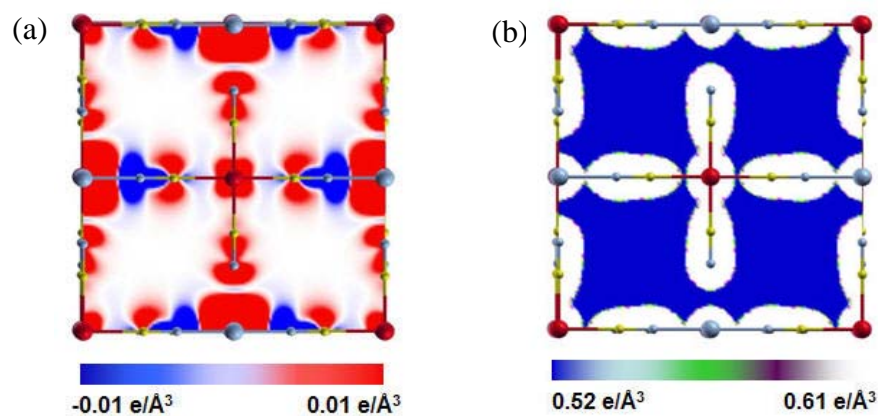


Figure 5.4 Plots of (a) the spin density and (b) a part of the charge density distribution obtained for the LT phase of $\text{RbMn}[\text{Fe}(\text{CN})_6]$ from GGA+U calculations with $U_{\text{Mn}} = 8$ eV and $U_{\text{Fe}} = 1$ eV. The large red and turquoise spheres represent the Fe and Mn atoms, respectively.

Synopsis

The temperature-induced charge transfer between the Mn and Fe sites in $\text{RbMn}[\text{Fe}(\text{CN})_6]$ was analyzed by density functional calculations. Our analysis shows that the extent of electron correlation (equivalently, the pairing energy or the on-site repulsion) is much greater for the Mn^{n+} ion than for the Fe^{n+} ($n = 2, 3$) ion. This surprising and counterintuitive finding is a consequence of the π -backdonation effect of the CN ligands.



Chapter 6

Conclusions

In this dissertation we discussed results of our theoretical studies on the multiferroics MnWO_4 and MnSb_2S_4 as well as the magnetic solids Sr_2MOsO_6 ($M = \text{Cu}, \text{Ni}$) and $\text{RbMn}[\text{Fe}(\text{CN})_6]$. Our conclusions concerning these systems are summarized as follows:

For MnWO_4 , our calculations show that the spin exchange interactions of MnWO_4 are frustrated within each $//c$ -chain and between $//c$ -chains along the a -direction, consistent with the experimental observation that a spiral-spin propagates along the c - and the a -directions in the incommensurate state AF2, and a $\uparrow\uparrow\downarrow\downarrow$ spin arrangement occurs along the c - and a -directions in the collinear magnetic state AF1. The classical spin analysis with the extracted spin exchange parameters leads to an incommensurate state with propagation vector in qualitative agreement with that found for the AF2 state. The Berry phase calculations for a model (4a, b, 2c) superstructure with spiral-spin order show FE polarization along the b -direction, in agreement with experiment.

Our GGA+U calculations reveal that the spin exchanges of monoclinic MnSb_2S_4 are frustrated not only within each MnS_4 chain but also between adjacent MnS_4 chains. This explains the occurrence of the helical spin arrangement in each MnS_4 chain and the noncollinear spin arrangement between adjacent MnS_4 chains along the a -direction. MnSb_2S_4 is predicted to be a multiferroic with FE polarization $P \approx -14 \mu\text{C}/\text{m}^2$ along the MnS_4 chain direction. A field-induced reversal of the FE polarization of MnSb_2S_4 is expected to occur by reversing the direction of the helical spin rotation in each MnS_4 chain. It should be noted that

the spin exchanges between adjacent MnS_4 chains are substantial in MnSb_2S_4 , which explains why MnSb_2S_4 can be a multiferroic in spite of a helical spiral spin order in each MnS_4 chain.

To describe the magnetic insulating states of $\text{Sr}_2\text{CuOsO}_6$ and $\text{Sr}_2\text{NiOsO}_6$ by DFT+U calculations, it is necessary to employ a substantially large U_{Os} value. This indicates that the 5d orbitals of the Os^{6+} ion are strongly contracted due to the high oxidation state. The magnetic structure of $\text{Sr}_2\text{CuOsO}_6$ is best approximated by the A-type AFM arrangement (AF2), and that of $\text{Sr}_2\text{NiOsO}_6$ by the FM arrangement. However, significant spin frustration exists within each //ab-layer and between adjacent //ab-layers in both compounds. The latter is most likely responsible for the divergence of their ZFC and FC magnetic susceptibility curves below ~ 20 K. The crucial difference between the magnetic properties of $\text{Sr}_2\text{CuOsO}_6$ and $\text{Sr}_2\text{NiOsO}_6$ lies in their $\text{M-O}_{\text{eq}}\text{-Os}$ and $\text{M-O}_{\text{ax}}\text{-Os}$ spin exchanges, which arises ultimately from the fact that the Cu^{2+} ion has only magnetic orbital (i.e., x^2-y^2) while the Ni^{2+} ion has two (i.e., x^2-y^2 and z^2). The $\text{Ni-O}_{\text{ax}}\text{-Os}$ exchange of $\text{Sr}_2\text{NiOsO}_6$ is strongly FM due to the z^2/xz and z^2/yz overlap densities. In contrast, the $\text{Cu-O}_{\text{ax}}\text{-Os}$ exchange of $\text{Sr}_2\text{CuOsO}_6$ is slightly AFM, which suggests indirect exchange interactions between the Cu^{2+} and Os^{6+} ions through the $\text{Cu-O}_{\text{eq}}\dots\text{Sr}^{2+}\dots\text{O}_{\text{eq}}\text{-Os}$ paths.

Our analysis of the electronic structure of $\text{RbMn}[\text{Fe}(\text{CN})_6]$ suggests that the extent of electron correlation is much greater for the Mn^{n+} ion than for the Fe^{n+} ($n = 2, 3$) ion. We believe this finding originates from the π -backdonation effect of the CN ligands, which delocalizes the electron density of the Fe^{n+} ion into the surrounding CN ligands. This makes

the electron distribution around the Fe^{n+} ion less contracted, but makes that around the Mn^{n+} ion more contracted. Consequently, $U_{\text{Mn}} \gg U_{\text{Fe}}$.

Part II

Statistical Methods on Drug Discovery Data

Chapter 7

Introduction

7.1 Drug Discovery

Drug discovery is the process by which drugs are discovered and/or designed. The process of drug discovery involves the identification of candidates, synthesis, characterization, screening, and assays for therapeutic efficacy. Once a compound has shown its value in these steps, the process of drug development prior to clinical trials will start. Despite advances in technology and understanding of biological systems, drug discovery is still a lengthy, expensive, difficult, and inefficient process with low rate of new therapeutic discovery [1]. It takes more than 10 years on average and lots of efforts and processes for a new drug to come into the market. Currently, the research and development cost of each new molecular entity is approximately 1.8 billion U.S. dollars [2].

After an objective, i.e., which disease to cure, is set up, the biologists and geneticists work together to determine which tissue in the body or what type of protein or enzyme they need to control to cure the disease based on pathology. After the protein or enzyme in a certain organ is targeted, the chemists are involved to determine what compounds they want to synthesize to alternate the function and cure the disease. However, it is almost impossible to determine exactly which compound will work, or even more basically, which types of functional groups will. They know neither how

large the molecules are, nor what kind of polarity it requires. They synthesize tons of chemical compounds that contain different functional groups and are different sizes. Their interactions with the biological target will be further tested. In pharmaceutical industry, millions of compounds are in the pool to be selected as new drug candidates. However, only tens of them or even less are really biologically active. Although recent technological advances in high-throughput screening (HTS, a method for scientific experimentation using robotics, data processing and control software, liquid handling devices, and sensitive detectors [3]) have allowed chemists to screen large numbers of chemical compounds against specific biological targets, they are very costly and time consuming. Experiments on all of the compounds are impossible.

Combinatorial chemistry was a central technology in generating large screening libraries for HTC. Although it increased efficiency in chemical synthesis, no increase in drug candidates has been found [4]. On the other hand, synthetic combinatorial library compounds seem to cover only a limited and quite uniform chemical space [5]. In order to utilize this property, chemists work together with other specialists such as statisticians to select drug candidates and make them final drugs. These drugs may be tested on animals first to ensure that they are not seriously toxic. If the new drug passed all of these preclinical stages, it will be put into clinical trials, where for the first time the new drug is used on human beings. Four phases with different focuses are involved in a clinical trial for a new drug application. The main objective for Phase I clinical trial is to explore possible toxic effects of drugs and determine a tolerated dose for further experimentations. Pharmacology of the drug, such as pharmacokinetics (PK) and pharmacodynamics (PD) are explored in this phase, as well as its interaction with other drugs, food, and alcohol. The objective for Phase II study is screening and feasibility by the initial assessment for therapeutic effects, dose

finding, and further assessment of toxicities. In Phase III study, the new intervention is compared with the current standard treatment with respect to efficacy and toxicity. The last phase is observational study for adverse effects and some safety related issues. Statistics are widely used in each phase of clinical trials and also in the preclinical stages where drug candidates are selected from hundreds of thousands of compounds in the compound library.

As a result of HTS, each compound can be classified as being active ($W = 1$) or inactive ($W = 0$) against the biological target under investigation. Here being active usually means that the compound is able to inhibit a certain protein hence protect the cells against the target such as a virus. In drug discovery problem, it is often the case that hundreds of thousands of compounds are available as drug candidates, while in these compounds, only hundreds or even less are really biologically active. It is very costly to test the activities of all the compounds through HTS to find just a very small percentage of active ones. Instead, people screen a proportion of the compounds, and use the results to build a statistical model or construct a computational method to screen the remaining compounds and identify those that would have been tested active. Such models or methods are possible because there is a relationship between the variation of biological activity within a group of molecular compounds and the variation of their respective structural and chemical features, which is the underlying assumption for structure-activity relationship (SAR) [6]. Once the models are formulated, they can even be used to virtually screen compounds which do not yet exist. The research goal of this dissertation is to promote new methodologies for preclinical drug discovery.

7.2 Statistics in Drug Discovery

Physical and chemical properties such as size, molar weights, melting points, polarity, and functional groups are involved in determining the interactions between the compounds and the target. They form the descriptor set X . In order to describe the compounds in a mathematical way, people construct atom pairs [7], weighted burden numbers [8], and continuous BCUT numbers [9], etc. from the compound properties. Note that, BCUT descriptors developed by [10] were designed to encode atomic properties relevant to intermolecular interactions, and they can also be used to define a low-dimensional chemistry space [11, 9]. Given a compound, a software, PowerMV [8], can be used to generate these descriptor sets easily. Each of these descriptor sets is a high dimensional data set. Sometimes, people use several of them combined together to depict the compound information. The activity of a compound can be directly depicted by percent inhibition or some other quantities, and these are used as response Y . Y can be continuous, such as the percent inhibition, or categorical, i.e., $Y = 1$ represents active class, and $Y = 0$ represents inactive class. With all these information, we can abstract drug discovery problem into a statistical modeling problem with activity of the drug as the response Y and chemical properties as the descriptor set X . Then we can see that the relationship between the descriptors and activity is extremely complex for HTS data, and there are several challenges in statistical modeling. First, the potent compounds of different chemical classes may act in different ways, caused by multiple mechanisms. In other words, there exist heterogeneous structure-activity relationships (SARs) [12] which determine the chemical and biological features of these drug compounds. Thus the identification of active chemical compounds can be formulated as a mixture regression problem,

in which a lurking categorical variable, which distinguishes multiple mechanisms but not among the observed covariates, exists. Second, the class of inactive compounds is dominating in size. In thousands of drug candidates, it is often the case that only several percent of them are potential drugs. Therefore, the drug discovery data is a highly unbalanced data. Finally, there are many predictors which are sometimes highly correlated.

Lots of efforts have been made to uncover the relationship between the response and the descriptor set by statistical methods, and thus to predict the active compounds without experiments.

Data mining techniques have been applied to SAR analysis, such as neural networks [13], genetic algorithms [14], and decision trees [15]. However, they all suffer from their limitations. Neural networks offers high accuracy but tends to have over fitting problem in training data [16]. It also has concerns about the reproducibility of results, due to random initialization of the network, the variation of stopping criteria, and lack of information regarding the classification produced [16]. Genetic algorithms can suffer in a similar manner due to its stochastic nature [17]. Decision trees [18] offer a large amount of information regarding their decisions. However they commonly require a great deal of tuning.

Cell-based analysis is an approach proposed by Raymond to analyze compound HTS data [19]. Cell-based analysis divides a high-dimensional descriptor space into many small, low-dimensional cells, scores cells according to the activities of their compounds, and uses the scores to prioritize further compounds for screening. A concern for cell-based analysis is that it is very slow or even fails for high dimension data set, although it works well for descriptor set with less than 10 dimensions.

Another common approach to analyze the assay data is to build a classification tree

to predict the activity of unscreened compounds [20]. Classification tree algorithms split the explanatory variables successively into smaller hyper-rectangles. In order to simplify the large tree, Welch proposed a “tree harvesting” method which allows global reorganization of the tree. However, it is common that classification tree is not a sensitive classification method for data with only variance difference involved.

ChemModLab is a toolbox for fitting and assessing quantitative SARs written by ECCR@NCSSU [21]. It includes 16 statistical modeling methods to analyze HTS data. They use the HTS data to fit the model and use the model to predict unscreened data. However, this web based modeling tool uses only sophisticated modeling methods such as support vector machine (SVM) [22] and classification tree, rather than promotes a new methodology that focuses on solving high dimensional data, and it does not always work well for unbalanced settings.

One more issue, all previous methods are based on the fact that some compounds are already identified by HTS and this information can be used as training data to fit a statistical model. What if we have no prior information, i.e., can we directly cluster the data just based on their similarities? It is intuitive to think that if one compound interacts with a certain protein, then those compounds with similar polarity, molar size, and functional groups are more likely to interact with the same protein rather than those which have nothing in common. This is also why the cell-based analysis works. Furthermore, if we have training set available, is there any way that we can take class weight information into account, and come up with a method that better resolves the unbalanced issue?

7.3 Summary and Outline of this Part of the Dissertation

Aiming at better addressing this high dimensional and unbalanced data issue, we propose two different approaches in this dissertation. For dimension reduction based clustering method, we combine sufficient dimension reduction (SDR) and clustering methods to address the compound discovery problem. We choose appropriate DR methods to reduce the dimension of the descriptor set, thus to find the reduced space that contains all regression information. Then we find an effective clustering strategy to cluster the compounds into different classes in the reduced space. For using this method, we do not need previous classification information since clustering itself is an unsupervised learning method. Another approach we propose is weighted boosting on classification tree. Different from traditional boosting method, we assign a large weight to the rare class, where the weight is reciprocal to the class proportion, and get a better classification result on the rare class. We prove that this method reach the theoretical minimal misclassification rate, i.e., it satisfies the Bayes rule.

We can depict the drug discovery problem and the methods proposed in this dissertation by the following flow chart, Figure 7.1.

To describe our organization in detail, we propose a dimension reduction based clustering in high dimensional unbalanced drug discovery data classification in Chapter 8. Unlike classical dimension reduction methods such as principal component analysis (PCA), which reduces the dimension in the descriptor set based on its covariance structure, we use a sufficient dimension reduction, which retains the regression information in the data while reducing the dimension. We give a background introduction and chapter organization in Section 8.1. We briefly review PCA and sufficient dimen-

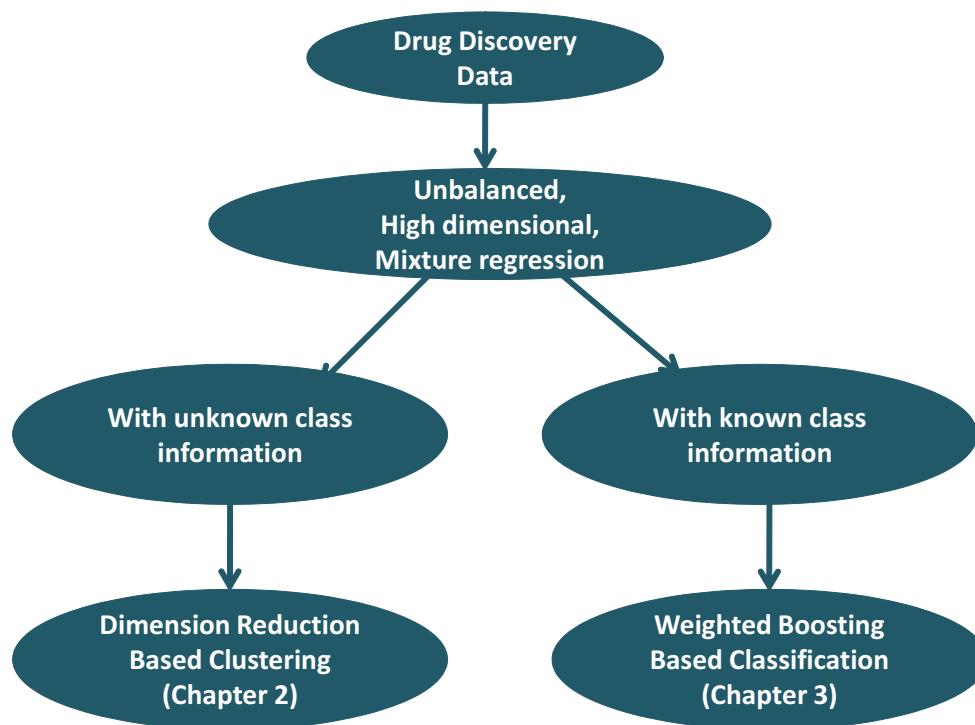


Figure 7.1: Connection between chapters

sion reduction on mixture regression to discuss the theoretical reason why DR based clustering works in drug discovery data and introduce four sufficient dimension reduction methods, i.e., sliced inverse regression (SIR), sliced average variance estimation (SAVE), directional regression (DR), and localized sliced inverse regression (L-SIR), in detail in Section 8.2. Two classical clustering methods used in this dissertation, i.e., k -means and the model based clustering method, as well as ranking along the dimension reduction direction are discussed in Section 8.3. We briefly review evaluation criteria in Section 8.4. Implementation and simulation studies on parameter tuning of localized sliced inverse regression, as well as our numerical studies on simulated drug discovery data are elaborated in Section 8.5. XUE data, a simulated data based

on real drug information is investigated by the DR based clustering method in 8.6. In Section 8.7, we conclude that the DR based clustering bring computation efficiency for high dimensional drug discovery data modeling with better clustering result. Ranking along the DR direction can be used to detect high dimensional unbalanced mixture from Gaussian distribution with both mean and variance differences.

Our focus in Chapter 9 is on promoting weighted boosting regression tree on unbalanced data classification. We start with a brief background introduction in Section 9.1. We introduce Adaboost algorithm and its connection with the forward stagewise additive modeling on minimizing exponential loss in Section 9.2. Two weighted Adaboost algorithms are proposed in Section 9.3, and we discuss that weighted Adaboost-2 is better than the other one because we have a closed form weight update coefficient. We introduce gradient boosting and its weighted version in Section 9.4. We test our algorithms on simulation and real data in Sections 9.5 and 9.6 finding that weighted boosting algorithms consistently have smaller mean-within-group misclassification error rate than traditional boosting algorithms. Finally, we wrap up the chapter with a summary in Section 9.7.

We summarize our findings on the two new methods, i.e., the dimension reduction based clustering and the weighted boosting based classification, in Chapter 10. Future research directions are discussed as well.

Chapter 8

Dimension Reduction Based Clustering on Drug Discovery Data

8.1 Introduction

Drug discovery dataset has several features which make it difficult to set up a statistical model. It has heterogenous structure-activity relationships which lead to a mixture regression problem. Drug discovery data usually has high dimensional descriptor set with correlation in it, and is extremely unbalanced, while our objective is to detect the rare class with high efficiency. All of these challenges make the classical clustering and classification methods fail in modeling drug discovery data.

In statistics, mixture of regressions occurs when there is an omitted categorical predictor, such as activity of compounds in our project, and different regressions occur in each category. Previous studies indicate that sufficient dimension reduction (SDR) and its regression graphics have been perceived as an effective way to facilitate high dimensional regression analysis[23]. They can suggest the presence of a lurking variable, although they cannot identify the variable itself. SDR transforms a high dimension problem to its low dimension projection, by providing a small set of composite predictors on which prediction and modeling are based. SDR achieves dimension reduction without loss of information and pre-specifying model structures,

and it is not affected by the correlation structure in the descriptor set. SDR also makes visualization of high dimensional data possible, and leads naturally to *sufficient summary plots*[24], which is useful for identifying mixture of regressions in a largely nonparametric context. All of these features of SDR make it a remedy of the classical clustering and classification methods in high dimensional unbalanced drug discovery data classification. In this chapter, we compare the performance of several SDR methods under different scenarios, and discuss SDR based clustering methods for drug discovery data classification.

The following of this chapter is organized as follows. We introduce classical and modern dimension reduction methods, such as principal component analysis (PCA) and sliced inverse regression (SIR) in Section 8.2. Clustering methods used in this chapter including K-means, model based clustering method, and ranking along dimension reduction direction are discussed in Section 8.3. Evaluation criteria are reviewed briefly in Section 8.4. Our simulation study and XUE data investigation are discussed in Section 8.5 and 8.6, respectively. Finally, we wrap up the chapter by a brief summary in Section 8.7.

8.2 Dimension Reduction Methods

To address the high dimensional data modeling problem, our first attempt is to reduce dimension of the predictor. We discuss two types of dimension reduction methods in this section, i.e., unsupervised dimension reduction method, which only considers the information in the descriptor set, and supervised dimension reduction method, which takes the response information into consideration, thus is also named sufficient dimension reduction. We briefly review one unsupervised dimension reduc-

tion method, and discuss sufficient dimension reduction methods in detail, since they retain all regression information in the reduced space.

8.2.1 Unsupervised Dimension Reduction

Herein we start with one of the most commonly used classical DR methods, i.e., principal component analysis (PCA). PCA is concerned with explaining the variance-covariance structure of the descriptor set through a few linear combinations of the original variables. Although p components are required to fully reproduce the total system variability, often much of the variability can be accounted for by a small number, d , of the principal components. Assume X is a p -dimension random variable with mean vector μ and covariance matrix $Cov(X) = \Sigma$, then PCA approaches dimension reduction by seeking a set of orthogonal linear combinations $a_1^T X, \dots, a_p^T X$ which satisfies $\max_{a_j} Cov(a_j^T X)$, where $a_j, \forall j \in 1, \dots, p$ are orthonormal vectors. The eigenvectors of the predictor covariance matrix $Cov(X)$, denoted by $\gamma_1 \geq \dots \geq \gamma_p$, corresponding to the eigenvalues $\lambda_1 \geq \dots \geq \lambda_p$ in descending order are the maximizers. Here the $\gamma_j, \forall j \in 1, \dots, p$ are defined as the *principal component directions*, and the linear combinations $\gamma_j^T X, \forall j \in 1, \dots, p$ are the *principal components* (PCs). One can choose the first d PCs to replace X and achieve the purpose of dimension reduction. The number of PCs, d , to use can be determined by the scree plot, i.e., the 'elbow' in the graph of eigenvalues λ_j 's. One can also choose d such that the total explained variation exceeds a pre-specified threshold percentage.

Assume the data x_1, x_2, \dots, x_n represent n independent drawings from X . The data yield the sample mean vector

$$\bar{x} = \frac{1}{n} \sum_{i=1}^n x_i,$$

and the sample covariance matrix

$$S = \sum_{i=1}^n \frac{1}{n} \hat{E}(x - \bar{x}) \hat{E}(x - \bar{x})^T.$$

Then the sample principal components are defined as the linear combinations with the maximum sample variance. The sample PCs are from eigen decomposition of S , i.e., $S\gamma_i = \lambda_i\gamma_i$. The first d eigenvectors $(\hat{\gamma}_1, \dots, \hat{\gamma}_d)$ which correspond to the eigenvalues $\hat{\lambda}_1 \geq \dots \geq \hat{\lambda}_d > 0$ form the basis of the reduced space.

PCA has widespread applications. However, it only bases on the marginal distribution of the descriptor variables while the response information is neglected completely. This drawback is remedied in the supervised dimension reduction methods, such as sliced inverse regression (SIR) [25], sliced average variance estimation (SAVE) [26], and directional regression (DIR) [27], by taking response into consideration in reducing the descriptor space.

8.2.2 Supervised Dimension Reduction

The goal of a regression study is to infer the conditional distribution of the response Y given the $p \times 1$ vector of predictors X . Let B denote a fixed $p \times d$, $d \leq p$, matrix so that

$$Y \perp\!\!\!\perp X | B^T X. \quad (8.1)$$

The statement (8.1) is equivalent to saying that the distribution of $Y|X$ is the same as that of $Y|B^T X$ for all values of X in its marginal sample space. It implies that the $p \times 1$ predictor vector X can be replaced by the $d \times 1$ predictor vector $B^T X$ without loss of regression information, and thus represents a potentially useful reduction in dimension of the predictor. It is clear that (8.1) holds if and only if

$$Y \perp\!\!\!\perp X | P_{S(B)} X. \quad (8.2)$$

Thus (8.1) is appropriately viewed as a statement about $S(B)$, which is called a *dimension-reduction subspace* for the regression of Y on X [25]. Let $S_{Y|X}$ denote the intersection of all *dimension-reduction subspaces*. Then if $S_{Y|X}$ is itself a dimension-reduction subspace, it is called the *central dimension-reduction subspace*, or simply the *central subspace* [28]. The dimension of $S_{Y|X}$, $d = \dim(S_{Y|X})$, is called the *structural dimension* of the regression. The *central subspace* is the unique smallest dimension-reduction subspace such that $Y \perp\!\!\!\perp X|\eta^T X$, where columns of the matrix η form a basis of the subspace. If $S_{Y|X}$ is known, then the minimal sufficient summary plots of Y versus $\eta^T X$ can be used to guide the subsequent analysis. Thus, for regression of $Y|X$, SDR seeks the *central subspace*.

We assume that the outcome of the experiment depends on three random variables: the scalar response Y , the $p \times 1$ vector of predictors X , and an underlying binary indicator W that identifies the subpopulation, with $W = 1$ or 0 . And either of the two subpopulations can be composed of multiple subpopulations. Let $S_{Y|X}^w$ denote the central subspace of the regression of $Y|W = w$ on $X|W = w$, $w = 0, 1$, and let $S_{W|X}$ denote the central subspace of W on X . Then the relation among the various central subspaces can be expressed as in (8.3)[28].

$$S_{Y|X} \subseteq S_{W|X} \oplus S_{Y|X}^0 \oplus S_{Y|X}^1 \quad (8.3)$$

We expect the equality to hold in (8.3). (8.3) implies that the central subspace of regression of Y on X without knowing the subpopulation information would contain both directions that separate the two subpopulation, as well as the directions that describe the response-predictor relation in each subpopulation. In our compound discovery application, we believe that the outcome variable is independent of all the predictors for the inactive compounds. As such, we have $S_{Y|X}^0 = \emptyset$, the origin. Thus

(8.3) suggests that $S_{Y|X}$ contains information that both separates the active class from the inactive class, as in $S_{W|X}$, and the structure information within the active class, as in $S_{Y|X}^1$. Let $\mu_w = E(X|W = w)$, and $\Sigma_w = Cov(X|W = w)$, $w = 0, 1$. Then $Span(\mu_1 - \mu_2, \Sigma_1 - \Sigma_2) \subseteq S_{W|X}$. $S_{W|X}$ contains information from the difference of locations and scales. If there are multiple subpopulations in the active class, $S_{Y|X}^1$ can be further decomposed in a sequential manner.

There are a number of dimension reduction estimators proposed to estimate the central subspace, such as sliced inverse regression (SIR) [25], sliced average variance estimation (SAVE) [26], directional regression (DIR) [27], local sliced inverse regression (L-SIR) [29], canonical correlation estimation [30], principal Hessian directions (PHD) [31], and iterative Hessian transformation [32]. Most of these methods for estimating the *central subspace* $S_{Y|X}(\eta)$ require the conditional expectation $E(X|\gamma^T X)$ to be linear, also known as linearity condition, which requires the following formula stands, i.e., $E(X|\gamma^T X) = P_\gamma X = \gamma\gamma^T X$. Under the linearity condition, the centered inverse regression curve is contained in the linear subspace spanned by the covariance matrix of $\gamma\Sigma_X$ [25], where Σ_X is the covariance matrix of X . The linearity condition is satisfied when the distribution of X is elliptically symmetric, such as in normal distribution. Thus it imposes a stringent requirement on the distribution of X . One implication is that at the stage of data collection, we better design the experiment so that the distribution of X will not violate the elliptic symmetry. On the other hand, after data collection, we analyze the data closely to remove the outliers. The good thing about the stringent is that when p is large and q is fixed, the condition is approximately true. Also, the linearity condition imposes no requirement on Y or $Y|X$, thus requires no model. The general procedure for estimating the *central subspace* is as follows. Suppose that we can find a consistent estimate M of a $p \times p^T$

procedure-specific population matrix with the property that $Span(M) \subseteq S_{Y|X}$, then inference on at least a part of $S_{Y|X}$ can be based on M . SAVE, SIR and other numerical procedures differ on M but have a common method of producing an estimate of $S_{Y|X}$ from M . Let $\lambda_1 \geq \lambda_2 \geq \dots \geq \lambda_p$ denote the eigenvalues of M , and let $\gamma_1, \dots, \gamma_p$ denote the corresponding left eigenvectors, then the linear combinations $\gamma_1^T X, \dots, \gamma_q^T X$ are the SIR or SAVE predictors depending on the method of analysis. For example, when using SIR, $\gamma_j^T X$ is the j th SIR predictor. The number of linear combinations d that is needed to fully capture the central subspace is determined by the number of nonzero eigenvalues, which can be determined by sequential asymptotic test[25], or permutation test[33]. Assuming that $d = dim(S(M))$ is known ($d \leq p$), $Span(M) = S(\gamma_1, \dots, \gamma_d)$ is a consistent estimate of $S_{Y|X}$.

In the following of this section, we will introduce in detail several sufficient dimension reduction methods used in our numerical studies, i.e., sliced inverse regression (SIR) [25], sliced average variance estimation (SAVE) [26], and directional regression (DIR) [27], as well as local sliced inverse regression (L-SIR) [29].

8.2.3 Sliced Inverse Regression (SIR)

SIR aims to estimate the *central subspace* $S_{Y|X}$ based on a key observation that, when X is elliptically symmetric, $\Sigma^{-1}E\{X - E(X)|Y\}$ belongs to $S_{Y|X}$, where $\Sigma = Cov(X)$ [25]. Further, it is assumed that whenever $Span(\Sigma^{-1}E\{X - E(X)|Y\}) \subseteq S_{Y|X}$, the two subspaces are equal. From the above observation, one can estimate the central space by the eigen decomposition of the matrix $CovE\{X - E(X)|Y\}$ with respect to $Cov(X)$,

$$Cov\{X - E(X)|Y\}\gamma_j = \lambda_j Cov(X)\gamma_j, j = 1, \dots, p. \quad (8.4)$$

Similar to PCA, the first d eigenvectors $(\gamma_1, \dots, \gamma_d)$ that correspond to the eigenvalues $(\lambda_1 \geq \dots \geq \lambda_d \geq 0)$ form a basis of the central space, and γ'_j 's are the SIR directions.

Given n independent identically distributed data observations $\{(x_i, y_i), i = 1, \dots, n\}$. One first obtains \tilde{y} by slicing the range of response y into h non-overlapping intervals, and then computes sample inverse mean and sample covariance estimator within each slice $s = 1, \dots, h$ by (8.5) and (8.6),

$$\hat{E}(x - E(x)|\tilde{y} = s) = \sum_{\tilde{y}_i \in \text{slice } s} \frac{1}{n_s} (x_i - \bar{x}), \quad (8.5)$$

$$\widehat{Cov}\{E(x - E(x)|\tilde{y})\} = \sum_{s=1}^h \frac{n_s}{n} \hat{E}(x - E(x)|\tilde{y} = s) \hat{E}(x - E(x)|\tilde{y} = s)^T. \quad (8.6)$$

Next we perform eigen decomposition with respect to the sample covariance estimator,

$$\widehat{Cov}\{E(x - E(x)|\tilde{y})\} \hat{\gamma}_j = \hat{\lambda}_j \widehat{Cov}\{E(x)\} \hat{\gamma}_j, \quad j = 1, \dots, p. \quad (8.7)$$

Thus the first d eigenvectors $(\hat{\gamma}_1, \dots, \hat{\gamma}_d)$ which correspond to the eigenvalues $\hat{\lambda}_1 \geq \dots \geq \hat{\lambda}_d > 0$ form a basis of the sample central space. The *structural dimensions* that captures the *central subspace* is determined by the number of nonzero eigenvalues, which can in turn be determined by sequential asymptotic test or permutation test.

The number of slices h is a tuning parameter in SIR, but the estimation results are not very sensitive to the choice of h , as long as $h > d$ and the number of observations in each slice is large enough for the asymptotic approximation. If Y takes categorical values as in classification problems, it is natural to divide the data into different groups by their responses. In the case of two groups, SIR is equivalent to linear discriminant analysis in that it can only obtain one direction.

SIR is simple to compute, and works for a variety of flexible models. However, it fails when $E(X|Y) = 0$, in which case $Cov\{E(X|Y)\}$ cannot provide information

about $S_{Y|X}$. The degeneracy of SIR also restricts its use in binary classification problems, since only one direction can be obtained. SAVE addresses these issues by using the second moment information on the conditional distribution of X given Y . We will discuss SAVE in the following subsection.

8.2.4 Sliced Average Variance Estimation (SAVE)

Instead of using $CovE\{X - E(X)|Y\}$ as in SIR, which fails when $E(X|Y) = 0$. $\Sigma_x^{1/2} E[\{I_p - Cov(Z|Y)\}^2] \Sigma_x^{1/2}$ is used as the kernel matrix in SAVE, where $Z = \Sigma_x^{-1/2}\{X - E(X)\}$. On the population level, we perform the eigen decomposition on

$$E[\{I_p - Cov(Z|Y)\}^2] \gamma_j = \lambda_j \gamma_j, \quad j = 1, \dots, p, \quad (8.8)$$

and obtain the first d eigenvectors $(\gamma_1, \dots, \gamma_d)$ corresponding to the largest d positive eigenvalues $\lambda_1 \geq \dots \geq \lambda_d \geq 0$, then $Span(\gamma_1, \dots, \gamma_d) \subseteq S_{Y|Z}$. Then we transform the eigen vectors from the Z space back to the X space, and thus

$$Span(\Sigma^{-1/2} \gamma_1, \dots, \Sigma^{-1/2} \gamma_d) \subseteq S_{Y|X}. \quad (8.9)$$

Given n independent identically distributed data observations $\{(x_i, y_i), i = 1, \dots, n\}$, as in SIR, one first obtains \tilde{y} by slicing the range of response y into h non-overlapping intervals. However, to use SAVE, it requires that the predictor vector x to be standardized by $\hat{z}_i = \hat{\Sigma}^{-1/2}(x_i - \bar{x})$, where $\bar{x} = \frac{1}{n} \sum_{i=1}^n x_i$, and $\hat{\Sigma} = \frac{1}{n} \sum_{i=1}^n (x_i - \bar{x})(x_i - \bar{x})^T$. Thus the sample covariance estimator within each slice $s = 1, \dots, h$ is

$$\widehat{Cov}\{E(z|\tilde{y} = s)\} = \sum_{\tilde{y}_i \in \text{slice } s} \frac{1}{n_s} (z_{is} - \bar{z}_s)(z_{is} - \bar{z}_s)^T. \quad (8.10)$$

And the eigen decomposition is on

$$\hat{M} = \sum_{s=1}^h \frac{n_s}{n} \{I_p - \widehat{Cov}(z|\tilde{y} = s)\} \{I_p - \widehat{Cov}(z|\tilde{y} = s)\}^T. \quad (8.11)$$

The first d eigenvectors $(\hat{\gamma}_1, \dots, \hat{\gamma}_d)$ which correspond to the eigenvalues $\hat{\lambda}_1 \geq \dots \geq \hat{\lambda}_d > 0$ form a basis of the sample central space. The *structural dimensions* that captures the *central subspace* is determined by the number of nonzero eigenvalues, which can in turn be determined by sequential asymptotic test or permutation test.

Besides linearity condition, SAVE requires the variance to be a constant, and is slower than SIR in computation, since it requires more parameters. However, SAVE does not require $h > d$ to work, which makes it suitable for solving a binary classification problem. SAVE also works well with $E(X|Y) = 0$.

8.2.5 Directional Regression for Dimension Reduction (DIR)

SIR and SAVE have wide application, but they have their own limitations. DIR combines the advantages of SIR and SAVE, and has shown substantial improvement in accuracy over SIR and SAVE. The kernel matrix used in DIR can be expressed as in (8.12) [27].

$$\begin{aligned} M = & 2E[\{E(ZZ^T|Y) - Cov(Z)\}^2] + 2E^2[E(Z|Y)E(Z^T|Y)] \\ & + 2E[E(Z^T|Y)E(Z|Y)]E[E(Z|Y)E(Z^T|Y)], \end{aligned} \quad (8.12)$$

where Z is the standardized form of X , i.e., $Z = \Sigma^{-1/2}(X - E(X))$. DIR performs the generalized spectral decomposition, $M\gamma_j = \lambda_j\gamma_j$, $j = 1, \dots, p$, where $\gamma_1, \dots, \gamma_p$ denote the eigenvectors corresponding to $\lambda_1 \geq \dots \geq \lambda_d > \lambda_{d+1} = \dots = \lambda_p = 0$. Thus from the linearity condition, i.e., $E(Z|\gamma^T Z)$ is a linear function of Z , $Span(\gamma_1, \dots, \gamma_d)$ forms a consistent estimate of the *central subspace* $S_{Y|Z}$. Transforming the Z space

back to the X space, $Span(\Sigma^{-1/2}\gamma_1, \dots, \Sigma^{-1/2}\gamma_d)$ forms a consistent estimate of the *central subspace* $S_{Y|X}$. Following sequential test procedure, the *structural dimension* d can be determined.

From the sample level, given n independent identically distributed data observations $\{(x_i, y_i), i = 1, \dots, n\}$, as in SIR and SAVE, one first obtains \tilde{y} by partitioning the feasible value space of response y into h mutually exclusive and collectively exhaustive intervals. DIR then requires to standardize the predictor vector x by $\hat{z}_i = \hat{\Sigma}^{-1/2}(x_i - \bar{x})$, where $\bar{x} = \frac{1}{n} \sum_{i=1}^n x_i$, and $\hat{\Sigma} = \frac{1}{n} \sum_{i=1}^n (x_i - \bar{x})(x_i - \bar{x})^T$. Thus the sample mean estimator within each slice $s = 1, \dots, h$ can be expressed as follows.

$$\hat{E}(z|\tilde{y} = s) = \frac{1}{n_s} \sum_{\tilde{y}_i \in \text{slice } s} z_i, \quad (8.13)$$

$$\hat{E}(z^T|\tilde{y} = s) = \frac{1}{n_s} \sum_{\tilde{y}_i \in \text{slice } s} z_i^T, \quad (8.14)$$

and

$$\hat{E}(zz^T - I_p|\tilde{y} = s) = \frac{1}{n_s} \sum_{\tilde{y}_i \in \text{slice } s} z_i z_i^T - I_p. \quad (8.15)$$

The eigen decomposition is on

$$\begin{aligned} \hat{M} = & 2 \sum_{s=1}^h \frac{n_s}{n} E^2(zz^T - I_p|\tilde{y} = s) + 2 \left[\sum_{s=1}^h \frac{n_s}{n} E(z|\tilde{y} = s) E(z^T|\tilde{y} = s) \right]^2 \\ & + 2 \sum_{s=1}^h \frac{n_s}{n} E(z^T|\tilde{y} = s) E(z|\tilde{y} = s) \times \sum_{s=1}^h \frac{n_s}{n} E(z|\tilde{y} = s) E(z^T|\tilde{y} = s). \end{aligned} \quad (8.16)$$

The first d eigenvectors $(\hat{\gamma}_1, \dots, \hat{\gamma}_d)$ which correspond to the eigenvalues $\hat{\lambda}_1 \geq \dots \geq \hat{\lambda}_d > 0$ form a basis of the sample central space $S_{Y|Z}$, and it can be easily transformed to $S_{Y|X}$.

DIR is a second-moment based method. It improves the accuracy of contour regression and decreases the computing time.

8.2.6 Local Sliced Inverse Regression (L-SIR)

L-SIR [29] extends SIR by taking into account the local structure of the explanatory variables conditioning on the response variable [34, 29]. In SIR we shift all the transformed data points by the corresponding group average, and then perform a spectral decomposition on the covariance matrix of the transformed and shifted data to identify the SIR directions. The logic behind this approach is that if a direction does not differentiate different groups well, the group means projected onto that direction would be very close, and therefore the variance of the transformed data will be small in that direction.

The idea of L-SIR is that Euclidean structure around a data point in R^p is only meaningful locally. From this point of view, a natural way to incorporate localization idea into SIR is to shift each transformed data point to the average of a local neighborhood instead of the average of its global neighborhood. The local neighborhoods are often defined by the k nearest neighbors, k -NN, of a point. Now in L-SIR, it takes into account the points in the ambient space as well as information about the response variable due to slicing. This is helpful in our context because it is common that compounds from the same class, or with similar activity, are closer than from different classes.

The reduced space can be obtained similarly as in SIR from the population level, except that the local information k is taken into consideration. Thus one can estimate the central space by performing the eigen decomposition of the matrix $CovE\{X - E(X)|Y, k\}$ with respect to $Cov(X)$,

$$Cov\{X - E(X)|Y, k\}\gamma_j = \lambda_j Cov(X)\gamma_j, j = 1, \dots, p. \quad (8.17)$$

The first d eigenvectors $(\gamma_1, \dots, \gamma_d)$ that correspond to the eigenvalues $(\lambda_1 \geq \dots \geq$

$\lambda_d \geq 0$) form a basis of the central space, and the $\gamma_j s$ are the L-SIR directions.

Given a data set (x_i, y_i) , as in SIR, it is divided into h non overlapping slices by response. We compute

$$\hat{E}(x|\tilde{y} = s, k) = \frac{1}{k} \sum_{j \in s_i} x_j, \quad (8.18)$$

where $s_i = \{j : x_j \text{ belongs to the } k \text{ nearest neighbors of } x_i \text{ in slice } h\}$, and

$$\hat{E}(x) = \frac{1}{n} \sum_{i=1}^n x_i. \quad (8.19)$$

The local version of kernel matrix is

$$\hat{M} = \frac{1}{n} \sum_{i=1}^n [\hat{E}(x|\tilde{y} = s, k) - \hat{E}(x)][\hat{E}(x|\tilde{y} = s, k) - \hat{E}(x)]^T. \quad (8.20)$$

After eigen decomposition on the kernel matrix in (8.20), one can obtain the L-SIR directions and eigenvalues as in (8.21).

$$\hat{M}\hat{\gamma}_j = \hat{\lambda}_j \widehat{Cov}(x)\hat{\gamma}_j, \quad j = 1, \dots, p, \quad (8.21)$$

The L-SIR dimension reduction directions are defined similarly as in SIR. Besides the number of slices h , the neighborhood size k in L-SIR is a tuning parameter. When k is sufficiently large, i.e., equivalent to or larger than the number of observations in each slice, the kernel matrix in L-SIR is the same as in SIR and L-SIR recovers all SIR directions. On the other hand, if k is small, e.g., equivalent to 1, L-SIR keeps all p dimensions. Thus it is essential for us to vary k to get the best performance of L-SIR. In other words, we need to find the optimal local information for using L-SIR. We will discuss the choice of k in our simulation studies in later sections.

SIR and SAVE are implemented in R *dr* package, and can be used directly by "dr" commands with method = 'sir' and 'save', respectively. We implement DIR and L-SIR for our numerical studies. The performance of these DR methods on unbalanced data clustering will be discussed with numerical results in later sections.

8.3 Clustering Methods

Clustering is the assignment of a set of observations into subsets (clusters) so that observations in the same cluster are similar in some sense. It is a method of unsupervised learning, and a common technique for statistical data analysis used in many fields.

There are a number of commonly used cluster analysis methods, such as classification tree, k -means clustering and model based clustering by expectation maximization (EM) algorithm. We review k -means and model based clustering in the following part of this section. In order to better cluster our simulation data, we propose ranking method, which sorts along the dimension reduction direction.

8.3.1 K -means Clustering

The k -means clustering method aims to partition n observations into k clusters in which each observation belongs to the cluster with the nearest mean. Given a set of observations (x_1, x_2, \dots, x_n) , where each observation is a S -dimensional real vector, then k -means clustering aims to partition the n observations into k sets ($k < n$) $S = S_1, S_2, \dots, S_k$ so as to minimize the within-cluster sum of squares (WCSS): $\sum_{i=1}^k \sum_{x_j \in S_i} \|x_j - \mu_i\|^2$, where μ_i is the mean of S_i .

In general, the k -means method will produce exactly k different clusters of greatest possible distinctions. The best number of clusters k leading to the greatest separation is not known a priori and must be computed from the data. The general algorithm of k -means is as follows.

Step 1: Choose the number of cluster, k . Randomly generate k clusters and determine the cluster centers, or directly generate k random points as cluster centers

(denote the cluster centers as $m_1^{(1)}, \dots, m_k^{(1)}$, (1) represent the first iterative step).

Step 2: Assign each point to the nearest cluster center $m_i^{(t)}$, i.e.

$$S_i^{(t)} = \{x_j : \|x_j - m_i^{(t)}\| \leq \|x_j - m_{i^*}^{(t)}\|, \forall i^* = 1, \dots, k\}. \quad (8.22)$$

Step 3: Recompute the new cluster centers.

$$m_i^{(t+1)} = \frac{1}{|S_i^{(t)}|} \sum_{x_j \in S_i^{(t)}} x_j. \quad (8.23)$$

Step 4: Repeat Step 2 and 3 until the assignment no longer changes.

The main advantage of this algorithm is its computational simplicity which allows it to run on large data sets. However, it does not yield the same result from each run, since the resulting clusters depend on the initial random assignments. Even it minimizes intra-cluster variance, it does not ensure that the result has a global minimum of variance. K -means is implemented in R *stats* package, and can be used directly by "kmeans" commends in R.

8.3.2 Model Based Clustering Method

Model based clustering method is first proposed by Wolfe in 1965 [35]. In model based clustering method, it is assumed that the data are generated by a mixture of clusters where each cluster has different underlying probability distributions. Given n observations $x = (x_1, \dots, x_n)$, denote $f_k(x_i, \theta_k)$ as the density function of an observation x_i from the k th cluster, where θ_k are the corresponding parameters, and G as the number of clusters in the mixture, then the model for the composite of the

clusters is usually formulated through the maximum likelihood approach, where the maximum likelihood is expressed in (8.24),

$$L_M(\theta_1, \dots, \theta_G, p_1, \dots, p_G) = \prod_{i=1}^n \sum_{k=1}^G p_k f_k(x_i, \theta_k). \quad (8.24)$$

p_k is the probability that an observation belongs to the k th cluster, and it satisfies the following condition, $\sum_{k=1}^G p_k = 1$, and $p_k \geq 0$.

We are mainly concerned about the case where the underlying probability distribution is Gaussian distribution, i.e., a multivariate normal distribution, where the parameters θ_k consist of a mean vector μ_k and a covariance vector Σ_k , and the density has the form

$$f_k(x_i | \mu_k, \Sigma_k) = \frac{\exp\{-1/2(x_i - \mu_k)^T \Sigma_k^{-1/2} (x_i - \mu_k)\}}{(2\pi)^{p/2} |\Sigma_k|^{1/2}}. \quad (8.25)$$

Banfield and Raftery [36] subsumed several earlier proposals based on Gaussian mixtures, and developed a model-based framework for clustering by parameterizing the covariance matrix in terms of eigen decomposition as follow,

$$\Sigma_k = \lambda_k D_k A_k D_k^T, \quad (8.26)$$

where D_k is the orthogonal matrix of eigenvectors, A_k is a diagonal matrix whose elements are proportional to the eigenvalues of Σ_k , and λ_k is a scalar.

Iterative relocation methods for clustering via mixture models are possible through EM algorithm [37]. EM algorithm [38, 39] is a general approach to find the maximum likelihood estimates of parameters in probabilistic models, where the model depends on unobserved latent variables. EM algorithm alternates between performing an expectation (E) step and a maximization (M) step iteratively. In the E step, an expectation of the log-likelihood with respect to the current estimate of the distribution for the latent variables is computed, while in the M step, the parameters

which maximize the expected log-likelihood found in the E step are observed. These parameters are then used to determine the distribution of the latent variables in the next E step.

Assume Y is a mixture of two normal distributions, i.e., $Y_1 \sim N(\mu_1, \sigma_1^2)$, $Y_2 \sim N(\mu_2, \sigma_2^2)$, and $Y = \pi \times Y_1 + (1 - \pi) \times Y_2$, where $Pr(Y = Y_1) = \pi$. We use this mixture distribution as an example to show EM algorithm.

Take an initial guess for μ_1 , μ_2 , σ_1^2 , σ_2^2 and π .

E step: compute the responsibilities:

$$\hat{\gamma}_i = \frac{\hat{\pi} \phi_{\hat{\sigma}_2}(y_i)}{(1 - \hat{\pi}) \phi_{\hat{\sigma}_1}(y_i) + \hat{\pi} \phi_{\hat{\sigma}_2}(y_i)}, \quad i = 1, 2, \dots, N. \quad (8.27)$$

M step: compute the weighted means and variances:

$$\hat{\mu}_1 = \frac{\sum_1^N (1 - \hat{\gamma}_i) y_i}{\sum_1^N (1 - \hat{\gamma}_i)}, \quad \hat{\sigma}_{2_1}^2 = \frac{\sum_1^N (1 - \hat{\gamma}_i) (y_i - \hat{\mu}_1)^2}{\sum_1^N (1 - \hat{\gamma}_i)}, \quad (8.28)$$

$$\hat{\mu}_2 = \frac{\sum_1^N \hat{\gamma}_i y_i}{\sum_1^N \hat{\gamma}_i}, \quad \hat{\sigma}_{2_2}^2 = \frac{\sum_1^N \hat{\gamma}_i (y_i - \hat{\mu}_2)^2}{\sum_1^N \hat{\gamma}_i}, \quad (8.29)$$

Repeat the E step and the M step until the result no longer changes.

This illustration uses two normal distributions with different means and different standard deviations, and only the mixture of the two normal distributions can be observed. The goal of EM clustering is to estimate the means and standard deviations for each cluster by maximizing the likelihood of the observed distribution. In other words, the EM algorithm attempts to approximate the observed distribution based on mixtures of different distributions in different clusters.

The EM algorithm for clustering is described in detail in Witten and Frank (2001). It is implemented in R *mclust* package. One can use "mclust" commend in R to get

the cluster result. In `mclust`, one is able to determine the number of mixtures, as well as the underlying density distributions for different clusters to obtain good clustering result.

8.3.3 Ranking Along Dimension Reduction Direction

Ranking along dimension reduction direction is a method we proposed to classify data in the reduced central space. As discussed in previous section, the relation among the various central subspaces can be expressed as in (8.30)[28],

$$S_{Y|X} \subseteq S_{W|X} \oplus S_{Y|X}^0 \oplus S_{Y|X}^1. \quad (8.30)$$

(8.30) implies that the central subspace of regression of Y on X contains the direction that separates the two classes, as well as the direction that describes the response-predictor relationship within each class. From (8.30), one can understand that the summary plot of the reduced space contains the direction that separates the two classes, that is, the two classes are aligned along the first or second dimension reduction direction. Thus if we sort the dataset along that direction, and get a certain percentage of the top and bottom of the data, we can claim them as one class, and the rest in between can be claimed as the other class. The reason we get both sides of that direction is that we cannot predict which direction one class distributes without visualization. For unbalanced data classification, it is acceptable to classify the data on both sides to be one class, since one is only getting several percent of the noise class. The borderline between the two classes, i.e., the percentage to cut off, is a tuning parameter in real clustering analysis. In our simulation study, we know the percentage of active compounds, and the easiest way is to use that percentage in ranking.

8.4 Evaluation Criteria

In this section, we briefly review the methods used in this dissertation to evaluate the clustering results.

8.4.1 Table of confusion

There are four possible outcomes from a binary classification problem. Assume outcomes are labeled either as positive (p) or negative (n) class. If the outcome from a prediction is p , and the actual value is also p , then it is called a true positive (TP); if the prediction is p , while the actual value is n , then it is said to be a false positive (FP). Conversely, a true negative (TN) occurs when both the prediction outcome and the actual value are n , and false negative (FN) stands for the case where the prediction outcome is n , while the actual value is p . We use p and n represent actual values, and use p' and n' represent prediction outcomes, respectively.

A *table of confusion (table)*, is a table with two rows and two columns that reports the number of (TN), (FP), (FN) and (TP), shown in Table 8.1(a). We use the percentage, i.e., each cell in Table 8.1(a) out of the total, in our discussion to evaluate different dimension reduction methods, depicted in Table 8.1(b). From the above

Table 8.1: Table of confusion (*table*)

(a) Original <i>table</i>			(b) <i>table</i> in percentage		
	p	n		p	n
p'	TP	FP	p'	$TP/(p+n)$	$FP/(p+n)$
n'	FN	TN	n'	$FN/(p+n)$	$TN/(p+n)$

table, we can calculate the mean within group misclassification error rate, using the

following formula, $\frac{1}{2}(\frac{FP}{FP+TN} + \frac{FN}{TP+FN})$.

8.4.2 Receiver Operating Characteristic (ROC) Curve

A ROC curve is a graphical plot of the sensitivity vs. (1 - specificity) for a binary classifier system as its discrimination threshold varies. The ROC curve can be represented equivalently by plotting the fraction of true positives, i.e., true positive rate (TPR), $TPR = TP/P = TP/(TP + FN)$ versus the fraction of false positives, i.e., false positive rate (FPR), $FPR = FP/N = FP/(FP + TN)$. ROC analysis provides tools to select possibly optimal models and to discard suboptimal ones independently from the class distribution. The area under the curve (AUC) can be used to determine which method is better. The machine learning community most often uses the ROC AUC statistic for model comparison.

8.5 Performance on High Dimensional Unbalanced Data

8.5.1 Simulation Setup

To analyze the compound discovery data, we have the following assumptions. There exists a relationship between response Y and the descriptor set X in the active compounds ($W=1$). However, such a relationship does not exist in the inactive compounds ($W=0$). In our simulation study, we have the indicator information (W). Thus we can construct ROC curve and *table* to evaluate different dimension reduction based clustering methods. We use the following two scenarios in our simulation data generation.

Case 1: X satisfies a univariate normal distribution. For active class ($W=1$), Y is a regression on X through β . While for inactive class ($W=0$), Y satisfies an independent normal distribution.

Case 2: X satisfies a normal distribution with mean difference, variance difference, or both mean and variance differences. Y is simulated as a regression on X through β in the active class ($W=1$), and satisfies independent normal distribution in the inactive class ($W=0$).

We choose Case 2 in the following numerical studies, since it is more reasonable that different classes of chemical compounds have different descriptor sets. The difference in our studies come from mean and variance in the normal distribution. We include three types of settings, mean difference ($\mu_1 \neq \mu_2$), variance difference ($\sigma_1 \neq \sigma_2$), and both mean and variance difference ($\mu_1 \neq \mu_2$) and ($\sigma_1 \neq \sigma_2$) in our discussion. Another point of our interest is proportion variation in the active class. Since the compound discovery data is highly unbalanced, with the inactive compounds dominating in size, it is common to get thousands or tens of thousands dataset with only tens active ones in it. We vary the proportion of the active class to compare the performance of different DR based clustering methods under extreme condition.

We first run simulation studies to compare the performance of DR methods under mean and variance difference scenarios. Dimension reduction is a new research area, and we want to explore the features of SIR, SAVE, L-SIR, and DIR. We use ranking along the dimension reduction direction to do clustering in the reduced space, and plot the summary plot to visualize the separation of the two classes. Another reason for choosing ranking method is that we need a good criterion to compare different methods. With ranking method, we can vary the percentage to separate the two class,

and use ROC curves and AUCs to perform model selection. We run 50 replications in all our simulation studies to reduce statistical error and make the ROC curves smooth. We compare the classification result of DR based clustering to those of k -means and model based clustering method to find that DR based clustering is more efficient in selecting the active class than the classical clustering methods. Our classification results are also evaluated by mean within group misclassification error rate, which is discussed in detail in Chapter 9.

8.5.2 Tune Parameter k in L-SIR

Before using L-SIR, we first discuss selection of the local information in L-SIR, i.e., the tuning parameter k , through numerical studies. Our simulation setting is as in Table 8.2. Through this chapter, we use μ_i and σ_i to denote the mean and the standard deviation of class i . ρ denotes the proportion of the active class. We run L-SIR with different k on simulation data of size 5000 ($n = 5000$) 50 times ($t = 50$), on both mean and variance differences. We run SIR on the same simulation data to validate our implementation of L-SIR. From our discussion of L-SIR, it is easy to understand that when k is sufficiently large, i.e., larger than the number of observation in each slice, results obtained from L-SIR converges to those obtained from SIR. We plot the ROC curves in Figure (8.2), and calculate the corresponding AUCs, presented in Table 8.2. Our clustering results from L-SIR indeed converge to those from SIR for large k , which indicates that our implementation is correct. Another observation from this numerical study is that L-SIR is not very sensitive to the selection of k , as long as k is not close to number of observations in each slice.

Since the results obtained from L-SIR are not sensitive to the choice of k , we can choose k easily without affecting the accuracy of the results in our numerical study

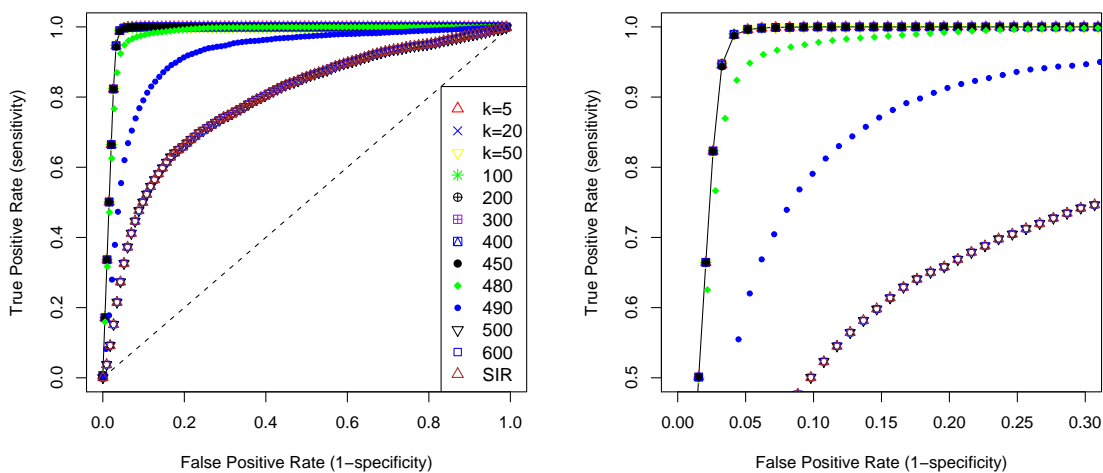
Table 8.2: Selection of k for L-SIR with AUCs

(a) Settings 1: $\mu_1 = \mu_2 = 0$; $\sigma_1 = 1$, $\sigma_2 = 2.3$, $\rho = 0.03$, $n = 5000$, $t = 50$

k	5	20	50	100	200	300
AUC	0.9736	0.9737	0.9737	0.9737	0.9737	0.9737
k	450	480	490	500	600	SIR
AUC	0.9736	0.9668	0.9070	0.7783	0.7783	0.7783

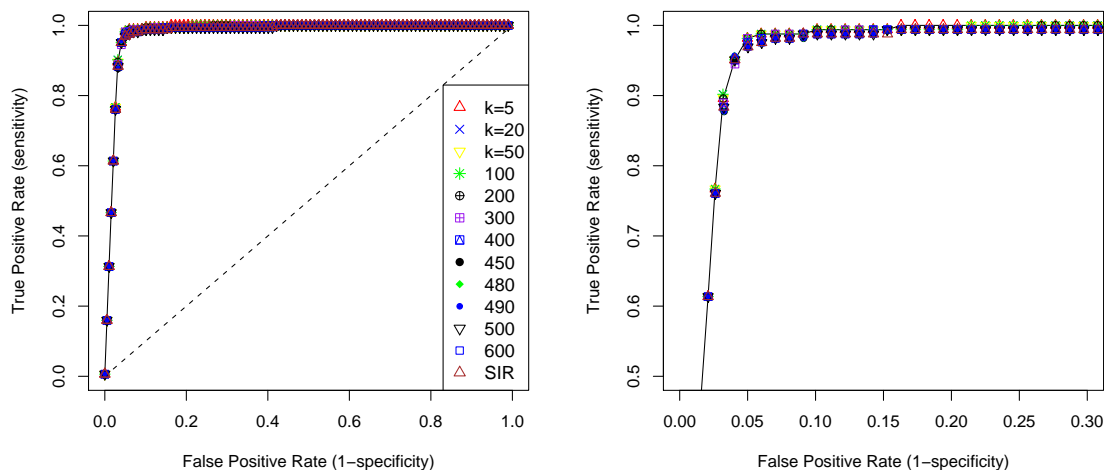
(b) Settings 2: $\mu_1 = -0.5$, $\mu_2 = 0.5$; $\sigma_1 = \sigma_2 = 1$, $\rho = 0.03$, $n = 5000$, $t = 50$

k	5	20	50	100	200	300
AUC	0.9710	0.9707	0.9707	0.9707	0.9703	0.9697
k	450	480	490	500	600	SIR
AUC	0.9683	0.9684	0.9684	0.9685	0.9685	0.9685



(a) ROC curve from L-SIR tune k for Setting 1 (b) Enlarge of a detail ROC curve from L-SIR

Figure 8.1: ROC curve of L-SIR for k equals to 5, 20, ..., 600 and SIR, the legend is illustrated in the figures for Setting 1 the variance difference



(a) ROC curve from L-SIR tune k for Setting 2 (b) Enlarge of a detail ROC curve from L-SIR

Figure 8.2: ROC curve of L-SIR for k equals to 5, 20,...,600 and SIR, the legend is illustrated in the figures for Setting 2 the mean difference

discussed in the following sections. Next we compare the performance of L-SIR to the other DR methods in our simulation studies.

8.5.3 Performance of Dimension Reduction (DR) Methods

Mean Difference in X

Our discussions in this part focus on mean difference in the descriptor set. We use $\sigma = 1$ for each class, and set the rare class as 1%, and the majority class as 99% to be comparable to drug discovery data. The regression is on X only. It is clear from the summary plot that two classes are separated along the first *dimension reduction direction* X_1 . Thus we sort the data along that direction, and claim the top and bottom 1% data points as one class. The rest in between are claimed as another

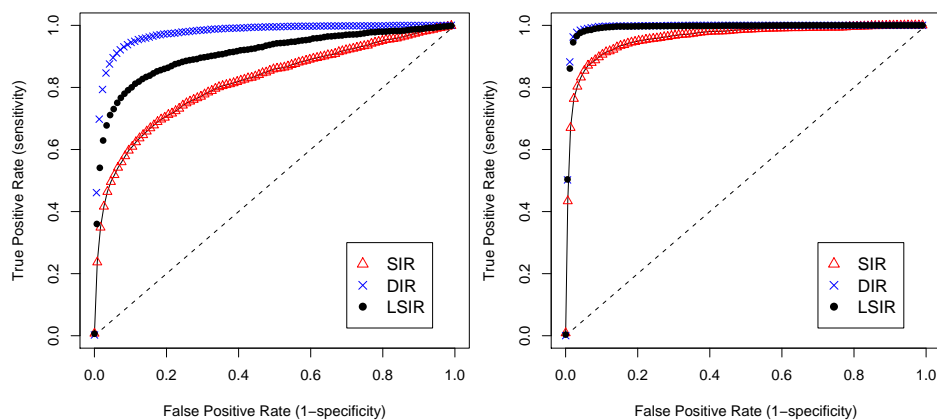
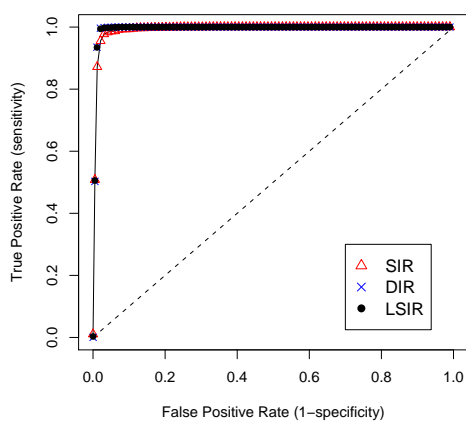
class. We list the AUCs in Table 8.3, and plot the ROC curves in Figure 8.3. From the ROC curves and the AUCs, we can see that when mean difference between the two classes gets larger than 1, all three DR methods work well. However, DIR seems to be more sensitive than L-SIR and SIR when the mean difference is smaller than 1. For $\mu = \pm 0.4$ case, DIR is better than the other two methods, while for $\mu = \pm 0.6$ case, the three ROC curves almost overlap with each other as seen in Figure 8.3.

Table 8.3: Mean difference settings and AUCs

Setup	AUC		
	SIR	DIR	L-SIR
$\mu_1 = -0.4, \mu_2 = 0.4$	0.8070	0.9636	0.8979
$\mu_1 = -0.5, \mu_2 = 0.5$	0.9499	0.9821	0.9806
$\mu_1 = -0.6, \mu_2 = 0.6$	0.9819	0.9841	0.9841

Variance difference in X

Herein we focus on variance difference in X for different classes. Our simulation setup is 1% for active class, and 99% for inactive class with $\mu_1 = \mu_2 = 0$. The regression is on X^2 . Similar to the previous discussion, we sort the data along the first *dimension reduction direction*, and claim the top and bottom 1% as the active class, all others as the inactive class. The standard deviation is: $\sigma_1 = 1$ for all cases, and $\sigma_2 = 1.3, 1.6, 2, 3, 5, 7$, respectively. The AUCs are listed in Table 8.4, and the ROC curves are depicted in Figure 8.5. From the AUCs and ROC curves, we can see that L-SIR is better than DIR and SIR on separation of variance difference. SIR and DIR have almost no separation, even worse than random guess (diagonal on ROC curve, and AUC is 0.5). With location information combined in the descriptor set, it is understandable that L-SIR is sensitive to variance difference. The summary

(a) $\mu = \pm 0.4$ (b) $\mu = \pm 0.5$ (c) $\mu = \pm 0.6$ Figure 8.3: ROC curve of SIR, DIR and L-SIR on X with mean difference

plots of SIR, DIR and L-SIR regression on X^2 are illustrated in Figure 8.4. One reason leading to the fail of SIR and DIR is the weak information of the active class. We increase the percentage in later discussion to see whether SIR and DIR have separation on variance difference.

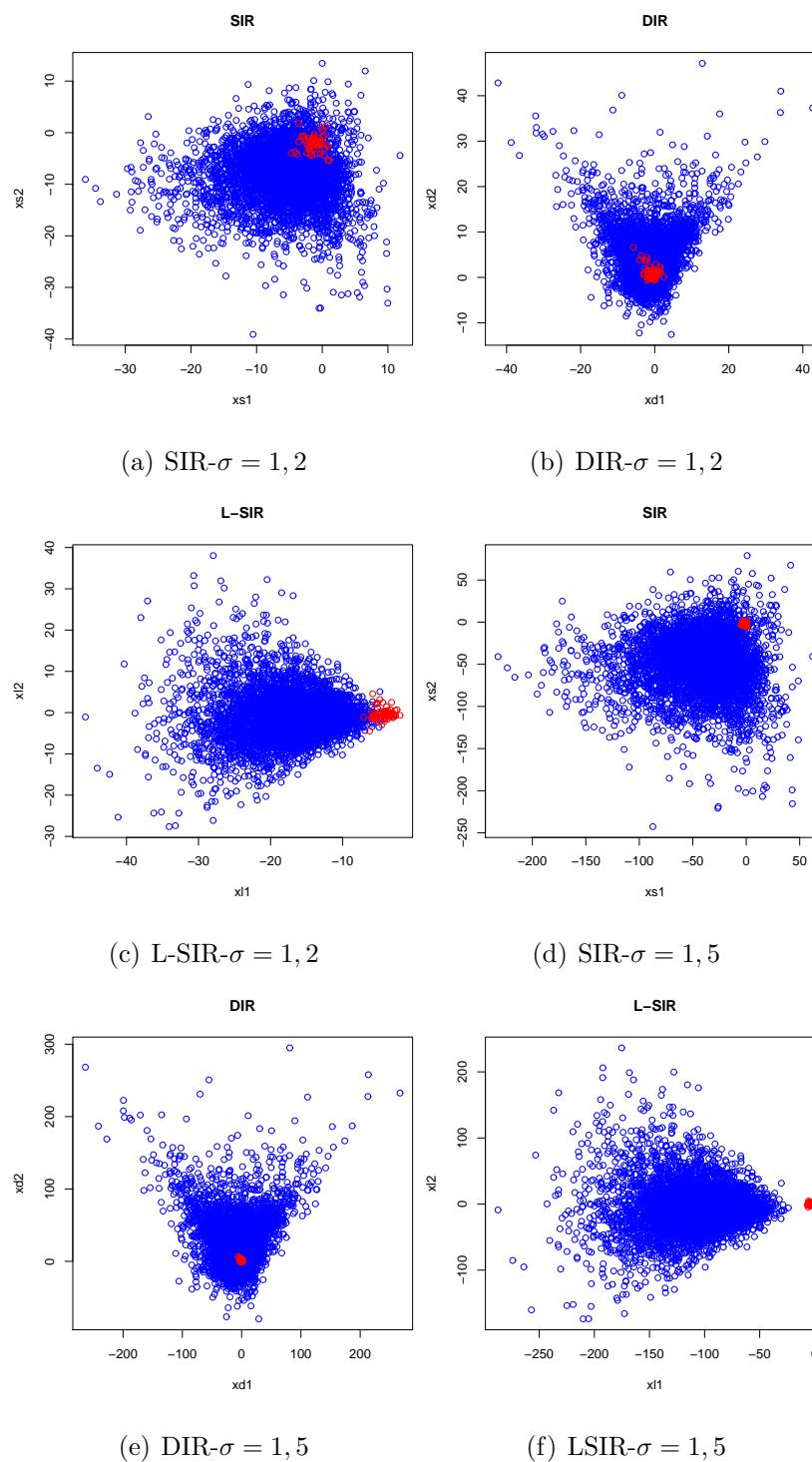


Figure 8.4: Summary plots of SIR, DIR and L-SIR on X^2 with variance difference. Blue dots represent inactive compounds, while red dots represent the active ones

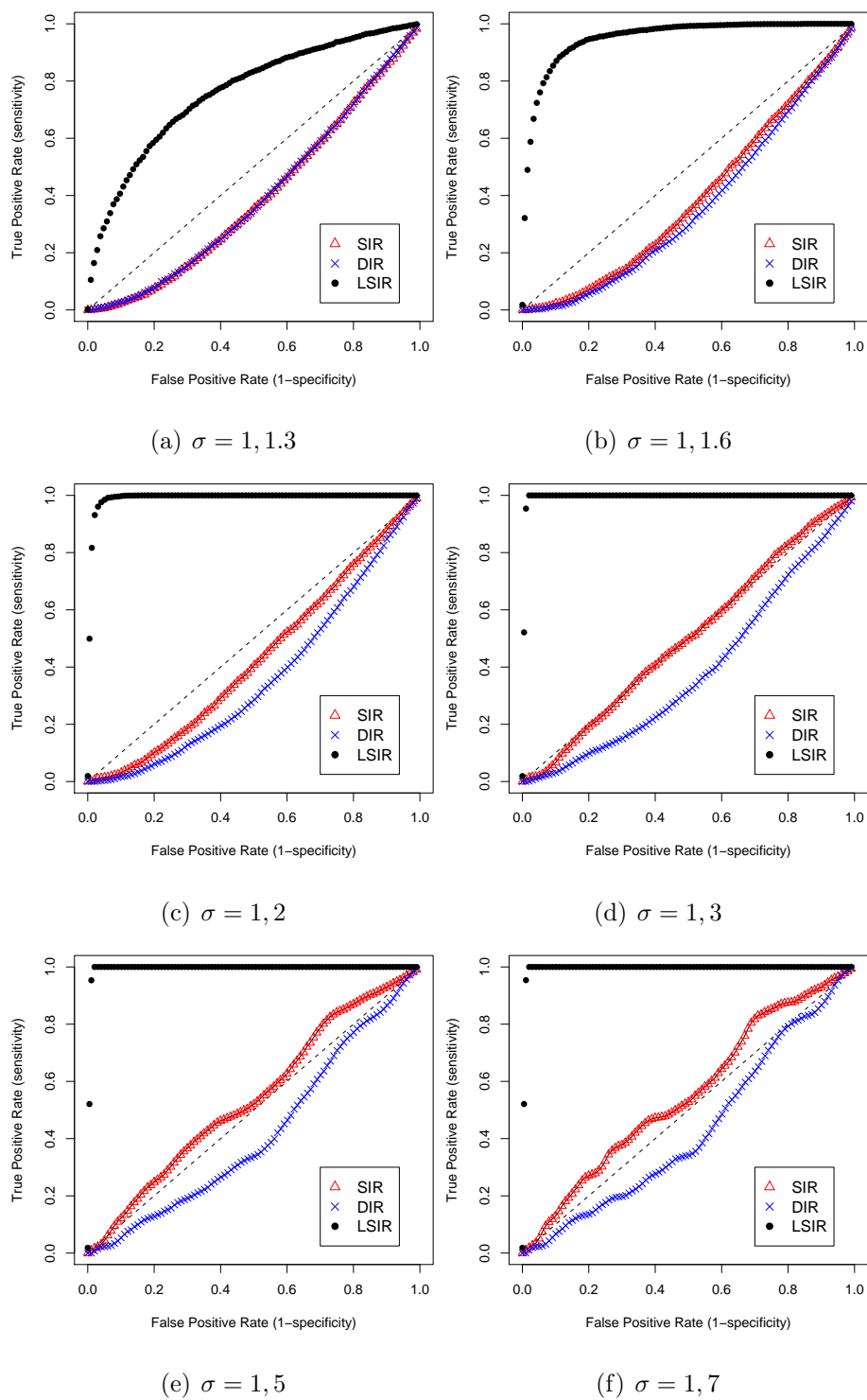


Figure 8.5: ROC curve of SIR, DIR and L-SIR on X^2 with variance difference

Table 8.4: Variance difference settings and AUCs

Setup	AUC		
	SIR	DIR	L-SIR
$\sigma_1 = 1, \sigma_2 = 1.3$	0.3860	0.3893	0.7519
$\sigma_1 = 1, \sigma_2 = 1.6$	0.3819	0.3572	0.9403
$\sigma_1 = 1, \sigma_2 = 2$	0.4191	0.3520	0.9813
$\sigma_1 = 1, \sigma_2 = 3$	0.4921	0.3772	0.9847
$\sigma_1 = 1, \sigma_2 = 5$	0.5330	0.4101	0.9847
$\sigma_1 = 1, \sigma_2 = 7$	0.5442	0.4214	0.9847

Both mean and variance difference in X

A more realistic case is that the distribution of X has different means and variances in different classes, and the regression is on X and X^2 . We set 1% active class, sort the data along the first dimension reduction direction, and claim the top and bottom 1% as one class. From the ROC curves (Figure 8.6) and the AUCs (Table 8.5), we can see that L-SIR is better than DIR and SIR for separation of unbalanced data when both mean and variance differences are involved.

Table 8.5: Mean and variance difference settings and AUCs

Setup	AUC		
	SIR	DIR	L-SIR
$\mu_1 = 0, \sigma_1 = 1, \mu_2 = 0.5, \sigma_2 = 2$	0.3648	0.3354	0.9823
$\mu_1 = 0, \sigma_1 = 1, \mu_2 = 0.5, \sigma_2 = 3$	0.3540	0.3170	0.9847
$\mu_1 = 0, \sigma_1 = 1, \mu_2 = 1, \sigma_2 = 2$	0.4082	0.3574	0.9838

To summarize our finding for 1% rare class case, of the three DR methods, DIR regression on X works the best for mean difference alone. SIR and L-SIR are also reasonably good when the mean difference is larger than 1. L-SIR is a promising method to separate classes with variance difference. It brings another issue, that is

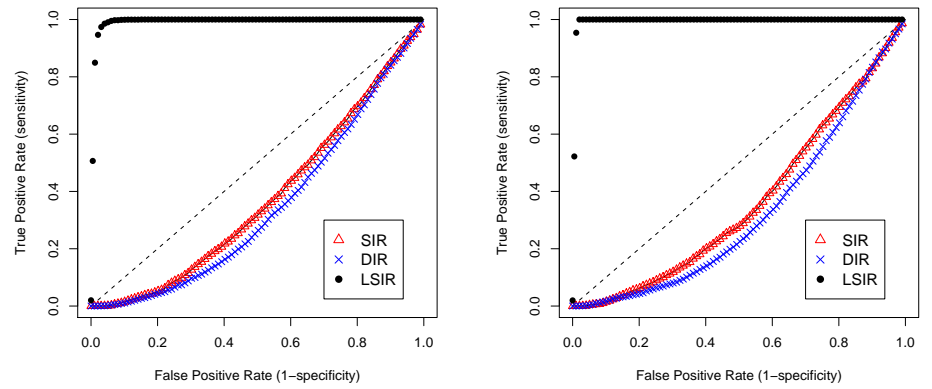
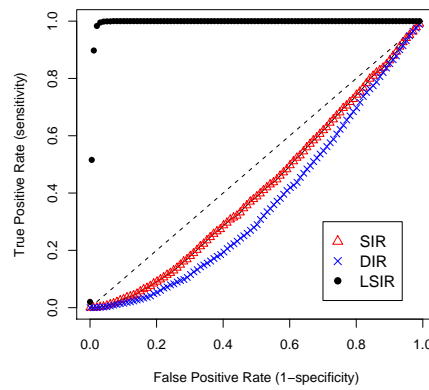
(a) $\mu_1 = 0, \sigma_1 = 1 \quad \mu_2 = 0.5, \sigma_2 = 2$ (b) $\mu_1 = 0, \sigma_1 = 1 \quad \mu_2 = 0.5, \sigma_2 = 3$ (c) $\mu_1 = 0, \sigma_1 = 1 \quad \mu_2 = 1, \sigma_2 = 2$

Figure 8.6: ROC curve of SIR, DIR and L-SIR on X and X^2 with mean and variance difference

when we have strong variance difference within each class, L-SIR may be the worst since the variance difference in each subclass may cover the classification information between classes.

Proportion variation

We have discussed our findings on three different setups in X for 1% active compounds and 99% inactive compounds. In this section, we present our simulation results on proportion variation of the active class of the above settings. Common sense is that the more balanced the data, the better separation we have, since we have more information for each class.

Our simulation setup and AUCs are summarized in Tables 8.6, 8.7 and 8.8 for mean difference, variance difference and both mean and variance difference, respectively. The corresponding ROC curves are illustrated in Figure 8.7, Figure 8.8 and Figure 8.9, respectively.

Table 8.6: Proportion variation for mean difference settings and AUCs

Setup	AUC		
	SIR	DIR	L-SIR
$\mu_1 = \pm 0.4, \rho = 0.01$	0.8070	0.9636	0.8979
$\mu_1 = \pm 0.4, \rho = 0.03$	0.9531	0.9601	0.9602
$\mu_1 = \pm 0.4, \rho = 0.05$	0.9447	0.9487	0.9507

Table 8.7: Proportion variation for variance difference settings and AUCs

Setup	AUC		
	SIR	DIR	L-SIR
$\sigma_1 = 1, \sigma_2 = 3, \rho = 0.01$	0.4921	0.3772	0.9847
$\sigma_1 = 1, \sigma_2 = 3, \rho = 0.03$	0.8521	0.5735	0.9742
$\sigma_1 = 1, \sigma_2 = 3, \rho = 0.05$	0.9472	0.6854	0.9631

From the Tables 8.6, 8.7, and 8.8 and ROC curves in Figure 8.7, Figure 8.8, and Figure 8.9, we can see that when only mean difference is involved in X , L-SIR and SIR almost overlap with DIR for higher proportion like 3%. However, when variance

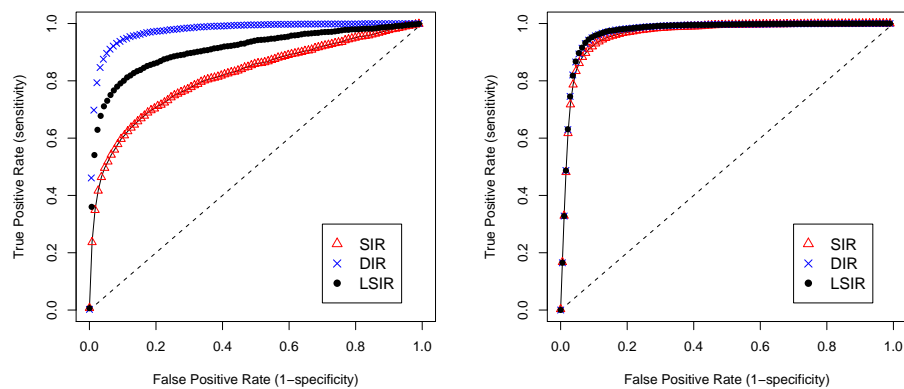
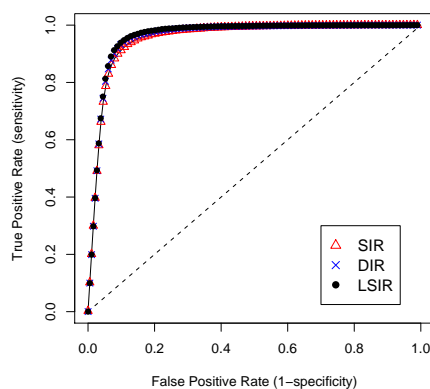
(a) $\mu = \pm 0.4, \rho = 0.01$ (b) $\mu = \pm 0.4, \rho = 0.03$ (c) $\mu = \pm 0.4, \rho = 0.05$

Figure 8.7: ROC curve of SIR, DIR and L-SIR on different proportion of mean difference

difference is involved, L-SIR always exceeds SIR and DIR for small proportion less than 5%. SIR has an increasing AUC along with percentage increasing, while DIR completely fails.

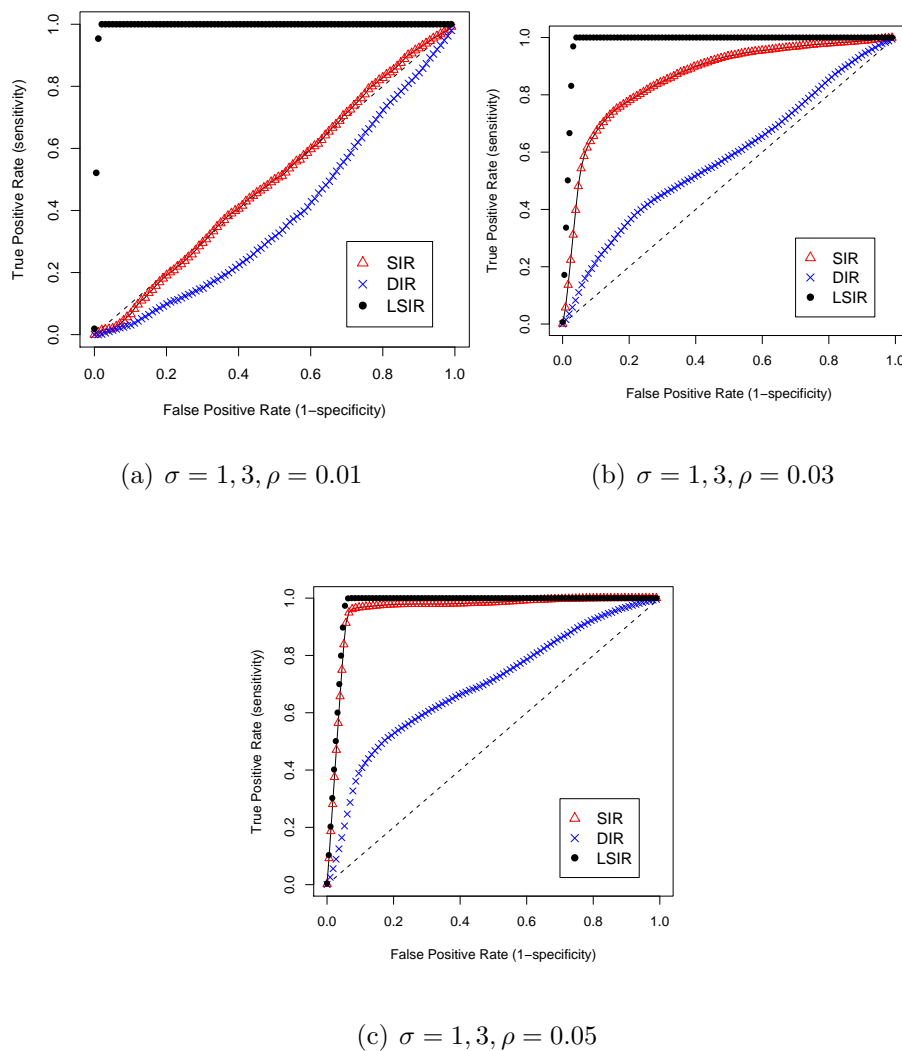


Figure 8.8: ROC curve of SIR, DIR and L-SIR on different proportion of variance difference

8.5.4 Comparison to Classical Clustering Methods

We run simulation studies on several settings as in Subsection 8.5.3 on Kmeans and model based clustering, and compare their classification results to L-SIR based clustering in this section. Our evaluation criteria is mean within group misclassifica-

Table 8.8: Proportion variation for both mean and variance difference settings and AUCs

Setup	AUC		
	SIR	DIR	L-SIR
$\mu = 0, 0.5, \sigma = 1, 2, \rho = 0.01$	0.3648	0.3354	0.9823
$\mu = 0, 0.5, \sigma = 1, 2, \rho = 0.03$	0.5596	0.3464	0.9717
$\mu = 0, 0.5, \sigma = 1, 2, \rho = 0.05$	0.7682	0.3868	0.9608

tion error rate. We list the classification results in Table 8.9. From the tables, we can see that ranking along L-SIR direction gives the best classification results with less than 0.1 mean within group misclassification error rate. Kmeans and model based clustering have better classification results on the reduced space than those on the original space for mean difference. L-SIR based ranking is the only method works on variance difference setting. However, if we have variance difference within the inactive class, which is a reasonable assumption in real data, L-SIR based ranking will lose its advantages.

Table 8.9: Mean Within Group Error Rate

Setup	L-SIR+rank	L-SIR+Kmeans	L-SIR+Mclust	Kmeans	Mclust
$\mu = \pm 0.5$ $\sigma = 1$ $\rho = 0.01$	0.0729	0.2407	0.0787	0.2983	0.3229
$\sigma_1 = 1$ $\sigma_2 = 3$ $\rho = 0.01$	0.0279	0.6807	0.6381	0.6290	0.7105
$\mu = \pm 0.5$ $\sigma = 1/3$ $\rho = 0.01$	0.0295	0.6880	0.6341	0.6222	0.3814

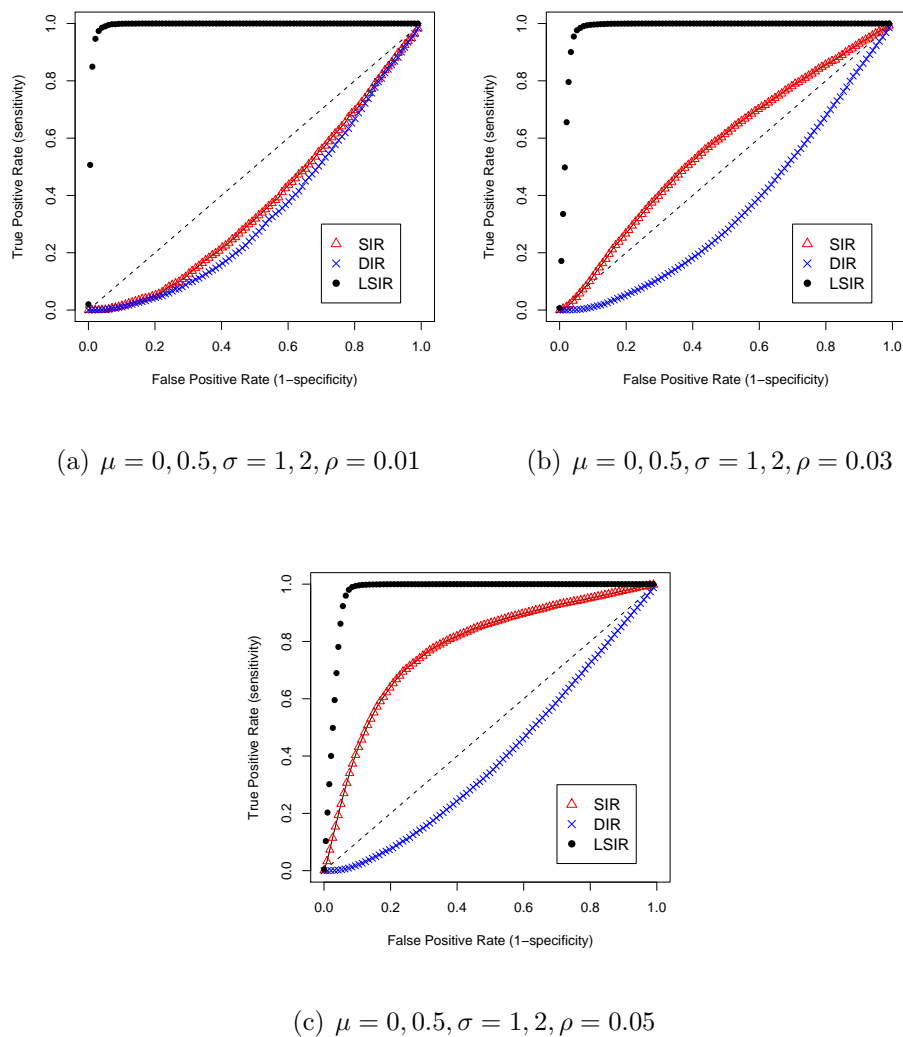


Figure 8.9: ROC curve of SIR, DIR and L-SIR on different proportion of mean and variance difference

8.6 XUE Data Investigation

XUE data is constructed based on 2017 real compound information. The descriptor X contains 8 compound properties and 24 WBNS. Response Y is a continuous descriptor of the compound activity. Within the 2017 compounds, 28 of them are

active compounds belonging to two different mechanisms ($W = 1$ and $W = 2$, 14 each). All other 1989 compounds are inactive ($W = 0$).

We examine the XUE data by DR based clustering. In our analysis, we use the $p = 24$ WBNs as our descriptor set, and perform dimension reduction to reduce it to two dimensions, which can be depicted by a summary plot. Then we cluster the data into 2 classes using Kmeans and model based clustering methods, and present the cluster result by *table*.

8.6.1 DR Based Clustering on XUE Data

We use SIR, DIR, and SAVE to perform dimension reduction on XUE data (the result of L-SIR is similar with that of SIR), and depict the summary plots in Figure 8.10. We run Kmeans and model based clustering on the reduced space. The clustering results are summarized in Table 8.10. We can see from Figure 8.10 that SIR separates all active compounds along the first *dimension reduction direction*. However, DIR and SAVE put the two subclasses along each of the first two *dimension reduction directions*. Thus the two subclasses have a better separation in DIR and SAVE than in SIR. This observation is consistent with Tables 8.10, 8.11, and 8.12.

Table 8.10 illustrates the result obtained from SIR. We can see that both Kmeans and Mclust classify the majority class reasonably well. Mclust has higher accuracy than Kmeans in the rare class, while both of them are around or higher than 50%. This is successful since the XUE data has complex data structure and weak separation information, i.e., only 1% active compounds with two different mechanisms. Tables 8.11 and 8.12 are the results for DIR and SAVE. We perform Kmeans and Mclust on the first two *dimension reduction directions* to ensure that we do not miss any information for active classes. Mclust has slightly better result than that of

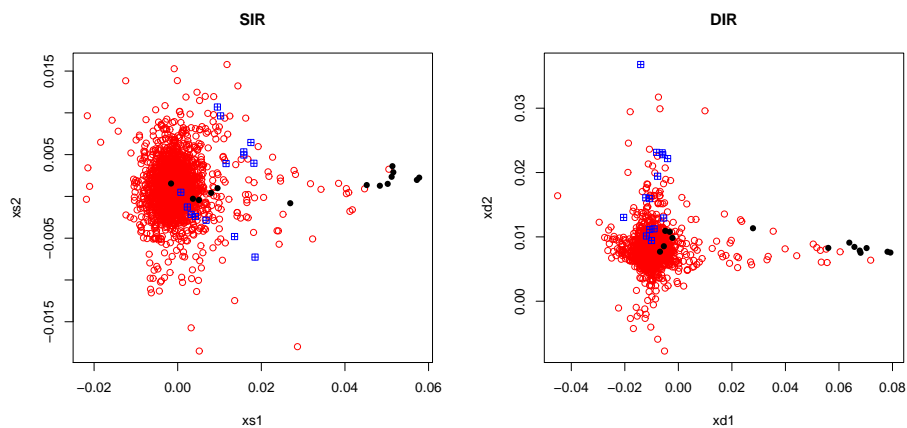
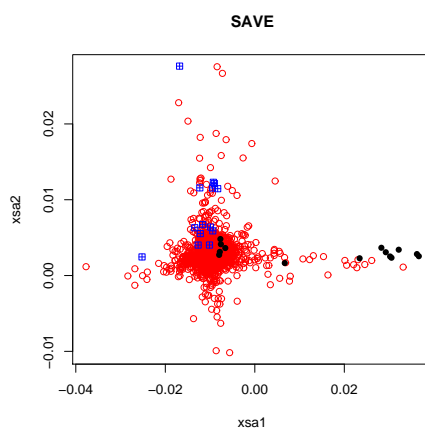
(a) SIR on X (b) DIR on X (c) SAVE on X

Figure 8.10: SIR, SAVE and DIR on X of XUE data. Red dots represent inactive compounds, blue and green dots represent active compounds of two different mechanisms.

Kmeans, and they both work reasonably well. We compare DR based clustering to clustering on original space, which is listed in Table 8.13, and find that by dimension reduction, we gain lots of calculation efficiency without losing classification accuracy.

Table 8.10: Kmeans and Mclust *table* of SIR on X along the first direction

(a) Kmeans along X_{s1}					(b) Mclust along X_{s1}				
		cid					cid		
W.hat		0	1	2	W.hat		0	1	2
	0	0.977	0.571	0.357		0	0.952	0.357	0.286
	1	0.023	0.429	0.643		1	0.048	0.643	0.714

Table 8.11: Kmeans and Mclust *table* of DIR on X along the first two directions

(a) Kmeans along X_{d1}					(b) Mclust along X_{d1}				
		cid					cid		
W.hat		0	1	2	W.hat		0	1	2
	0	0.987	1.000	0.357		0	0.950	0.929	0.357
	1	0.013	0.000	0.643		1	0.050	0.071	0.643

(c) Kmeans along X_{d2}					(d) Mclust along X_{d2}				
		cid					cid		
W.hat		0	1	2	W.hat		0	1	2
	0	0.958	0.286	1.000		0	0.932	0.286	1.000
	1	0.042	0.714	0.000		1	0.068	0.714	0.000

Table 8.12: Kmeans and Mclust *table* of SAVE on X along the first two directions

(a) Kmeans along X_{sa1}					(b) Mclust along X_{sa1}				
		cid					cid		
W.hat		0	1	2	W.hat		0	1	2
	0	0.986	1.000	0.357		0	0.933	0.857	0.357
	1	0.014	0.000	0.643		1	0.067	0.143	0.643

(c) Kmeans along X_{sa2}					(d) Mclust along X_{sa2}				
		cid					cid		
W.hat		0	1	2	W.hat		0	1	2
	0	0.977	0.571	1.000		0	0.948	0.357	1.000
	1	0.023	0.429	0.000		1	0.052	0.643	0.000

Table 8.13: Kmeans and Mclust *table* on Original Space

(a) Kmeans on XUE					(b) Mclust on XUE				
cid					cid				
W.hat		0	1	2	W.hat		0	1	2
	0	0.645	0.786	0.214		0	0.654	0.071	0.357
	1	0.355	0.214	0.786		1	0.346	0.929	0.643

XUE data has three classes, and two of them are active classes with different regression relationships, while our previous discussions focus on two-class situation. We delete one active class, and analyze the rest two classes. We compare the classification result of DR based clustering to clustering on the original space of the two-class XUE data. We use DIR in our simulation to avoid the underlying variance difference in the subclass, and use mean within group misclassification error rate as the comparison criterion. We sort the data along the direction with better separation, and compare the classification result to clustering on the original space. The results are listed in Table 8.14. From Table 8.14, we can see that DIR based Kmeans and DIR based Mclust have better classification result than Kmeans and Mclust on the original space. However, DIR based ranking does not obtain a similar result due to the underlying differences in the subclasses.

Table 8.14: Mean Within Group Error Rate

Setup	DIR+rank	DIR+Kmeans	DIR+Mclust	Kmeans	Mclust
class 1,0	0.3275	0.1975	0.1610	0.5695	0.2030
class 2,0	0.2555	0.1840	0.1610	0.2835	0.3800

8.6.2 Cross Validation

We perform cross validation on XUE data to evaluate our method. There is only 1% active compounds in XUE data, thus we set up the cross-validation as follows.

1. Randomly select 50% of the noise compounds as the training set, and keep the rest in the testing set.
2. Use all the active compounds in both training set and testing set.

We utilize three DR methods on the training set to obtain the *dimension reduction directions*. Then we cluster the training set along the first two *dimension reduction directions* by both Kmeans and model based clustering. Next, we apply the *dimension reduction directions* and the center of each class observed from the training set on the testing set, and obtain the classification results. We run this cross-validation 10 times to reduce statistical error. The results are summarized in Tables 8.15, 8.16, and 8.17 for SIR, DIR, and SAVE, respectively.

Table 8.15: Cross-validation *table* of SIR on X along the first direction

(a) Kmeans on X_{s1}, X_{s2} for the training

set	cidr			
W.hat	0	1	2	
	0	0.9	0.329	0.214
	1	0.1	0.671	0.786

(b) Mclust on X_{s1}, X_{s2} for the training set

	cidr			
W.hat	0	1	2	
	0	0.756	0.407	0.379
	1	0.244	0.593	0.621

(c) Kmeans on X_{s1}, X_{s2} for the testing set

	cids			
W.hat	0	1	2	
	0	0.904	0.321	0.2
	1	0.096	0.679	0.8

(d) Mclust on X_{s1}, X_{s2} for the testing set

	cids			
W.hat	0	1	2	
	0	0.747	0.4	0.386
	1	0.253	0.6	0.614

Table 8.16: Cross-validation *table* of DIR on X along the first direction

(a) Kmeans on X_{d1}, X_{d2} for the training set					(b) Mclust on X_{d1}, X_{d2} for the training set				
set					set				
cidr					cidr				
W.hat		0	1	2	W.hat		0	1	2
	0	0.942	0.7	0.429		0	0.93	0.4	0.343
	1	0.058	0.3	0.571		1	0.07	0.6	0.657

(c) Kmeans on X_{d1}, X_{d2} for the testing set					(d) Mclust on X_{d1}, X_{d2} for the testing set				
cids					cids				
W.hat		0	1	2	W.hat		0	1	2
	0	0.939	0.829	0.364		0	0.839	0.429	0.393
	1	0.061	0.171	0.636		1	0.161	0.571	0.607

Table 8.17: Cross-validation *table* of SAVE on X along the first direction

(a) Kmeans on X_{sa1}, X_{sa2} for the training set					(b) Mclust on X_{sa1}, X_{sa2} for the training set				
cidr					cidr				
W.hat		0	1	2	W.hat		0	1	2
	0	0.861	0.686	0.521		0	0.744	0.393	0.414
	1	0.139	0.314	0.479		1	0.256	0.607	0.586

(c) Kmeans on X_{sa1}, X_{sa2} for the testing set					(d) Mclust on X_{sa1}, X_{sa2} for the testing set				
cids					cids				
W.hat		0	1	2	W.hat		0	1	2
	0	0.881	0.764	0.521		0	0.916	0.414	0.357
	1	0.119	0.236	0.479		1	0.084	0.586	0.643

The classification results on the testing set have higher than 60% accuracy. It is a reasonably good result for XUE data which has complicated underlying data structure and 1% active compounds. The cross-validation results assure that our method, which combines dimension reduction, such as SIR, DIR, and SAVE, and clustering, including Kmeans and model based clustering, is effective in high dimensional unbalanced data

classification.

8.7 Concluding Remarks

Corresponding to the challenges in drug discovery data, i.e., an unbalanced mixture regression problem with high dimensional correlated descriptor set, we propose dimension reduction based clustering methods to model it. Our standing point is that dimension reduction can reduce the high dimensional descriptor set into its low dimension central space without losing regression information. The reduced space contains the direction that separates the two classes as well as the direction that describes the underlying structure in the active class. We introduce 4 sufficient DR methods and 2 classical clustering methods. Ranking along the dimension reduction direction is proposed to cluster the data.

Our simulation study is devoted to the following three parts. We tune parameter k in L-SIR to find a certain range of k for good performance. We investigate the DR methods and clustering methods to see their performance on different settings. We also compare the performance of DR based clustering versus clustering on the original space. Our findings of the numerical studies can be summarized in the following points.

First, choice of k is flexible within a certain range. When set k close to the number in each slices, L-SIR converges to SIR. The smaller k is, the more sensitive L-SIR is to local information. By incorporating the local information in it, L-SIR is sensitive to variance difference setting.

Second, of the 3 DR methods, i.e., SIR, DIR, and L-SIR, DIR is the most sensitive to mean difference under extreme conditions. Here the extreme condition means less

than 2% for the rare class or mean difference smaller than 1 while variance is 1. L-SIR is slightly better than SIR under the extreme condition. All three methods work well when mean difference is larger than 1. L-SIR is the only DR method that has differentiation with variance difference setting under the Gaussian mixture model.

Third, ranking along the appropriate DR directions give the best classification result for our Gaussian mixture model with both mean and variance differences. DR based clustering works better in general than clustering on the original space in our simulation study. For model based clustering method, clustering on the reduced space is a lot faster than on the original space.

The investigation on XUE data are carried out in three parts. First we try to understand the data structure by comparing all DR methods and clustering methods, we find that DIR works the best for XUE data due to the underlying variance difference in the inactive class. Then we compare the DIR based clustering versus clustering on the original space to find that DIR based Kmeans and Mclust performs better than on the original space, while ranking along DIR direction does not have a comparable result as that of Kmeans and Mclust. The cross validation result further supports that DR based clustering is a good method for modeling drug discovery data.

Chapter 9

Boosting Method for Unbalanced Data Classification

9.1 Introduction

Class imbalance problem can be interpreted in two aspects: the unbalanced class distribution and the non-uniform misclassification costs. Corresponding to these two aspects, our solution method can be described at the data level and the algorithm level. At the data level, the objective is to re-balance the class distribution by resampling the data space. At the algorithm level, existing classifier learning algorithms are adapted to strengthen learning with regard to the small class. Data level method, i.e., resampling the data by over sampling the rare class or under sampling the major class, does not work well for drug discovery problem, since the rare class may only contribute less than 5% of the total population. However, from the algorithm level, we can increase the misclassification costs of the data in the rare class and minimize the high cost errors. This is equivalent to increasing class weight for the rare class.

In this chapter, the focus of our research work is the development of boosting method for solving class imbalance problem. Boosting method was first proposed in the computational learning theory literature ([40],[41],[42]). It is an important classification methodology. Boosting works by sequentially applying a classification

algorithm to reweighted versions of the training data and then taking a weighted majority vote of the sequence of classifiers thus produced [43]. This simple strategy results in great improvements in performance for many classification algorithms.

Yanmin Sun ([44],[45]) improved Adaboost algorithms by including the misclassification costs into the weight update formula. The new method is called cost-sensitive Adaboost, and the essence of the new method is to increase the misclassification costs of the minority class. Even though cost-sensitive Adaboost gains efficiency in finding the rare class, in Yanmin Sun's paper, they did not provide a good criterion to determine the best misclassification cost to add on the minority class, neither did they pick the best way of including the misclassification costs of the three cost-sensitive Adaboost methods they proposed. Our work in this chapter provides theoretical discussion on the best way of adding unequal class weights, and proves that if we add a class weight reciprocal to the percentage of that class, the classification result reaches the theoretical minimum misclassification error rate, i.e., the Bayes rule. Hereafter we use class weight rather than misclassification cost, since it is more intuitive in discussion, and we can easily transform class weight to misclassification cost mathematically.

The following of this chapter is organized as follows. In Section 9.2, we introduce Adaboost algorithm, and its connection with minimizing exponential loss through forward stagewise additive modeling. The weighted Adaboost algorithm, which adds a class weight reciprocal to the percentage of that class, is presented in Section 9.3. We briefly introduce gradient boosting and negative binomial log-likelihood, as well as the weighted version of gradient boosting in Section 9.4. In order to compare the performance of Adaboost and weighted Adaboost, we run simulation studies and a real data application in Section 9.5 and Section 9.6, respectively. Our numerical

studies show that weighted Adaboost has good detection rate on the rare class, while Adaboost sometimes completely fails. Finally, we wrap up the chapter by a brief summary in section 9.7.

9.2 AdaBoost and Exponential Loss

AdaBoost procedure is first proposed by Freund and Schapire in 1996 [46] for binary data classification. Assume training set $(x_1, y_1), \dots, (x_N, y_N)$ with x_i , which is a vector valued feature, and $y_i = 1$ or -1 . The classification rule of Adaboost is $F(x) = \text{sign}(\sum_1^M \alpha_m f_m(x))$ where each $f_m(x)$ is a weak classifier producing prediction taking one of the two values, $\{-1, 1\}$, and α_m is a constant for each boosting step which we will discuss in detail later. The error rate on the training set is $\overline{err} = \frac{1}{N} \sum_{i=1}^N (I(y_i \neq G(x_i)))$, and the expected error rate on future prediction is $E_{XY} = I(Y \neq G(X))$.

The algorithm of Adaboost can be described as follows.

1. Initialize the observation weights, $w_i = 1/N, i = 1, \dots, N$
2. For $m = 1, \dots, M$,
 - a) Fit a classifier $f_m(x)$ to the training data using weights w_i^m
 - b) Compute error rate $err_m = \frac{\sum_{i=1}^N w_i I(y_i \neq f_m(x_i))}{\sum_{i=1}^N w_i^m}$
 - c) Compute $\alpha_m = \log \frac{1-err_m}{err_m}$
 - d) Set $w_i^{m+1} = w_i^m \cdot \exp[\alpha_m I(y_i \neq f_m(x_i))]$
3. Output $F(x) = \text{sign}[\sum_{i=1}^M \alpha_m f_m(x)]$

To describe the procedure in detail, Adaboost first runs an equal weight classification, and gets a misclassification error rate, denoted by $err_m = \frac{\sum_{i=1}^N w_i I(y_i \neq f_m(x_i))}{\sum_{i=1}^N w_i^m}$, where w_i is the weight on the i th observation, and m is the number of boosting steps. Then it updates class weight by $w_i^{m+1} = w_i^m \cdot \exp[\alpha_m I(y_i \neq f_m(x_i))]$ for each observation, where $\alpha_m = \log \frac{1-err_m}{err_m}$. For each boosting step, Adaboost fits a weighted classifier, $f_m(x)$, to the training data set using weights w_i^m corresponding to each observation. The final classification rule is $F(x) = \text{sign}[\sum_1^M \alpha_m f_m(x)]$. Adaboost algorithm works by adding a larger weight on those data points which are classified in the wrong class from the previous step, and reducing weight on data points which are correctly classified. Through the iteration process, data points which are difficult to classify receive an ever-increasing influence. Each classifier thus is forced to concentrate on those training observations which are misclassified by previous steps.

The success of Adaboost is theoretically supported by minimizing exponential loss through forward stagewise additive modeling.

9.2.1 Additive Model

We consider the additive regression models (ARMs) (Hastie and Tibshirani, 1986) [47]. Let the response variable $y_i = \{1, -1\}$ be the i th observation of n observation units ($i = 1, \dots, n$). We assume y_i s are independent. The data also consists of p covariates $\{t_{i1}, \dots, t_{ip}\}$. The additive regression models have the following form $y_i = \beta_0 + f_1(t_{i1}) + f_2(t_{i2}) + \dots + f_p(t_{ip}) + \epsilon_i$, where β_0 represents a scalar intercept, and $f_j(t)$'s ($j = 1, \dots, p$) are arbitrary smooth functions associated with covariates t_{ij} , respectively. The error term ϵ_i is usually assumed to be independent and identically distributed from normal distribution $N(0, \sigma_\epsilon^2)$. The above expression provides a general modeling formulation, where additivity is the only assumption made for the

relationship between the response variable and the covariates.

A common way to fit the above additive model is to minimize a certain penalized sum of squares by an iterative fitting method, such as back-fitting algorithm and forward stagewise additive modeling. A forward stagewise modeling approximates the solution to an additive model by sequentially adding new basis functions to the expansion without adjusting the parameters and coefficients of those that have already been added. The forward stagewise additive modeling algorithm can be described as follows ([38]):

Step 1. Initialize $f_0(x) = 0$.

Step 2. For $m = 1$ to M :

1. Compute $(\beta_m, \gamma_m) = \arg \min_{\beta, \gamma} \sum_{i=1}^N L(y_i, f_{m-1}(x_i) + \beta b(x_i; \gamma))$,
2. Set $f_m(x) = f_{m-1}(x) + \beta_m b(x, \gamma_m)$.

At each iteration, an optimal basis function $b(x, \gamma_m)$ and the corresponding coefficient β is added to the current expansion $f_{m-1}(x)$. Through this iteration process, we fit all parameters by minimizing the loss function.

9.2.2 Adaboost versus Forward Stagewise Additive Modeling

Denote the exponential loss as $L(Y, F(X)) = \exp[-YF(X)]$, where $Y = \{1, -1\}$ is the class indicator. We follow the forward stagewise additive modeling algorithm in Section 9.2.1 to find the minimizer of the exponential loss,

$$(\beta_m, f_m(X)) = \arg \min_{\beta, f} \sum_{i=1}^N \exp\{-y_i [F_{m-1}(x_i) + \beta_m f_m(x_i)]\}. \quad (9.1)$$

Denote the weight function of the m th step as follows,

$$w_i^m = \exp[-y_i F_{m-1}(x_i)], \quad (9.2)$$

and substitute w_i^m in equation 9.1, we can rewrite the equation in the following format,

$$(\beta_m, f_m(X)) = \arg \min_{\beta, f} \sum_{i=1}^N w_i^m \exp[-y_i \beta_m f_m(x_i)]. \quad (9.3)$$

For our classification problem, y_i and $f(x_i)$ are both class indicators that belong to $\{1, -1\}$. We separate the loss function in equation (9.3) into two cases, one is that the real class information is consistent with prediction from our classifier, the other one is not consistent with our prediction. Then equation (9.3) can be simplified as follows,

$$\begin{aligned} & \sum_{y_i=f(x_i)} w_i^m e^{-\beta} + \sum_{y_i \neq f(x_i)} w_i^m e^{\beta} \\ &= \sum_{i=1}^N (e^{\beta} - e^{-\beta}) I(y_i \neq f(x_i)) w_i^m + \sum_{i=1}^N w_i^m e^{-\beta}. \end{aligned} \quad (9.4)$$

There are two unknown parameters, i.e., β and $f(x)$. We minimize the loss function in equation (9.4) by varying these two parameters. We do it in two steps. First we fix β and minimize the loss function by varying $f(x)$, after we find a solution of $f(x)$, we take the loss function as a function of β alone, and find the solution for β . We can see that the second summation in (9.4) is not related to $f_m(X)$. Thus we only need to consider the first part to minimize the exponential loss. Without loss of generosity, we assume $\beta > 0$, then the solution is $f_m(X) = \arg \min_f \sum_{i=1}^N w_i^m I(y_i \neq f(x_i))$, which is Bayes Rule under unequal weights which we will discuss later in this chapter. Now we consider (9.4) as a function of β , denoted by $l(\beta)$, then the minimizer of $l(\beta)$ can

be obtained by solving the following partial differential equation:

$$\frac{\partial l(\beta_m)}{\beta_m} = (e^{\beta_m} + e^{-\beta_m}) \sum_{i=1}^N w_i^m I(y_i \neq f(x_i)) + \sum_{i=1}^N w_i^m e^{-\beta_m} = 0. \quad (9.5)$$

We can rewrite the above equation as

$$(e^{2\beta} + 1) = \frac{\sum_{i=1}^N w_i^m}{\sum_i w_i^m I(y_i \neq f(x_i))}.$$

The error rate of the m th step is

$$err_m = \frac{\sum_i w_i^m I(y_i \neq f(x_i))}{\sum_{i=1}^N w_i^m},$$

then β only depends on the error rate of each iteration step, and is one half α , where α is a coefficient in Adaboost algorithm,

$$\beta_m = \frac{1}{2} \log \frac{1 - err_m}{err_m} = \frac{1}{2} \alpha_m.$$

Since y_i and $f_m(x_i)$ are both class indicators and both belong to $\{1, -1\}$, the following equation $-y_i f_m(x_i) = 2I(y_i \neq f(x_i)) - 1$ stands. Thus the weight update function for the forward stagewise additive modeling (9.2) is

$$w_i^{m+1} = w_i^m \exp[-y_i \beta_m f_m(x_i)] = w_i^m \exp[\alpha_m I(y_i \neq f_m(x_i))] \exp[-\beta_m],$$

where $\exp[-\beta_m]$ is a constant in the m th boosting step and can be canceled out if we normalize the weight.

From the above discussion, $F(X)$ that minimizes the exponential loss by forward stagewise additive modeling is in the following format,

$$F(X) = \sum_{m=0}^M \beta_m f_m(X). \quad (9.6)$$

For classification problem, the classification rule will be

$$F(X) = \text{sign}\left[\sum_{m=0}^M \beta_m f_m(X)\right]. \quad (9.7)$$

Compare (9.6) and (9.7) to the AdaBoost algorithm in the previous section, we can see that, each $f_m(X)$ from the additive modeling is the fitted classifier using the training data in the m th step; the coefficient in the weight update step in Adaboost and forward stagewise additive modeling has the following relationship, $\alpha_m = 2\beta_m$; the observation weights are updated using the same formula; finally, the final classification rule is the same. Thus we can conclude that AdaBoost minimizes exponential loss through forward stagewise additive modeling.

On the other hand, we can prove the following lemma which describes the property of the minimizer of exponential loss.

Lemma 9.1. *The minimizer of exponential loss $E\{\exp[-YF(X)]\}$ is one half log odds, i.e.,*

$$F(X) = \arg \min_F \left(E\{\exp[-YF(X)]\} \right) = \frac{1}{2} \log \left[\frac{P(Y = 1|X)}{P(Y = -1|X)} \right].$$

Proof.

$$\begin{aligned} \arg \min_F \left(E\{\exp[-YF(X)]\} \right) &= \arg \min \left(E_{Y|X}\{\exp[-YF(X)]\} \right) \text{ for every } X \\ E_{Y|X}\{\exp[-YF(X)]\} &= P(Y = 1|X) \exp[-F(X)] + P(Y = -1|X) \exp[F(X)] \\ \Rightarrow \frac{\partial E_{Y|X}\{\exp[-YF(X)]\}}{\partial F(X)} &= -P(Y = 1|X) \exp[-F(X)] + P(Y = -1|X) \exp[F(X)] = 0 \\ \Rightarrow \exp[2F(X)] &= \frac{P(Y=1|X)}{P(Y=-1|X)} \\ \Rightarrow F(X) &= \frac{1}{2} \log \left[\frac{P(Y=1|X)}{P(Y=-1|X)} \right]. \end{aligned}$$

□

Lemma (9.1) indicates that the final classifier of AdaBoost has the same sign as that of the log odds, expressed in equation (9.8).

$$\text{sign}[F(x)] = \begin{cases} 1 & \text{when } P(Y = 1|X) > P(Y = -1|X), \\ -1 & \text{when } P(Y = 1|X) < P(Y = -1|X). \end{cases} \quad (9.8)$$

(9.8) follows the general Bayes rule.

From our discussion above, the following proposition stands.

Proposition 9.1. *The classifier of Adaboost satisfies Bayes rule if the base learner satisfies Bayes rule.*

If we use a base learner which satisfies the Bayes rule, such as classification tree and SVM, we can get a classifier that meets the theoretical minimum overall misclassification error rate through AdaBoost algorithm.

The connection between boosting and minimization of exponential loss through forward stagewise additive modeling explains the good performance of boosting as a good classification method in general. However, the same conclusion cannot be generalized to our drug discovery problem easily. Because of the extremely unbalanced nature, overall misclassification error rate fails to select the good classification methods. Thus the Bayes rule in general case is not a good classification rule any more. Imagine that we have a data set with 2% active compounds, such that $P(Y = 1|X) = 0.02$, and $P(Y = -1|X) = 0.98$. In this case, from Bayes rule, all compounds will be classified to the majority class with only 2% overall misclassification error rate. Thus the overall misclassification error rate as a classification criterion completely fails in detecting the rare class of drug discovery problem, and we need a new criterion to compare the performance of different classification methods on unbalanced data classification.

9.3 Weighted Adaboost

For better performance in unbalanced data classification, a different approach is proposed to increase the weight of the rare class, i.e., cost-sensitive boosting. In

Yanmin Sun *et al.*'s paper, they proposed three cost-sensitive Adaboost by including misclassification cost inside the exponent, outside the exponent, and both inside and outside the exponent. However, they neither gave any reasoning on why they did it in this way, nor did they provide a way of predicting a reasonable misclassification cost. In the following of this section, we introduce our criteria in comparing different classification methods of unbalanced data classification. We follow the forward stagewise additive modeling algorithm to find the minimizer of an unequal weighted exponential loss, and propose two weighted Adaboost algorithms. In our weighted Adaboost algorithms, we add the unequal weights in two ways, i.e., inside the exponent and outside the exponent. We use a class weight reciprocal to the proportion of that class in our sample, and prove that the weighted Adaboost using the reciprocal class weight gives the minimized average misclassification error rate, i.e., it satisfies Bayes rule under unequal weights.

9.3.1 Mean Within Group Error Rate

Classic classification criterion, i.e., overall misclassification error rate completely fails in detecting the rare class, thus is not a good criterion to compare the performance on unbalanced data classification problem. Mean within group error rate is proposed in Xingye Qiao's paper [48] to remedy the fail of overall misclassification error rate on unbalanced data classification. Misclassification error rate is calculated separately in each class, and their average is mean within group error rate. Mean within group error rate can be calculated as $(1 - \text{sensitivity} - \text{specificity})/2$ for binary classification, where sensitivity and specificity can be calculated from the contingency table. The classification rule corresponding to mean within group error rate will put more emphasis on the rare class comparing to the classic classification criterion. The

Bayes rule for k class classification under the mean within group error rate criteria is expressed as

$$\phi_B(x) = \arg \min_i \sum_{l=1}^k (p_l(x) \overline{\delta_{il}}) / \pi_i = \arg \max_i \sum_{l=1}^k (p_l(x)) / \pi_l. \quad (9.9)$$

Hereinafter we define Equation (9.9) as the weighted Bayes rule.

9.3.2 Weighted Adaboost-1

Similar to Yanmin Sun's paper, we include the unequal class weight inside the exponent, and name it weighted Adaboost-1. We use a class weight inversely proportional to the class proportion, and define the unequal weighted loss function as

$$L(Y, F(X)) = \exp \left[-Y F(X) \left(\frac{I(Y=1)}{\pi} + \frac{I(Y=-1)}{1-\pi} \right) \right],$$

where π is the proportion of $Y = 1$ class. Then we minimize the loss function following forward stagewise additive modeling,

$$(\beta_m, f_m(x)) = \arg \min_{\beta, f} \sum_{i=1}^N \exp \left\{ \left(-\frac{I(y_i=1)}{\pi} + \frac{I(y_i=-1)}{1-\pi} \right) [F_{m-1}(x_i) + \beta f(x_i)] \right\}. \quad (9.10)$$

Similar to Adaboost, we denote weight function as

$$w_i^m = \exp \left[\left(\frac{-I(y_i=1)}{\pi} + \frac{I(y_i=-1)}{1-\pi} \right) F_{m-1}(x_i) \right],$$

and replace w_i^m in equation (9.10) to get

$$(\beta_m, f_m(x)) = \arg \min_{\beta, f} \sum_{i=1}^m w_i^m \cdot \exp \left[\left(-\frac{I(y_i=1)}{\pi} + \frac{I(y_i=-1)}{1-\pi} \right) \right] \cdot \beta f(x_i).$$

We rewrite the above equation as follows, and solve it in two steps similar to Adaboost.

$$\begin{aligned}
& \sum_{i=1}^N w_i^m \cdot \exp \left[\left(-\frac{I(y_i = 1)}{\pi} + \frac{I(y_i = -1)}{1 - \pi} \right) \cdot \beta_m f_m(x_i) \right] \\
&= \sum_{y_i=-1} w_i^m e^{\frac{\beta_m f(x_i)}{1-\pi}} + \sum_{y_i=1} w_i^m e^{-\frac{\beta_m f(x_i)}{\pi}} \\
&= \sum_{y_i=f(x_i)=-1} w_i^m e^{-\frac{\beta_m}{1-\pi}} + \sum_{y_i=-1, f(x_i) \neq y_i} w_i^m e^{\frac{\beta_m}{1-\pi}} + \sum_{y_i=f(x_i)=1} w_i^m e^{-\frac{\beta_m}{\pi}} + \sum_{y_i=1, f(x_i) \neq y_i} w_i^m e^{\frac{\beta_m}{\pi}} \\
&= \sum_{y_i=f(x_i)} w_i^m \left[e^{-\frac{\beta_m}{1-\pi}} \cdot I(y_i = -1) + e^{-\frac{\beta_m}{\pi}} \cdot I(y_i = 1) \right] \\
&\quad + \sum_{y_i \neq f(x_i)} w_i^m \cdot \left[e^{\frac{\beta_m}{1-\pi}} I(y_i = -1) + e^{\frac{\beta_m}{\pi}} I(y_i = 1) \right] \\
&= \sum_{i=1}^N w_i^m I(y_i \neq f(x_i)) \left[e^{\frac{\beta_m}{1-\pi}} I(y_i = -1) + e^{\frac{\beta_m}{\pi}} I(y_i = 1) - e^{-\frac{\beta_m}{1-\pi}} I(y_i = -1) \right. \\
&\quad \left. - e^{-\frac{\beta_m}{\pi}} I(y_i = 1) \right] + \sum_{i=1}^N w_i^m \left[e^{-\frac{\beta_m}{1-\pi}} I(y_i = -1) + e^{-\frac{\beta_m}{\pi}} I(y_i = 1) \right] \\
&= l(\beta_m).
\end{aligned}$$

Our objective is to minimize $l(\beta_m)$ by varying $f_m(X)$ and β_m , respectively. We can see that

$$\sum_{i=1}^N w_i^m \left[e^{-\frac{\beta_m}{1-\pi}} I(y_i = -1) + e^{-\frac{\beta_m}{\pi}} I(y_i = 1) \right]$$

is not related to $f(x_i)$. Thus if we set β as a constant, then $f(x)$ can be solved by minimizing the first summation in $l(\beta)$ as follows,

$$\begin{aligned}
f_m(X) = \arg \min_f \sum_{i=1}^N I(y_i \neq f(x_i)) w_i^m & \left[I(y_i = 1) (e^{\frac{\beta_m}{\pi}} - e^{-\frac{\beta_m}{\pi}}) \right. \\
& \left. + I(y_i = -1) (e^{\frac{\beta_m}{1-\pi}} - e^{-\frac{\beta_m}{1-\pi}}) \right]. \tag{9.11}
\end{aligned}$$

(9.11) is a classifier minimizing the weighted misclassification error rate. Next, we solve β_m from $\frac{\partial l(\beta_m)}{\partial \beta_m} = 0$.

$$\begin{aligned} \frac{\partial l(\beta_m)}{\partial \beta_m} &= \sum_{i=1}^N w_i^m I(y_i \neq f(x_i)) \left[\frac{I(y_i = 1)}{\pi} (e^{\frac{\beta_m}{\pi}} + e^{-\frac{\beta_m}{\pi}}) + \frac{I(y_i = -1)}{1 - \pi} (e^{\frac{\beta_m}{1-\pi}} + e^{-\frac{\beta_m}{1-\pi}}) \right] \\ &\quad - \sum_{i=1}^N w_i^m \left[\frac{I(y_i = -1)}{1 - \pi} e^{-\frac{\beta_m}{1-\pi}} + \frac{I(y_i = 1)}{\pi} e^{-\frac{\beta_m}{\pi}} \right] \\ &= 0. \end{aligned} \tag{9.12}$$

Denote

$$\begin{aligned} \sum_{i=1}^N w_i^m I(y_i \neq f_m(x_i)) \frac{I(y_i = -1)}{1 - \pi} &= A, \\ \sum_{i=1}^N w_i^m I(y_i \neq f_m(x_i)) \frac{I(y_i = 1)}{\pi} &= B, \\ \sum_{i=1}^N w_i^m \frac{I(y_i = -1)}{1 - \pi} &= C, \\ \sum_{i=1}^N w_i^m \frac{I(y_i = 1)}{\pi} &= D, \end{aligned}$$

then $w_i^m > 0$, $D > B$ and $C > A$, and (9.12) can be simplified using A , B , C , and D as

$$A \exp\left(\frac{\beta}{1 - \pi}\right) + (A - C) \exp\left(-\frac{\beta}{1 - \pi}\right) + B \exp\left(\frac{\beta}{\pi}\right) + (B - D) \exp\left(-\frac{\beta}{\pi}\right) = 0. \tag{9.13}$$

There is no close form for equation (9.13), and we can only solve the numerical solution for β . The weight update function for weighted Adaboost-1 is

$$w_i^{m+1} = w_i^m \exp \left[-\beta_m f_m(x_i) \cdot \left(\frac{I(y_i = 1)}{\pi} - \frac{I(y_i = -1)}{1 - \pi} \right) \right],$$

and the final classifier is

$$F_m(X) = F_{m-1}(X) + \beta_m f_m(X) = \sum_{m=0}^M \beta_m f_m(X).$$

Following the previous discussion, a detailed algorithm is described as follows for weighted AdaBoost-1 which we add unequal class weight inside the exponent.

Step 1. Initialize the observation weights, $w_i = 1/N$, $i = 1, \dots, N$, and fit a classifier

$$f_1(x) \text{ on the training data using weights } \left(\frac{I(y_i=1)}{\pi} + \frac{I(y_i=-1)}{1-\pi} \right).$$

Step 2. For $m = 1, \dots, M$,

a) Solve numerical solution of β_m from equation (9.13),

b) Fit a classifier $f_m(x) = \arg \min_f \sum_{i=1}^N I(y_i \neq f(x_i)) w_i^m [I(y_i = 1)(e^{\frac{\beta_m}{\pi}} - e^{-\frac{\beta_m}{\pi}}) + I(y_i = -1)(e^{\frac{\beta_m}{1-\pi}} - e^{-\frac{\beta_m}{1-\pi}})]$ to the training data using weights w_i^m ,

c) Update $w_i^{m+1} = w_i^m \exp[-\beta_m f_m(x_i) \cdot (\frac{I(y_i=1)}{\pi} - \frac{I(y_i=-1)}{1-\pi})]$.

Step 3. Output $F(x) = \text{sign}[\sum_{i=1}^M \beta_m f_m(x)]$.

To describe the weighted Adaboost-1, we add class weight that is reciprocal to the corresponding class proportion for each class, i.e., denote π the percentage of class $Y = 1$, and $1 - \pi$ the percentage of class $Y = -1$, then use $1/\pi$ as the class weight for $Y = 1$ class, and $1/(1 - \pi)$ as the class weight for $Y = -1$ class. We fit a classifier based on the weighted exponential loss function in each boosting step and solve coefficient β_m numerically. We include class weight in the weight update function. Our final classifier is in the same format as in Adaboost. Thus we can derive the following proposition by using the following lemma.

Proposition 9.2. *The classifier of Weighted Adaboost-1 satisfies weighted Bayes rule.*

Proof. We have already stated above that Weighted Adaboost-1 minimize the weighted exponential loss through forward stagewise additive modeling, where the weighted ex-

ponential loss can be written as:

$$L(Y, F(X)) = \exp \left\{ - \left[\frac{I(Y = 1) \times F(X)}{\pi} - \frac{I(Y = -1) \times F(X)}{1 - \pi} \right] \right\}.$$

The minimizer of this weighted exponential loss can be derived as follows:

$$\begin{aligned} & E_{Y|X} \left\{ \exp \left[- \left(\frac{I(Y = 1) \times F(X)}{\pi} - \frac{I(Y = -1) \times F(X)}{1 - \pi} \right) \right] \right\} \\ &= P(Y = 1|X) \times \exp \left(\frac{-F(X)}{\pi} \right) + P(Y = -1|X) \times \exp \left(\frac{F(X)}{1 - \pi} \right), \\ \Rightarrow & \frac{\partial E_{Y|X} \left\{ \exp \left[- \left(\frac{I(Y=1) \times F(X)}{\pi} - \frac{I(Y=-1) \times F(X)}{1-\pi} \right) \right] \right\}}{\partial F(X)} \\ &= - \frac{P(Y = 1|X)}{\pi} \times \exp \left(\frac{-F(X)}{\pi} \right) + \frac{P(Y = -1|X)}{1 - \pi} \times \exp \left(\frac{F(X)}{1 - \pi} \right) = 0, \\ \Rightarrow & \exp \left(\frac{F(X)}{\pi \times (1 - \pi)} \right) = \frac{P(Y = 1|X)/\pi}{P(Y = -1|X)/(1 - \pi)}, \\ \Rightarrow & F(X) = \pi(1 - \pi) \log \left[\frac{P(Y = 1|X)/\pi}{P(Y = -1|X)/(1 - \pi)} \right]. \end{aligned} \quad (9.14)$$

As in Adaboost, $\text{sign}[F(x)]$ is our classification rule.

$$\text{sign}[F(x)] = \begin{cases} 1 & \text{if } \frac{P(Y=1|X)}{P(Y=-1|X)} > \frac{\pi}{1-\pi} \\ -1 & \text{if } \frac{P(Y=1|X)}{P(Y=-1|X)} < \frac{\pi}{1-\pi} \end{cases} \quad (9.15)$$

From equation (9.15), $\text{sign}[F(X)]$ satisfies weighted Bayes rule. \square

This result can be generalized to balanced situation. One test is to assume $\pi = 1 - \pi = \frac{1}{2}$, then from (9.14), $F(X) = \frac{1}{4} \log \left[\frac{P(Y=1|X)}{P(Y=-1|X)} \right]$.

$$\begin{aligned} & E_{Y|X} \left\{ \exp \left[- \left(\frac{I(Y = 1) \times F(X)}{1/2} - \frac{I(Y = -1) \times F(X)}{1/2} \right) \right] \right\} \\ &= P(Y = 1|X) \times \exp \left[\frac{-F(X)}{1/2} \right] + P(Y = -1|X) \times \exp \left[\frac{F(X)}{1/2} \right] \\ \Rightarrow & \frac{\partial E_{Y|X} \{ \exp[-(2I(Y=1) \times F(X) - 2I(Y=-1) \times F(X))] \}}{\partial F(X)} \\ &= -2P(Y = 1|X) \times \exp[-2F(X)] + 2P(Y = -1|X) \times \exp[2F(X)] = 0 \\ \Rightarrow & \exp[4F(X)] = \frac{2P(Y=1|X)}{2P(Y=-1|X)} \\ \Rightarrow & F(X) = \frac{1}{4} \log \left(\frac{P(Y=1|X)}{P(Y=-1|X)} \right) \end{aligned}$$

From the discussion above in this subsection, our weighted Adaboost-1 can achieve the theoretical minimum of mean within group misclassification error rate by adding unequal class weights that are reciprocal to class proportion inside the exponent. We can implement weighted Adaboost-1 following the description in the above algorithm. However, there is a shortcoming in this weighted boosting algorithm, that is we can only numerically solve β , since equation (9.13) has no close form. This shortcoming can be resolved by moving the unequal class weight outside the exponent as in weighted Adaboost-2.

9.3.3 Weighted Adaboost-2

We add unequal class weight outside the exponent, and get weighted Adaboost-2. The exponential loss for weighted Adaboost-2 is like this:

$$L(Y, F(X)) = \frac{I(Y = 1)}{\pi} \exp[-YF(X)] + \frac{I(Y = -1)}{1 - \pi} \exp[-YF(X)],$$

where π is the proportion for $Y = 1$ class. Similar to weighted Adaboost-1, we minimize this weighted exponential loss function via forward stagewise additive modeling,

$$(\beta_m, f_m(X)) = \arg \min_{\beta, f} \sum_{i=1}^N \left[\frac{I(y_i = 1)}{\pi} + \frac{I(y_i = -1)}{1 - \pi} \right] \exp\{-y_i[F_{m-1}(x_i) + \beta_m f_m(x_i)]\}.$$

Denote the weight in the m th boosting step as

$$w_i^m = \exp[-y_i F_{m-1}(x_i)],$$

and substitute w_i^m in the loss function to get

$$\arg \min_{\beta, f} \sum_{i=1}^N w_i^m \left[\frac{I(y_i = 1)}{\pi} + \frac{I(y_i = -1)}{1 - \pi} \right] \exp[-\beta_m f_m(x_i) y_i].$$

Rewrite the above equation on separate summation of $y_i = f(x_i)$ and $y_i \neq f(x_i)$, respectively, and minimize the following function in two steps.

$$\begin{aligned}
& \sum_{y_i=f(x_i)} w_i^m \left[\frac{I(y_i=1)}{\pi} + \frac{I(y_i=-1)}{1-\pi} \right] e^{-\beta_m} + \sum_{y_i \neq f(x_i)} w_i^m \left[\frac{I(y_i=1)}{\pi} + \frac{I(y_i=-1)}{1-\pi} \right] e^{\beta_m} \\
&= \sum_{i=1}^N (e^{\beta_m} - e^{-\beta_m}) I(y_i \neq f(x_i)) w_i^m \left[\frac{I(y_i=1)}{\pi} + \frac{I(y_i=-1)}{1-\pi} \right] \\
& \quad + \sum_{i=1}^N w_i^m e^{-\beta_m} \left[\frac{I(y_i=1)}{\pi} + \frac{I(y_i=-1)}{1-\pi} \right] \\
&= l(\beta_m). \tag{9.16}
\end{aligned}$$

We first minimize $l(\beta_m)$ by varying $f_m(X)$ which is only included in the first summation in equation (9.16), then $f_m(X)$ can be written into the following equation:

$$f_m(X) = \arg \min_f \sum_{i=1}^N I(y_i \neq f(x_i)) w_i^m \left[\frac{I(y_i=1)}{\pi} + \frac{I(y_i=-1)}{1-\pi} \right]. \tag{9.17}$$

$f_m(X)$ is a classifier in the m th boosting step, and from equation (9.17), it satisfies weighted Bayes Rule. We solve β_m by setting its partial differential equation to 0 as follows,

$$\begin{aligned}
\frac{\partial l(\beta_m)}{\partial \beta_m} &= (e^{\beta_m} + e^{-\beta_m}) \sum_{i=1}^N I(y_i \neq f(x_i)) w_i^m \left[\frac{I(y_i=1)}{\pi} + \frac{I(y_i=-1)}{1-\pi} \right] \\
& \quad + \sum_{i=1}^N w_i^m e^{-\beta_m} \left[\frac{I(y_i=1)}{\pi} + \frac{I(y_i=-1)}{1-\pi} \right] \\
&= 0. \tag{9.18}
\end{aligned}$$

Equation (9.18) can be written as

$$(e^{2\beta_m} + 1) = \frac{\sum_{i=1}^N w_i^m \left[\frac{I(y_i=1)}{\pi} + \frac{I(y_i=-1)}{1-\pi} \right]}{\sum_i w_i^m \left[\frac{I(y_i=1)}{\pi} + \frac{I(y_i=-1)}{1-\pi} \right] I(y_i \neq f(x_i))}.$$

The error rate of the m th boosting step is

$$err_m = \frac{\sum_i w_i^m \left[\frac{I(y_i=1)}{\pi} + \frac{I(y_i=-1)}{1-\pi} \right] I(y_i \neq f(x_i))}{\sum_{i=1}^N w_i^m \left[\frac{I(y_i=1)}{\pi} + \frac{I(y_i=-1)}{1-\pi} \right]},$$

then β_m only depends on the error rate in each boosting step,

$$\beta_m = \frac{1}{2} \log \frac{1 - \text{err}_m}{\text{err}_m}.$$

Thus the weight update function is

$$w_i^{m+1} = w_i^m \exp[-y_i \beta_m f(x_i)] = w_i^m \exp[\alpha_m I(y_i \neq f_m(x_i))] \exp(-\beta_m),$$

and the final classifier is

$$F(X) = \text{sign}\left[\sum_{m=0}^M \beta_m f_m(X)\right].$$

The algorithm of weighted Adaboost-2 based on loss function $L(Y, F(X)) = \frac{I(Y=1)}{\pi_1} \exp[-YF(X)] + \frac{I(Y=-1)}{1-\pi} \exp[-YF(X)]$ can be written as follows.

Step 1. Initialize the observation weights, $w_i = 1/N$, $i = 1, \dots, N$.

Step 2. For $m = 1, \dots, M$,

a) fit a classifier $f_m(x) = \arg \min_f \sum_{i=1}^N I(y_i \neq f(x_i)) w_i^m \left[\frac{I(y_i=1)}{\pi} + \frac{I(y_i=-1)}{1-\pi} \right]$ to the training data using weights w_i^m ,

b) compute error rate

$$\text{err}_m = \frac{\sum_i w_i^m \left[\frac{I(y_i=1)}{\pi} + \frac{I(y_i=-1)}{1-\pi} \right] I(y_i \neq f(x_i))}{\sum_{i=1}^N w_i^m \left[\frac{I(y_i=1)}{\pi} + \frac{I(y_i=-1)}{1-\pi} \right]},$$

c) set $w_i^{m+1} = w_i^m \exp[-y_i \beta f(x_i)] = w_i^m \exp[\alpha_m I(y_i \neq f_m(x_i))] \exp(-\beta_m)$,

d) compute $\alpha_m = \log \frac{1 - \text{err}_m}{\text{err}_m} = 2\beta_m$.

Step 3. Output $F(x) = \text{sign}\left[\sum_{i=1}^M \beta_m f_m(x)\right]$.

Weighted AdaBoost-2 minimizes the weighted exponential loss, i.e., $L(Y, F(X)) = \frac{I(Y=1)}{\pi} \exp[-YF(X)] + \frac{I(Y=-1)}{1-\pi} \exp[-YF(X)]$, through forward stagewise additive modeling. Then we have the following proposition stands.

Proposition 9.3. *The classifier of Weighted Adaboost-2 satisfies weighted Bayes Rule.*

Proof. We have already stated that weighted Adaboost-2 minimize weighted exponential loss through forward stagewise additive modeling. The minimizer of this loss function satisfies weighted Bayes rule can be derived as follows.

$$\begin{aligned}
F(X) &= \arg \min_{F(X)} \left\{ \frac{I(Y = 1)}{\pi} \exp[-YF(X)] + \frac{I(Y = -1)}{1 - \pi} \exp[-YF(X)] \right\}. \\
&= E_{Y|X} \left\{ \exp[-YF(X)] \left(\frac{I(Y = 1)}{\pi} + \frac{I(Y = -1)}{1 - \pi} \right) \right\} \\
&= \frac{P(Y = 1|X)}{\pi} \exp[-F(X)] + \frac{P(Y = -1|X)}{1 - \pi} \times \exp[F(X)] \\
\Rightarrow & \frac{\partial E_{Y|X} \left\{ \exp[-YF(X)] \left[\frac{I(Y=1)}{\pi} + \frac{I(Y=-1)}{1-\pi} \right] \right\}}{\partial F(X)} \\
&= - \frac{P(Y = 1|X)}{\pi} \times \exp[-F(X)] + \frac{P(Y = -1|X)}{1 - \pi} \times \exp[F(X)] = 0 \\
\Rightarrow & \exp[2F(X)] = \frac{P(Y = 1|X)/\pi}{P(Y = -1|X)/(1 - \pi)} \\
\Rightarrow & F(X) = \frac{1}{2} \log \left[\frac{P(Y = 1|X)/\pi}{P(Y = -1|X)/(1 - \pi)} \right] \tag{9.19}
\end{aligned}$$

$\text{sign}[F(X)]$ is our classifier, i.e.,

$$\text{sign}[F(x)] = \begin{cases} 1 & \text{if } \frac{P(Y=1|X)}{P(Y=-1|X)} > \frac{\pi}{1-\pi}, \\ -1 & \text{if } \frac{P(Y=1|X)}{P(Y=-1|X)} < \frac{\pi}{1-\pi}, \end{cases} \tag{9.20}$$

and it satisfies weighted Bayes Rule. \square

Generalize this to balanced data classification as in weighted Adaboost-1, we

assume $\pi = 1 - \pi = \frac{1}{2}$, then from (9.19), $F(X) = \frac{1}{2} \log \left[\frac{P(Y=1|X)}{P(Y=-1|X)} \right]$.

$$\begin{aligned}
& E_{Y|X} \left\{ \left(\frac{I(Y=1)}{1/2} + \frac{I(Y=-1)}{1/2} \right) \exp[-YF(X)] \right\} \\
&= 2P(Y = 1|X) \times \exp[-F(X)] + 2P(Y = -1|X) \times \exp[F(X)] \\
\Rightarrow & \frac{\partial E_{Y|X} \left\{ \left(\frac{I(Y=1)}{1/2} + \frac{I(Y=-1)}{1/2} \right) \exp[-YF(X)] \right\}}{\partial F(X)} \\
&= -2P(Y = 1|X) \times \exp[-F(X)] + 2P(Y = -1|X) \times \exp[F(X)] = 0 \\
\Rightarrow & \exp[2F(X)] = \frac{2P(Y=1|X)}{2P(Y=-1|X)} \\
\Rightarrow & F(X) = \frac{1}{2} \log \left[\frac{P(Y=1|X)}{P(Y=-1|X)} \right]
\end{aligned}$$

In theory we can reach the theoretical minimized mean within group misclassification error rate using weighted Adaboost-2. Weighted Adaboost-2 is superior than weighted Adaboost-1 in that it has close form solution for β . We implement weighted Adaboost-2 in R package following the algorithm above, and use it in our numerical study discussed in Sections 9.5 and 9.6.

9.4 Gradient Boosting and Negative Binomial Log-likelihood

The idea of adding unequal class weights is not limited to Adaboost, but can be generalized to other boosting algorithms. In this section, we introduce another boosting method commonly used in function estimation, i.e., gradient boosting [49]. We modify the gradient boosting following similar procedure as in Adaboost to get a weighted gradient boosting. We prove that with negative binomial log-likelihood as its loss function, weighted gradient boosting satisfies weighted Bayes rule. The following of this section is organized as follows. We introduce general gradient boosting algorithm in Subsection(9.4.1). Gradient boosting using negative binomial log-likelihood

as well as its weighted version is discussed in Subsection(9.4.2). Finally, we show that binomial log-likelihood with unequal class weights satisfies weighted Bayes rule in Subsection(9.4.3).

9.4.1 Gradient Boosting Algorithm

In order to understand how gradient boosting works, we first introduce the steepest descent. We use $f(x)$ to predict y , where $f(x)$ is the classifier we get from classification method, and y is the actual class information of our data set. Our goal is to minimize the loss function, expressed in the following equation

$$L(f) = \sum_{i=1}^N L(y_i, f(x_i)). \quad (9.21)$$

If we choose steepest descent gradient $h_m = -\rho_m g_m$, where ρ_m is a scalar, and g_m is the gradient of $L(f)$ evaluated at $f = f_{m-1}$, and can be derived by

$$g_{im} = \left[\frac{\partial L(y_i, f(x_i))}{\partial f(x_i)} \right]_{f(x_i)=f_{m-1}(x_i)}. \quad (9.22)$$

Then ρ_m is the solution to $\rho_m = \arg \min_{\rho} L(f_{m-1} - \rho g_m)$, and f_m is updated by $f_m = f_{m-1} - \rho_m g_m$. It is straight forward to solve the steepest descent if we just want to minimize loss on the training data. Unfortunately the gradient is only defined on the training data, whereas the ultimate goal is to generalize $f_m(x)$ to new data not represented in the training set. One way to solve this problem is to fit a tree denoted by $T(x, \Theta_m)$ at each iteration whose prediction is as close as possible to the negative gradient. We use squared error to measure the closeness, and get

$$\tilde{\Theta}_m = \arg \min_{\Theta} \sum_{i=1}^N (-g_{im} - T(x_i, \Theta))^2. \quad (9.23)$$

That is we fit a tree T to the negative gradient values by least squares, which is the gradient boosting. From the above discussion, the generic gradient tree boosting algorithm without specification of loss function can be summarized as follows [49]:

Step 1. $F_0(x) = \arg \min_{\rho} \sum_{i=1}^N L(y_i, \rho).$

Step 2. For $m = 1, \dots, M,$

a) $-g_m(x) = - \left(\frac{\partial L(y_i, F(x_i))}{\partial F(x_i)} \right)_{F(x)=F_{m-1}(x)}, i = 1 \dots N,$

b) $a_m = \arg \min_a \sum_{i=1}^N [-g_m(x_i) - h(x_i, a)]^2,$

c) $\rho_m = \arg \min_{\rho} \sum_{i=1}^N L(y_i, F_{m-1}(x_i) + \rho h(x_i, a_m)),$

d) $F_m(x) = F_{m-1}(x) + \rho h(x_i, a_m).$

Step 3. End For, end algorithm.

9.4.2 Gradient Boosting Using Negative Binomial

Log-likelihood

As discussed in the previous subsection, gradient boosting can minimize the expected value of some specified loss function over the joint distribution of all (y, x) -values. For two class classification problem, negative binomial log-likelihood, i.e., $\log(1 + \exp(-2yF))$, $y \in \{-1, 1\}$, is the common loss function used in gradient boosting. Using regression tree as the base learner, the gradient tree boosting algorithm for two class classification using binomial log-likelihood as the loss function can be described as follows [49]:

Step 1. $F_0(x) = \frac{1}{2} \log \frac{1 + \bar{y}}{1 - \bar{y}}.$

Step 2. For $m = 1, \dots, M$,

- a) $-g_m(x) = \frac{2y_i}{1 + \exp[2y_i F_{m-1}(x_i)]}$, $i = 1 \dots N$,
- b) $\{R_{jm}\}_1^J = J$ -terminal node tree($\{-g_m(x_i), x_i\}_1^N$),
- c) $r_{jm} = \frac{\sum_{x_i \in R_{jm}} -g_m(x_i)}{\sum_{x_i \in R_{jm}} |g_m(x_i)|(2 - |g_m(x_i)|)}$, $j = 1 \dots J$,
- d) $F_m(x) = F_{m-1}(x) + \sum_{j=1}^J r_{jm} I(x \in R_{jm})$.

Step 3. End For, end algorithm.

If we change the loss function to a weighted version, as in Adaboost, we can add unequal class weights, which is reciprocal to the class proportion, inside the exponent and outside the log function. Then the loss function can be written as

$$L(Y, F(X)) = \log \left\{ 1 + \exp \left[-2YF(X) \times \left(\frac{I(Y=1)}{\pi} + \frac{I(Y=-1)}{1-\pi} \right) \right] \right\}, \quad (9.24)$$

and

$$L(Y, F(X)) = \left(\frac{I(Y=1)}{\pi} + \frac{I(Y=-1)}{1-\pi} \right) \log \{ 1 + \exp[-2YF(X)] \}, \quad (9.25)$$

respectively, where π is the proportion of class $Y = 1$. We only need to adjust Step 2a) accordingly in the above algorithm to get the weighted gradient boosting.

9.4.3 Minimization of Negative Binomial Log-likelihood

Through gradient boosting and weighted gradient boosting, we can get the minimizer of negative log-likelihood and weighted negative log-likelihood. In this section, we will discuss the property of these minimizers.

Negative Binomial Log-likelihood

The property of the minimizer of negative binomial log-likelihood is described in the following proposition.

Proposition 9.4. *The minimizer of negative binomial log-likelihood is one half log odds.*

Proof.

$$\begin{aligned}
 F(X) &= \arg \min_F E\left(\log\{1 + \exp[-2YF(X)]\}\right) \\
 &= \arg \min E_{Y|X}\left(\log\{1 + \exp[-2YF(X)]\}\right), \forall X \\
 &\quad E_{Y|X}\left(\log\{1 + \exp[-2YF(X)]\}\right) \\
 &= P(Y = 1|X) \log\{1 + \exp[-2F(X)]\} + P(Y = -1|X) \log\{1 + \exp[2F(X)]\}. \\
 \Rightarrow &\quad \frac{\partial E_{Y|X}\left(\log\{1 + \exp[-2YF(X)]\}\right)}{\partial F(X)} \\
 &= -P(Y = 1|X) \frac{\exp[-2F(X)]}{1 + \exp[-2F(X)]} + P(Y = -1|X) \frac{\exp[2F(X)]}{1 + \exp[2F(X)]} = 0, \\
 \Rightarrow &\quad \exp[2F(X)] = \frac{P(Y = 1|X)}{P(Y = -1|X)}, \\
 \Rightarrow &\quad F(X) = \frac{1}{2} \log\left(\frac{P(Y = 1|X)}{P(Y = -1|X)}\right).
 \end{aligned}$$

□

Since the minimizer of negative binomial log-likelihood is one half log odds, it means that the classifier of negative binomial log-likelihood satisfies Bayes rule.

Weighted Negative Binomial Log-likelihood-1

We can add unequal weights for each class inside the exponent as in weighted Adaboost-1. Denote π as the proportion of class $Y = 1$, then we rewrite the weighted

negative binomial log-likelihood loss function as

$$L(Y, F(X)) = \log \left\{ 1 + \exp \left[-2YF(X) \times \left(\frac{I(Y=1)}{\pi} + \frac{I(Y=-1)}{1-\pi} \right) \right] \right\},$$

thus

$$F(X) = \arg \min_F E \left(\log \left\{ 1 + \exp \left[-2YF(X) \times \left(\frac{I(Y=1)}{\pi} + \frac{I(Y=-1)}{1-\pi} \right) \right] \right\} \right). \quad (9.26)$$

From the following derivation, there is no close form for $F(X)$.

$$\begin{aligned} & \arg \min_F E \left(\log \left\{ 1 + \exp \left[-2YF(X) \left(\frac{I(Y=1)}{\pi} + \frac{I(Y=-1)}{1-\pi} \right) \right] \right\} \right) \\ &= \arg \min_F E_{Y|X} \left(\log \left\{ 1 + \exp \left[-2YF(X) \left(\frac{I(Y=1)}{\pi} + \frac{I(Y=-1)}{1-\pi} \right) \right] \right\} \right), \quad \forall X \\ & E_{Y|X} \left(\log \left\{ 1 + \exp \left[-2YF(X) \left(\frac{I(Y=1)}{\pi} + \frac{I(Y=-1)}{1-\pi} \right) \right] \right\} \right) \\ &= P(Y=1|X) \log \left\{ 1 + \frac{\exp[-2F(X)]}{\pi} \right\} + P(Y=-1|X) \log \left\{ 1 + \frac{\exp[2F(X)]}{1-\pi} \right\}. \end{aligned}$$

Therefore,

$$\begin{aligned} & \frac{\partial E_{Y|X} \left(\log \left\{ 1 + \exp \left[-2YF(X) \left(\frac{I(Y=1)}{\pi} + \frac{I(Y=-1)}{1-\pi} \right) \right] \right\} \right)}{\partial F(X)} \\ &= -\frac{2P(Y=1|X)}{\pi} \frac{\exp[-2F(X)/\pi]}{1 + \exp[-2F(X)/\pi]} + \frac{2P(Y=-1|X)}{1-\pi} \frac{\exp[2F(X)/(1-\pi)]}{1 + \exp[2F(X)/(1-\pi)]} \\ &= 0. \end{aligned}$$

Therefore,

$$\exp[2F(X)/(1-\pi)] \frac{1 + \exp[2F(X)/\pi]}{1 + \exp[2F(X)/(1-\pi)]} = \frac{P(Y=1|X)/\pi}{P(Y=-1|X)/(1-\pi)}.$$

Weighted Negative Binomial Log-likelihood-2

We add unequal weights outside the log function on negative binomial log-likelihood, i.e., $L(Y, F(X)) = \left(\frac{I(Y=1)}{\pi} + \frac{I(Y=-1)}{1-\pi} \right) \log \{ 1 + \exp[-2YF(X)] \}$, thus

$$F(X) = \arg \min_F E \left[\left(\frac{I(Y=1)}{\pi} + \frac{I(Y=-1)}{1-\pi} \right) \log \{ 1 + \exp[-2YF(X)] \} \right].$$

Proposition 9.5. *The minimizer of weighted negative binomial log-likelihood-2 is weighted log odds.*

Proof.

$$\begin{aligned}
& \arg \min_F E \left(\left(\frac{I(Y=1)}{\pi} + \frac{I(Y=-1)}{1-\pi} \right) \log \{1 + \exp[-2YF(X)]\} \right) \\
= & \arg \min_F E_{Y|X} \left[\left(\frac{I(Y=1)}{\pi} + \frac{I(Y=-1)}{1-\pi} \right) \log \{1 + \exp[-2YF(X)]\} \right], \forall X \\
& E_{Y|X} \left[\left(\frac{I(Y=1)}{\pi} + \frac{I(Y=-1)}{1-\pi} \right) \log \{1 + \exp[-2YF(X)]\} \right] \\
= & \frac{P(Y=1|X)}{\pi} \log \{1 + \exp[-2F(X)]\} + \frac{P(Y=-1|X)}{1-\pi} \log \{1 + \exp[2F(X)]\} \\
\Rightarrow & \frac{\partial E_{Y|X} \left[\left(\frac{I(Y=1)}{\pi} + \frac{I(Y=-1)}{1-\pi} \right) \log \{1 + \exp[-2YF(X)]\} \right]}{\partial F(X)} \\
= & -\frac{2P(Y=1|X)}{\pi} \cdot \frac{\exp[-2F(X)]}{1 + \exp[-2F(X)]} + \frac{2P(Y=-1|X)}{1-\pi} \cdot \frac{\exp[2F(X)]}{1 + \exp[2F(X)]} = 0 \\
\Rightarrow & \exp[2F(X)] = \frac{P(Y=1|X)/\pi}{P(Y=-1|X)/(1-\pi)} \\
\Rightarrow & F(X) = \frac{1}{2} \log \left[\frac{P(Y=1|X)/\pi}{P(Y=-1|X)/(1-\pi)} \right].
\end{aligned} \tag{9.27}$$

□

We use $\text{sign}[F(X)]$ as our classifier, and it satisfies Bayes rule as expressed in (9.28).

$$\text{sign}[F(x)] = \begin{cases} 1 & \text{if } \frac{P(Y=1|X)}{P(Y=-1|X)} > \frac{\pi}{1-\pi}, \\ -1 & \text{if } \frac{P(Y=1|X)}{P(Y=-1|X)} < \frac{\pi}{1-\pi}. \end{cases} \tag{9.28}$$

Balanced data classification is a special case where $\pi = 1 - \pi = \frac{1}{2}$, and the minimizer of the negative binomial log-likelihood is $F(X) = \frac{1}{2} \log \left[\frac{P(Y=1|X)}{P(Y=-1|X)} \right]$. The proof is as

follows:

$$\begin{aligned}
& \arg \min_F E \left(\left(\frac{I(Y=1)}{1/2} + \frac{I(Y=-1)}{1/2} \right) \log \{1 + \exp[-2YF(X)]\} \right) \\
= & \arg \min_F E_{Y|X} \left[\left(\frac{I(Y=1)}{1/2} + \frac{I(Y=-1)}{1/2} \right) \log \{1 + \exp[-2YF(X)]\} \right], \forall X \\
& E_{Y|X} \left[\left(\frac{I(Y=1)}{1/2} + \frac{I(Y=-1)}{1/2} \right) \log \{1 + \exp[-2YF(X)]\} \right] \\
= & 2P(Y=1|X) \log \{1 + \exp[-2F(X)]\} + 2P(Y=-1|X) \log \{1 + \exp[2F(X)]\} \\
\Rightarrow & \frac{\partial E_{Y|X} \left[\left(\frac{I(Y=1)}{1/2} + \frac{I(Y=-1)}{1/2} \right) \log \{1 + \exp[-2YF(X)]\} \right]}{\partial F(X)} \\
= & -\frac{2P(Y=1|X)}{1/2} \cdot \frac{\exp[-2F(X)]}{1 + \exp[-2F(X)]} + \frac{2P(Y=-1|X)}{1/2} \cdot \frac{\exp[2F(X)]}{1 + \exp[2F(X)]} = 0 \\
\Rightarrow & \exp[2F(X)] = \frac{P(Y=1|X)}{P(Y=-1|X)} \\
\Rightarrow & F(X) = \frac{1}{2} \log \left[\frac{P(Y=1|X)}{P(Y=-1|X)} \right]
\end{aligned} \tag{9.29}$$

Following this discussion, we can see that weighted gradient boosting satisfies weighted Bayes rule, which will improve classification result for unbalanced data. Implementation of weighted gradient boosting regression tree will be our future work on this topic.

9.5 Simulation Studies

We implement Adaboost and weighted Adaboost-2, which we call Adaweight from here on, in R 2.11.1. We use *rpart* package for classification tree, and the default depth for tree in *rpart* is 30 steps. We use *bag=0.5* as a default in our code to reduce variance of regression tree. It has been discussed that Adaboost is usually resistant to overfitting problem [43]. However, for better performance on extremely unbalanced data classification, we add a very large class weight on the rare class, which is brought into the weight update process in Adaweight. The rigorous class

weight tends to lead to over fit problem in Adaweight. Thus we add a parameter ν in the weight update function to slow down converging process. The criteria used to compare the performance of Adaboost and Adaweight is mean within group error rate and the number of boosting steps, since our goal is to obtain the classification result better and faster.

Numerical studies are performed to compare the performance of Adaboost and Adaweight on unbalanced data classification. Our simulation data is generated based on two scenarios, i.e., mean difference and logistic regression. We generate training, validation, and testing data with sample size $n = 10000$ for each data set, and X has $p = 6$ dimension. We use X , X^2 and X , and $X^2 - 2X$ as our descriptor set.

Here is the detail information of the data construction of our 8 mean difference and 4 logistic regression models. For our 8 mean difference datasets, denote by $M1$ through $M8$, we first generate 2% rare class $Y = 1$, and 98% $Y = -1$ majority class using binary distribution. Then we generate descriptor set on each class using normal distribution. Mean in normal distribution denoted by μ is different in the descriptor set for the two classes. For $M1$ and $M2$, we set $\mu = 0.5$ for $Y = 1$ class on each dimension, and $\mu = -0.5$ for $Y = -1$ class on each dimension. In $M1$ we bind X^2 and X together, while in $M2$ we use $X^2 - 2X$ to construct our descriptor set. In $M3$, $M4$, and $M5$, we set mean difference $\mu = \pm 0.5$ for $Y = 1$ and $Y = -1$ in the first 2 directions, and $\mu = 0$ for both classes for the rest 4 directions. Our descriptor set in $M3$ is X , bind X^2 and X in $M4$, and $X^2 - 2X$ in $M5$, respectively. For $M6$, $M7$, and $M8$, X is correlated rather than independent as in the first 5 models, we construct X with auto regression correlation 0.5, i.e., $AR(0.5)$, with mean difference $\mu = \pm 0.5$ in the first direction. Then we construct the descriptor set the same way

as in $M3$, $M4$, and $M5$. The descriptor set has the following distribution.

$$X_i \sim N(0, 1)$$

$$\text{cov}(X_i, X_j) = 0.5^{(i-j)}.$$

For the 4 logistic regression models, denoted by $L1$, $L2$, $L3$, and $L4$, respectively, we set $\gamma = (1, -0.8, 0.5, 0, 0, 0)$, and we vary γ_0 in each model to get 2% $Y = 1$ class. In $L1$ and $L2$, we set $\mu = 0.5$ and $\mu = 1$ for all directions. In $L3$ and $L4$, we construct X by $AR(0.5)$ model with $\mu = 0.5$ and $\mu = 1$ in the first direction, respectively.

We run boosting on the training data to find classification rule, and plot the mean within group error rate versus boosting steps for both Adaboost and Adaweight on training and validation data. We find the boosting steps corresponding to the minimum mean within group misclassification error rate from the validation data, and stop boosting in that step in testing data to avoid over trained problem. Our simulation study is run 50 times to reduce variance. We compare the performance of Adaboost and Adaweight on the iteration number and mean within group error rate on testing data result. The plots are depicted in Figure 9.1 through 9.12, and mean within group misclassification error rates are listed in Table 9.1.

From our simulation studies, we can see that Adaweight converges faster on the training and validation set comparing to Adaboost. We can get an almost error free classification on the training data if we run boosting long enough. On the validation data set, the optimal result of Adaweight which has the smallest mean within group error rate is better than Adaboost in every case. Adaboost does not have any separation on several cases with mean within group error rate 0.5. Our final result on testing data shows a similar trend as in validation data. Adaboost has worse performance on each case with almost no separation for cases $M3$ through $M8$, since they

Table 9.1: Mean Within Group Misclassification Error Rate on Testing Data

(a) Mean Difference

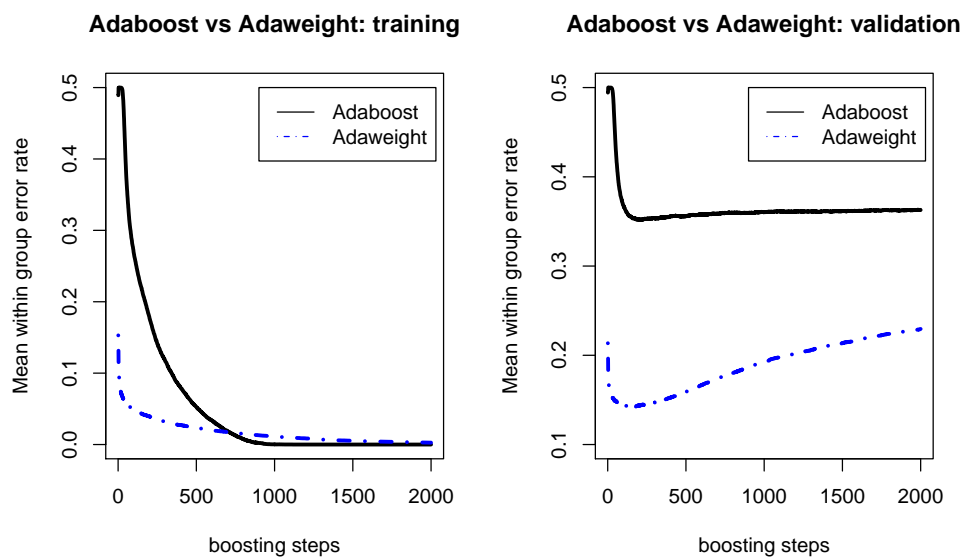
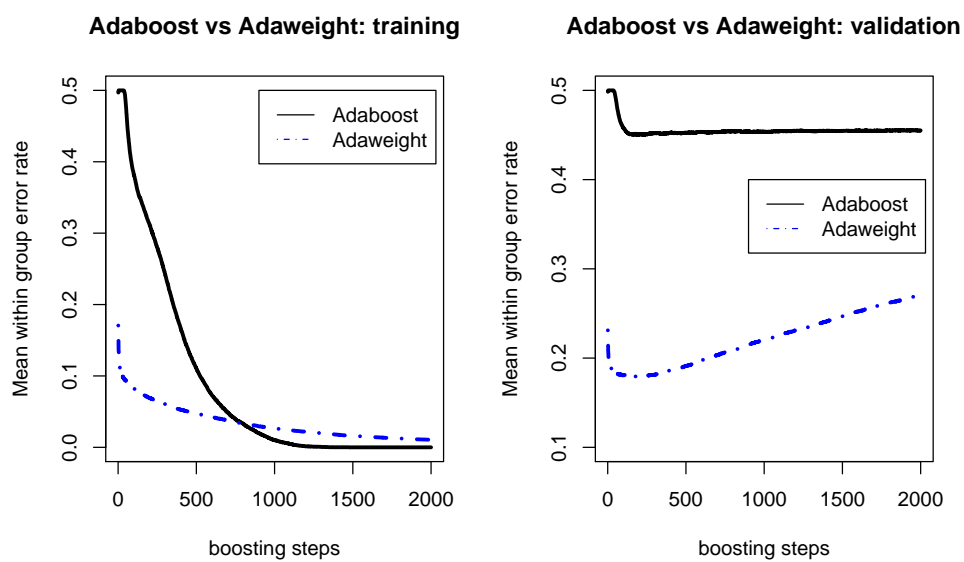
Study	$\mu(p)$ in X	descriptor set	Adaboost(var)	Adaweight(var)
<i>M1</i>	$\pm 0.5(6)$	X^2, X	0.366(0.0002)	0.150(0.0002)
<i>M2</i>	$\pm 0.5(6)$	$X^2 - 2X$	0.443(0.0002)	0.187(0.0002)
<i>M3</i>	$\pm 0.5(2), 0(4)$	X	0.495(0)	0.268(0.0002)
<i>M4</i>	$\pm 0.5(2), 0(4)$	X^2, X	0.495(0)	0.273(0.0001)
<i>M5</i>	$\pm 0.5(2), 0(4)$	$X^2 - 2X$	0.500(0)	0.298(0.0002)
<i>M6</i>	$0.5(1), AR(0.5)(5)$	X	0.500(0)	0.338(0.0002)
<i>M7</i>	$0.5(1), AR(0.5)(5)$	X^2, X	0.500(0)	0.344(0.0003)
<i>M8</i>	$0.5(1), AR(0.5)(5)$	$X^2 - 2X$	0.500(0)	0.357(0.0005)

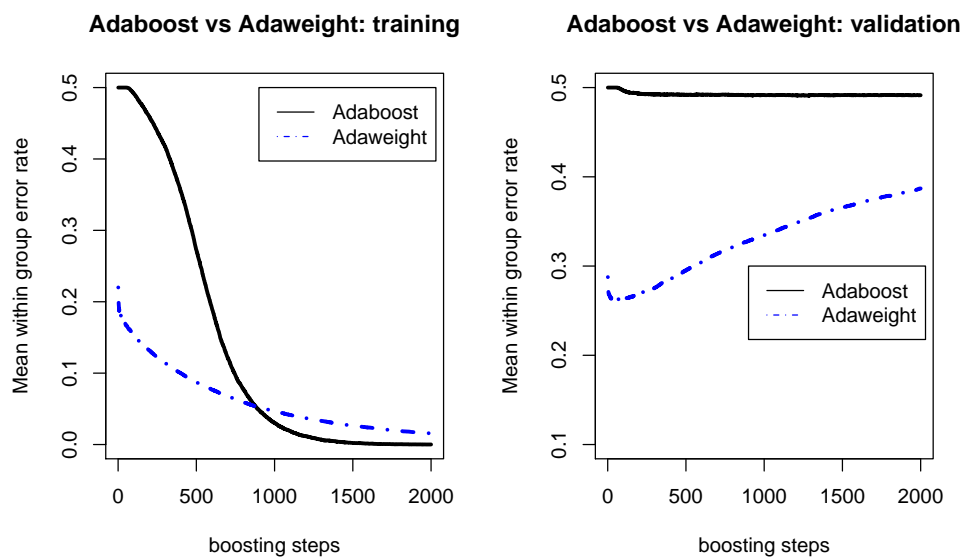
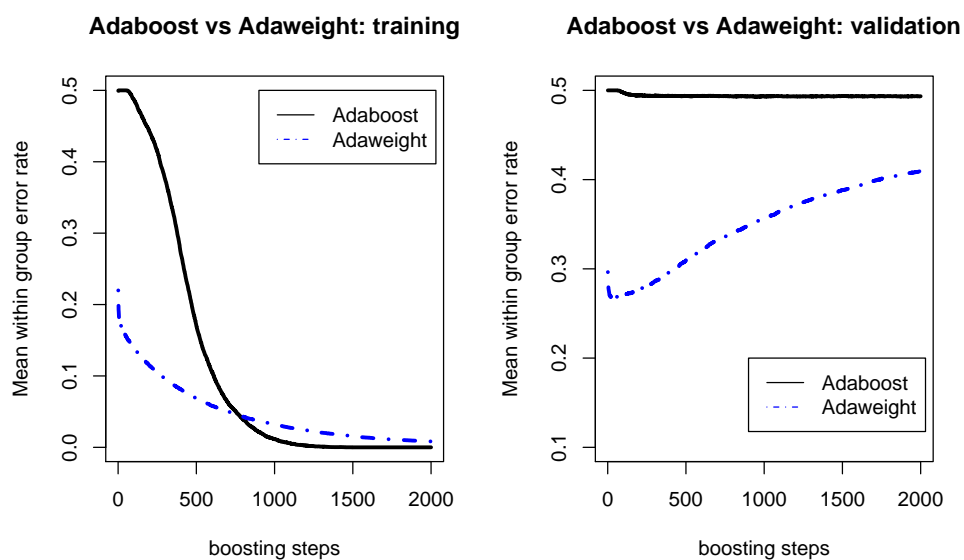
(b) Logistic Regression

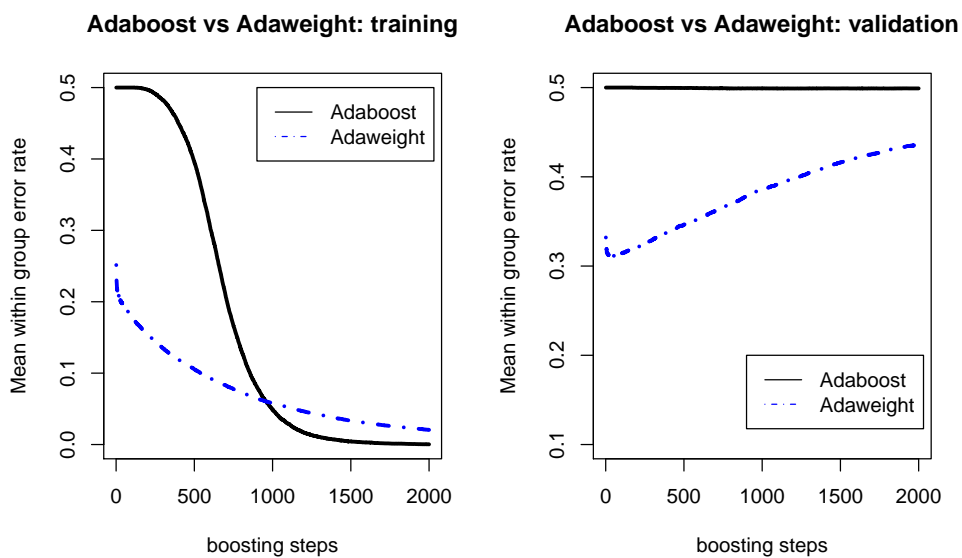
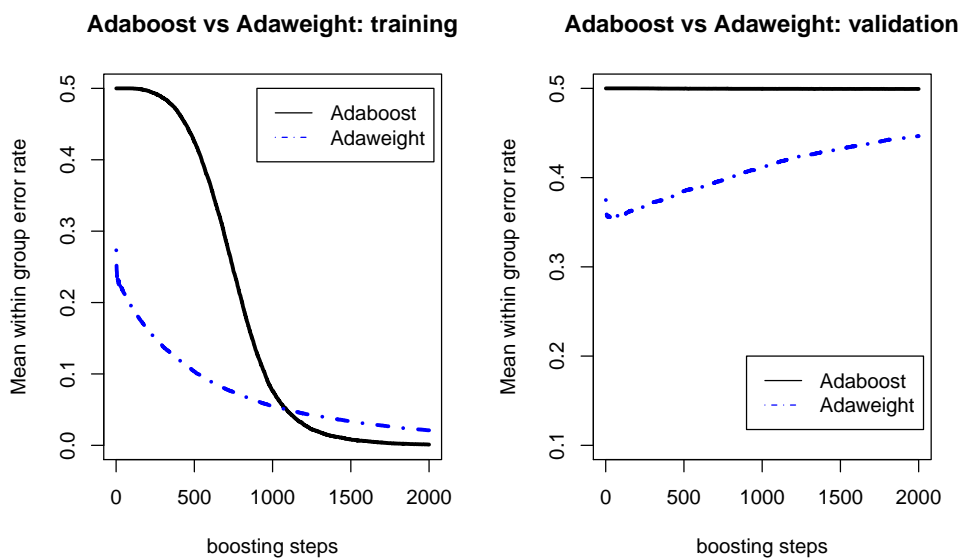
Study	$\mu(p)$ in X	γ_0	Adaboost(var)	Adaweight(var)
<i>L1</i>	$0.5(6)$	-5.449	0.5(0)	0.362(0.0004)
<i>L2</i>	$1(6)$	-5.102	0.496(0)	0.297(0.0002)
<i>L3</i>	$0.5(1), AR(0.5)(5)$	-5.008	0.5(0)	0.360(0.0004)
<i>L4</i>	$1(1), AR(0.5)(5)$	-4.644	0.5(0)	0.359(0.0004)

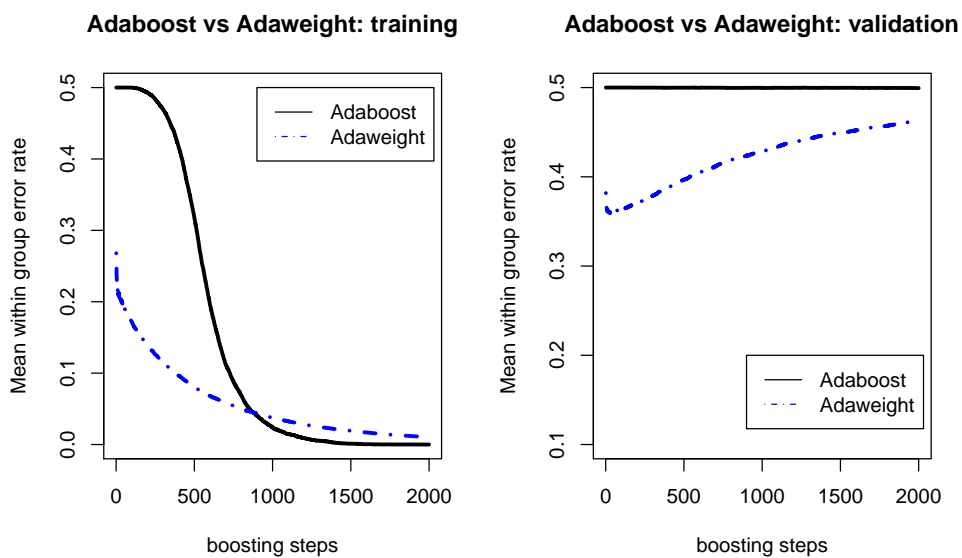
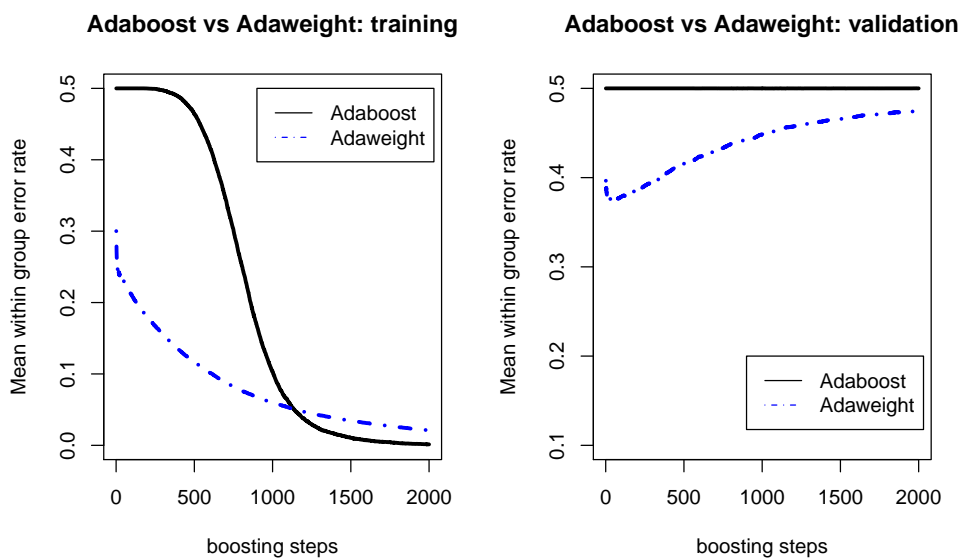
have weaker separation information, i.e., fewer dimensions contain mean differences comparing to *M1* and *M2*.

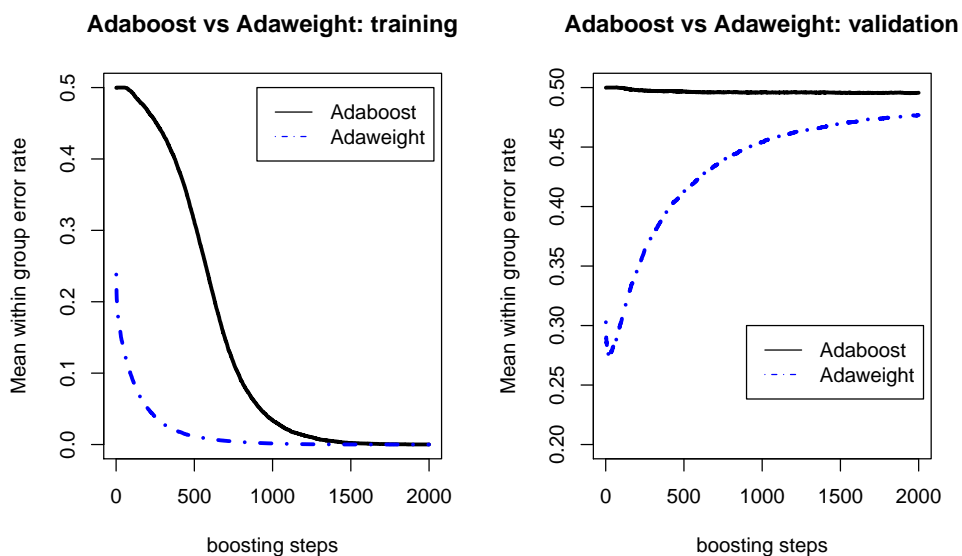
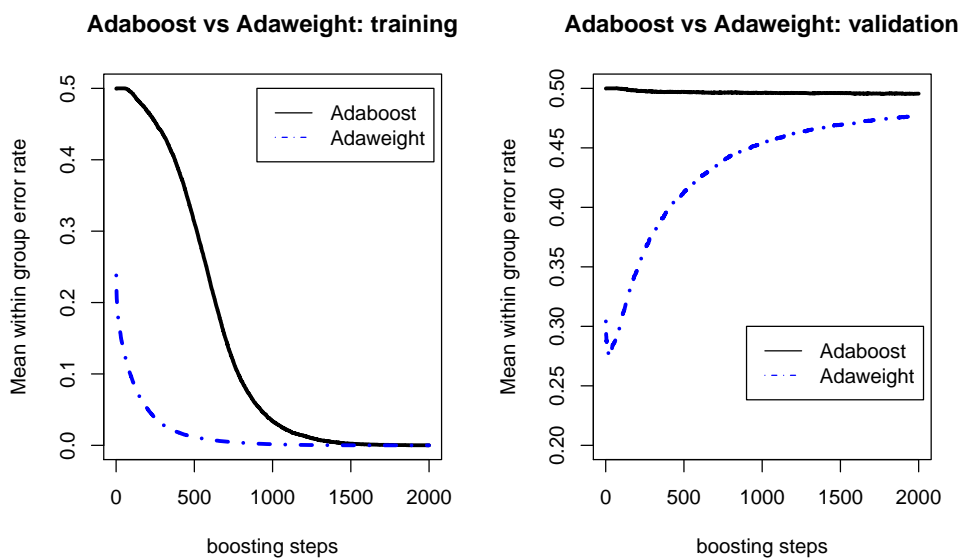
Our main objective is to get a good detection rate of the rare class, since they have the potential to become a new drug under further investigation, while the majority class is just noise compounds in our drug discovery problem. With that said, it is intuitive that we put more emphasis on the rare class as in Adaweight. For all of our simulation studies, Adaweight has smaller mean within group error rate and converge much faster than Adaboost, with a higher true positive rate on the rare class. Adaboost tends to put all data in major class and cannot detect the rare class when the information differentiating the two classes are not very strong. Adaweight performs better than Adaboost for unbalanced data classification in general. However, we can see from the plots that Adaweight are easier over-fitted than Adaboost, and we

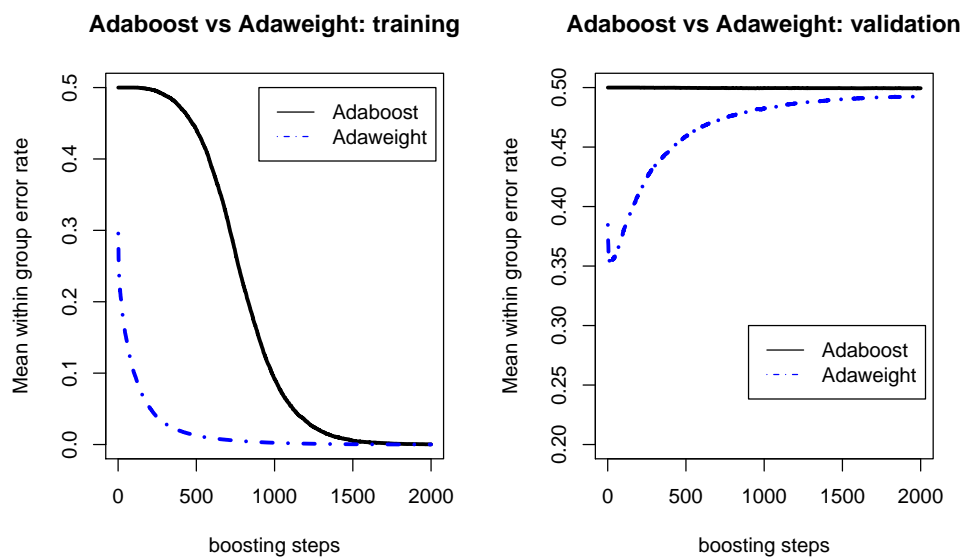
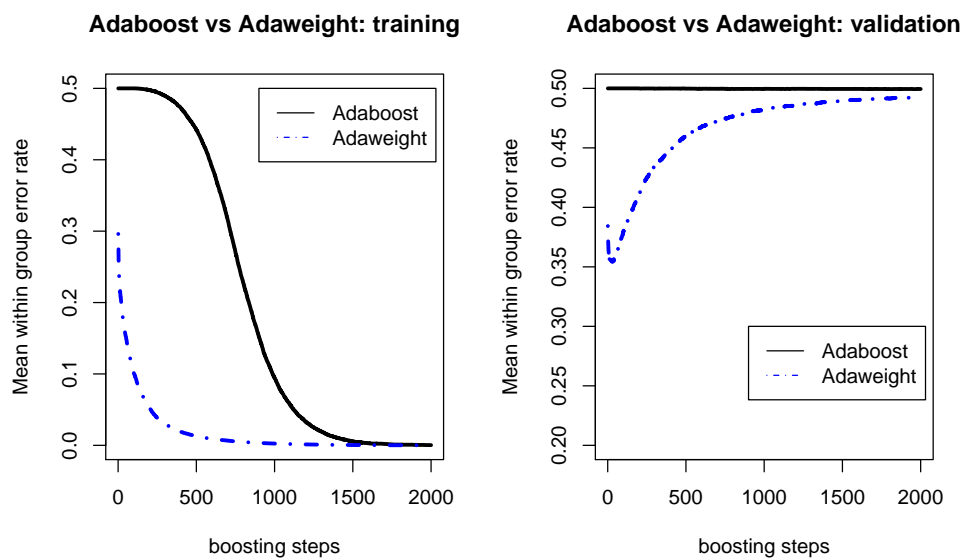
Figure 9.1: Mean Within Group Misclassification Error Rate of $M1$ Figure 9.2: Mean Within Group Misclassification Error Rate of $M2$

Figure 9.3: Mean Within Group Misclassification Error Rate of $M3$ Figure 9.4: Mean Within Group Misclassification Error Rate of $M4$

Figure 9.5: Mean Within Group Misclassification Error Rate of $M5$ Figure 9.6: Mean Within Group Misclassification Error Rate of $M6$

Figure 9.7: Mean Within Group Misclassification Error Rate of $M7$ Figure 9.8: Mean Within Group Misclassification Error Rate of $M8$

Figure 9.9: Mean Within Group Misclassification Error Rate of L_1 Figure 9.10: Mean Within Group Misclassification Error Rate of L_2

Figure 9.11: Mean Within Group Misclassification Error Rate of L_3 Figure 9.12: Mean Within Group Misclassification Error Rate of L_4

need to add validation data to stop the boosting process at the step with minimized error rate.

Besides the above simulation studies that are included in our discussion. We also perform other studies on data set with variance difference, and on data with high dimensional descriptor set, i.e., $p = 24$. From our study on variance difference data set, we find that Adaboost has no separation between the two classes, while Adaweight can detect more than half of the rare class with a higher percentage of the noise class. This finding is consistent with the above simulation studies. Our study on $p = 24$ mean difference data shows similar classification result as $p = 6$.

From all our simulation studies, we can conclude that with the help of validation data or cross validation such that we can find the optimal stopping steps, Adaweight is consistently superior than Adaboost on unbalanced data classification. Boosting classification tree works well on classifying correlated high dimensional data, which makes it a good classifier for drug discovery data.

9.6 Real Data Investigation

In this dissertation, we use real data from National Cancer Institute (NCI) with class labels added by GlaxoSmithKlein, Inc. [50]. There are 29,812 chemical compounds which are measured for their ability to protect human CEM cells from HIV-1 infection. Of the 29,812 chemical compounds, only 608 are active against the HIV virus. Each compound is described by $p = 6$ chemometric descriptors known as BCUT numbers. The data is randomly split into training and testing set. Each contains 14602 inactive compounds and 304 active compounds.

From the simulation studies in Section 9.5, we have seen that Adaweight tends

to have over fit problem, and the mean within group misclassification error rate increases after a certain iteration number. We need to find the boosting step with the minimum misclassification. In order to find the stopping criteria, we run five fold cross validation on the training set to determine when to stop the boosting process, and apply the iteration number on the testing data set. Our results on Adaboost and Adaweight are presented in Table 9.2 and Figure 9.13.

Table 9.2: Mean Within Group Misclassification Error Rate on Real Data

Data	Adaboost	Adaweight
Training	0.0074	0.0332
Testing	0.4023	0.2924

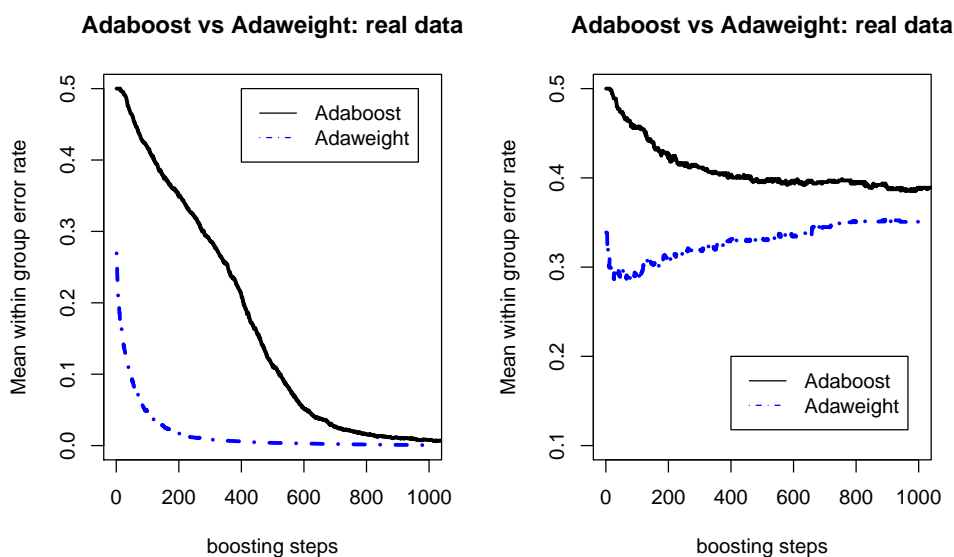


Figure 9.13: Mean Within Group Misclassification Error Rate of Real Data

Adaweight has better performance than Adaboost in terms of the mean within group misclassification error rate and the number of iterations in finding the rare class

in the real data. Since we put higher weight on the rare class in Adaweight, it has better chance to be differentiated than in Adaboost. Cross validation is needed to avoid over fitting problem.

9.7 Concluding Remarks

In this chapter, we introduce weighted boosting algorithms for two class classification and its connection with forward stagewise additive modeling to get the minimizer of exponential loss. We propose two weighted Adaboost algorithms, i.e., weighted Adaboost-1 and weighted Adaboost-2, which can generate a classifier reaching the theoretical minimum mean within group misclassification error rate, and claim that Weighted Adaboost-2 is superior than weighted Adaboost-1 in terms of getting a close-form solution for β which is a constant in each boosting step. We demonstrate that the best class weight is reciprocal to the class proportion. We discuss the use of validation data to find the stopping criteria, since the rigorous weight update process in Adaweight tends to lead to over fitting problem.

The idea of adding unequal class weights for better performance of unbalanced data classification can be generalized to other boosting methods. We introduce gradient boosting and weighted gradient boosting on regression tree with negative log-likelihood as loss function. We prove that weighted gradient boosting on negative log-likelihood satisfies weighted Bayes rule. Implementation of weighted gradient boosting regression tree and evaluation of its performance, as well as investigation on other weighted boosting methods are our future research objectives on this topic.

Our numerical studies on both simulation data and real data have shown that Adaweight gives smaller mean within group misclassification error rate for unbalanced

data classification. Adaweight tends to converge faster than Adaboost because of its rigorous weight update process. Adaweight is a better classifier for modeling drug discovery data than the benchmark method Adaboost.

Chapter 10

Conclusions

As the first step of a new drug development, modeling drug discovery data is very important and we can benefit a lot from a good statistical model. In this research, we approached drug discovery data classification through two statistical methods.

The complexity of the drug discovery data is high dimensional data with correlation. It is extremely unbalanced while our focus is to detect the rare class. Multiple mechanisms are involved in determining the active class which leads to a mixture regression problem. According to these properties of the drug discovery data, we proposed two methods on its classification.

In Chapter 8, we proposed to use sufficient dimension reduction based clustering methods to classify drug discovery data. The theoretical background that supports these methods is that the central space from dimension reduction retains the regression information needed, such that we will not lose any information by clustering on the reduced space. The reduced space was constructed by the direction that separates the two classes as well as the underlying regression structure within each class. Since the SDR directions contain the class separation information, we justified to sort the data along DR directions and claimed a certain percentage on both sides of that direction as one class. Ranking method provided a good classification result in our simulation studies. Besides SIR, DIR, and SAVE, we implemented L-SIR and compare its performance with the other DR methods. Our simulation studies from

different scenarios showed that DIR is sensitive to mean difference structure, while L-SIR is more efficient in clustering data with variance difference structure. Our simulation study and XUE data investigation results showed that the DR based clustering is better than clustering on the original space. We also obtained an improved computation efficiency by clustering on a reduced space. However, there are some limitations in this work. First, to satisfy linearity condition, we need to assume that the underlying structure of the data is normal distributed, which on one side orients the data collection in the planing stage, but on the other side may violate the foundation of the sufficient dimension reduction if the data has been collected. In this situation, we need to analyze the data first to understand the underlying structure of the data by plotting the histogram, or some other regression methods, and may need to delete some outliers of normal distribution, then choose the dimension reduction and clustering method to best address the classification problem. Second, the current SDR methods all have their own advantages and restrictions, i.e., DIR works the best with mean difference, but completely fails in variance difference, while L-SIR is superior in variance difference, but fails when variance difference is within class noise information. One of the our future research objectives is to search for new SDR methods that works better on real drug discovery data classification, where the data structure is more complicated than in our simulation studies.

In Chapter 9, we proposed a weighted boosting based classification tree to classify drug discovery data. Boosting worked by sequentially applying a classification algorithm to reweighted versions of the training data, then taking a weighted majority vote of the sequence of classifiers thus produced. Our work proved that if we add class weight that is reciprocal to a proportion of the class inside or outside the exponent, we can obtain a final classifier that meets the theoretical minimum of mean within group

misclassification error rate. Our research focused on implementation of weighted Adaboost on regression tree. Regression tree neither get affected by high dimensional data, nor is sensitive to correlation structure. This makes boosting regression tree a good method for high dimensional data classification, which we did not emphasize in our simulation studies included in Chapter 9. We ran simulation study on high dimensional data with $p = 24$ in the descriptor set with mean difference 1 along each dimension and no variance difference. Our classification result was very close to the one we discussed with $p = 6$, only slightly better since we have stronger information, i.e., 24 dimensional differences.

Another point we need to discuss here is that in real drug discovery data set, it is not always possible to have pre information of the percentage of the rare class. The good thing is that as long as we put a large weight on the rare class, it will improve the detection rate, and it does not require the percentage to be the same as the reciprocal of the class proportion. From our theoretical derivation, the closer the two, the closer to the theoretical mean within group misclassification error rate we get. Thus we need to find a good estimate of the proportion of the rare class even though it will not change that much if we use a wrong class weight.

The idea of adding unequal class weights on boosting method is not only limited to Adaboost but can also be generalized to other boosting algorithms, such as gradient boosting. Instead of focusing on classification, gradient boosting is a function estimation method that minimizes a certain loss function. Thus it can be used for both regression and classification problems. In this dissertation, we discussed gradient boosting with negative binomial log-likelihood to perform 2 class classification. We also proved that with unequal class weights, gradient boosting can approach minimized mean within group misclassification error rate. We will implement weighted

gradient boosting with different loss functions for unbalanced data classification and regression as an extension to our current research. Instead of performing cross validation to find the number of components M to be included in our classification rule, regularization through shrinkage is another approach we want to utilize in the next stage. As for the base learner, the limitation is that we have to satisfy Bayes rule. One substitute of classification tree is support vector machine (SVM). Our future objectives include implementation and model selection of these boosting methods and base learners, and generalization from the current 2-class classification to multiclass classification.

Our work in this dissertation provides a theoretical improvement and sheds a light on future research directions in statistical modeling on drug discovery data.

Bibliography

- [1] B. D. Anson, J. Ma, and J.-Q. He, “Identifying cardiotoxic compounds,” *Genetic Engineering & Biotechnology News*, vol. 29, no. 9, 2009.
- [2] S. M. Paul, D. S. Mytelka, C. T. Dunwiddie, C. C. Persinger, B. H. Munos, S. R. Lindborg, and A. L. Schacht, “How to improve r&d productivity: the pharmaceutical industry’s grand challenge.,” *Nat. Rev. Drug Discov.*, vol. 9, pp. 203–214, Mar 2010.
- [3] J. R. Broach and J. Thorner, “High-throughput screening for drug discovery.,” *Nature*, vol. 384, pp. 14–16, Nov 1996.
- [4] D. J. Newman and G. M. Cragg, “Natural products as sources of new drugs over the last 25 years.,” *J. Nat. Prod.*, vol. 70, pp. 461–477, Mar 2007.
- [5] M. Feher and J. M. Schmidt, “Property distributions: differences between drugs, natural products, and molecules from combinatorial chemistry.,” *J. Chem. Inf. Comput. Sci.*, vol. 43, no. 1, pp. 218–227, 2003.
- [6] R. Burbidge, M. Trotter, B. Buxton, and S. Holden, “Drug design by machine learning: support vector machines for pharmaceutical data analysis,” *Computers and Chemistry*, vol. 26, pp. 5–14, 2001.
- [7] R. E. Carhart, D. H. Smith, and R. Ventkataraghavan, “Atom pairs as molecular features in structure-activity studies: Definition and application,” *Journal of Chemical Information and Computer Sciences*, vol. 25, pp. 64–73, 1985.

- [8] K. Liu, J. Feng, and S. S. Young, "Powervm: A software environment for molecular viewing, descriptor generation, data analysis and hit evaluation," *J. Chem. Inf. Model*, vol. 45, no. 2, pp. 515–522, 2005.
- [9] R. S. Pearlman and K. M. Smith, "Metric validation and the receptor-relevant subspace concept," *Journal of Chemical Information and Computer Sciences*, vol. 39, pp. 28–35, 1999.
- [10] F. R. Burden, "Molecular identification number for substructure searches," *Journal of Chemical Information and Computer Sciences*, vol. 29, 1989.
- [11] R. S. Pearlman and K. Smith, "Novel software tools for chemical diversity," *Perspectives in Drug Discovery and Design*, vol. 9–11, no. 0, 1998.
- [12] R. D. King, S. H. Muggleton, A. Srinivasan, and M. J. Sternberg, "Structure-activity relationships derived by machine learning: the use of atoms and their bond connectivities to predict mutagenicity by inductive logic programming.," *Proc Natl Acad Sci U S A*, vol. 93, pp. 438–442, Jan 1996.
- [13] J. Devillers, *Neural Networks and Drug Design*. New York: Academic Press, 1999b.
- [14] J. Devillers, *Genetic Algorithms in Molecular Modeling*. New York: Academic Press, 1999a.
- [15] D. M. Hawkins, S. S. Young, and A. Rusinko, "Analysis of a large structure-activity data set using recursive partitioning," *Quantitative Structure-Activity Relationships*, vol. 16, 1997.

- [16] D. Manallack and D. Livingstone, “Neural networks in drug discovery: have they lived up to their promise?,” *European Journal of Medicinal Chemistry*, vol. 34, 1999.
- [17] D. Goldberg, *Genetic Algorithms In Search, Optimization and Machine Learning*. MA: Addison-Wesley, 1989.
- [18] S. K. Murthy, S. Kasif, and S. Salzberg, “A system for oblique induction of decision trees,” *Journal of Artificial Intelligence Research*, vol. 2, pp. 1–32, 1994.
- [19] R. L. H. Lam, W. J. Welch, and S. S. Young, “Cell based analysis of high throughput screening data for drug discovery,” tech. rep., Institute for Improvement in Quality and Productivity, University of Waterloo, 2002. Research Report RR-02-02.
- [20] Y. Yuan, H. A. Chipman, and W. J. Welch, “Harvesting classification tree for drug discovery,” tech. rep., University of British Columbia, Canada, 2006. Preprint submitted to *Elsevier Science*.
- [21] J. M. Hughes-Oliver, A. Brooks, W. J. Welch, M. G. Khaledi, D. Hawkins, S. S. Young, K. Patil, G. W. Howell, R. G. Ng, and M. T. Chu, “Chemmodlab: A web-based cheminformatics modeling laboratory,” *Cheminformatics*, 2010.
- [22] V. Vapnik, *Statistical Learning Theory*. New York: Wiley, 1998.
- [23] R. D. Cook, “Graphics for regressions with a binary response,” *Journal of American Statistical Association*, vol. 91, pp. 983–992, 1996.
- [24] R. D. Cook, *Regression Graphics: Ideas for studying regressions through graphics*. New York: Wiley, 1998.

- [25] K. C. Li, “Sliced inverse regression for dimension reduction,” *Journal of American Statistical Association*, vol. 86, pp. 316–342, 1991.
- [26] R. D. Cook and S. Weisberg, “Discussion of “sliced inverse regression for dimension reduction”,” *Journal of American Statistical Association*, vol. 86, pp. 316–342, 1991.
- [27] B. Li and S. Wang, “On directional regression for dimension reduction,” *Journal of American Statistical Association*, vol. 102, no. 479, pp. 997–1008, 2007.
- [28] R. D. Cook and F. Critchley, “Identifying regression outliers and mixtures graphically,” *Journal of American Statistical Association*, vol. 95, no. 451, pp. 781–794, 2000.
- [29] Q. Wu, F. Liang, and S. Mukherjee, “Localized sliced inverse regression,” in *Proceedings of Neural Information Processing Systems: Annual Conference*, vol. 22, 2008.
- [30] W. K. Fung, X. He, L. Liu, and P. Shi, “Dimension reduction based on canonical correlation,” *Statist. Sinica*, vol. 12, 2002.
- [31] K. C. Li, “On principle hessian directions for data visualization and dimension reduction: Another application of stein’s lemma,” *Journal of American Statistical Association*, vol. 87, pp. 1025–1039, 1992.
- [32] R. D. Cook and B. Li, “Dimension reduction for the conditional mean in regression,” *Ann. Statist.*, vol. 30, 2002.
- [33] R. D. Cook and X. Yin, “Dimension reduction and visualization in discriminant

- analysis,” *Australian and New Zealand Journal of Statistics*, vol. 43, pp. 147–177, 2001.
- [34] Q. Wu, F. Liang, and S. Mukherjee, “Localized sliced inverse regression,” *Journal of Computational and Graphical Statistics*, vol. 19, no. 4, 2010.
- [35] J. H. Wolfe, “A computer program for the maximum-likelihood analysis of types,” tech. rep., U.S. Naval, San Diego, CA, 1965. NPRA-STB-65-15, Naval Personnel Research Activity. (NTIS No. AD-620 026).
- [36] J. D. Banfield and A. E. Raftery, “Model-based gaussian and non-gaussian clustering,” *Biometrics*, vol. 49, no. 3, 1993.
- [37] C. Fraley and A. E. Raftery, “Model-based clustering, discriminant analysis, and density estimation,” *Journal of the American Statistical Association*, vol. 97, no. 458, 2002.
- [38] T. Hastie, R. Tibshirani, and J. Friedman, *The Elements of Statistical Learning: Data Mining, Inference, and Prediction*. New York: Springer, 2nd ed., 2008.
- [39] G. J. McLachlan and T. Krishnan, *The EM Algorithm and Extensions*. Wiley, 1997.
- [40] R. E. Schapire, “The strength of weak learnability,” *Machine Learning*, vol. 5, pp. 197–227, 1990.
- [41] Y. Freund, “Boosting a weak learning algorithm by majority,” *Inform. and Comput.*, vol. 121, pp. 256–285, 1995.

- [42] Y. Freund and R. E. Schapire, “A decision-theoretic generalization of online learning and an application to boosting,” *J. Comput. System Sciences*, vol. 55, 1997.
- [43] J. Friedman, T. Hastie, and R. Tibshirani, “Additive logistic regression: a statistical view of boosting,” *The Annals of Statistics*, vol. 28, pp. 337–407, 2000.
- [44] Y. Sun, A. K. C. Wong, and Y. Wang, “Parameter inference of cost-sensitive boosting algorithms,” in *Proceedings of Machine Learning and Data Mining in Pattern Recognition*, vol. 3587, pp. 21–30, 2005.
- [45] Y. Sun, M. S. Kamel, A. K. C. Wong, and Y. Wang, “Cost-sensitive boosting for classification of imbalanced data,” *Pattern Recognition*, vol. 40, pp. 3358–3378, 2007.
- [46] Y. Freund and R. E. Schapire, “Experiments with a new boosting algorithm,” in *Machine Learning: Proceedings of the Thirteenth International Conference* (M. Kaufman, ed.), (San Francisco), 1996.
- [47] T. Hastie and R. Tibshirani, “Generalized additive models,” *Statistical Science*, vol. 1, pp. 297–318, 1986.
- [48] X. Qiao and Y. Liu, “Adaptive weighted learning for unbalanced multicategory classification,” *Biometrics*, vol. 65, pp. 159–168, 2008.
- [49] J. Friedman, “Greedy function approximation: a gradient boosting machine,” *The Annals of Statistics*, vol. 29, pp. 1189–1232, 2001.
- [50] National Cancer Institute. http://dtp.nci.nih.gov/docs/aids/aids_data.html.